N° d'ordre NNT : 2016LYSEI133

THESE de DOCTORAT DE L'UNIVERSITE DE LYON
opérée au sein de
INSA de Lyon

Ecole Doctorale MEGA EDA162
Mécanique, Energétique, Génie Civil, Acoustique

Spécialité/ discipline de doctorat : Génie Mécanique

Soutenue publiquement le 09/12/2016, par :
Nina Sainte-Marie

A transmission-error-based gear dynamic model – Applications to single- and multi-mesh transmissions

---

Devant le jury composé de :

Dion, Jean-Luc	Professeur	Supméca	Président
Özgüven, Nevzat	Professeur	Middle East TU	Rapporteur
Tenberge, Peter	Professeur	Ruhr-Universität Bochum	Rapporteur
Guingand, Michèle	Maître de Conférences	INSA de Lyon	Examinatrice
Ville, Fabrice	Professeur	INSA de Lyon	Examinateur
Velex, Philippe	Professeur	INSA de Lyon	Directeur de thèse
Roulois, Guillaume	Docteur	Airbus Helicopters	Invité

Département FEDORA – INSA Lyon – Ecoles Doctorales – Quinquennal 2016-2020

SIGLE	ECOLE DOCTORALE	NOM ET COORDONNEES DU RESPONSABLE
CHIMIE	**CHIMIE DE LYON** **http://www.edchimie-lyon.fr** Sec : Renée EL MELHEM Bat Blaise Pascal 3e etage secretariat@edchimie-lyon.fr Insa : R. GOURDON	M. Stéphane DANIELE Institut de Recherches sur la Catalyse et l'Environnement de Lyon IRCELYON-UMR 5256 Équipe CDFA 2 avenue Albert Einstein 69626 Villeurbanne cedex directeur@edchimie-lyon.fr
E.E.A.	**ELECTRONIQUE, ELECTROTECHNIQUE, AUTOMATIQUE** **http://edeea.ec-lyon.fr** Sec : M.C. HAVGOUDOUKIAN Ecole-Doctorale.eea@ec-lyon.fr	M. Gérard SCORLETTI Ecole Centrale de Lyon 36 avenue Guy de Collongue 69134 ECULLY Tél : 04.72.18 60.97 Fax : 04 78 43 37 17 Gerard.scorletti@ec-lyon.fr
E2M2	**EVOLUTION, ECOSYSTEME, MICROBIOLOGIE, MODELISATION** **http://e2m2.universite-lyon.fr** Sec : Sylvie ROBERJOT Bât Atrium - UCB Lyon 1 04.72.44.83.62 Insa : H. CHARLES secretariat.e2m2@univ-lyon1.fr	M. Fabrice CORDEY CNRS UMR 5276 Lab. de géologie de Lyon Université Claude Bernard Lyon 1 Bât Géode 2 rue Raphaël Dubois 69622 VILLEURBANNE Cédex Tél : 06.07.53.89.13 cordey@univ-lyon1.fr
EDISS	**INTERDISCIPLINAIRE SCIENCES-SANTE** **http://www.ediss-lyon.fr** Sec : Sylvie ROBERJOT Bât Atrium - UCB Lyon 1 04.72.44.83.62 Insa : M. LAGARDE secretariat.ediss@univ-lyon1.fr	Mme Emmanuelle CANET-SOULAS INSERM U1060, CarMeN lab, Univ. Lyon 1 Bâtiment IMBL 11 avenue Jean Capelle INSA de Lyon 696621 Villeurbanne Tél : 04.72.68.49.09 Fax :04 72 68 49 16 Emmanuelle.canet@univ-lyon1.fr
INFOMATHS	**INFORMATIQUE ET MATHEMATIQUES** **http://infomaths.univ-lyon1.fr** Sec :Renée EL MELHEM Bat Blaise Pascal 3e etage infomaths@univ-lyon1.fr	Mme Sylvie CALABRETTO LIRIS – INSA de Lyon Bat Blaise Pascal 7 avenue Jean Capelle 69622 VILLEURBANNE Cedex Tél : 04.72. 43. 80. 46 Fax 04 72 43 16 87 Sylvie.calabretto@insa-lyon.fr
Matériaux	**MATERIAUX DE LYON** **http://ed34.universite-lyon.fr** Sec : M. LABOUNE PM : 71.70 –Fax : 87.12 Bat. Direction Ed.materiaux@insa-lyon.fr	M. Jean-Yves BUFFIERE INSA de Lyon MATEIS Bâtiment Saint Exupéry 7 avenue Jean Capelle 69621 VILLEURBANNE Cedex Tél : 04.72.43 71.70 Fax 04 72 43 85 28 jean-yves.buffiere@insa-lyon.fr
MEGA	**MECANIQUE, ENERGETIQUE, GENIE CIVIL, ACOUSTIQUE** **http://mega.universite-lyon.fr** Sec : M. LABOUNE PM : 71.70 –Fax : 87.12 Bat. Direction mega@insa-lyon.fr	M. Philippe BOISSE INSA de Lyon Laboratoire LAMCOS Bâtiment Jacquard 25 bis avenue Jean Capelle 69621 VILLEURBANNE Cedex Tél : 04.72 .43.71.70 Fax : 04 72 43 72 37 Philippe.boisse@insa-lyon.fr
ScSo	**ScSo*** **http://recherche.univ-lyon2.fr/scso/** Sec : Viviane POLSINELLI Brigitte DUBOIS Insa : J.Y. TOUSSAINT Tél : 04 78 69 72 76	M. Christian MONTES Université Lyon 2 86 rue Pasteur 69365 LYON Cedex 07 Christian.montes@univ-lyon2.fr

*ScSo : Histoire, Géographie, Aménagement, Urbanisme, Archéologie, Science politique, Sociologie, Anthropologie

ACKNOWLEDGMENTS

I would like to acknowledge all the people who have, each in his one way, contributed to achieving this research work.

I am very grateful to Philippe Velex, professor at INSA Lyon, for the constant support (and occasional indulgence) he has granted me over the years. It has been a real honor to learn from him, from the very basics of general mechanics to the arcana of gear dynamics. None of this work would have been possible without him and I sincerely thank him for that.

I am thankful to my collaborators and supervisors at Airbus Helicopters for welcoming me in their team and helping me with this project. In particular, I would like to thank Guillaume Roulois, Julien Caillet, Franck Marrot and Matthias Gatti, for offering their help every time I needed it.

I want to express my deep gratitude to Nevzat Özgüven, Professor at the Middle East Technical University, and to Peter Tenberge, Professor at the Ruhr-Universität Bochum for accepting to review this Ph.D. work. I acknowledge them for the time they spent examining this memoir.

I am very much obliged to Michèle Guingand, Associate Professor at INSA Lyon, Jean-Luc Dion, Professor at Supmeca, and Fabrice Ville, Professor at INSA Lyon for accepting to be members of this jury. I thank Mme Guingand for her assistance along this project and Fabrice Ville for teaching me everything he knows about kinematics and for his perpetual good humour.

I have an amicable thought to all my laboratory fellows, past and present. I thank them for all the unforgettable conferences, passionate discussions, comforting cups of coffee, intricate crossword grids, exciting card games (…) we shared together. You have made the past three years a very good souvenir. I address special thanks to my mentor associate Matthieu, to my writing mates JD, Nico and Vincent, to my friends at Loft Chalopin, and to my dearest neighbor Grégoire, for his invaluable benevolence.

Finally, I warmly thank all my friends and family for their unfailing support. I give a big hug to my brother for his indescribable fraternal love and for being my best communication advisor. I have an infinite gratitude for my parents for helping me back on the right track when needed and for their loving kindness. I could not have made – or even started – such a long journey without you, thank you for contributing to its success.

ABSTRACT

The research work presented in this thesis was conducted at the Contact and Structural Mechanics Laboratory (LaMCoS) of INSA Lyon (UMR CNRS 5259) in partnership with Airbus Helicopters.

Noise measurements have shown that helicopters main gearboxes highly contribute to the overall cabin noise. Gear mesh vibrations propagate through the shafts to the rolling element bearings and the casing which becomes a source of radiated noise. The latter is characterized by high-amplitude tones emerging from broadband noise whose frequencies lie in the range of maximum human ear sensitivity.

In the context of continuous improvement in the acoustic comfort of helicopter passengers, it is therefore necessary to analyse and optimize gearbox vibrations in order to reduce casing noise radiations. The research work presented in this memoir is focused on the development of a numerical model dedicated to the prediction of gear system dynamic behaviour, comprising several gear stages and different types of gears. This model relies on classic beam and lumped parameter elements along with specific two-node gear elements for both cylindrical (spur, helical) and spiral-bevel gears. The equations of motion are developed based on time-varying functions representative of mesh excitations which comprise: (a) mesh stiffness functions, (b) quasi-static transmission error under load, and (c) kinematic (or no-load) transmission error.

A number of comparisons with benchmark numerical and experimental results from the literature are presented which demonstrate that the proposed approach is sound as far as single-stage systems with spur, helical or spiral-bevel gears are considered. Validations are then extended to double-stage gears and, here again, it is confirmed that the proposed transmission error based formulation is accurate and can account for tooth shape modifications.

In the second part of the memoir, several examples of application are presented and commented upon. First, the combined influence of tooth pitch errors and load on the dynamic behaviour of gear transmissions is tackled. An extended three-dimensional model and a reduced torsional version are then confronted in order to investigate the dependency between dynamic transmission errors and mesh force / root stress dynamic factors. Further investigations on bearing dynamic response in two-stage spur gear systems are conducted and the particular contributions of profile modifications are analysed. Finally, a system combining a cylindrical gear and a spiral-bevel gear is considered and particular attention is paid to the dynamic couplings between the various meshes and their influence on bearing dynamic responses.

RESUME

Les travaux de recherche présentés dans ce manuscrit ont été conduits au sein du Laboratoire de Mécanique des Contacts et des Structures (LaMCoS) de l'INSA de Lyon (UMR CNRS 5259) en partenariat avec Airbus Helicopters.

Des mesures ont montré que la boîte de transmission principale contribue fortement au bruit perçu en cabine. Les vibrations induites par les engrènements se propagent à travers les arbres jusqu'aux roulements, générant ainsi des efforts dynamiques aux roulements. Ceux-ci sont une source d'excitation pour le carter, lequel devient à son tour une source de bruit rayonné. Ce phénomène se caractérise par des raies émergeant fortement du bruit large bande et dont les fréquences se situent dans la plage de sensibilité maximale de l'oreille humaine.

Dans un contexte d'amélioration permanente du confort acoustique des usagers, il est donc nécessaire d'analyser et d'optimiser le comportement vibratoire des boîtes afin de réduire le niveau de bruit rayonné par le carter. Les travaux de recherche présentés dans ce manuscrit se concentrent sur le développement d'un modèle numérique permettant de prédire le comportement dynamique de transmissions composées de plusieurs étages d'engrenages de types divers. Ce modèle combine des éléments classiques de type poutre, des éléments à paramètres concentrés et des éléments à deux nœuds dédiés à la représentation d'engrenages cylindriques et spiro-coniques. En supposant les corps des engrenages rigides, les équations du mouvement sont écrites sur la base de fonctions du temps, lesquelles sont représentatives des excitations générées par l'engrènement. Ces fonctions, définies en conditions quasi-statiques sont : (a) la raideur d'engrènement, (b) l'erreur de transmission quasi-statique (sous charge) et (c) l'erreur de transmission cinématique (à vide).

Après que les fondements mathématiques de la formulation proposée aient été détaillés, plusieurs éléments de validation sont présentés afin de confirmer sa pertinence. Différents résultats numériques et expérimentaux de la littérature sont utilisés à des fins de comparaison. Il est ainsi démontré que le modèle s'applique aux systèmes à simple étage de réduction, par engrenage cylindrique ou spiro-conique, et que les excitations liées à l'engrènement, ainsi que les phénomènes de flexion d'arbres sont correctement représentés. La validation est ensuite étendue aux systèmes à deux étages de réduction et les résultats confirment que la formulation basée sur les erreurs de transmission permet de tenir compte des corrections de profil.

Finalement, le modèle est utilisé pour diverses applications. Premièrement, l'influence des erreurs de pas sur le comportement dynamique de transmissions par engrenages est discutée, ainsi que l'influence combinée du niveau de chargement appliqué. Dans un second temps, une confrontation est réalisée entre un système tridimensionnel et un système réduit torsionnel afin d'étudier la possible existence d'une relation linéaire entre l'erreur de transmission dynamique et différents coefficients dynamiques (portant sur l'effort à la denture ou la flexion en pied de dent). Le contenu spectral de la réponse au niveau des roulements est ensuite étudié pour des systèmes à deux engrènements cylindriques et l'influence d'une part des corrections de profil et d'autre part du déphasage entre les engrènements est discutée. Enfin, une application est réalisée sur un système comprenant un engrenage cylindrique combiné à un engrenage spiro-conique. Les phénomènes de couplage entre les étages successifs sont mis en évidence ainsi que la contribution des deux engrènements au contenu spectral de la réponse aux roulements.

TABLE OF CONTENTS

LIST OF FIGURES

LIST OF TABLES

NOMENCLATURE

α_t	Apparent pressure angle
β_b	Base helix angle
δe	Initial shape deviation
δ_N	Normal displacement
Δ	Tooth deflection
ε	Variable depending on the sense of rotation and helix orientation of the pinion
ς	Variable depending on the sense of rotation of the pinion
θ	Torsional angular perturbation
ρ	Percentage of modal strain energy stored in the gear mesh
σ	Bending stress
τ	Dimensionless time variable
$\varphi(t, \boldsymbol{X})$	Time-varying, possibly non-linear scalar function
Ω	Rigid-body angular velocity
$[\boldsymbol{C}]$	Global damping matrix
C_m, C_r	Motor and resistive torques
DF_σ	Dynamic stress factor
DF_{mf}	Dynamic mesh force factor
$\boldsymbol{F}_0$	Vector of the nominal input and output torques
$\boldsymbol{F}_{mesh}$	Inter-mesh force wrench
F_S	Static normal mesh force
F_t	Tooth force
G	Centroid of mesh force distribution
I, J	Transverse and polar moments of inertia
$[\boldsymbol{K_{sys}}]$	Global stiffness matrix (excluding gears)
$[\bar{\boldsymbol{K}}]$	Global stiffness matrix incl. average mesh stiffness
$[\boldsymbol{K}_G]$	Gear stiffness matrix
$k(t, \boldsymbol{q})$	Time-varying, possibly non-linear mesh stiffness
k_m	Time-averaged mesh stiffness
L_b	Distance to base radius
$\bar{M}_b$	Normalized tooth bending moment

M_b^{max}	Maximum static bending moment
$[\boldsymbol{M}]$	Global mass matrix
$[\boldsymbol{M}_G]$	Gear mass matrix
$\boldsymbol{n}$	Unit outward-pointing normal vector
$NLTE$	No-load transmission error
$O_{1,2}$	Center of pinion, gear
$\boldsymbol{q}$	Pinion and gear DOFs vector
R_b	Base radius
T_m	Mesh period
TE	Transmission error under load
$u, v, w, \theta, \varphi, \psi$	Degrees-of-freedom associated to any node
$\boldsymbol{v}_G$	Gear structural vector
$\boldsymbol{V}_G$	$\boldsymbol{v}_G$ extended to total number of DOFs
$\boldsymbol{W}$	Projection vector for transmission error
$\boldsymbol{X}$	Global DOF vector
$\boldsymbol{X_0}$	Static solution with averaged mesh stiffness
$\widehat{\boldsymbol{X}}_0$	Solution of the auxiliary problem

Subscripts

d	Dynamic
1	Relative to the pinion
2	Relative to the gear
S	Static

Superscripts

$\dot{A}$, $\ddot{A}$	First and second time-derivatives of A
-1	Matrix inverse
$0-p$	Half of peak-to-peak value
(L)	Relative to mesh (L)
rms	Root-mean-square value
T	Matrix transpose

GENERAL INTRODUCTION

Helicopters are known to be particularly noisy with cabin noise levels above 90 dB hardly endurable without appropriate ear protections. Customer satisfaction can naturally be significantly impacted by noise quality and environmental noise directives are issued to regulate noise exposure. Helicopter noise reduction is therefore a serious concern for designers. On-board noise measurements highlight the prominent contributions of main gearboxes which generate high-amplitude peaks in cabin noise spectra, exceeding broadband noise by up to 30 dB and located in the frequency range of maximum human ear sensitivity (between 1000 Hz and 5000 Hz).

The present work was conducted in partnership between the Contact and Structural Mechanics Laboratory (LaMCoS) of INSA Lyon and Airbus Helicopters and focuses on the development of a numerical model aimed at predicting gearbox vibrations. Helicopter power transmissions range from 300 kW for light helicopters to 2500 kW for heavy models and provide very large speed reductions between the engine(s) (rotational speeds up to 23000 rpm) and the main rotor (rotational speed around 300 rpm). The main gearbox is therefore composed of multiple gear stages of different types. Spur and helical gears are used to transmit low or medium torque between parallel shafts whereas spiral-bevel gears are required to transfer rotation to the main rotor shaft. A planetary gear with rotating carrier (epicyclic gear) generally ensures a large final speed reduction to the helicopter blades. At high speeds, gears become a significant source of vibrations propagating through the supporting elements of the transmission (shafts and bearings) to the housing which is a source of radiated structure-borne noise. The definition of gearboxes at the early design stage appears therefore as a compromise between contradictory constraints, i.e., vibration and noise reduction versus mass reduction which remains a major objective in aeronautical applications

The first two chapters of this memoir are devoted to providing the reader with sufficient information for a full understanding of the following sections. **Chapter I** presents the excitation sources associated with gears along with the relevant parameters in gear dynamics and proposes a state of the art of the existing gear dynamic models. **Chapter II** describes the numerical model developed for the prediction of gear transmissions dynamic behaviour. It relies on a transmission-error based formulation of mesh excitations which is adaptable to both cylindrical (spur / helical) and spiral-bevel gears. The theory is first introduced on a simplified one-degree-of-freedom system and then extended to three-dimensional multi-stage gear systems.

The validation of the proposed formulation is addressed in **Chapter III**. Single-stage systems with cylindrical and spiral-bevel gears are analysed and simulation results are compared with various numerical and experimental findings from the literature. The applicability of the formulation to double-stage systems is then assessed based on benchmark results from the literature on gear dynamics. A number of comparisons with other modelling strategies are presented which confirm the validity of the proposed methodology for ideal gears and also gears with tooth profile modifications.

In **Chapter IV**, the model is applied to the specific analysis of the combined influence of pitch errors and load on the dynamic response of a single-stage gear system. The link between dynamic transmission errors and dynamic tooth loads is then investigated by using two

different models: a) a full three-dimensional approach including the pinion, gear, shafts, bearings and couplings, and b) a simplified torsional model restricted to the pinion and gear only. Another example of application concerns the dynamic response of bearings in double-stage spur gear systems. The influence of the relative phase shift on the dynamic response of the idler gear system is also evaluated. Finally, a system combining a cylindrical and a spiral-bevel gear, as is the case in helicopter transmissions, is studied. The couplings between the various meshes are clearly illustrated and the role of the shaft connecting the two gears is highlighted.

Chapter I
Gear dynamics – State of the art

This first chapter proposes a state of art of gear dynamics.

The first section will provide an overview of the process of vibrations by gear transmissions and their consequences will be presented through a few examples. The issue of gear noise in helicopters will be discussed.

The second section will focus on the different types of excitations generated at the mesh. These excitations will be presented in two categories and we will show how the contributions of each one of them can be accounted for in gear modelling.

The concepts of transmission error and dynamic factor will then be introduced as key parameters for gear dynamic studies. Their definition is crucial for the understanding of the work presented in the following chapters of this thesis.

A review of the literature will be proposed in a final section. The different types of existing dynamic models will be exposed and an attempt is made to classify these models into distinct categories in order to facilitate the reading. Models for cylindrical and bevel gears will be treated separately before presenting the existing models of multi-stage systems.

In conclusion, the strategy adopted for gear noise modelling will be detailed and the objectives of this PhD work will be highlighted.

1 THE GEAR NOISE ISSUE IN HELICOPTERS

Geared transmissions are widely used in industry because of their high efficiency and low power-to-weight ratio. Gears have the capacity to transmit high loads and operate at high speeds thus making them interesting in aeronautics, naval or automotive applications. However, high rotational speeds can generate dynamic phenomena which may have severe consequences not only for the gears and but also the surrounding mechanical elements.

When operating at high rotational speeds, gears become a significant source of vibrations which are transferred to the rest of the transmission system via the supporting elements (shafts, bearings, housing). Such vibrations are detrimental for the gears themselves as they can cause dynamic overloads between the mating teeth possibly leading to contact failures such as pitting and tooth breakage.

The other direct consequence of gear vibrations is the noise, main issue considered in this research work. Gear noise manifests itself in two different ways: a) under light loads, momentary contact losses can occur between gear teeth, leading to vibro-impacts and so-called rattle noise very common in automotive transmissions [1] and, b) tonal sound known as whining noise at larger loads. The latter is typically the kind of noise produced by helicopters main gearboxes, which transmit power up to several megawatts.

The supporting elements of the transmission (shafts and bearings) ensure structure-borne propagation of the vibrations from the gears to the housing which becomes a source of radiated noise [2]. In most cases, airborne propagation of housing radiations are considered as the predominant source of noise. Moreover, vibrations propagate through the gearbox suspension to the structure, inducing sound radiation of the structure itself. This structure-borne noise highly contributes to helicopter global cabin noise, because of the MGB location and suspension system. In some cases, it is considered to represent at least 40% of the global MGB noise propagated to the cabin.

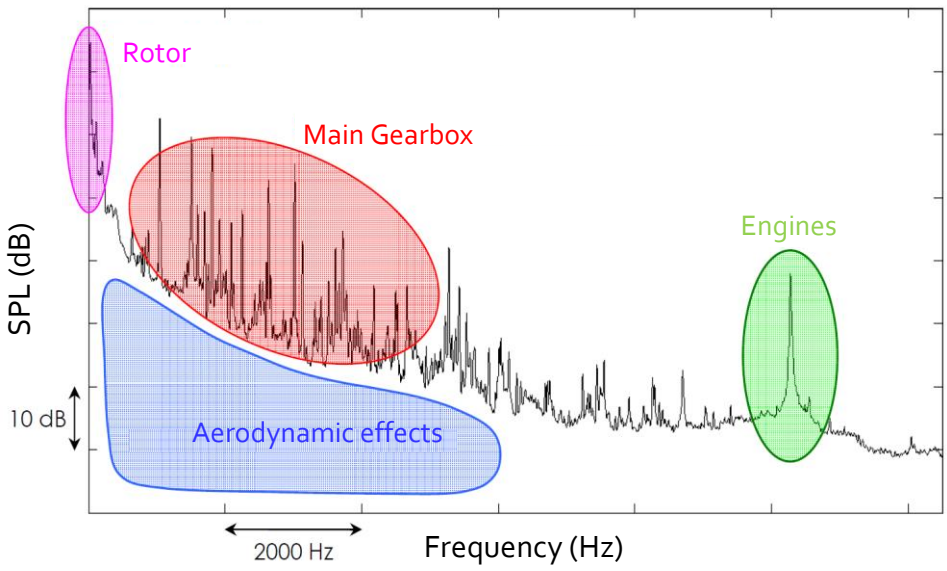

Figure I-1 : Measured cabin noise spectrum (advanced flight phase), acc. to Roulois [3]

The study of noise spectra recorded inside helicopter cabins allowed to identify the main contributors to cabin noise [3–5]. A typical cabin noise spectrum is shown in Figure I-1. The main rotor generates high-level noise (above 100 dB) at low frequency (around 20 Hz). Aerodynamic effects manifest themselves as broadband noise whose level decreases with increasing frequencies. The engines are characterized by noise at high frequency (around 10 kHz). This noise emerges significantly from broadband noise but is not the most annoying because of its elevated frequency. The MGB however, generates several level rays which emerge from the broadband noise from up to 30 dB and lie in a range of human ear maximum sensitivity (between 1 and 5 kHz). For these reasons, MGB is considered as one of the main preponderant source of noise inside the cabin of a helicopter.

The main rotor speed in a helicopter is relatively low (200-400 rpm) compared with that of engines (up to 23 000 rpm) and several gear stages are needed to reduce speed accordingly. The main gearbox architecture depends on helicopter characteristics (power needed, engines speeds and locations, rotor speed, etc.) and Figure I-2 shows a typical example for twin-engine helicopters. Main gearboxes usually comprise several types of gears: spur and helical gears are used to transmit low or medium torque between parallel shafts whereas spiral-bevel gears are required to transfer rotation to the main rotor shaft. A planetary gear with rotating carrier (epicyclic gear) generally ensures a large final speed reduction to the helicopter main rotor.

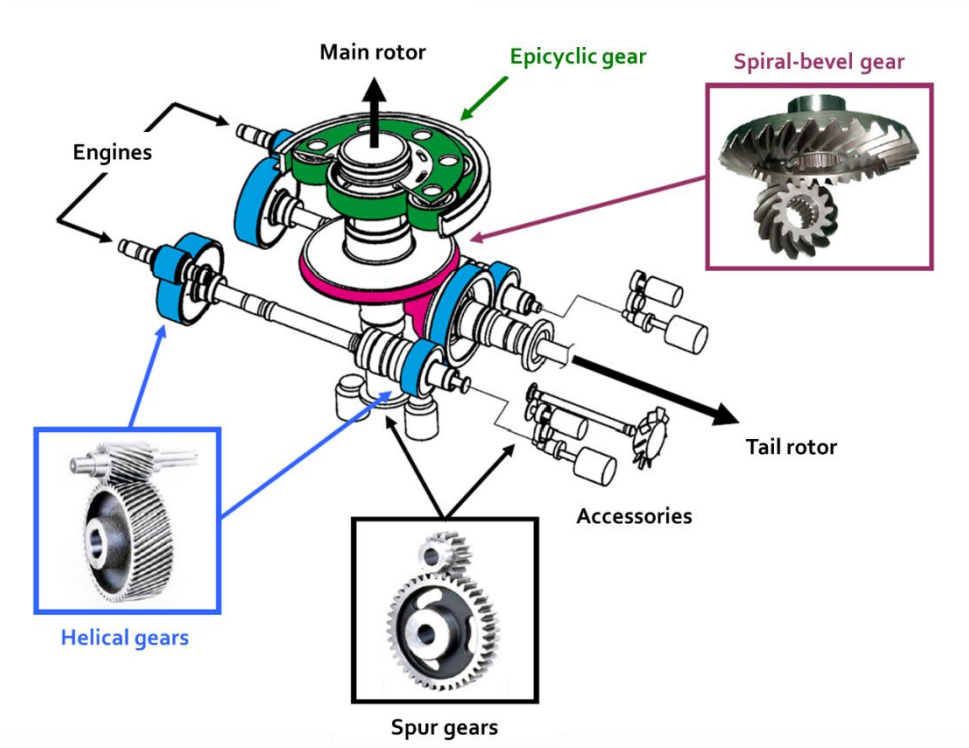

Figure I-2 : Components of the main gearbox of a twin-engine helicopter (from Roulois [3])

The propagation of gear noise to helicopter cabin is rather well understood in terms of sources and paths. The meshing process generates gear vibrations (as detailed in **Chapter I – Section 2**) which are transferred from the gears to the bearings through the supporting shafts. Under the action of the dynamic forces induced at the bearings, the casing vibrates and radiates air-borne noise as illustrated in Figure I-3. Transmission noise then follows two simultaneous paths [6] : direct airborne radiation and structure borne radiation. The magnitude of airborne contribution is mostly governed by the geometry of the casing and its ability to radiate acoustic power. Structure borne radiation is particularly difficult to stem. The transmission mounts must be strong enough to allow helicopter lift-off and rigid enough for stable control. They are therefore very favourable to the transmission of gear vibrations to the airframe, causing vibrations of its structure and direct radiation of noise inside the cabin.

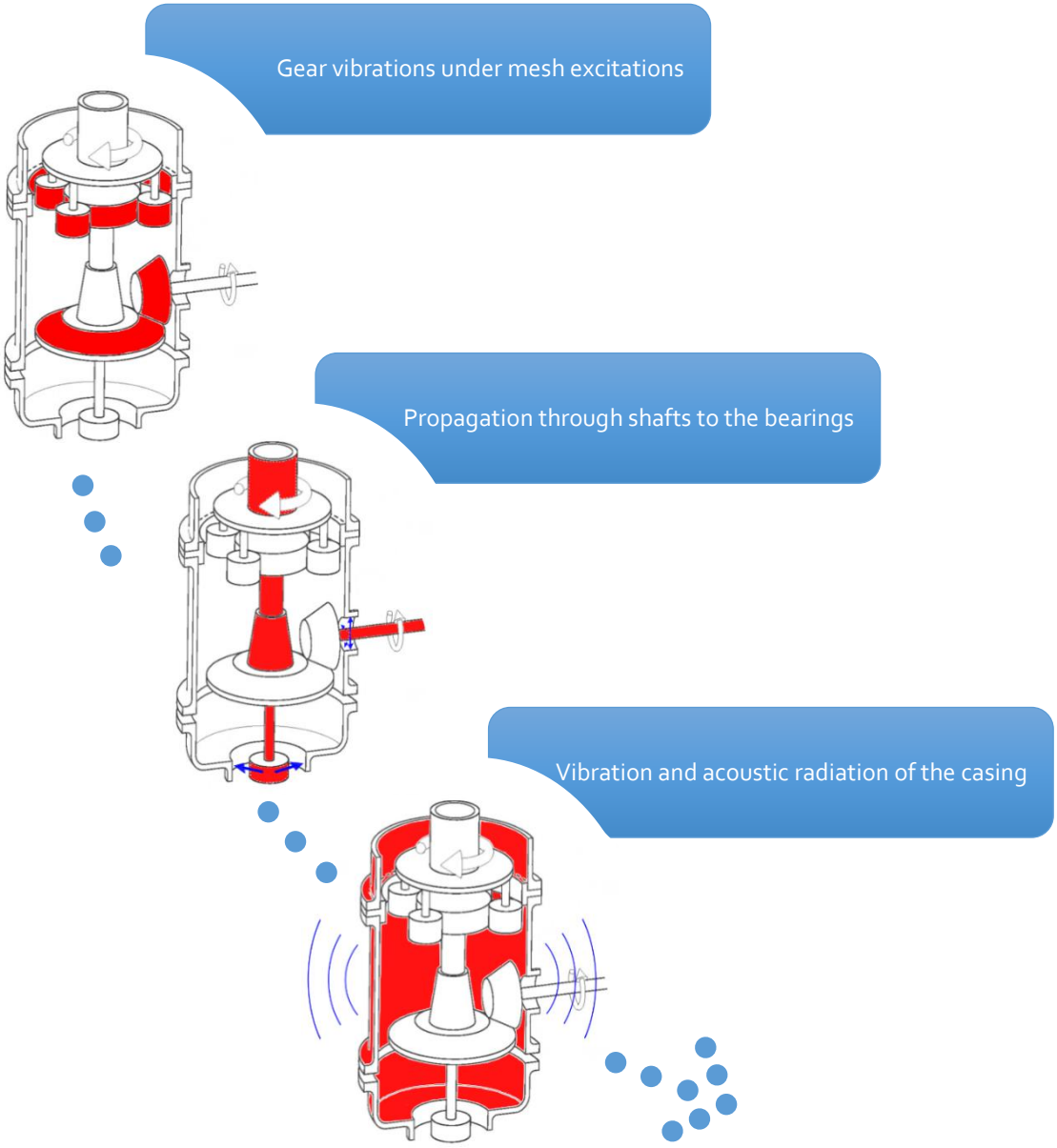

Figure I-3 : From mesh excitations to acoustic radiation of the gearbox casing

The prevalence of gear noise inside the cabin has been experimentally demonstrated since internal noise spectra exhibit several tones highly emerging from broadband noise which correspond to the fundamentals and first harmonics of the mesh frequencies. Noise spectra also indicate that all gear types contribute to cabin noise (cf. Figure I-4).

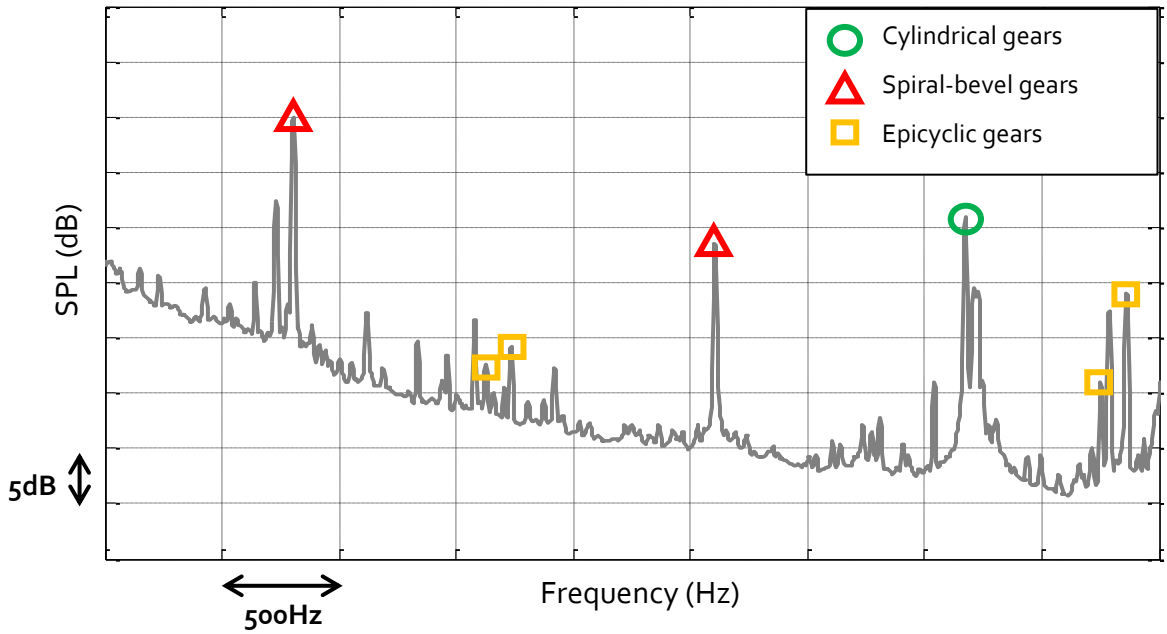

Figure I-4 : Typical noise spectrum registered in a helicopter cabin – Identification of main contributing gears

Over the last years, noise reduction has become a major challenge in aeronautics (and especially for helicopter manufacturers). Since MGB appears as one of the main source of noise inside the cabin, efforts are devoted to the reduction of its contribution. Besides, helicopters mass and production costs both have to be kept limited. Therefore, the addition of soundproofing solutions is not a reliable solution to the MGB noise issue. For these reasons, noise optimization of the MGB has to be considered at the early design stage.

Numerous dynamic models have been developed to address the major issue of acoustic comfort, especially in the field of transports. A review of these models is proposed in **Section 4** of this chapter. Beforehand, the excitation sources associated with gears and the relevant parameters in gear dynamics are briefly presented.

2 EXCITATION SOURCES

As shown earlier, gears are significant sources of vibrations because of their operating principle for transmitting power and their unavoidable manufacturing inaccuracies.

Gears transmit loads by obstacles (gear teeth) which undergo elastic deflections when loaded. Stiffness is often used to characterize how much teeth deflect under load, depending on gear geometry. The number of teeth in contact is not constant with time and therefore, the stiffness of the pinion-gear pair varies during the meshing process thus giving rise to parametric excitations even for perfect gear geometries. Manufacturing and assembly always lead to small positioning errors within tolerances depending on the quality grade of the gears. Besides, it is sometimes necessary to voluntarily modify gear tooth shapes in order to avoid premature engagements and delayed recesses, improve tooth load distributions, reduce transmission errors etc. Both errors and tooth shape modifications can also generate excitations and will be further addressed under the generic terminology of shape deviations.

2.1 Elastic deformations and mesh stiffness

Since the early spring-mass models developed by Tuplin [7], Figure I-5, the pinion-gear interface is usually represented as a spring acting in the plane of action whose stiffness is characterised from the elastic deflections under load. The very first models of this kind were based on constant stiffness elements which were rapidly improved to account for mesh stiffness time-variations [8,9]. The transmitted load is generally constant (imposed by the input torque) but teeth deflections vary along the mesh cycle with the change in the number of tooth pairs in contact. Schematically for spur gears, the pinion-gear pair is often considered as twice as stiff when two pairs of teeth are in contact compared with the situation of one single tooth pair in mesh.

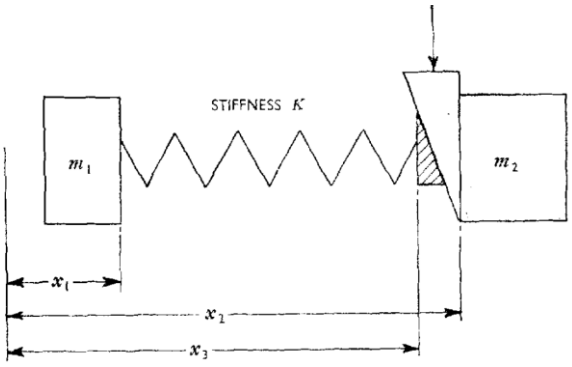

Figure I-5 : Constant stiffness spring-mass model (acc. to Tuplin [7])

Several approaches have been proposed to quantify mesh stiffness and its fluctuations. A first category considers that the global mesh stiffness results from different individual contributions comprising:

- tooth bending,
- tooth base deflections,
- contact deformations.

Tooth bending deflections are determined by approximating one tooth by a cantilever of variable cross-section (bi-dimensional approach, [10–12]) or a plate of variable thickness on an elastic foundation (3-dimensional approach, [13,14]).

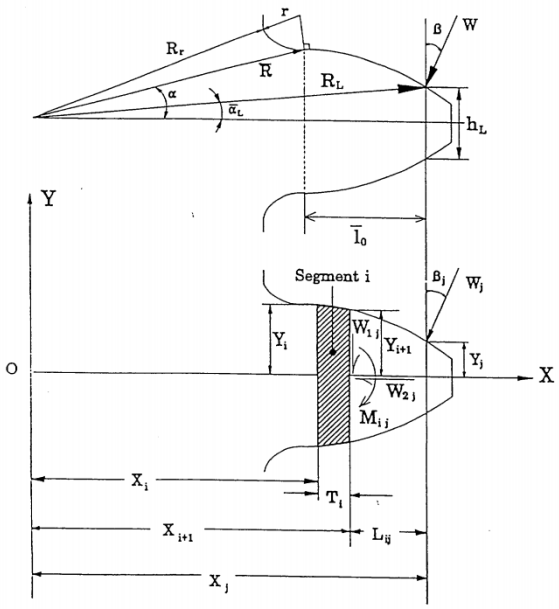

Figure I-6 : Estimation of bending deflections using beam theory, acc. to Lin et Liou [12]

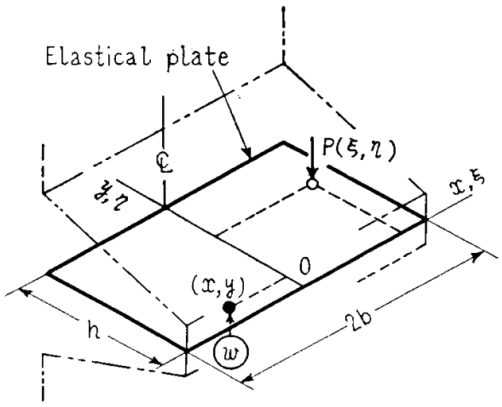

Figure I-7 : Estimation of bending deflections using tapered plate theory, acc. to Umezawa [13]

Tooth base deflections are often derived by considering that the tooth-gear body junction can be represented by a semi-infinite elastic half space submitted to the stress distributions representative of the influence of the load applied on the tooth profile [10]. A better approximation was developed by Sainsot *et al*. who simulated gear body as an elastic annulus [15]. The validity of the method was proved by comparing the analytical results with those obtained using 2D finite elements. Stegemiller and Houser performed a three-dimensional analysis of base deflections, using the moment image method to account for tooth end effects [16]. The authors derived a simple model whose results compare well with those given by 3D finite elements.

Contact compliance is usually determined by assimilating the contact between teeth to two infinite elastic half spaces each submitted to a semi-elliptical Hertzian pressure distribution. The most commonly used formulas for contact deflection are those developed by Weber and Banascheck [10] or Lundberg [17]. It must be noted that these approaches do not account for elastic convectivity implying that the displacements are nil at points which are not directly loaded. Ajmi and Velex proposed to use Pasternak's elastic foundations (superposition of bending and shearing elements lying on independent springs) to convey deflections from any loaded points to the neighbouring points, as illustrated in Figure I-8 [18].

All individual contributions are finally combined as lumped stiffness elements in series and / or in parallel to lead to the overall mesh stiffness function [19].

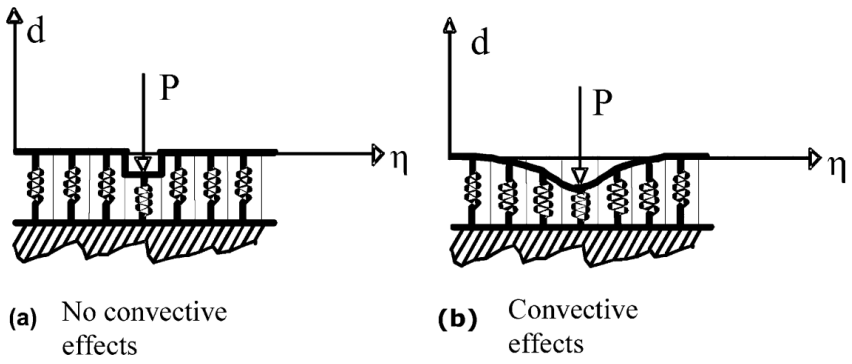

Figure I-8 : Illustration of convective effects on contact compliance, acc. to Ajmi and Velex [18]

Aside from the elementary methods exposed earlier, other global / hybrid approaches can be used to quantify all (global methods) or some (hybrid methods) of the contributions to mesh stiffness.

Complex potential method can be used to determine tooth bending and foundation deflections [20]. Contact compliance could also be estimated from the same method by introducing a realistic pressure distribution. For the sake of simplicity, loading is usually represented by a lumped force and Saint-Venant's principle is applied to determine the structural deflections. Contact contributions are then estimated from an analytical method.

With the steady improvement of computational capacities, finite elements (FE) are widely used and are commonly applied to estimate bending and foundation stiffness. An advantageous method consists in characterizing each contribution by using influence coefficients. These coefficients can be calculated all at once for all angular positions of the pinion/gear pair and allow to account for complex geometries.

The calculation of contact deflections by finite elements requires to use a very fine meshing of the contact zone and to adjust it depending on the contact position on tooth flank [21]. However, such computations remain highly time-consuming and FE models are generally coupled to analytical contact formulation based on Boussinesq's theory [22,23]. The main advantage of the finite element method is the possibility to account for the pinion and gear real geometries thus including the contribution of rim deflections to mesh stiffness, as opposed to most of the other formulations presented so far. This aspect become crucial in a number of industrial applications such as aeronautics for which weight reduction is critical and thin-rimmed gears are often used for which gear body deflections cannot be discarded.

More global approaches consider that mesh stiffness is proportional to contact length which, for spur and helical gears, can be estimated analytically using Fourier series [24] (see Figure I-9). In the ISO 6336 standard [25], mesh stiffness per unit contact length is supposed to be constant and its value is derived from a polynomial curve-fitted equation depending on tooth geometrical parameters. Assuming a parabolic variation of mesh stiffness per unit contact length between engagement and the end of recess, Gu *et al.* proposed an improved formulation [26] which shows that mesh stiffness variations are mostly controlled by profile and face contact ratios and that some values of these parameters can theoretically eliminate mesh parametric excitations, as illustrated in Figure I-10.

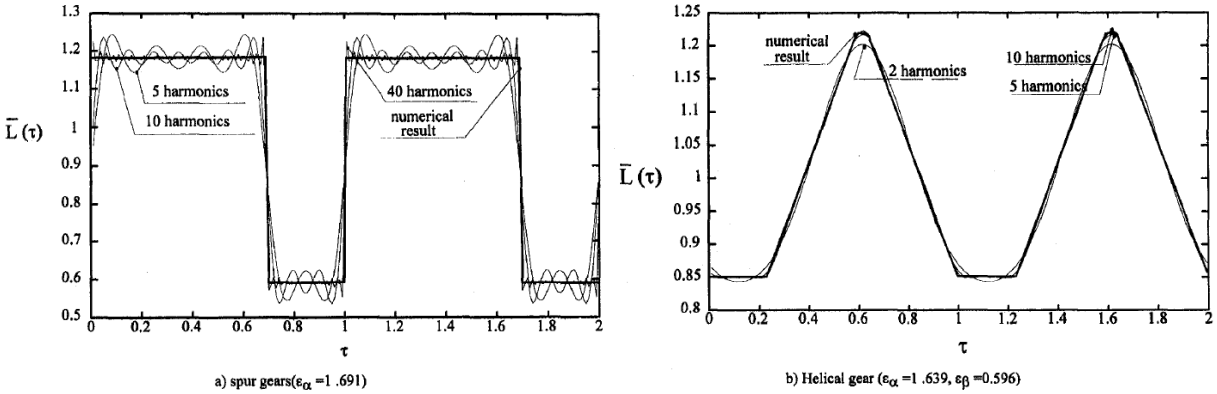

Figure I-9 : Time fluctuations of contact length for a) spur and b) helical gears – Comparison of analytical and numerical approximations, acc. to Maatar and Velex [24]

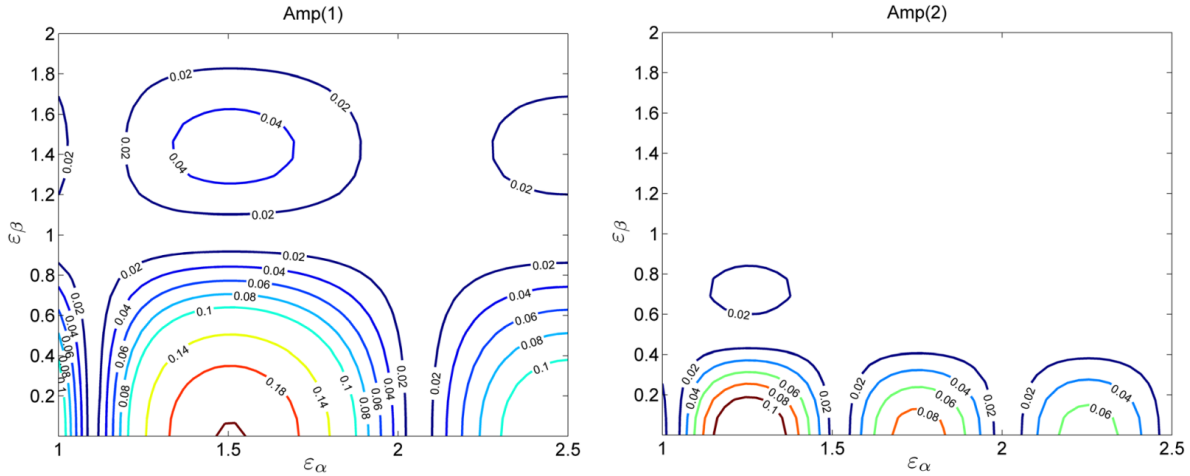

Figure I-10 : Contour plots of the RMS of the dimensionless mesh stiffness function for the first two mesh harmonics versus profile and face contact ratio, acc. to Gu et al. [26]

2.2 Shape deviations and assembly errors

Tooth profiles are the traces of tooth flanks in planes perpendicular to the axis of rotation and, except for very specific applications such as horology [27], the vast majority of cylindrical gears exhibit involute profiles. One advantage of involute mating profiles is that they are conjugate thus ensuring a uniform velocity transfer from the pinion to the gear [28]. Besides, centre distance variations do not impact on involute gears operation, as opposed to cycloidal gears for example and a constant speed ratio is conserved. For involute spur and helical gears, the contacts between the teeth are line contacts which all lie in a plane tangent to the base cylinders, i.e. keeping a constant orientation in space or a line when considering bi-dimensional representations which is known as the line of action.

Although modern manufacturing processes can reach very high precision levels, gear teeth will never be perfect and the deviations with respect to the theoretical tooth flanks are characterised by a number of geometrical parameters whose tolerances define gear quality grades [29,30]. The main tooth shape deviations are classified into distinct categories:

- pitch errors which represent the differences between the theoretical pitch (distance between two successive teeth) and the real pitches measured around the pinion and the gear,
- profile deviations which give, at any point on the tooth flank, the distance between the theoretical and real profiles,
- helix deviations which correspond to the quantity from which the actual helix deviates from the helix of reference.

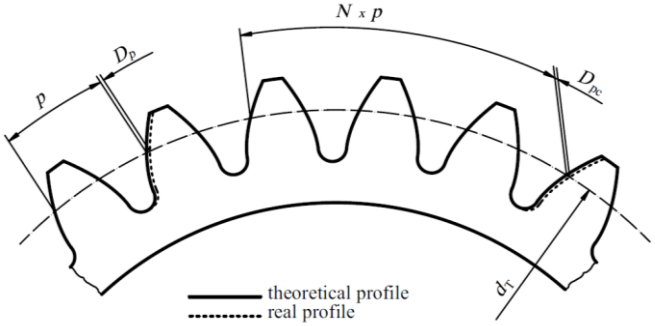

Figure I-11 : Illustration of single (D_p) and cumulated pitch errors (D_{pc}) acc. to Jelaska [31]

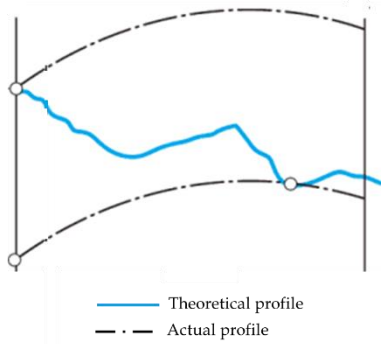

Figure I-12 : Illustration of total profile deviations acc. to ISO1328 [29]

Assembly or mounting errors often add up to tooth shape deviations. For example, if the shafts are not perfectly parallel, misalignments arise and the contact zones between the mating teeth can be significantly altered. Other common assembly errors comprise position errors of the centres of the pinion and gear or deviations between the axes of rotation and the principal polar axes of inertia of the pinion and the gear. These errors generate eccentricities and run-out characterised by strong once-per-revolution excitations.

On the other hand, voluntary profile deviations are frequently employed: gear teeth are modified by removing material at the tip and/or the root in order to improve contact conditions. These shape modifications can be achieved along the profile or in the direction of the face width (longitudinal or "lead" modifications). Profile modifications are applied at the top and/or root of the teeth (on the pinion and/or gear) mostly to prevent from premature engagements and shocks due to tooth deflections. They are usually characterized by their amplitude (or depth) and by their extent (or length) which can either be measured along the profile or along the line of action

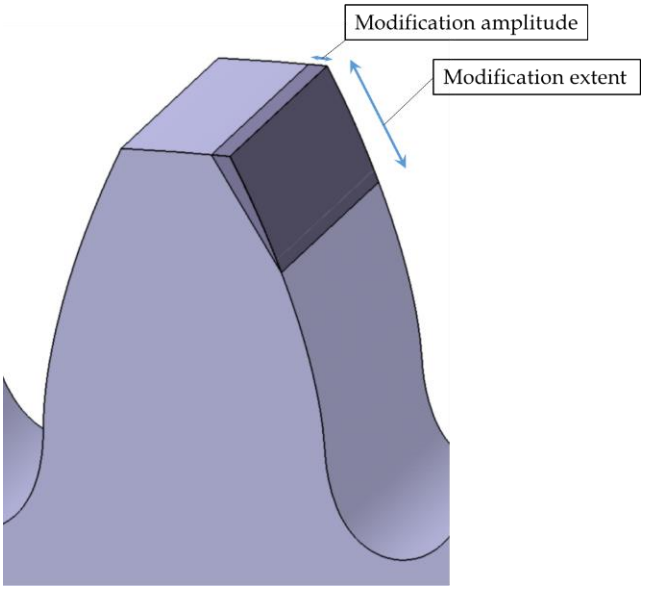

Figure I-13 : Illustration of linear profile modification (tip relief)

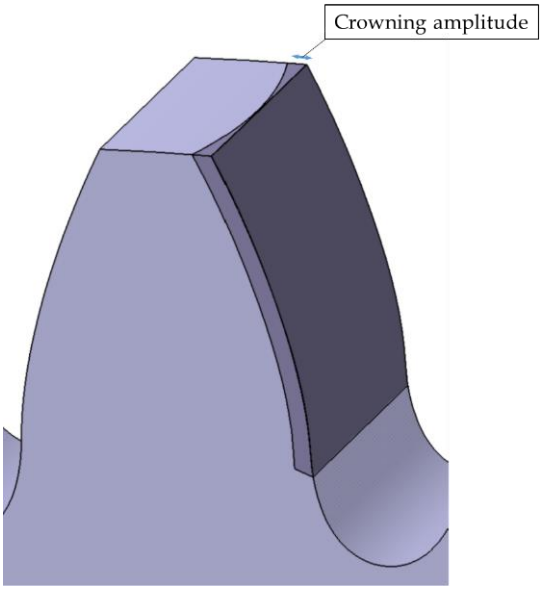

Figure I-14 : Illustration of longitudinal modification (crowning)

All shape deviations alter the contact conditions between mating teeth and experimental results prove that they can also be influential on gear dynamics [32]. The excitations induced by shape deviations and assembly errors are often accounted for via the concept of transmission errors, which will be presented in **Section 3.1**. In particular, quasi-static transmission error is commonly used as a forcing term in dynamic models but also as a design criterion to reduce mesh excitations.

3 PARAMETERS IN GEAR DYNAMICS

A few key parameters are commonly employed in the literature on gear dynamics which are introduced in the following section.

No-load and quasi-static transmission errors are used to characterize mesh excitations and the influence of shape and mounting errors whereas dynamic transmission errors and dynamic factors are widely used metrics to quantify the dynamic response of geared systems.

3.1 Transmission errors

The concept of transmission error was first introduced by Harris in 1958 [33]. Starting from the consideration that dynamic tooth loads depend on tooth elasticity, errors and modifications, the author suggested that the variations in relative displacements between gears at low speeds were at the origin of vibrations when operating at higher speeds. Numerous experiments confirmed that the time-variations of static transmission errors are actually representative of mesh excitations. Since transmission errors include the influence of mesh deflections, they depend on load. In the specific context of profile modification in spur gears, Harris introduced the notion of design load which corresponds to that particular load or torque for which transmission error is theoretically constant, i.e., mesh excitations are minimal. By plotting for one given gear, the transmission error curves at different loads on the same graph, the author generated the so-called Harris maps which provide a clear overview of the system behaviour in terms of profile modifications and load (cf. Figure I-15), and which have since been extensively used in the literature.

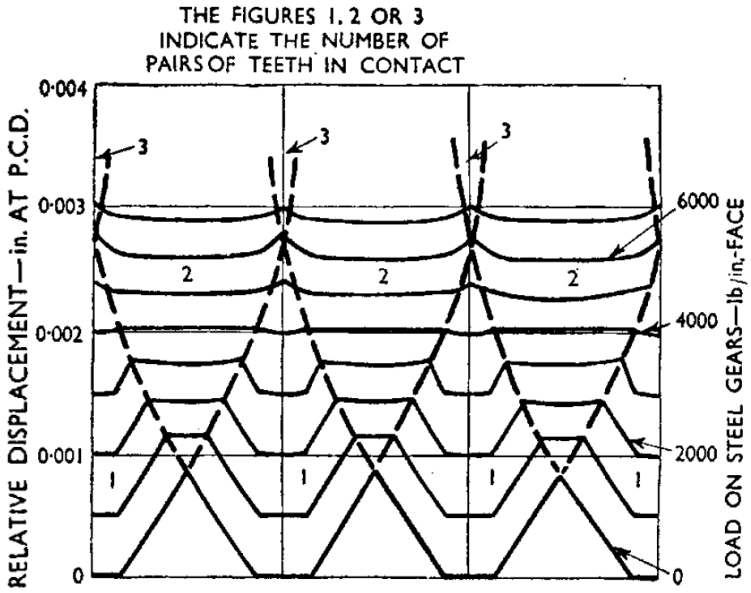

Figure I-15 : Harris map - Variation of transmission error with load, from [33]

Transmission error was later defined as "for any instantaneous angular position of one gear, the angular displacement of the mating gear from the position it would occupy if the teeth were rigid and unmodified" [9] as illustrated in Figure I-16.

Transmission error can be expressed as an angular deviation but it is also often expressed as a distance by projection on the base plane.

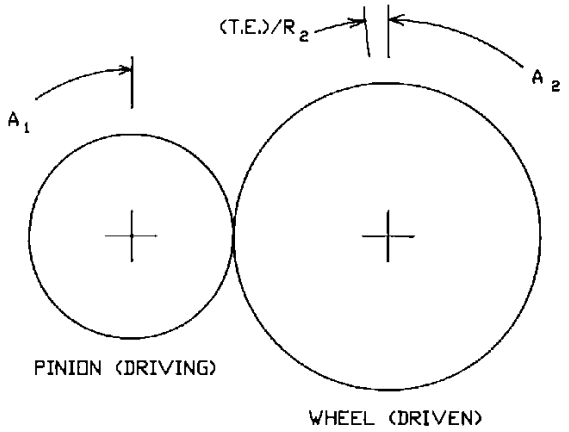

	PINION	WHEEL
NUMBER OF TEETH	Z_1	Z_2
BASE RADIUS	R_1	R_2
THEORETICAL ANGULAR POSITION	A_1	$A_2 = A_1.Z_1/Z_2$
ACTUAL ANGULAR POSITION	A_1	$A_2 + (T.E.)/R_2$
ACTUAL POSITION IN LINEAR TERMS	A_1R_1	$A_2R_2 + (T.E.) = A_1R_1 + (T.E.)$

Figure I-16 : Definition of transmission error, acc. to Munro [34]

3.1.a) *No-load transmission error*

No-load transmission error, also referred to as kinematic transmission error, is relevant for assembly errors, pitch errors and some types of tooth modifications. For any angular position of the driving member, no-load transmission error is dictated by the maximum deviation from perfect tooth flanks when considering all the contacts in the base plane at one given time. It therefore describes the rigid-body rotation of the driven member with respect to its theoretical position if the pinion and gear were perfect and rigid.

In the absence of errors and if tooth flanks are unmodified (perfect involute profile), the no-load transmission error is nil. If the profile is modified over a large extent or in the presence of lead crowning (for helical gears), no-load transmission error is not nil and its value varies along the mesh cycle with a period equal to that of meshing (assuming that all the teeth of the pinion (respectively the gear) have the same modification). Pitch errors however generate a no-load transmission error function whose period is the least common multiple of the pinion and gear rotational periods. A radial run-out on one of the gears generates a sine-wave shaped no-load transmission error at once-per-revolution frequency. Records of no-load transmission error typically show the influence of both phenomena (revolution- and tooth-periodic), as illustrated in Figure I-17.

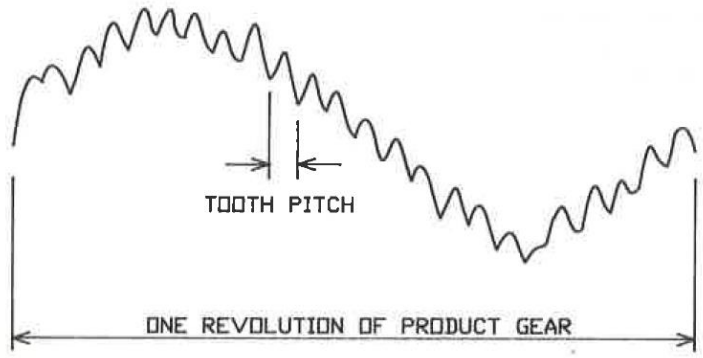

Figure I-17: Typical no-load transmission error signal, acc. to Munro [34]

3.1.b) *Quasi-static transmission error*

In addition to tooth modifications and errors, the departure from perfect motion is also due to tooth deflections under load which is also captured by quasi-static transmission errors. As the load transmitted by gears is often constant, quasi-static transmission errors vary with the number of tooth pairs in contact or contact length, opposite to mesh stiffness functions.

It has been experimentally verified that the time-variations of quasi-static transmission error correlate well with gear noise and vibrations [35]. Transmission error is therefore recognized as a reliable indicator of mesh excitations and often, by extension, of gear noise quality. Lin *et al.* have studied the dynamic response of a spur gear pair with various modifications and their results show that the lowest amplifications are obtained when the modifications give the lowest peak-to-peak transmission error [36], as shown in Figure I-18.

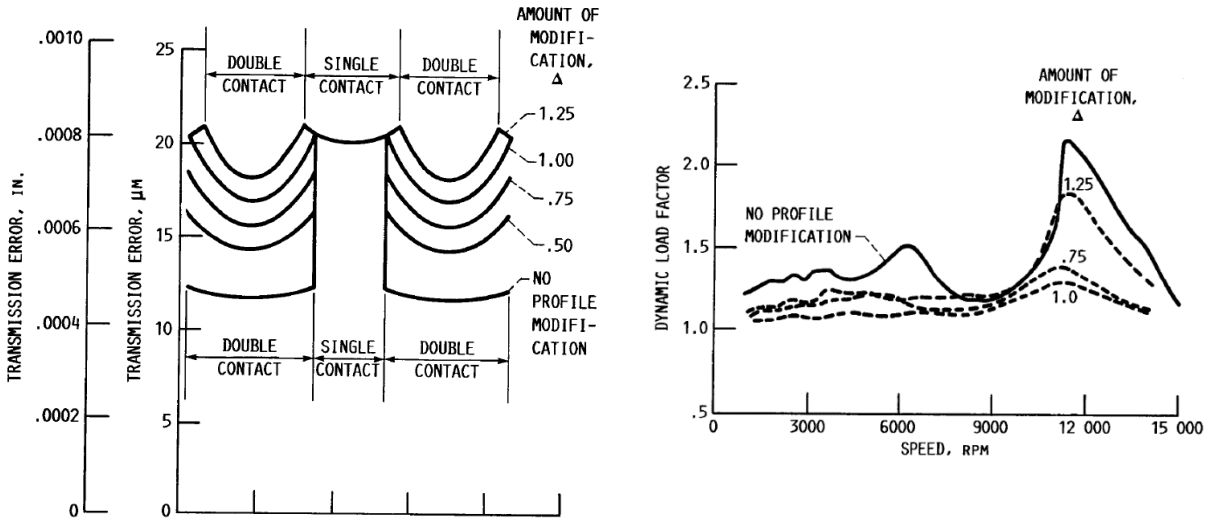

Figure I-18 : Quasi-static transmission and dynamic factor for various profile modifications, acc. to Lin et al. [36]

Consequently, transmission error is frequently employed as a design criterion to define tooth modifications minimizing dynamic tooth loads and noise. Beghini *et al.* led parametrical studies on the influence of the extent of profile modifications on peak-to-peak quasi-static transmission error for high and low contact ratio spur gears and provided optimization guidelines [37]. Using an objective function based on quasi-static transmission error and

genetic algorithms, Bonori *et al.* defined optimum profile modifications for spur gears, and proved the efficiency of the predicted optima [38]. Artoni *et al.* proposed an algorithm for the optimization of hypoid gear ease-off with regard to quasi-static transmission error variations [39]. Astoul *et al.* developed an algorithm for the optimization of a spiral bevel pinion topography with the aim of reducing the maximum contact pressure along the loaded contact path [40]. The authors later showed that the method could be used to reduce the variations of quasi-static transmission error and performed comparisons between numerical predictions and experimental measurements of transmission error [41]. Based on different mesh stiffness formulations, Bruyère *et al.* have recently proposed a set of analytical formulae to predict optimum profile modifications with regards to transmission error fluctuations for both spur and helical gears. The authors introduced the concept of Master Curve defining the set of optimum linear symmetric tip reliefs [42–44]. Velex *et al.* proved that local transmissions errors are also representative of mesh excitations in multi-stage gear systems [45].

Since its reliability to represent mesh excitations has been largely demonstrated, quasi-static transmission error is directly used as a forcing term in many gear dynamic models, as discussed in **Section 4** of this chapter.

3.1.c) *Dynamic transmission error*

Dynamic transmission error is the extension of quasi-static transmission error for higher rotational speeds when dynamic effects cannot be ignored. It is often used to characterize the vibratory and acoustic behaviour of gear transmissions. Measurement of transmission error can generally be performed by the use of accelerometers mounted tangentially on the gear wheel [46,47] or by optical means using graduated disks and light integration [48] or encoders [49,50]). The time-fluctuations of dynamic transmission error can be used as an element of comparison between model predictions and experimental evidences, as illustrated in Figure I-19.

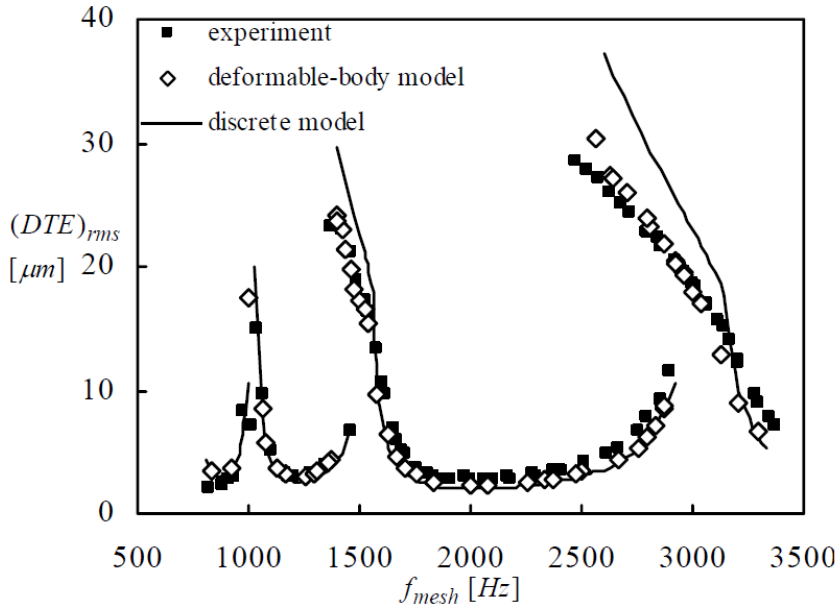

Figure I-19 : Comparison of measured and predicted RMS values of dynamic transmission error, from [51]

Another indicator of gear transmissions dynamic behaviour is the evolution of the dynamic tooth loads, often related to the concept of dynamic factor presented in the next section.

3.2 Dynamic factors

As mentioned in the first section of this chapter, a direct consequence of the dynamic behaviour of gear systems is the occurrence of overloads in the contact zones between the mating teeth. The estimation of the mesh force in dynamic conditions is crucial to predict wear [52], determine the lubrication regimes [53,54] and understand the different modes of tooth failure [55,56].

In this context, the concept of dynamic factor initially introduced by Walker in 1868 is now often used to quantify dynamic overloads and is defined as the ratio of the maximum dynamic to static tooth load. Depending on the authors, the dynamic factor can be expressed based on:

- the global inter-mesh force,
- the force acting on one tooth of the pinion / gear,
- the stress at the root of one tooth of the pinion / gear.

The dynamic factor is therefore not relevant for tooth load distribution analyses but only for characterizing overall dynamic tooth loads.

From an experimental viewpoint, dynamic factor is often correlated with tooth root stresses measured by strain gauges cemented at the root of the teeth. As an example, the dynamic root strains recorded experimentally by Kubo on a spur gear set [57] have been extensively used for dynamic models validation [58–60] (cf. Figure I-20). Such measurements are always delicate and require a very cautious set up of the gauges on the root fillet in order to prevent them from being expelled by centrifugal forces or damaged by the tooth tips of the other member during the course of meshing. They also impose the use of slip rings or telemetry to transfer the measured signal from the rotary to the stationary system.

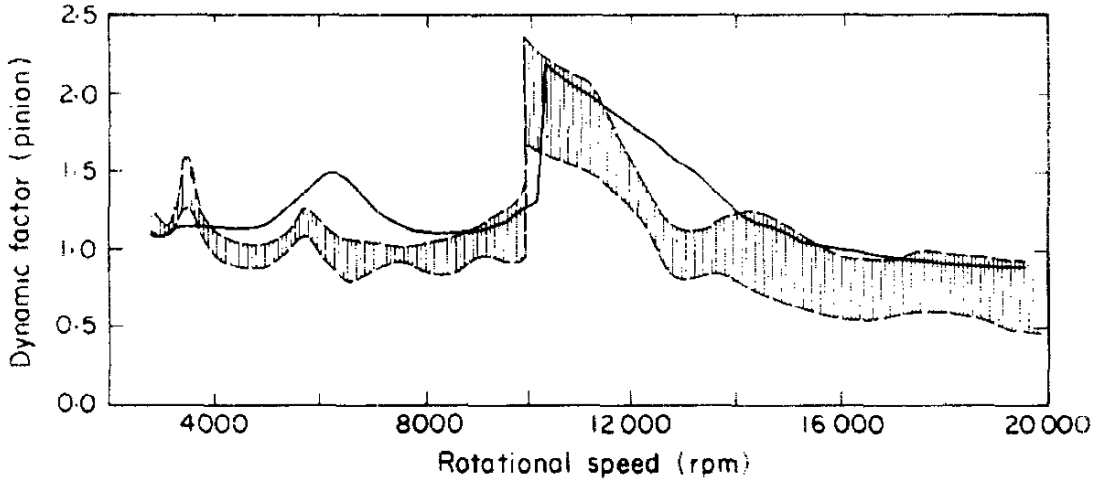

Figure I-20 :Comparison between Kubo's experimental results [57] *and numerical predictions, acc. to Ozguven and Houser* [58]

Measurements of dynamic transmission error are usually more convenient, and this is why many authors have examined the possibility to establish a direct correlation between dynamic transmission error and dynamic factors. Based on numerical simulations conducted on a one-degree-of-freedom torsional model, Tamminana and Kahraman proposed linear relationships between dynamic mesh forces or root stress factors and dynamic transmission errors for permanent contact conditions between the teeth [51]. Hotait and Kahraman later confirmed these findings through experimental measurements performed on a bench instrumented for both root stress and dynamic transmission error measurements [61]. In parallel, Velex found that this linear dependency can only be analytically demonstrated for systems for which torsion is prevalent [62]. Very recently, Dai *et al.* studied dynamic tooth root strains of spur gears and showed that they are not directly related to dynamic transmission error [63]. The authors observed that different rotating speeds below and above resonances having the same RMS of dynamic transmission error present different tooth root strain curves, in both shape and peak amplitude. They justified this phenomenon by the phase shift of dynamic transmission error when moving across resonance areas. Sainte-Marie *et al.* [64] exploited two different models of a highly instrumented spur / helical test-rig: a) a full three-dimensional approach including pinion, gear, shafts, bearings and couplings, and b) a simplified torsional model restricted to the pinion and gear only. They observed that, even if some degree of correlation may exist between dynamic tooth loads and dynamic transmission errors, the linear relationships in [51,61,62] are not fully satisfactory for three-dimensional systems. However, they identified clear linear relationships on the torsional model. They therefore postulated that the linear dependency observed by Tamminana [51] and Hotait [61] could be a particular case related to the system characteristics and should be extrapolated with care.

4 GEAR DYNAMIC MODELS – LITERATURE REVIEW

The literature on dynamic gear models is abundant and comprises several kind of models of varying complexity depending on the objectives of the study, the numerical technique used to solve the state equations, etc. In this section, the literature survey is organized in three sections, depending on the type of transmission (single-stage cylindrical gear, single-stage bevel gear, multi-stage system). In each category, and especially in the first one, the models will be presented from the simplest to the most comprehensive approach which more or less follow the chronology of the developments.

4.1 Single-stage gear systems with parallel axes

The organisation is based on that proposed by Özgüven and Houser [65]. The first models are limited to the study of tooth compliance and consider tooth stiffness as the only potential energy storing element. In these models, the flexibility of the surrounding elements (shafts, bearings, etc.) is discarded. The second category references models for gear dynamics, accounting for shafts and bearings, as well as tooth compliance. Finally, models aimed at studying complete gearboxes are tackled.

4.1.a) *Models with tooth compliance*

The first mathematical models of gear dynamics date back to 1950's. One of the very first contributions in this field is attributed to Tuplin [7] who introduced the first spring-mass model, based on an equivalent constant mesh stiffness and used wedges of various shapes at the base of the spring to simulate gear errors (cf. Figure I-5).

These models were then improved to account for mesh stiffness time-variations leading to second order parametrically-excited linear differential equations referred to as linear time-varying formulations by Blankenship and Singh [66], whose solutions can only be approximated by numerical time integration techniques. Harris [33] developed a benchmark single degree of freedom model based on the notion of transmission error which incorporated three internal sources of excitation (manufacturing errors, variation in tooth stiffness and contact loss non-linearity). Gregory *et al.* extended Harris' work and developed a torsional model capable of predicting tooth contact losses [9]. The authors demonstrated experimentally the influence of load and damping on the occurrence of amplitude jumps in the vicinity of critical speeds (see Figure I-21).

Other models, designated as linear time invariant, rely on constant mesh stiffness and quasi-static transmission error as forcing term [58,67–69] leading to second order linear differential equations with constant coefficients for which analytical closed-form solutions can be found.

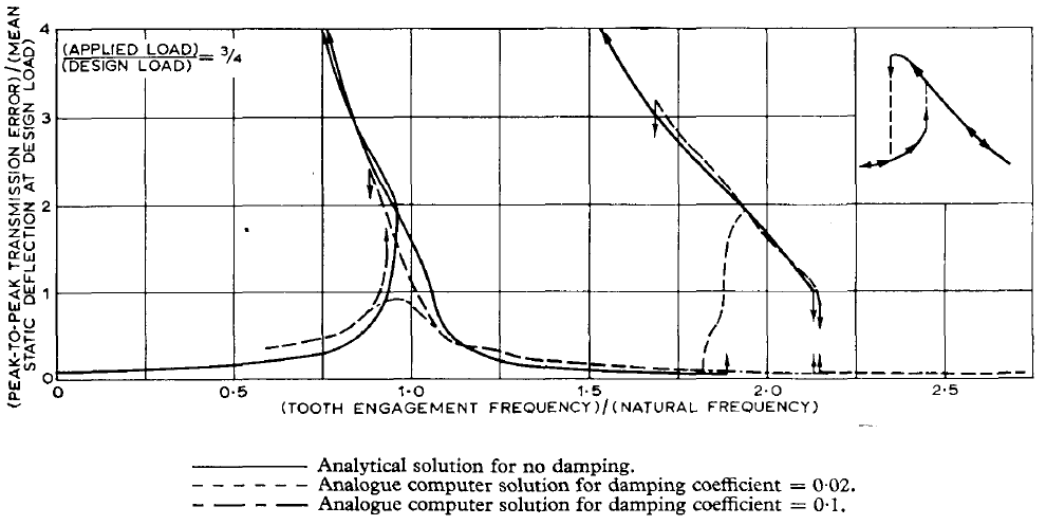

Figure I-21 : Experimental observation of tooth contact losses, from Gregory et al. [9]

More recently, Parker and Vijayakar developed a finite element model for spur gears and conducted contact analysis at each time step [70] (Figure I-22). Their model is able to predict contact losses and eliminates the need for a preliminary determination of mesh stiffness or static transmission error. The computational cost of this kind of modelling is however significantly higher compared with one-DOF lumped parameter models.

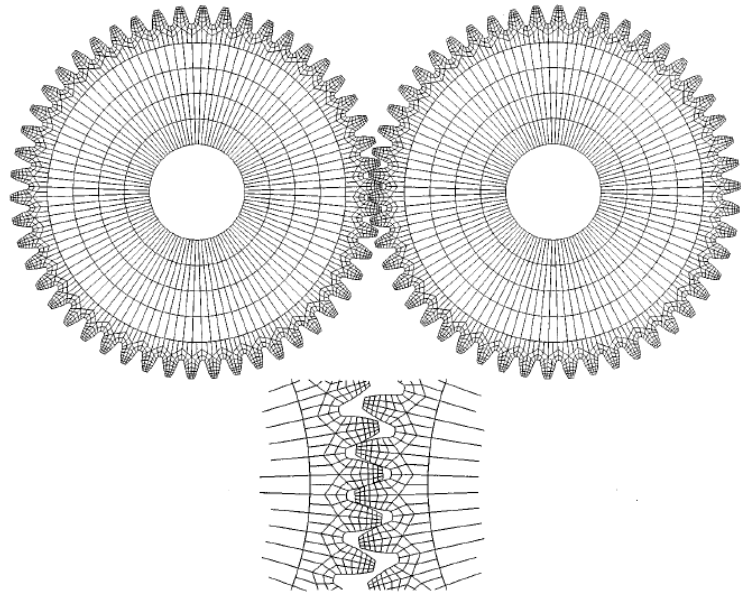

Figure I-22 : Finite element model of a spur gear pair, acc. to Parker et al. [70]

Most of the models limited to the study of tooth compliance were reduced to torsional one-DOF models as shown in Figure I-23. Despite their simplicity, these models provide results in close agreement with experimental measurements, essentially because the majority of the test rigs were designed accordingly i.e., torsion was prevalent so that the test rig meet the basic assumptions of the mathematical modelling. In real applications, the vibration couplings between the different elements of the transmission cannot be discarded and it was realized in the late 1960s that for more general models, it was necessary to account for shaft and bearing flexibilities.

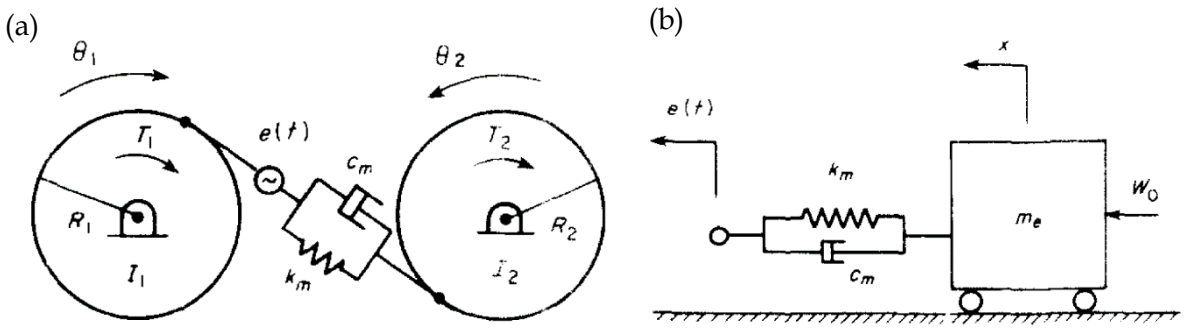

Figure I-23 : (a) Two-degree-of-freedom torsional model of a gear pair and (b) its equivalent single degree-of-freedom system (acc. to Özgüven and Houser [58]*)*

4.1.b) *Models including shafts and bearings*

In 1970, Kohler *et al.* developed a 6-DOF torsional model of a helical gear which included shaft and bearing flexibility [71] along with a constant mesh stiffness function (linear time invariant formulation) and forcing terms based on transmission error. Fukuma *et al.* studied three-dimensional gear vibrations using a multi-degree of freedom model including shaft and bearing flexibility along with a lumped shaft mass [72]. The authors compared their findings with experimental measurements.

With the improvement of computer performance, the number of degrees-of-freedom in dynamic models has constantly increased over the years. In 1992, Kahraman *et al.* presented a model based on a finite element discretization of gear shafts [73] which comprised 10 degrees-of-freedom per shaft element (axial translations excluded) and 4 degrees-of-freedom for the pinion/gear pair (two translations along the line of action and two torsional rotations). Mesh stiffness was considered constant and a transmission error excitation was used. The authors conducted parametric studies on shaft dimensions and bearing compliance to analyse the influence of these elements on dynamic responses.

Velex *et al.* developed a formulation which is not based on *a priori* defined transmission error or mesh stiffness functions. Instead, the contact problem is solved at each time step in the base plane and is coupled to the solution of the dynamic equations [18,60,74]. To account for shape deviations, each contact line on the base plane is discretized in elementary cells and at each cell, the deviation is defined as the normal distance between a point of the pinion and a point of the wheel that would be in contact for perfect geometries (cf. Figure I-24). Contact lines are translated on the base plane to simulate the course of meshing. The other elements of the system are modelled by classic shaft and lumped parameter elements.

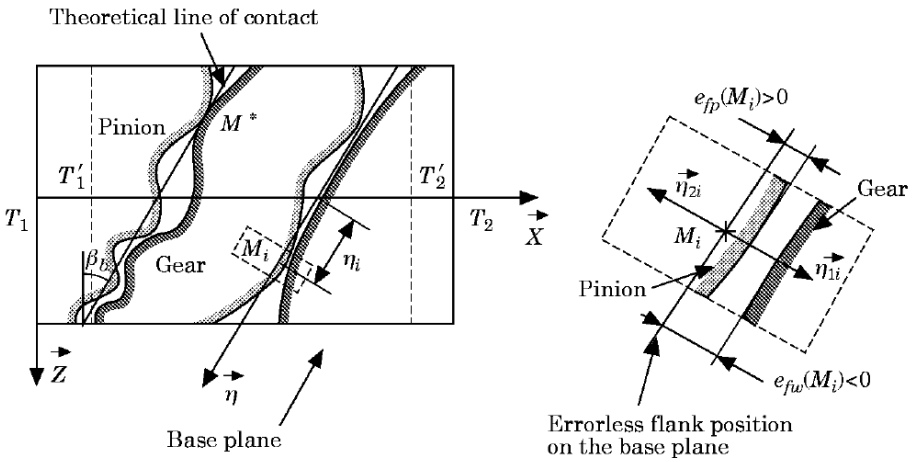

Figure I-24 : Definition of shape deviations on the base plane, acc. to Velex and Maatar [60]

A similar discretization of the contact lines was used by Eritenel and Parker [75] to develop an equivalent lumped parameter model. The authors showed that the distribution of contact forces on the contact lines can be reduced to two discrete stiffness elements: a translational one acting at a point called the centre of stiffness and a twist one. The model was then applied to a nonlinear helical gear dynamic model with rigid shafts resting on bearings represented by constant stiffness elements [76]. The proposed formulation allows to capture partial contact losses but the parameters of the equivalent lumped stiffness elements must be determined at each mesh frequency.

Recent experimental results proved the influence of shaft flexibility on gear dynamics [47]. In this study, two gears (spur and helical) were instrumented with tri-axial accelerometers to measure dynamic transmission error as well as rocking and axial motions. The reported results show that increasing shaft flexibility can lead to additional natural modes hence additional critical speeds. Furthermore, the helical gear mounted on compliant shafts exhibited additional rocking and axial motions, thus justifying that purely torsional models may not be suited for all real applications.

4.1.c) *Models of complete gearboxes*

Evaluation of noise radiation requires the analysis of housing vibrations, as mentioned in the first section of this chapter. In this regard, the aforementioned gear-shaft-bearing dynamic models were upgraded to include the housing and predict its response to mesh excitations.

Early models addressed the dynamic problem of the gear-shaft-bearing set and of the housing independently and considered simple housing geometries [2]. The first models coupling the housing with the interior of the gearbox in the dynamic analysis appeared in the 1990s [77,78]. Rigaud, Perret-Liaudet *et al.* coupled a hybrid finite element / lumped parameter element model of the gear-shaft-bearing system with a finite element model of the housing [79,80]. The gearbox was submitted to transmission error excitations and the influence of its component stiffness was analysed. The authors concluded that any change in the elastic properties of the gearbox components modifies its dynamic behaviour, thus justifying the need for an accurate model of the global gearbox.

Recently, Abbes *et al.* proposed an alternative method for the modelling of complete gearboxes based on substructures. They compared the natural frequencies and mode shapes

of a parallelepiped gearbox obtained with the dynamic substructure method with those from a finite element model [81]. The same model was used to compute the forced response of the gearbox to transmission error excitations and the influence of a stretcher on the vibratory level of the gearbox was studied [82]. The authors then developed a coupled structural-acoustic model accounting for the fluid inside the gearbox. They used it to predict surrounding acoustic pressure distributions and showed that the acoustic field is dependent on the resonance frequencies of the gearbox [83].

Zhou *et al.* [84] analysed the vibrations of a gearbox housing using a refined finite element discretization as illustrated in Figure I-25. In this approach, the dynamic response of the geared transmission is analysed independently and dynamic bearing forces are used as excitations sources in the housing model. Hemispherical sound fields were defined around the housing to study sound pressure levels and the authors analysed different solutions (additive thickness and ribs) for low-noise gearbox design.

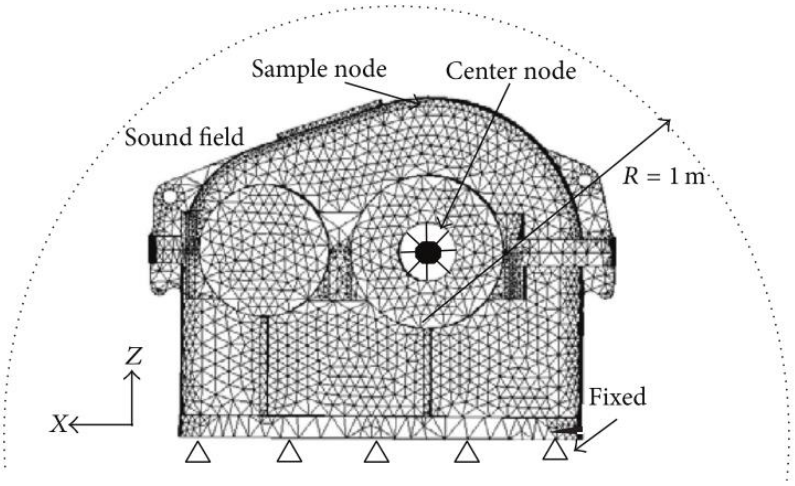

Figure I-25 : Finite element model of a realistic housing geometry, acc. to Zhou et al. [84]

Guo *et al.* [85] proposed a complete finite element / contact mechanics model of the gearbox including the housing. This model provides a complete analysis of gear tooth contacts and rolling element contacts including the fluctuations of bearing stiffness due to rolling elements coming in and out of the loaded zone. However, the contact models for rolling element bearings were not used for dynamic calculations as they require enormous computational effort. To reduce computational costs and make it possible to cover a range of speeds (speed-sweeps), the authors proposed an equivalent lumped-parameter model in which gear tooth contact is solved by discretizing contact lines into distributions of linear springs. Both of the aforementioned models allow to predict dynamic bearing forces which are used as input data for the acoustic modeling and analysis of the housing using boundary elements. Correlations with experimental noise measurements prove the validity of the computational procedure to predict gearbox noise radiation.

4.2 Single-stage gear systems with non-parallel axes

As seen in **Section 4.1**, the literature comprises a very large number of dynamic models for parallel-axis gear systems whereas it is sparser for gears with non-parallel axes. However, bevel gears are widely used in power transmissions in order to change the direction of rotation (automotive, aeronautics to name a few). Bevel gears can have straight or curved teeth and are referred to as spur- or spiral-bevel gears respectively. In some applications, the pinion is shifted below or above the gear centreline so that bigger pinions with larger contact areas can be used. In this case, the pinion and gear axes do not intersect and such gears are called hypoid gears. An illustration of the different types of bevel gears is given in Figure I-26.

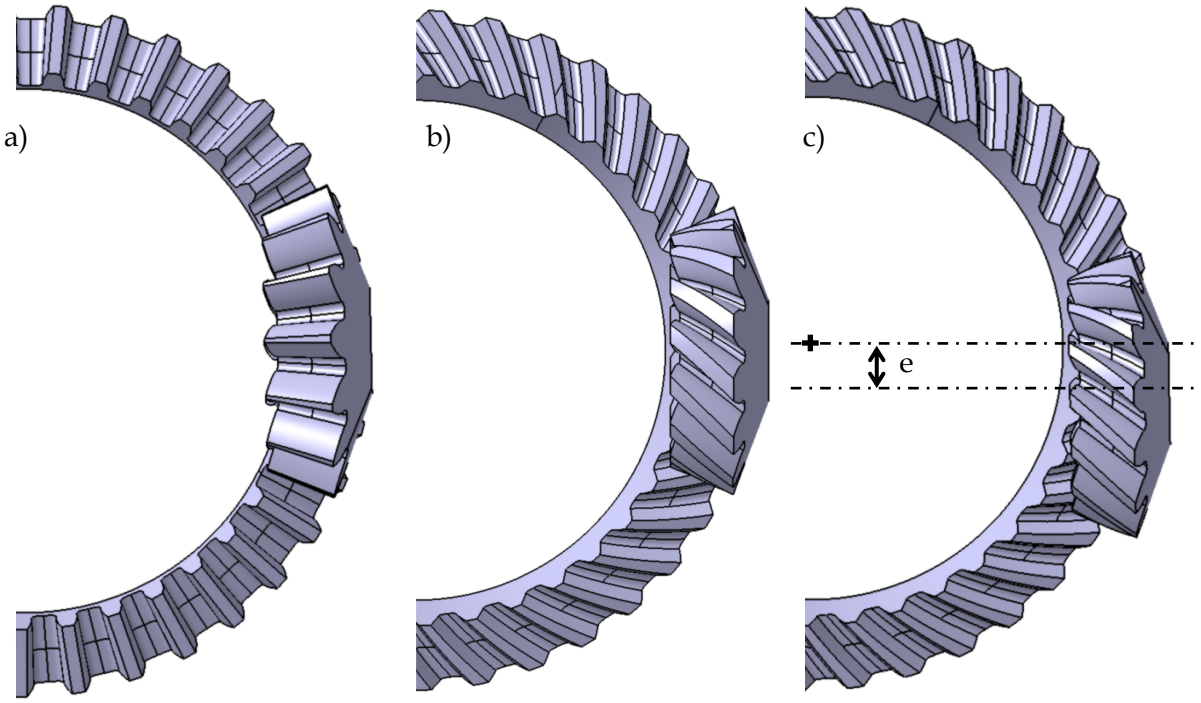

Figure I-26 : Scheme of a) a spur bevel gear pair, b) a spiral-bevel gear pair and c) an hypoid gear pair with offset e

Although many authors have performed loaded tooth contact analyses of hypoid or bevel gears [86–89], only limited effort was dedicated to the dynamic analysis and modelling of bevel gears. The first dynamic models seem to date back to the late 1990s. In 1999, Lim and Cheng [90] proposed a three-dimensional model for the vibratory analysis of high-speed loaded hypoid gears including shaft and bearing flexibilities. It is based on a linear mesh interface formulation. The mesh point position and normal orientation are assumed to be time-invariant and kinematic transmission error is used as the only source of excitation (cf. the schematic representation in Figure I-27). The results obtained from this model revealed the influence of pinion offset on dynamic mesh force and bearing reactions loads.

A few years later, this model was improved to account for time-varying mesh characteristics [91,92]. The model includes gear backlash (clearance between mating teeth) and a constant tooth friction coefficient. A preliminary quasi-static tooth contact analysis is performed to obtain the time-varying mesh line-of-action, mesh position and load dependent mesh stiffness. These preliminary results are then introduced into a three-dimensional multiple-degree-of-freedom dynamic model whose forcing terms stem from loaded

transmission error (cf. Figure I-28). The results show that lateral, axial and bending displacements are coupled by the gear emphasizing the need for multi-degree-of-freedom models. A simplified single-degree-of-freedom model was derived by Wang and Lim to study the effect of backlash and mesh stiffness non-linearity [93,94].

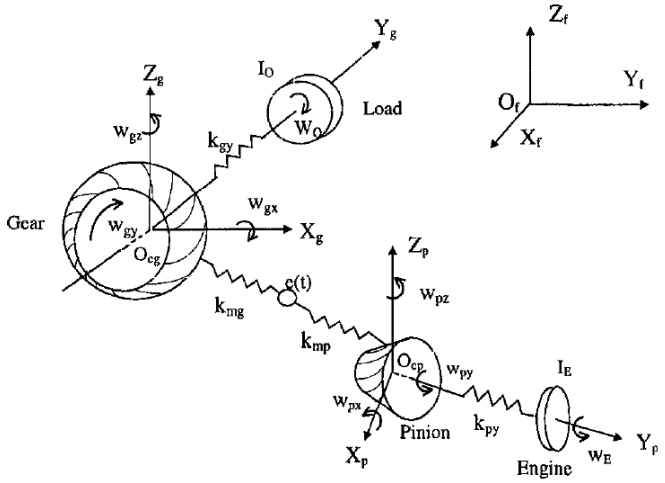

Figure I-27 : Schematic representation of the three-dimensional dynamic model proposed by Lim and Cheng for hypoid gears [90]

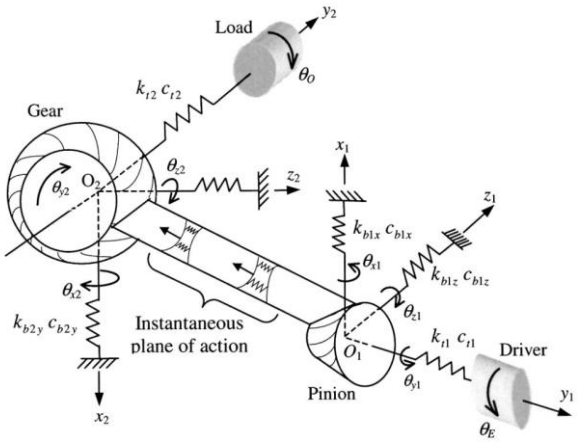

Figure I-28 : Evolution of the model presented in Figure I-27 to account for time-varying mesh characteristics [92]

In parallel, Li *et al.* developed a model for the prediction of the dynamic behaviour of a rotor-bearing system coupled by a spur bevel gear pair [95] based on the assumption of perfect rotation transfer and using a time-varying mesh stiffness function. The model was adapted for spiral bevel gears [96] and the authors studied the influence of the spiral angle and mesh stiffness on the dynamic behaviour. Gao *et al.* [97] proposed a finite element model to predict the contact-impact behaviour of the bevel gear pair of an electric disk grinder.

In 2010, Peng and Lim [98] included the large rotations of the shafts in a coupled multi-body dynamic and vibration model for both hypoid and bevel gears. Gear mesh interactions are modelled as non-linear spring and damper combinations whose locations, directions, stiffness and damping properties vary with gear angular positions. The time-varying mesh characteristics are deduced from the results of a three-dimensional loaded tooth contact analysis. External excitations such as torque and speed fluctuations are accounted for and transient analyses are performed. In the same time, the same gear mesh interaction

formulation was used by Hua and Lim [99] in a study focusing on the modelling of gear-shaft-bearing structures. To this end, the authors employed beam elements to model the shafts and the bearing stiffness formulation developed by Lim and Singh [100] to express the bearing stiffness matrices. A new method was proposed to include effective supporting stiffness in lumped parameter dynamic models.

In 2012, Teixeira, Wang *et al.* [101,102] presented and compared the results from two lumped parameter dynamic models of spiral-bevel gears. Both models use beam elements to represent shafts and lumped stiffness elements for bearings but they differ in the mesh stiffness formulation. In the first one, the pinion and gear in mesh are connected by a single time-varying mesh stiffness in the normal direction and located at the centroid of the contact area. In the second model, the instantaneous local contact conditions are obtained by using elementary stiffness elements distributed over the potential contact area. Both models predict similar dynamic response while the second one makes it possible to estimate instant tooth load distributions.

Wang and Lim [103] used the coupled multi-body dynamics and vibration model proposed by Peng [98] to study the influence of load on dynamic response. Yang *et al.* [104] compared the results from three models where the mesh characteristics (mesh point, line of action, mesh stiffness and transmission error) are obtained from a) the gear design parameters (pitch cone-based mesh model), b) an unloaded tooth contact analysis or c) a loaded tooth contact analysis, respectively. It was concluded that a) the pitch cone method was the simplest to obtain an estimate of the dynamic response and, b) loaded tooth contact analyses were required for accurate predictions of gear dynamics.

Song *et al.* [105] used a lumped parameter model similar to that developed by Peng [98] and they estimated equivalent shaft-bearing stiffness matrices via finite elements. The authors applied the time-varying dynamic bearing forces predicted by the lumped parameter model in a full finite element model of the housing. The simulated housing vibrations were compared with experimental measurements from a marine gearbox, showing reasonable agreement. However, the experimental results showed a response peak not predicted by simulation which corresponded to the mesh frequency of a upstream reduction stage not taken into account in the dynamic model, thus emphasizing the importance of dynamic couplings in multi-mesh units.

Using a similar approach, Wang *et al.* [106] predicted the vibro-acoustic behaviour of a vehicle final drive gearbox. Dynamic bearing loads were determined by a finite element model of the gearbox and the housing frequency response functions were used as input data for a boundary element model to estimate the sound radiated. No experimental correlation was presented but extended parametric studies were conducted to evaluate the sensitivity of the dynamic response of a gearbox to gear-shaft-bearing design.

4.3 Multi-stage gear systems

In order to reach high reduction ratios, transmissions often comprise several stages and experimental results [107] have shown, in this context, that a) couplings are observed between the various tooth mesh excitations and, b) single-mesh models are not relevant any longer. The early models of double-stage systems included only two-degrees-of-freedom and were used to analyse the influence of the phase lag between the two meshes [107]. Rapidly, more degrees-of-freedom have been considered to account for shaft and bearing flexibility [108].

Choy *et al.* studied the vibrational behaviour of a spur gear system with three gears and two meshes. Their model accounted for imbalance along with mesh excitations and a modal method was used to reduce the system order [109,110].

Kahraman set up a three-dimensional model of a drive train composed of three helical gears excited by time-varying mesh stiffness and tooth profile errors [111]. Shafts were supposed to be rigid compared to bearing and gear mesh. The model included the non-linear effects of gear backlash, possibly generated by momentary tooth separations. Two configurations (represented in Figure I-29) were studied to analyse the influence of loading conditions on dynamic mesh forces: an idler gear configuration (middle gear is idle) and a split-torque configuration (power input on the middle gear). The mesh phase was also varied by changing the angular position of the third gear.

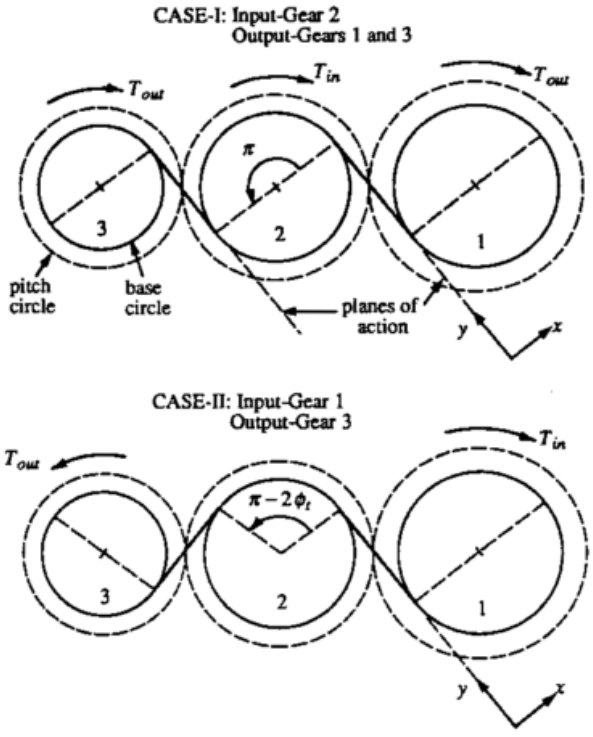

Figure I-29 : Split torque (Case I) and idler gear (Case II) configurations studied by Kharaman on a helical gear system [111]

Vinayak and Singh adapted a multi-body dynamics modelling strategy to multi-mesh spur or helical systems using time-varying mesh stiffness and static transmission errors as excitations sources. In a first approach, each gear was considered as rigid [112] and the model was later modified to account for gear blank flexibility [113].

Raclot and Velex [114] proposed a model for single or multi-stage gear systems accounting for shape deviations and assembly errors. Beam elements were used to represent shafts and bearings were modelled by lumped stiffness matrices. A refined three-dimensional analysis of tooth contact was performed to deal with shape deviations and mounting errors. An iterative spectral method was developed to solve the equations of motion in the frequency domain. The authors pointed out the dynamic couplings for different system configurations (with or without intermediate shaft) and assessed the interest of profile modifications in multi-stage systems.

A model for multiple counter-shaft helical gear systems was developed by Kubur and Kahraman [115]. More attention was given to the flexibility of the gear supporting structures and shafts were simulated by finite elements. Conversely, gear backlash and mesh stiffness fluctuations were both neglected. A model of single-stage helical test rig was set up for validation purposes. Dynamic transmission error was recorded by two methods (encoder- and accelerometer based) and the simulation results for various loads over a range of speeds agreed well with the experimental evidence. The model was then employed to estimate the influence of shaft length, gear angle position and gear hand configuration on dynamic forces for a three-shaft, two-gear mesh unit.

Al-Shyyab and Kahraman developed a lumped parameter dynamic model of multi-mesh gears including gear backlash non-linearity and parametrically varying mesh stiffness. The system order was reduced to two-degrees-of-freedom and the equations of motion were solved by a multi-term harmonic balance method which predicted both period-one and sub-harmonic motions [116,117].

Liu and Parker [118–120] proposed a nonlinear model enabling to capture partial and total contact losses and studied the influence of tooth profile modifications on the dynamic response of multi-mesh systems. Walha *et al.* [121] also proposed a model including non-linear effects of gear backlash and time-varying mesh stiffness for a two-stage spur gear system. The non-linear differential system is decomposed into piecewise linear equations which are solved in the time domain using a Newmark integration scheme.

The model of multi-stage idler spur and helical gears developed by Fakhfakh *et al.* [122,123] accounts for time-varying internal and external excitations (e.g. fluctuating external torques). The contact lines in each plane of action are discretized into elemental cells which are all attributed a time-varying mesh stiffness element (Weber-Banaschek model) as well as an initial separation due to tooth shape deviations. The resulting non-linear differential system is solved step by step in time using a Newmark integration scheme and a normal contact algorithm.

5 CONCLUSION

5.1 Gearbox noise modelling strategy

Noise reduction analyses, when performed after the gearbox design has been defined, often lead to additional damping materials and thus to a possible mass increase, which has to be avoided for aeronautic applications. However, it has been shown that gears can be optimized with regard to noise at the early design stage by modifying the tooth flank geometry for example [124] and it seems therefore interesting to perform noise analysis and gearbox design in parallel.

With this objective in mind, it is necessary to develop numerical models dedicated to gear noise prediction and optimization. These models should provide reliable estimates of gearbox noise and make it possible to perform extensive parametric studies with minimum computational effort. Different types of gears should be taken into account and a variety of supporting elements should also be integrated since, most of the time, their contributions cannot be ignored as mentioned earlier (cf. **Section 4.1.b)**).

The literature review indicates that a three-step methodology is commonly used for the simulation of the vibro-acoustic behaviour of geared transmissions [85,125]:

a) Characterization of the principal sources of excitations (mainly relying on mesh stiffness and transmission error [126])
b) Computation of the dynamic response of the transmission submitted to mesh excitations and determination of the dynamic forces generated at the bearings
c) Simulation of the acoustic radiations of the casing excited by the dynamic forces at the bearings.

In step a), a kinematic and quasi-static analysis of each mesh must be performed to solve the load distribution problem and determine the time variations of the excitation functions. Step b) consists in the dynamic resolution of the equations of motion for the gear-shaft-bearing system and step c) involves a vibro-acoustic simulation of the gearbox including its casing.

The main advantage of this methodology is to enable designers to perform extensive parametric analyses and optimization at each step of the design process. For example, iterations on quasi-static analyses of step a) can lead to the definition of gear macro- and/or micro-geometries reducing mesh excitation amplitudes. The strategy of characterizing mesh excitations by preliminary quasi-static analyses is also less time-consuming than the simultaneous solution of the equations of motion and the dynamic contact conditions.

Step c) of the aforementioned methodology is usually conducted by using commercial software solutions dedicated to the vibro-acoustic study of radiating structures. This analysis is beyond the scope of this work, which is kept limited to the study of mesh excitations and induced dynamic response of the components inside gearboxes (gears, shafts, couplings and bearings).

5.2 Objectives of the thesis

In the direct continuity of Roulois' developments [3], the main objective of this research work is to develop a dynamic model of geared transmissions composed of several reduction or multiplication stages with different gear geometries. To this end, a common theoretical formulation for spur, helical and spiral-bevel gears is proposed which can be applied to a variety of gear architectures with the exception of planetary gears.

Emphasis is placed on the prediction of bearing dynamic forces in gear-shaft-bearing assemblies which relies on an original transmission error based approach to represent mesh excitations. Particular attention will be given to the validation of the formulation. Simulation results are confronted with a number of experimental measurements and benchmark numerical results obtained by using different modelling strategies. It will be shown that the model is adapted to spur, helical and spiral-bevel gears and that tooth shape modifications and errors can be accurately accounted for.

The soundness of the model will also be demonstrated for multi-stage systems and transmissions composed of both cylindrical and spiral-bevel gears will be studied.

Chapter II
Dynamic model of gear systems based on transmission error

The main objective of this thesis is to develop and validate a dynamic model for multi-stage gear systems using the concept of transmission error to characterize mesh excitations. The next chapter is dedicated to the presentation of its mathematical grounding.

In a first section, the formulation is presented using a simplified one-degree-of-freedom system to help identify the contribution of each of the following excitation functions: mesh stiffness, quasi-static transmission error under load and no-load kinematic transmission error.

The theory is extended to three-dimensional multi-stage systems. The model combines classic shaft, lumped parameter and specific two-node gear elements. Each type of element is presented individually and the assembly of the different components is then discussed, leading to the final formulation of the equations of motion.

Finally, the techniques of resolution are presented for the definition of the excitations (quasi-static problem) and for the computation of the dynamic response of the complete system.

1 THEORY – ONE-DEGREE-OF-FREEDOM SYSTEM

As shown in the literature review of **Chapter I**, many of the early models of gear systems were limited to the pinion and gear pair and their torsional degrees-of-freedom. For the sake of clarity, the theory developed in this research will first be presented on such a simple torsional model.

1.1 Reduced model

The system considered is similar to that shown in Figure II-1 (the base radii have been reduced for the sake of clarity). The contributions of the shafts and bearings are ignored and the only displacements taken into account are the small angular perturbations denoted θ_1 and θ_2 caused by mesh elasticity superimposed on rigid-body rotations. The pinion and the gear are considered as two rigid cylinders of centres O_1 and O_2, radii R_{b1} and R_{b2}, and polar moments of inertia J_1 and J_2, respectively. The plane of action is the plane tangent to both cylinders and it is considered that all tooth contacts lie in this plane. A torque C_m is applied to the pinion while the resisting torque on the gear is denoted C_r. In what follows; vector $\boldsymbol{X}$ is in the pinion and gear axial direction.

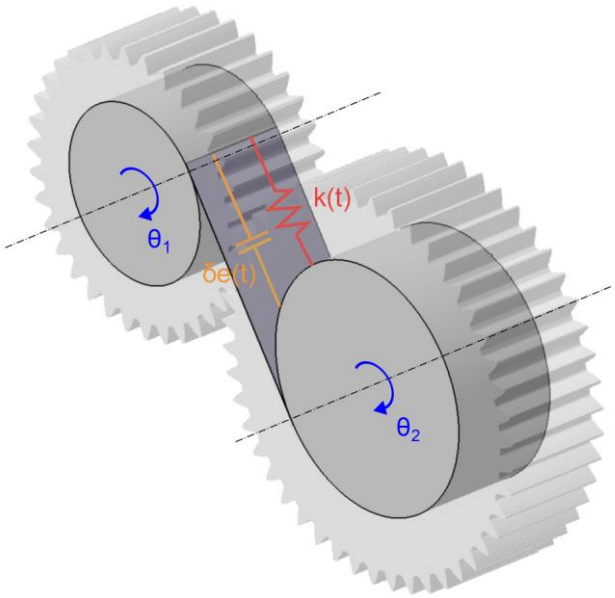

Figure II-1 : Illustration of a torsional model of a cylindrical gear pair

1.2 Mesh forces

The lines of contact are discretized into elementary cells, centred at a potential point of contact M and all attributed an elementary stiffness function $k(M)$ and a possible initial shape deviation caused by tooth modifications and errors, $\delta e(M)$. At any potential point of contact M, the relative normal approach under load (with respect to rigid-body positions) reads:

$$\delta_N(M) = \cos\beta_b \left(R_{b1}\theta_1 + R_{b2}\theta_2\right) \qquad \textit{(II-1)}$$

where β_b is the helix angle measured in the base plane.

The deflection at point M is the difference between the normal approach and the initial deviation:

$$\Delta(M) = \cos\beta_b \,(R_{b1}\theta_1 + R_{b2}\theta_2) - \delta e(M) \qquad (II\text{-}2)$$

Introducing $\boldsymbol{n}_1(M)$ the outward unit normal vector to the pinion tooth flank at point M and considering that elasticity can be concentrated at the contact interface (hypothesis of rigid bodies), the force exerted by the gear onto the pinion at each cell is:

$$d\boldsymbol{F}_{2/1}(M) = -k(M).\big(\cos\beta_b \,(R_{b1}\theta_1 + R_{b2}\theta_2) - \delta e(M)\big).\boldsymbol{n}_1(M) \qquad (II\text{-}3)$$

Assuming that the outward unit normal vectors are the same at every point of contact such that $\boldsymbol{n}_1(M) = \boldsymbol{n}_1$ and neglecting the friction forces on tooth flanks, the global mesh force exerted by the gear onto the pinion reads:

$$\begin{aligned}\boldsymbol{F}_{2/1} &= -\int_M k(M).\big(\cos\beta_b \,(R_{b1}\theta_1 + R_{b2}\theta_2) - \delta e(M)\big)\,.\boldsymbol{n}_1 \\ &= -k(t).\cos\beta_b \,(R_{b1}\theta_1 + R_{b2}\theta_2)\boldsymbol{n}_1 + \int_M k(M).\delta e(M)\,.\boldsymbol{n}_1\end{aligned} \qquad (II\text{-}4)$$

where $k(t) = \int_M k(M)$ is the global time-varying mesh stiffness.

The moment generated at the center of the pinion is:

$$\begin{aligned}\boldsymbol{M}_{2/1}(O_1).\boldsymbol{X} &= \big(\boldsymbol{O_1M} \times \boldsymbol{F}_{2/1}\big).\boldsymbol{X} \\ &= -k(t)\,R_{b1}\varsigma\cos^2\beta_b \,(R_{b1}\theta_1 + R_{b2}\theta_2) + R_{b1}\varsigma\cos\beta_b \int_M k(M)\delta e(M)\end{aligned} \qquad (II\text{-}5)$$

And from the action / reaction principle, the moment at the gear center is:

$$\begin{aligned}\boldsymbol{M}_{1/2}(O_2).\boldsymbol{X} &= \big(\boldsymbol{O_2M} \times \boldsymbol{F}_{1/2}\big).\boldsymbol{X} \\ &= -k(t)\,R_{b2}\varsigma\cos^2\beta_b \,(R_{b1}\theta_1 + R_{b2}\theta_2) + R_{b2}\varsigma\cos\beta_b \int_M k(M)\delta e(M)\end{aligned} \qquad (II\text{-}6)$$

where $\varsigma = +1$ for a positive rotation of the pinion (thick line in Figure II-2) and $\varsigma = -1$ for a negative rotation of the pinion (thin line in Figure II-2).

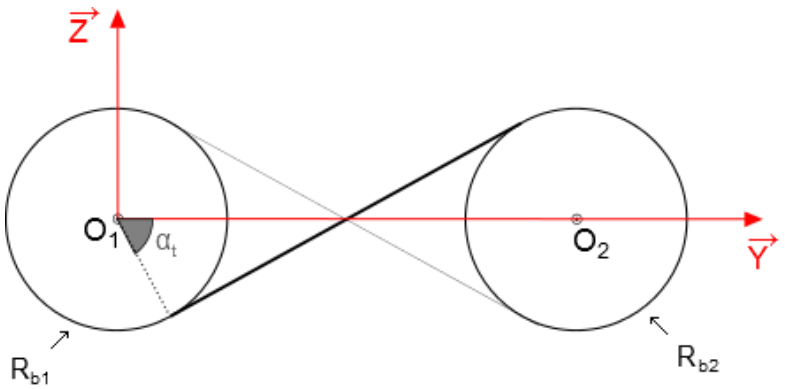

Figure II-2 : Torsional model – Orientation of the base plane

1.3 Equations of motion

Using a rigid-solid mechanics approach, one can successively isolate the pinion and the gear and apply the dynamic moment theorem on each of them. The resulting equations are the following:

$$J_1\left(\ddot{\theta}_1 + \dot{\Omega}_1\right) = R_{b1}\varsigma\cos\beta_b\left[-k(t)\cos\beta_b\left(R_{b1}\theta_1 + R_{b2}\theta_2\right) + \int_M k(M)\delta e(M)\right] + C_m \qquad (II\text{-}7)$$

$$J_2\left(\ddot{\theta}_2 + \dot{\Omega}_2\right) = R_{b2}\varsigma\cos\beta_b\left[-k(t)\cos\beta_b\left(R_{b1}\theta_1 + R_{b2}\theta_2\right) + \int_M k(M)\delta e(M)\right] + C_r \qquad (II\text{-}8)$$

Ω_1 and Ω_2 are the rigid-body angular velocity of the pinion and gear, respectively. The following differential system can be derived:

$$\begin{bmatrix} J_1 & 0 \\ 0 & J_2 \end{bmatrix}\begin{bmatrix} \ddot{\theta}_1 \\ \ddot{\theta}_2 \end{bmatrix} + k(t)\varsigma\cos^2\beta_b\begin{bmatrix} R_{b1}^2 & R_{b1}R_{b2} \\ R_{b1}R_{b2} & R_{b2}^2 \end{bmatrix}\begin{bmatrix} \theta_1 \\ \theta_2 \end{bmatrix} = \begin{bmatrix} C_m \\ C_r \end{bmatrix} - \begin{bmatrix} J_1 & 0 \\ 0 & J_2 \end{bmatrix}\begin{bmatrix} \dot{\Omega}_1 \\ \dot{\Omega}_2 \end{bmatrix} + \varsigma\cos\beta_b\int_M k(M)\delta e(M)\begin{bmatrix} R_{b1} \\ R_{b2} \end{bmatrix} \qquad (II\text{-}9)$$

To solve the semi-definite system in (II-9), the first equation is multiplied by $R_{b1}J_2$, the second one by $R_{b2}J_1$. Then both equations are added term by term and then divided by $\left(J_1R_{b2}^2 + J_2R_{b1}^2\right)$. Taking into account that $C_mR_{b2} = C_rR_{b1}$, one obtains:

$$m_{eq}\left(R_{b1}\ddot{\theta}_1 + R_{b2}\ddot{\theta}_2\right) + k(t)\varsigma\cos^2\beta_b\left(R_{b1}\theta_1 + R_{b2}\theta_2\right) = \frac{C_m}{R_{b1}} - m_{eq}\left(R_{b1}\dot{\Omega}_1 + R_{b2}\dot{\Omega}_2\right) + \varsigma\cos\beta_b\int_M k(M)\delta e(M) \qquad (II\text{-}10)$$

$$\text{with } m_{eq} = \frac{J_1J_2}{J_1R_{b2}^2 + J_2R_{b1}^2}$$

A new variable x can be introduced to get a classic equation of motion for a single-degree-of-freedom system:

$$m_{eq}\ddot{x} + k(t)\varsigma\cos^2\beta_b\,x = \frac{C_m}{R_{b1}} - m_{eq}\left(R_{b1}\dot{\Omega}_1 + R_{b2}\dot{\Omega}_2\right) + \varsigma\cos\beta_b\int_M k(M)\delta e(M) \qquad (II\text{-}11)$$

At this point, it is interesting to replace the time variable by a dimensionless variable $\tau = t/T_m$ where T_m is the mesh period. T_m being constant, the equation of motion (II-11) can be rewritten as:

$$\frac{1}{T_m^2}m_{eq}x'' + k(\tau)\varsigma\cos^2\beta_b\,x = \frac{C_m}{R_{b1}} - \frac{1}{T_m}m_{eq}\left(R_{b1}\Omega_1' + R_{b2}\Omega_2'\right) + \varsigma\cos\beta_b\int_M k(M)\delta e(M) \qquad (II\text{-}12)$$

$$\text{where} \quad A' = \frac{dA}{d\tau}$$

The equation can be derived for quasi-static conditions when $\Omega_1 \to 0$ $\left(\frac{1}{T_m} \to 0\right)$:

$$k(\tau)\zeta \cos^2 \beta_b \, x_S = \frac{C_m}{R_{b1}} + \zeta \cos \beta_b \int_M k(M)\delta e(M) \qquad \textit{(II-13)}$$

Combining (II-12) and (II-13), and considering that the input speed is imposed constant on the pinion such that $\Omega_1' = 0$, one finally gets:

$$\frac{1}{T_m^2} m_{eq} x'' + k(\tau)\zeta \cos^2 \beta_b \, x = k(\tau)\zeta \cos^2 \beta_b \, x_S - \frac{1}{T_m} m_{eq} R_{b2} \Omega_2' \qquad \textit{(II-14)}$$

1.4 Introduction of transmission errors

No-load transmission error ($NLTE$) is representative of geometrical deviations and is defined from the rigid-body rotations of the pinion and gear Θ_1 and Θ_2, respectively as a linear deviation on the base plane:

$$NLTE = R_{b1}\Theta_1 + R_{b2}\Theta_2 \qquad \textit{(II-15)}$$

Its time derivatives are thus linked to the rigid-body angular velocities of the pinion and gear as:

$$\frac{d}{dt} NLTE = R_{b1}\Omega_1 + R_{b2}\Omega_2 \qquad \textit{(II-16)}$$

$$\frac{d^2}{dt} NLTE = R_{b1}\dot{\Omega}_1 + R_{b2}\dot{\Omega}_2 \qquad \textit{(II-17)}$$

Equation (II-17) can be reinjected in (II-14) and considering that the input speed Ω_1 is kept constant, it comes:

$$\frac{1}{T_m^2} m_{eq} x'' + k(\tau)\zeta \cos^2 \beta_b \, x = k(\tau)\zeta \cos^2 \beta_b \, x_S - \frac{1}{T_m^2} m_{eq} NLTE'' \qquad \textit{(II-18)}$$

Quasi-static transmission error under load TE_S is the result of the angular perturbations θ_{1S}, θ_{2S} caused by mesh elasticity in quasi-static conditions along with rigid-body rotations. Projected on the base plane, it reads:

$$\begin{aligned} TE_S &= R_{b1}(\Theta_1 + \theta_{1S}) + R_{b2}(\Theta_2 + \theta_{2S}) \\ &= NLTE + R_{b1}\theta_{1S} + R_{b2}\theta_{2S} \\ &= NLTE + x_S \end{aligned} \qquad \textit{(II-19)}$$

The equation of motion (II-18) can be rewritten by decomposing the global displacement x into its quasi-static and dynamic components $x = x_S + x_D$:

$$\frac{1}{T_m^2} m_{eq} x_D'' + k(\tau) \zeta \cos^2 \beta_b \, x_D = -\frac{1}{T_m^2} \, m_{eq} x_S'' - \frac{1}{T_m^2} m_{eq} NLTE'' \qquad \text{(II-20)}$$

and using (II-19) to introduce TE_S instead of x_S, one gets:

$$\begin{aligned} \frac{1}{T_m^2} m_{eq} x_D'' + k(\tau) \zeta \cos^2 \beta_b \, x_D &= -\frac{1}{T_m^2} m_{eq} (TE_S - NLTE)'' - \frac{1}{T_m^2} m_{eq} NLTE'' \\ &= -\frac{1}{T_m^2} \, m_{eq} TE_S'' \end{aligned} \qquad \text{(II-21)}$$

(II-21) evidences that the dynamic response is controlled by the time-variations of quasi-static transmission error TE_S. Since the latter is necessarily a periodic function, minimum excitations will occur when TE_S is constant.

2 APPLICATION TO MULTIPLE-DEGREE-OF-FREEDOM SYSTEMS

The model developed in this research work combines classic beam and lumped parameter elements along with specific two-node gear elements. The formulation for each type of element is detailed in the following section and the equations of motion are developed.

2.1 Simulation of the mesh interface

2.1.a) *Mesh force distribution*

We here consider a single stage reduction unit, composed of one pinion (denoted 1) and one gear (denoted 2) in mesh. At this stage, the gear geometry is not defined and the contact area between the pinion and the gear is possibly time- and/or load-dependent and is denoted (A). The following therefore applies for any type of gears. Assuming that the pinion and the gear have rigid kernels so that elasticity can be transferred to the contact interfaces, a rigid-solid mechanics approach can be used leading to mesh forces that can be characterised by wrenches of the form:

$$\begin{cases} \boldsymbol{R}_{2/1} = \displaystyle\int_{M\in(A)} d\boldsymbol{F}_{2/1}(M)\, dS \\ \boldsymbol{M}_{2/1}(O_1) = \displaystyle\int_{M\in(A)} \boldsymbol{O_1M} \times d\boldsymbol{F}_{2/1}(M) dS \end{cases} \qquad \textit{(II-22)}$$

It is assumed that the friction forces on the tooth flanks can be neglected compared to the normal contact forces. Moreover, we consider that the outward unit normal vectors with respect to the pinion tooth flanks are the same at every point of contact such that $\boldsymbol{n}_1(M) = \boldsymbol{n}_1$. Then equation (II-22) can be rewritten as:

$$\begin{cases} \boldsymbol{R}_{2/1} = -\displaystyle\int_{M\in(A)} dF_{2/1}(M)\, \boldsymbol{n}_1 dS \\ \boldsymbol{M}_{2/1}(O_1) = -\left(\displaystyle\int_{M\in(A)} dF_{2/1}(M) \boldsymbol{O_1M}\, dS \right) \times \boldsymbol{n}_1 \end{cases} \qquad \textit{(II-23)}$$

From equation (II-23), it can be deduced that $\boldsymbol{R}_{2/1}.\boldsymbol{M}_{2/1}(O_1) = 0$ with $\boldsymbol{R}_{2/1} \neq \boldsymbol{0}$ so that the mesh force wrench reduces to a single sliding vector of intensity $\|\boldsymbol{R}_{2/1}\|$ and whose line of action is collinear with $\boldsymbol{n}_1$.

Introducing G, the instant centroid of the mesh force distribution, defined as:

$$\int_{M\in(A)} dF_{2/1}(M) \boldsymbol{GM}\, dS = \boldsymbol{0} \qquad \textit{(II-24)}$$

It can be concluded from the moment equation in (II-23) that $\boldsymbol{M}_{2/1}(G) = \boldsymbol{0}$ and consequently that G lies on the line of action of the sliding vector.

Based on these properties, the mesh force wrench coordinates can be simplified as:

$$\begin{Bmatrix} \boldsymbol{R}_{2/1} \\ \boldsymbol{M}_{2/1}(O_1) \end{Bmatrix} = -F_m \begin{Bmatrix} \boldsymbol{n}_1 \\ \boldsymbol{O_1G} \times \boldsymbol{n}_1 \end{Bmatrix} \quad (II\text{-}25)$$

where F_m is the total normal mesh force.

Repeating the same reasoning for the mesh force from the pinion onto the gear, the inter-mesh force wrench can be expressed in a compact form as:

$$\boldsymbol{F}_{mesh} = \begin{bmatrix} \boldsymbol{R}_{2/1} \\ \boldsymbol{M}_{2/1}(O_1) \\ \boldsymbol{R}_{1/2} \\ \boldsymbol{M}_{1/2}(O_2) \end{bmatrix} = -F_m \begin{bmatrix} \boldsymbol{n}_1 \\ \boldsymbol{O_1G} \times \boldsymbol{n}_1 \\ -\boldsymbol{n}_1 \\ -\boldsymbol{O_2G} \times \boldsymbol{n}_1 \end{bmatrix} = -F_m \boldsymbol{v}_G \quad (II\text{-}26)$$

$\boldsymbol{v}_G$ will be referred to as the structural vector and is dependent on the geometrical characteristics of the gears.

2.1.b) *Deformed state*

The pinion and the gear are attributed 6 degrees-of-freedom to account for traction/compression, bending and torsion. These degrees-of-freedom represent small displacements superimposed on large rigid-body rotations and can be represented by the degree-of-freedom vector $\boldsymbol{q}$:

$$\boldsymbol{q} = \begin{bmatrix} \boldsymbol{u}_1(O_1) \\ \boldsymbol{w}_1 \\ \boldsymbol{u}_2(O_2) \\ \boldsymbol{w}_2 \end{bmatrix} \quad (II\text{-}27)$$

$\boldsymbol{u}_i(O_i)$ represents the translational degrees-of-freedom at the centre of the pinion ($i = 1$) and of the gear ($i = 2$) and $\boldsymbol{w}$ represents their rotational degrees-of-freedom.

Under the effect of the degrees-of-freedom, a relative normal displacement with respect to rigid-body positions can be defined at every potential point of contact M as:

$$\delta_N(M) = \big(\boldsymbol{u}_1(M) - \boldsymbol{u}_2(M)\big).\boldsymbol{n}_1 = \boldsymbol{v}^T(M)\boldsymbol{q} \quad (II\text{-}28)$$

$$\boldsymbol{v}(M) = \begin{bmatrix} \boldsymbol{n}_1 \\ \boldsymbol{O_1M} \times \boldsymbol{n}_1 \\ -\boldsymbol{n}_1 \\ -\boldsymbol{O_2M} \times \boldsymbol{n}_1 \end{bmatrix} = \begin{bmatrix} \boldsymbol{n}_1 \\ \boldsymbol{O_1G} \times \boldsymbol{n}_1 \\ -\boldsymbol{n}_1 \\ -\boldsymbol{O_2G} \times \boldsymbol{n}_1 \end{bmatrix} + \begin{bmatrix} \boldsymbol{0} \\ \boldsymbol{GM} \times \boldsymbol{n}_1 \\ \boldsymbol{0} \\ -\boldsymbol{GM} \times \boldsymbol{n}_1 \end{bmatrix} = \boldsymbol{v}_G + \Delta\boldsymbol{v}(M) \quad (II\text{-}29)$$

Positive values of $\delta_N(M)$ correspond to a normal approach whereas negative values indicate that the points on the pinion and the gear move apart. The mesh deflection at M, $\Delta(M)$ is the difference between the normal approach and the initial normal separation $\delta e(M)$ at the same point:

$$\Delta(M) = \boldsymbol{v}^T(M)\boldsymbol{q} - \delta e(M) \quad (II\text{-}30)$$

Introducing a normal mesh stiffness per unit contact length $k(M)$, the total normal mesh force is derived as:

$$F_m = \int_{M\in(A)} dF_{2/1}(M)dS = \int_{M\in(A)} k(M)\Delta(M)dS \qquad (II\text{-}31)$$

Reinjecting (II-30), the inter-mesh force in (II-26) can be rewritten as:

$$\boldsymbol{F}_{mesh} = -\int_{M\in(A)} k(M)\big(\boldsymbol{v}^T(M)\boldsymbol{q} - \delta e(M)\big)dS\,\boldsymbol{v}_G \qquad (II\text{-}32)$$

After separating the terms dependent on the integration variable (M) and those which are constant and using decomposition (II-29), one gets:

$$\boldsymbol{F}_{mesh} = -k(t,\boldsymbol{q})[\boldsymbol{v}_G\boldsymbol{v}_G^T]\boldsymbol{q} - \int_{M\in(A)} (k(M)\Delta\boldsymbol{v}^T(M)dS)\,\boldsymbol{q}\,\boldsymbol{v}_G + f\big(t,\delta e(M)\big)\boldsymbol{v}_G \qquad (II\text{-}33)$$

$k(t,\boldsymbol{q}) = \int_{M\in(A)} k(M)dS$ is the time-varying, possibly non-linear global mesh stiffness. $f\big(t,\delta e(M)\big) = \int_{M\in(A)} k(M)\delta e(M)dS$ is a forcing term induced by initial separations.

It can be observed from (II-29) that $\Delta\boldsymbol{v}^T(M)$ contains only rocking moment components. The term $\int_{M\in(A)}(k(M)\Delta\boldsymbol{v}^T(M)dS)\,\boldsymbol{q}\,\boldsymbol{v}_G$ in (II-33) can therefore be neglected if the latter are discarded. In such conditions, the inter-mesh force wrench reads:

$$\boldsymbol{F}_{mesh} = -k(t,\boldsymbol{q})[\boldsymbol{v}_G\boldsymbol{v}_G^T]\boldsymbol{q} + f\big(t,\delta e(M)\big)\boldsymbol{v}_G \qquad (II\text{-}34)$$

2.2 Gear elements

Gears are modelled by specific two-node elements with 6 degrees-of-freedom per node, to account for traction, bending and torsion.

From equation (II-34), each gear element is attributed a 12x12 stiffness matrix defined as:

$$[\boldsymbol{K}_G(t)] = k(t,\boldsymbol{q})[\boldsymbol{v}_G\boldsymbol{v}_G^T] \qquad (II\text{-}35)$$

This matrix is derived from the time-varying mesh stiffness $k(t,\boldsymbol{q})$ and must therefore be calculated at each time step. Mesh stiffness is obtained from a preliminary quasi-static analysis which will be detailed in **Section 3.1** of this chapter.

A 12x12 mass matrix is also attributed to the gear element, and defined as follows:

$$[\boldsymbol{M}_G] = diag(m_1, m_1, m_1, J_1, I_1, I_1, m_2, m_2, m_2, J_2, I_2, I_2) \qquad (II\text{-}36)$$

where subscripts 1 and 2 refer to the pinion and the gear, respectively and m, I and J respectively designate the associated mass, transverse and polar moments of inertia.

The following sections detail the specificity associated with each kind of gear.

2.2.a) *Cylindrical gear element*

For cylindrical gears, the pinion and gear bodies are considered as two rigid cylinders of centres O_1 and O_2 whose radii are the base radii of the pinion and gear respectively. A local coordinate system is associated with the gear element which is rooted at node O_1, such that axis $\boldsymbol{X}$ is in the axial (shaft) direction and axis $\boldsymbol{Y}$ is collinear to $\boldsymbol{O_1O_2}$. Each node O_1 and O_2 is attributed 6 degrees-of-freedom (illustrated in Figure II-3), representative of traction/compression (u_1, u_2), torsion (θ_1, θ_2) and bending $(v_1, v_2, w_1, w_2, \varphi_1, \varphi_2, \psi_1, \psi_2)$.

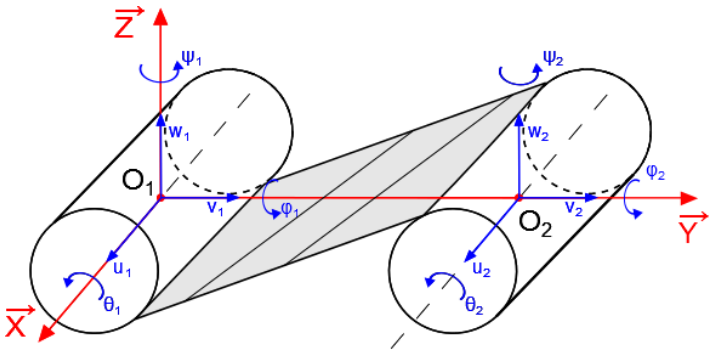

Figure II-3 : Cylindrical gears – Degrees of freedom

The structural vector $\boldsymbol{v_G}$ can be deduced from the geometrical characteristics of the gear pair. An intermediate frame $(O_1, \boldsymbol{X}, \boldsymbol{P}, \boldsymbol{Q})$ can be defined with vector $\boldsymbol{P}$ oriented along the line of action, such that (cf. Figure II-4):

$$\boldsymbol{P} = \begin{bmatrix} 0 \\ sin\alpha_t \\ \zeta cos\alpha_t \end{bmatrix}_{(\boldsymbol{X},\boldsymbol{Y},\boldsymbol{Z})} \qquad \boldsymbol{Q} = \begin{bmatrix} 0 \\ -\zeta cos\alpha_t \\ sin\alpha_t \end{bmatrix}_{(\boldsymbol{X},\boldsymbol{Y},\boldsymbol{Z})} \tag{II-37}$$

with $\zeta = 1$ for a positive rotation of the pinion (thick line in Figure II-4) and $\zeta = -1$ for a negative rotation of the pinion (thin line in Figure II-4). α_t is the apparent pressure angle.

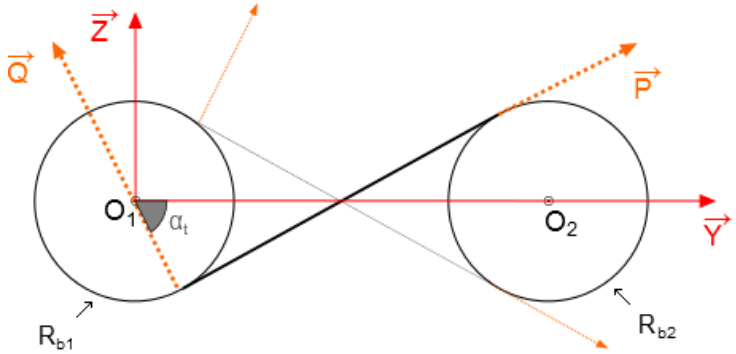

Figure II-4 : Cylindrical gears – Base plane orientations and gear coordinate systems

The normal to the pinion tooth flanks $\boldsymbol{n_1}$ is contained in the base plane. Its direction is also related to the base helix angle β_b in the case of helical gears, as illustrated in Figure II-5.

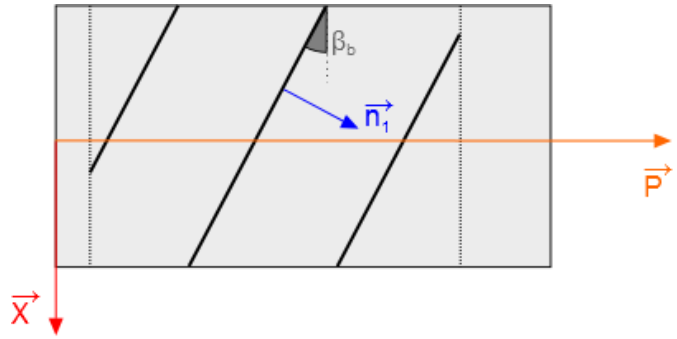

Figure II-5 : Cylindrical gears – Orientation of the normal to the tooth flanks in the base plane

Its coordinates in the frame $(O_1, \boldsymbol{X}, \boldsymbol{P}, \boldsymbol{Q})$ are:

$$\boldsymbol{n}_1 = \begin{bmatrix} \varepsilon sin\beta_b \\ cos\beta_b \\ 0 \end{bmatrix}_{(\boldsymbol{X},\boldsymbol{P},\boldsymbol{Q})} \qquad (II\text{-}38)$$

where ε depends both on the direction of rotation of the pinion and on the orientation of the helix, as shown in Table II-1. LH designates a pinion with left-handed helical teeth while RH stands for a pinion with right-handed helical teeth.

Table II-1 : Cylindrical gears – Orientation of the normal according to helix orientation

Direction of rotation of the pinion	Mesh interface	
Positive	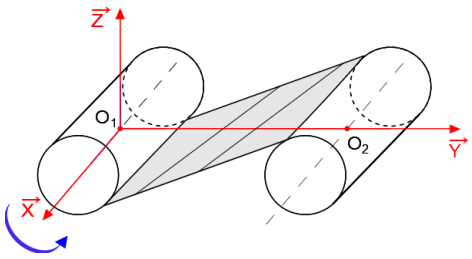 LH	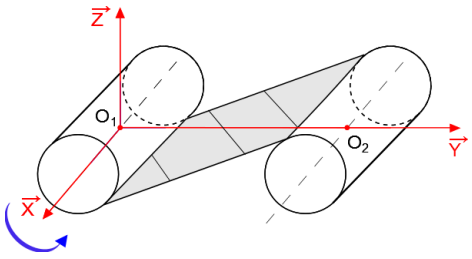 RH
Negative	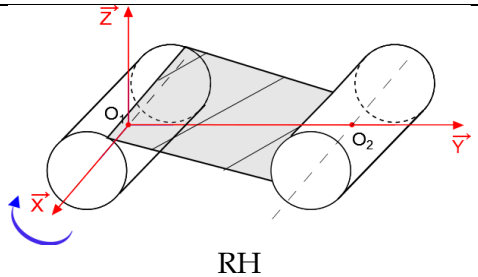 RH	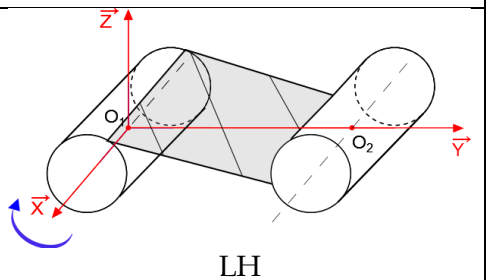 LH
Base plane	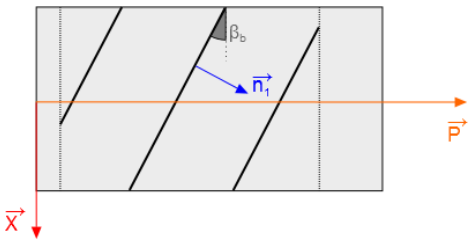	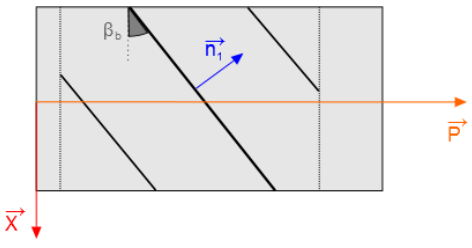
	$\varepsilon = 1$	$\varepsilon = -1$

Denoting $x(G)$ and $p(G)$ the coordinates of the centroid of mesh force distribution G in the base plane, we have:

$$\boldsymbol{O_1G} = \begin{bmatrix} x(G) \\ p(G) \\ -\zeta R_{b_1} \end{bmatrix}_{(\boldsymbol{X},\boldsymbol{P},\boldsymbol{Q})} \tag{II-39}$$

$$\boldsymbol{O_2G} = \begin{bmatrix} x(G) \\ p(G) - \left(R_{p_1} + R_{p_2}\right) sin\alpha_t \\ \zeta R_{b_2} \end{bmatrix}_{(\boldsymbol{X},\boldsymbol{P},\boldsymbol{Q})} = \begin{bmatrix} x(G) \\ p_2(G) \\ \zeta R_{b_2} \end{bmatrix}_{(\boldsymbol{X},\boldsymbol{P},\boldsymbol{Q})} \tag{II-40}$$

Using equations (II-38) to (II-40), the structural vector $\boldsymbol{v_G}$ can finally be expressed as a function of the geometrical characteristics of the gear pair:

$$\boldsymbol{v_G} = \begin{bmatrix} \varepsilon sin\beta_b \\ cos\beta_b \\ 0 \\ \zeta R_{b_1} cos\beta_b \\ -\varepsilon\zeta R_{b_1} sin\beta_b \\ x(G)cos\beta_b - \varepsilon p(G) sin\beta_b \\ -\varepsilon sin\beta_b \\ -cos\beta_b \\ 0 \\ \zeta R_{b2} cos\beta_b \\ -\varepsilon\zeta R_{b2} sin\beta_b \\ -x(G)cos\beta_b + \varepsilon p_2(G) sin\beta_b \end{bmatrix}_{(\boldsymbol{X},\boldsymbol{P},\boldsymbol{Q})} \tag{II-41}$$

And projected in frame $(\boldsymbol{X}, \boldsymbol{Y}, \boldsymbol{Z})$:

$$\boldsymbol{v_G} = \begin{bmatrix} \varepsilon sin\beta_b \\ cos\beta_b sin\alpha_t \\ \zeta cos\beta_b cos\alpha_t \\ \zeta R_{b1} cos\beta_b \\ -\varepsilon\zeta R_{b1} sin\beta_b sin\alpha_t - \zeta(x(G)cos\beta_b - \varepsilon p(G) sin\beta_b) cos\alpha_t \\ -\varepsilon R_{b1} sin\beta_b cos\alpha_t + (x(G)cos\beta_b - \varepsilon p(G) sin\beta_b) sin\alpha_t \\ -\varepsilon sin\beta_b \\ -cos\beta_b sin\alpha_t \\ -\zeta cos\beta_b cos\alpha_t \\ \zeta R_{b2} cos\beta_b \\ -\varepsilon\zeta R_{b2} sin\beta_b sin\alpha_t + \zeta(x(G)cos\beta_b - \varepsilon p_2(G) sin\beta_b) cos\alpha_t \\ -\varepsilon R_{b2} sin\beta_b cos\alpha_t - (x(G)cos\beta_b - \varepsilon p_2(G) sin\beta_b) sin\alpha_t \end{bmatrix}_{(\boldsymbol{X},\boldsymbol{P},\boldsymbol{Q})} \tag{II-42}$$

2.2.b) *Bevel gear element*

For bevel gears, the pinion and gear bodies are considered as two rigid cones, corresponding to the pinion and gear pitch cones (cf. Figure II-6). A local coordinate system is associated to the element, with the origin located at node O_1, centre of the pinion. The driving cone axis is the direction of the $\boldsymbol{X}$ axis and the driven cone axis is contained in plane $(O_1, \boldsymbol{X}, \boldsymbol{Z})$. Each node O_1 and O_2 is attributed 6 degrees-of-freedom (illustrated in Figure II-3), representative of traction/compression, torsion and bending.

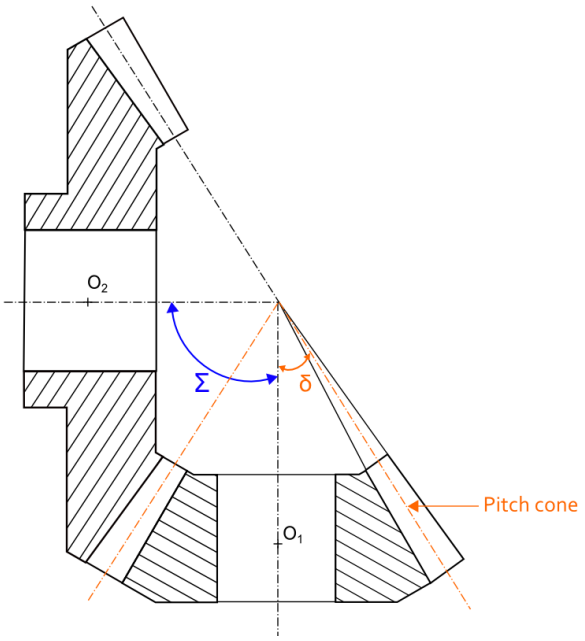

Figure II-6 : Spiral bevel gear pair – Representation of pitch cone of angle δ, and of the shaft angle Σ

In order to define the structural vector $\boldsymbol{v}_G$ of the bevel gear pair, a quasi-static analysis is performed which gives at each time step:

- the direction of the mesh force $\boldsymbol{n}_1$,
- the position of the centroid of the mesh force distribution.

Details of this analysis are given in **Section 3.1.b)** of this chapter.

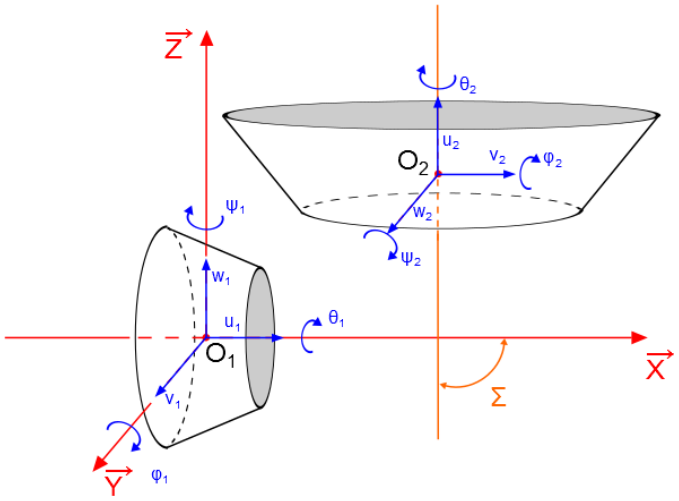

Figure II-7 : Bevel gears – Degrees of freedom

2.3 Shaft element

The shaft elements rely on Timoshenko's beam theory. Each element comprises two nodes with six degrees-of-freedom per node (three translations and three rotations) and is attributed 12x12 mass, stiffness and damping matrices. This type of element allows to account for traction/compression (u_1, u_2), bending $(v_1, v_2, w_1, w_2, \varphi_1, \varphi_2, \psi_1, \psi_2)$ and torsion (θ_1, θ_2).

In order to reproduce complex geometries of gearbox shafts by a minimum number of degrees-of-freedom, a conical beam finite element has been implemented [127]. Following the works of Cowper [128], shear effects are accounted for by using a shear coefficient K which, for a hollow circular cross-section, reads:

$$K = \frac{6(1+\nu)(1+m^2)^2}{(7+6\nu)(1+m^2)^2 + (20+12\nu)m^2} \qquad \textit{(II-43)}$$

where ν is Poisson's ratio of the shaft material and m is the ratio of inner to outer radius.

A complete description of the shaft element mass and stiffness matrices is given in **Appendix A**.

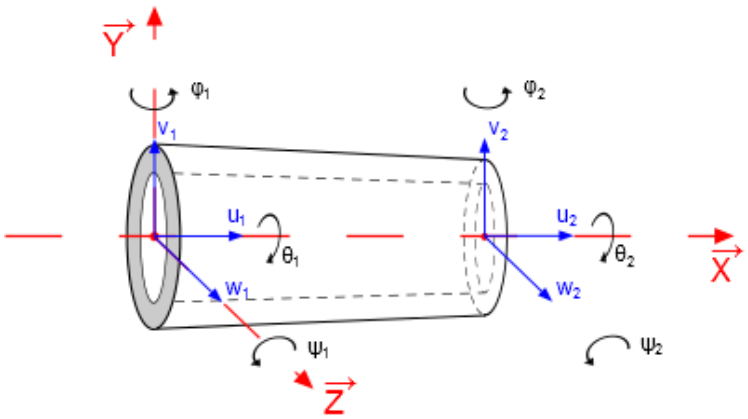

Figure II-8 : Conical shaft element – Degrees of freedom and local frame

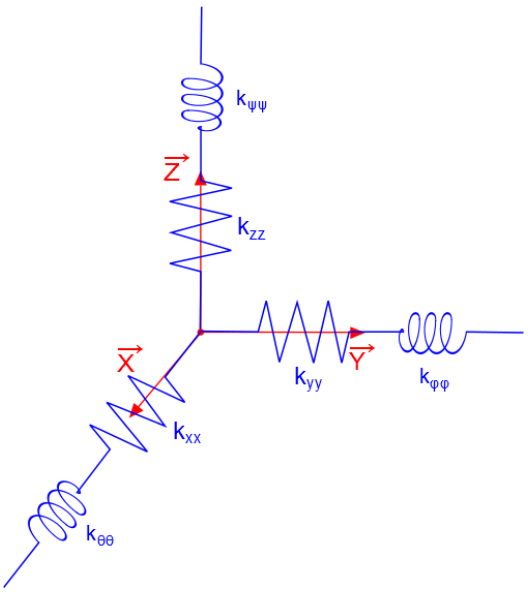

Figure II-9 : Stiffness associated to the bearing element

2.4 Lumped parameter elements

2.4.a) *Bearings*

Bearings are assimilated to linear elastic supports characterized by time invariant stiffness elements. 6x6 stiffness matrices are consequently added at the node of the supported shaft. ***X*** is the axial direction of the supported shaft. k_{xx} is the axial stiffness, k_{yy} and k_{zz} are the values of the radial stiffness. $k_{\varphi\varphi}$ and $k_{\psi\psi}$ act on bending rotations and $k_{\theta\theta}$ can be used to represent a resisting torque.

Damping matrices can be defined similarly, to account for the properties of hydrodynamic bearings for example.

2.4.b) *Elastic couplings*

Two coaxial beam elements can be connected by a 12x12 stiffness matrix representative of an elastic coupling. The matrix is symmetric and ensures the transfer of translations and rotations in all directions (traction/compression, bending and torsion).

A diagonal 12x12 mass matrix can also be defined to account for the mass of the elastic coupling.

2.4.c) *Additional polar inertias*

The external elements connected to the helicopter main gearbox (engines and main rotor) have very high polar inertias which strongly influence the dynamic response of the transmission. Additional polar inertias are therefore implemented in the model:

- If the coupling between the external inertia and the gearbox is considered infinitely rigid in torsion, the external inertia influences only the mass matrix of the system. In this case, the external polar inertia is directly superimposed on the polar inertia of the node to which it is connected (cf. Figure II-10).
- If the connection between the external inertia and the gearbox is flexible, an additional node is introduced and linked to the transmission by a torsional stiffness element equivalent to the stiffness of the coupling (cf. Figure II-11). The external polar inertia is added in the global mass matrix at the torsional degree-of-freedom associated with the newly created node. This configuration therefore influences both the stiffness and mass matrices of the complete system, as well as the total number of degrees-of-freedom.

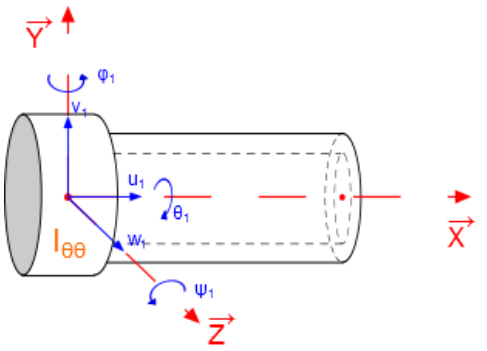

Figure II-10 : Additional inertia $I_{\theta\theta}$ with rigid coupling

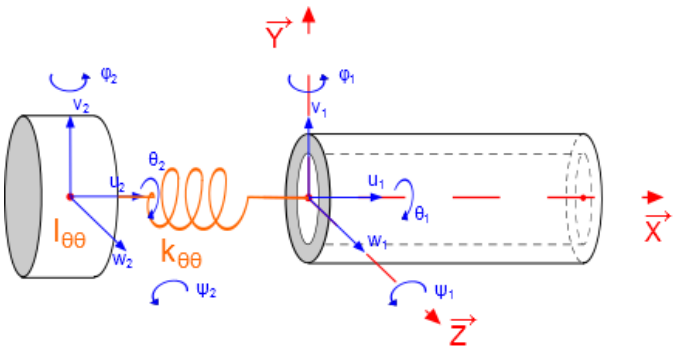

Figure II-11 : Additional inertia $I_{\theta\theta}$ with flexible coupling $k_{\theta\theta}$

2.5 Assembly and equations of motion

2.5.a) *Assembly of the system components*

The elemental matrices described earlier are assembled to form global square matrices of dimension equal to the total number of degrees-of-freedom of the system.

In what follows, an N-mesh system is considered. For each gear pair, subscript 1 is used to designate the driving member and subscript 2 refers to the driven one. In accordance with equation (II-34), the inter-mesh force wrench for each mesh (L) is:

$$\boldsymbol{F}_{mesh}^{(L)} = -\boldsymbol{K}_G^{(L)}(t)\boldsymbol{q}^{(L)} + \boldsymbol{F}_{\delta e}^{(L)}(t) \qquad \textit{(II-44)}$$

The equations of motion for the complete system therefore read:

$$\boldsymbol{M}\ddot{\boldsymbol{X}} + \boldsymbol{C}\dot{\boldsymbol{X}} + \left(\boldsymbol{K}_{sys} + \sum_{L=1}^{N} \boldsymbol{K}_G^{(L)}(t)\right)\boldsymbol{X} = \boldsymbol{F}_0 + \sum_{L=1}^{N} \boldsymbol{F}_{\delta e}^{(L)}(t) + \boldsymbol{F}_{\dot{\Omega}}(t) \qquad \textit{(II-45)}$$

$\boldsymbol{X}$ is the vector containing the degrees-of-freedom of the complete system.
$\boldsymbol{M}$ and $\boldsymbol{C}$ are the mass and damping matrices of the global system.
$\boldsymbol{K}_{sys}$ is the stiffness matrix of the global system, excluding the gear elements.
$\boldsymbol{F}_0$ is the static load vector (containing input and output torques).
$\boldsymbol{F}_{\delta e}^{(L)}(t) = f^{(L)}\left(t, \delta e^{(L)}(M)\right)\boldsymbol{V}_G^{(L)}$ with $\boldsymbol{V}_G^{(L)}$ the structural vector associated with mesh (L) $\boldsymbol{v}_G^{(L)}$ extended to the total number of degrees-of-freedom (completed by zeros).
$\boldsymbol{F}_{\dot{\Omega}}(t)$ is a forcing term due to the possible fluctuations of rotational speeds caused by initial deviations.

2.5.b) *Equations of motion*

Introducing a time variable normalized by the smallest mesh period of the system $\tau = t/T_m$ and noticing that T_m is considered constant, the equations of motion (II-45) can be rewritten:

$$\frac{1}{T_m^2}\boldsymbol{M}\boldsymbol{X}'' + \frac{1}{T_m}\boldsymbol{C}\boldsymbol{X}' + \left(\boldsymbol{K}_{sys} + \sum_{L=1}^{N} \boldsymbol{K}_G^{(L)}(\tau)\right)\boldsymbol{X} = \boldsymbol{F}_0 + \sum_{L=1}^{N} \boldsymbol{F}_{\delta e}^{(L)}(\tau) + \boldsymbol{F}_{\dot{\Omega}}(\tau) \qquad \textit{(II-46)}$$

where $A' = \frac{d}{d\tau}(A)$

The quasi-static equations are derived by considering the limiting case $\frac{1}{T_m} \to 0$ and read:

$$\left(\boldsymbol{K}_{sys} + \sum_{L=1}^{N} \boldsymbol{K}_G^{(L)}(\tau)\right)\boldsymbol{X}_S = \boldsymbol{F}_0 + \sum_{L=1}^{N} \boldsymbol{F}_{\delta e}^{(L)}(\tau) \qquad \textit{(II-47)}$$

The mesh stiffness of each gear stage can be decomposed into its mean value $k_m^{(L)}$ and its time fluctuations $\Delta k^{(L)}(\tau)$ such that:

$$\begin{aligned}\left[\boldsymbol{K}_G^{(L)}(\tau)\right] &= \left(k_m^{(L)} + \Delta k^{(L)}(\tau)\right)\left[\boldsymbol{V}_G^{(L)}\boldsymbol{V}_G^{(L)^T}\right] \\ &= k_m^{(L)}\left(1 + \alpha^{(L)} g^{(L)}(\tau)\right)\left[\boldsymbol{V}_G^{(L)}\boldsymbol{V}_G^{(L)^T}\right]\end{aligned} \qquad \textit{(II-48)}$$

where $g^{(L)}(\tau)$ describes the shape of the time variations of mesh stiffness and varies between -1 and +1, $\alpha^{(L)}$ is the relative variation amplitude and $\alpha < 1$.

A new stiffness matrix is defined which combines the stiffness of all supporting elements (bearings, shafts, couplings) with the average stiffness of the gears:

$$\bar{\boldsymbol{K}} = \boldsymbol{K}_{sys} + \sum_{L=1}^{N} k_m^{(L)}\left[\boldsymbol{V}_G^{(L)}\boldsymbol{V}_G^{(L)^T}\right] \qquad \textit{(II-49)}$$

so that equation (II-47) becomes:

$$\bar{\boldsymbol{K}}\,\boldsymbol{X}_S = \boldsymbol{F}_0 + \sum_{L=1}^{N} \boldsymbol{F}_{\delta e}^{(L)}(\tau) - \sum_{L=1}^{N} k_m^{(L)}\alpha^{(L)} g^{(L)}(\tau)\left[\boldsymbol{V}_G^{(L)}\boldsymbol{V}_G^{(L)^T}\right]\boldsymbol{X}_S \qquad \textit{(II-50)}$$

$\boldsymbol{X}_S$ is the static deflection of the complete system. It is possible to consider that there is a unique solution to the static problem and therefore that $\bar{\boldsymbol{K}}$ is invertible. Using a fixed-point theorem (cf. [129]), (II-50) leads to:

$$\begin{aligned}\boldsymbol{X}_S &= \boldsymbol{X}_0 + \sum_{L=1}^{N}\left(f^{(L)}\left(\tau, \delta e^{(L)}(M)\right) - k_m^{(L)}\alpha^{(L)} g^{(L)}(\tau)\boldsymbol{V}_G^{(L)^T}\boldsymbol{X}_S\right)\bar{\boldsymbol{K}}^{-1}\boldsymbol{V}_G^{(L)} \\ &= \boldsymbol{X}_0 + \sum_{L=1}^{N}\varphi^{(L)}\left(\tau, \delta e^{(L)}(M), \boldsymbol{X}_S\right)\bar{\boldsymbol{K}}^{-1}\boldsymbol{V}_G^{(L)}\end{aligned} \qquad \textit{(II-51)}$$

with $\boldsymbol{X}_0 = \bar{\boldsymbol{K}}^{-1}\boldsymbol{F}_0$, the static deflection with average mesh stiffness.
$\varphi^{(L)}\left(\tau, \delta e^{(L)}(M), \boldsymbol{X}_S\right)$ is an unknown scalar function of time, associated with the tooth shape deviations at mesh (L).

Replacing $\boldsymbol{X}_S$ in equation (II-47) by (II-51), one obtains:

$$\left(\boldsymbol{K}_{sys} + \sum_{L=1}^{N}\boldsymbol{K}_G^{(L)}(\tau)\right)\left(\boldsymbol{X}_0 + \sum_{P=1}^{N}\varphi^{(P)}\left(\tau, \delta e^{(P)}(M), \boldsymbol{X}_S\right)\bar{\boldsymbol{K}}^{-1}\boldsymbol{V}_G^{(P)}\right) = \boldsymbol{F}_0 + \sum_{L=1}^{N}\boldsymbol{F}_{\delta e}^{(L)}(\tau) \qquad \textit{(II-52)}$$

Re-using (II-48) and (II-49) leads to:

$$\begin{aligned}&\left(\bar{\boldsymbol{K}} + \sum_{L=1}^{N}\Delta k^{(L)}(\tau)\left[\boldsymbol{V}_G^{(L)}\boldsymbol{V}_G^{(L)^T}\right]\right)\left(\boldsymbol{X}_0 + \sum_{P=1}^{N}\varphi^{(P)}\left(\tau, \delta e^{(P)}(M), \boldsymbol{X}_S\right)\bar{\boldsymbol{K}}^{-1}\boldsymbol{V}_G^{(P)}\right) \\ &\qquad = \boldsymbol{F}_0 + \sum_{L=1}^{N}\boldsymbol{F}_{\delta e}^{(L)}(\tau)\end{aligned} \qquad \textit{(II-53)}$$

Noting that $\bar{\boldsymbol{K}}\boldsymbol{X}_0 = \boldsymbol{F}_0$ and developing (II-53), one obtains:

$$\sum_{P=1}^{N} \varphi^{(P)}\left(\tau, \delta e^{(P)}(M), \boldsymbol{X}_S\right) \boldsymbol{V}_G^{(P)} + \sum_{L=1}^{N} \Delta k^{(L)}(\tau) \left[\boldsymbol{V}_G^{(L)} \boldsymbol{V}_G^{(L)^T}\right] \left(\boldsymbol{X}_0 + \sum_{P=1}^{N} \varphi^{(P)}\left(\tau, \delta e^{(P)}(M), \boldsymbol{X}_S\right) \bar{\boldsymbol{K}}^{-1} \boldsymbol{V}_G^{(P)}\right) = \sum_{L=1}^{N} \boldsymbol{F}_{\delta e}^{(L)}(\tau) \quad \text{(II-54)}$$

2.5.c) *Introduction of transmission errors*

An auxiliary problem is introduced which corresponds to the isolated gear stage (L) with average stiffness submitted to the static loading $F_S^{(L)} \boldsymbol{V}_G^{(L)}$ instead of $\boldsymbol{F}_0$. This loading corresponds to a constant compressive mesh force F_S in the base plane acting on the pinion and the gear with no torque on the pinion nor the gear shaft. The mesh deflections for the auxiliary problem (denoted $\widehat{\boldsymbol{X}}_0^{(L)}$) and the actual static problem with average mesh stiffness in the absence of tooth shape deviations are identical so that:

$$\boldsymbol{V}_G^{(L)^T} \boldsymbol{X}_0 = \boldsymbol{V}_G^{(L)^T} \widehat{\boldsymbol{X}}_0^{(L)} = \frac{F_S^{(L)}}{k_m^{(L)}} \quad \text{(II-55)}$$

Besides:

$$\widehat{\boldsymbol{X}}_0^{(L)} = \bar{\boldsymbol{K}}^{-1} F_S^{(L)} \boldsymbol{V}_G^{(L)} \quad \text{(II-56)}$$

By definition of the auxiliary problem:

- The pinion-gear pair of mesh (L) is submitted to the sole internal force $F_S^{(L)} \boldsymbol{V}_G^{(L)}$.
- This loading generates no torsion of the shafts. $\widehat{\boldsymbol{X}}_0^{(L)}$ contains only torsional angles, constant on every shaft. The bending and axial displacements in $\widehat{\boldsymbol{X}}_0^{(L)}$ are all nil.
- No external action is induced on the rest of the system.
- No other loading acts on the rest of the system.
- Deflections at all other meshes $(P) \neq (L)$ are nil:

$$\boldsymbol{V}_G^{(P)^T} \widehat{\boldsymbol{X}}_0^{(L)} = 0 \quad \text{if } (P) \neq (L) \quad \text{(II-57)}$$

Using property (II-57) and equalities (II-55) and (II-56), it comes:

$$\sum_{L=1}^{N} \varphi^{(L)}\left(\tau, \delta e^{(L)}(M), \boldsymbol{X}_S\right) \boldsymbol{V}_G^{(L)} + \sum_{L=1}^{N} \Delta k^{(L)}(\tau) \frac{F_S^{(L)}}{k_m^{(L)}} \boldsymbol{V}_G^{(L)} + \sum_{L=1}^{N} \Delta k^{(L)}(\tau) \left[\boldsymbol{V}_G^{(L)} \boldsymbol{V}_G^{(L)^T}\right] \varphi^{(L)}\left(\tau, \delta e^{(L)}(M), \boldsymbol{X}_S\right) \frac{\widehat{\boldsymbol{X}}_0^{(L)}}{F_S^{(L)}} = \sum_{L=1}^{N} \boldsymbol{F}_{\delta e}^{(L)}(\tau) \quad \text{(II-58)}$$

(II-58) holds true if the following is verified for each mesh (L):

$$\begin{aligned} f^{(L)}\left(\tau, \delta e^{(L)}(M)\right) & \\ &= \varphi^{(L)}\left(\tau, \delta e^{(L)}(M), \boldsymbol{X}_S\right) + \Delta k^{(L)}(\tau)\frac{F_S^{(L)}}{k_m^{(L)}} \\ &+ \frac{\Delta k^{(L)}(\tau)}{F_S^{(L)}}\varphi^{(L)}\left(\tau, \delta e^{(L)}(M), \boldsymbol{X}_S\right) \boldsymbol{V}_G^{(L)^T}\widehat{\boldsymbol{X}}_0^{(L)} \end{aligned} \quad \text{(II-59)}$$

and (II-59) can be rewritten:

$$f^{(L)}\left(\tau, \delta e^{(L)}(M)\right) = \left(1 + \frac{\Delta k^{(L)}(\tau)}{k_m^{(L)}}\right)\left(F_S^{(L)} + \varphi^{(L)}\left(\tau, \delta e^{(L)}(M), \boldsymbol{X}_S\right)\right) - F_S^{(L)} \quad \text{(II-60)}$$

Projected on the base plane, the local quasi-static transmission error under load of mesh (P) is defined as:

$$TE_S^{(P)} = \boldsymbol{W}^{(P)^T}\boldsymbol{X}_S + NLTE^{(P)} \quad \text{(II-61)}$$

where $\boldsymbol{W}^{(P)}$ is a projection vector, not specified at this stage and $NLTE^{(P)}$ designates the no-load transmission error associated with mesh (P), defined from the same projection vector $\boldsymbol{W}^{(P)}$ and the rigid-body angular positions of the gears in the presence of tooth errors and modifications $\boldsymbol{X}_R$ as:

$$NLTE^{(P)} = \boldsymbol{W}^{(P)^T}\boldsymbol{X}_R \quad \text{(II-62)}$$

Reinjecting (II-51) in (II-61) leads to:

$$TE_S^{(P)} = \boldsymbol{W}^{(P)^T}\left(\boldsymbol{X}_0 + \sum_{L=1}^{N}\varphi^{(L)}\left(\tau, \delta e^{(L)}(M), \boldsymbol{X}_S\right)\frac{\widehat{\boldsymbol{X}}_0^{(L)}}{F_S^{(L)}}\right) + NLTE^{(P)} \quad \text{(II-63)}$$

Providing that the projection vectors $\boldsymbol{W}^{(P)}$ are chosen such that:

$$\boldsymbol{W}^{(P)} = \alpha^{(P)}\boldsymbol{V}_G^{(P)} \quad \text{(II-64)}$$

(II-57) gives :

$$\boldsymbol{W}^{(P)^T}\widehat{\boldsymbol{X}}_0^{(L)} = 0 \quad \text{if } (P) \neq (L) \quad \text{(II-65)}$$

Rearranging (II-63) and using (II-65), one obtains:

$$\varphi^{(P)}\left(\tau, \delta e^{(P)}(M), \boldsymbol{X}_S\right) = F_S^{(P)}\frac{TE_S^{(P)} - NLTE^{(P)} - \boldsymbol{W}^{(P)^T}\boldsymbol{X}_0}{\boldsymbol{W}^{(P)^T}\widehat{\boldsymbol{X}}_0^{(P)}} \quad \text{(II-66)}$$

Finally, (II-60) can be rewritten as:

$$f^{(L)}\left(\tau, \delta e^{(L)}(M)\right) = F_S^{(L)}\left[\left(1+\frac{\Delta k^{(L)}(\tau)}{k_m^{(L)}}\right)\left(\frac{TE_S^{(L)} - NLTE^{(L)} - \boldsymbol{W}^{(L)^T}\left(\boldsymbol{X}_0 - \widehat{\boldsymbol{X}}_0^{(L)}\right)}{\boldsymbol{W}^{(L)^T}\widehat{\boldsymbol{X}}_0^{(L)}}\right) - 1\right] \quad (II\text{-}67)$$

Assuming that the dynamic contact conditions are close to those in quasi-static conditions, the combination of (II-46) and (II-67) gives the following equations of motion expressed in terms of transmission errors:

$$\frac{1}{T_m^2}\boldsymbol{M}\boldsymbol{X}'' + \frac{1}{T_m}\boldsymbol{C}\boldsymbol{X}' + \left(\boldsymbol{K}_{sys} + \sum_{L=1}^{N}\boldsymbol{K}_G^{(L)}(\tau)\right)\boldsymbol{X} = \boldsymbol{F}_0 + \sum_{L=1}^{N} F_S^{(L)}\left[\left(1+\frac{\Delta k^{(L)}(\tau)}{k_m^{(L)}}\right)\left(\frac{TE_S^{(L)} - NLTE^{(L)} - \boldsymbol{W}^{(L)^T}\left(\boldsymbol{X}_0 - \widehat{\boldsymbol{X}}_0^{(L)}\right)}{\boldsymbol{W}^{(L)^T}\widehat{\boldsymbol{X}}_0^{(L)}}\right) - 1\right]\boldsymbol{V}_G^{(L)} + \boldsymbol{F}_{\dot{\Omega}}(\tau) \quad (II\text{-}68)$$

In the presence of shape deviations, the rotation transfer between the pinion and the gear is altered giving rise to an inertial forcing term $\boldsymbol{F}_{\dot{\Omega}}(\tau)$ due to unsteady rotational speeds of the form:

$$\boldsymbol{F}_{\dot{\Omega}}(\tau) = [\boldsymbol{M}]\dot{\boldsymbol{\Omega}} \quad (II\text{-}69)$$

where $\dot{\boldsymbol{\Omega}}$ contains the angular rigid-body accelerations at each node of the system.

The fluctuations of the driving and driven member angular velocities of stage (L) can be expressed from the local no-load transmission error, following (II-62):

$$\frac{d}{dt}NLTE^{(L)} = \boldsymbol{W}^{(L)^T}\dot{\boldsymbol{X}}_R = \boldsymbol{W}^{(L)^T}\boldsymbol{\Omega} \quad (II\text{-}70)$$

$\dot{\boldsymbol{X}}_R = \boldsymbol{\Omega}$ contains the rigid-body angular velocities at positions corresponding to the torsional degrees-of-freedom. Denoting ${w_{TOR}}_1^{(L)}$ and ${w_{TOR}}_2^{(L)}$ the corresponding torsional components in $\boldsymbol{W}^{(L)}$, the time-derivative of no-load transmission error becomes:

$$\frac{d}{dt}NLTE^{(L)} = {w_{TOR}}_1^{(L)}\dot{\Omega}_1^{(L)} + {w_{TOR}}_2^{(L)}\dot{\Omega}_2^{(L)} \quad (II\text{-}71)$$

The accelerations of the driven member of stage (L) therefore read:

$$\dot{\Omega}_2^{(L)} = \frac{1}{{w_{TOR}}_2^{(L)}}\left(\frac{d^2}{dt^2}NLTE^{(L)} - \dot{\Omega}_1^{(L)}\,{w_{TOR}}_1^{(L)}\right) \quad (II\text{-}72)$$

And using the dimensionless variable $\tau = t/T_m$:

$$\frac{1}{T_m}{\Omega_2^{(L)}}' = \frac{1}{T_m^2\,{w_{TOR}}_2^{(L)}}\left({NLTE^{(L)}}'' - {\Omega_1^{(L)}}'\,{w_{TOR}}_1^{(L)}\right) \quad (II\text{-}73)$$

It is further considered that the input speed of the system is constant so that $\dot{\Omega}_1^{(I)} = 0$. Under this condition, the acceleration of the driven member of stage (I) reduces to:

$$\frac{1}{T_m}\Omega_2^{(I)} = \frac{1}{T_m^2\, w_{TOR_2}^{(L)}} NLTE^{(I)''} \qquad \textit{(II-74)}$$

For the following stages in the system (in the sense of the power circulation), the acceleration of the driven member is subsequently deduced from the no-load transmission errors of each preceding stage as:

$$\frac{1}{T_m}\Omega_2^{(L)} = \frac{1}{T_m^2\, w_{TOR_2}^{(L)}} \sum_{P=I}^{L} NLTE^{(P)''} \qquad \textit{(II-75)}$$

2.6 Damping

Damping largely controls the dynamic response of a system especially near the critical speeds. Yet, its characterization remains a challenge and the literature on gear damping is still sparse. Damping factors are usually employed and adjusted based on experimental evidence but, so far, it seems that no formulation can be generalized to any gear geometry. Two global formulations are commonly used in gear dynamics:

a) Rayleigh's damping

Damping is introduced as a constant matrix which is expressed as a combination of the average stiffness and mass matrices of the complete system under the form:

$$[\boldsymbol{C}] = a[\boldsymbol{M}] + b[\overline{\boldsymbol{K}}] \qquad \textit{(II-76)}$$

$[\overline{\boldsymbol{K}}]$ is defined in (II-49) and empirical values of coefficients a and b are used which i) for a are between 10^2 and 10^4 while ii) b ranges approximately from 10^{-7} to 10^{-4}.

b) Modal damping factors

The damping matrix $[\boldsymbol{C}]$ is characterized using a modal approach with damping factors either constant for all modes or dependent on the mesh contribution to the overall modal strain energy such that:

$$\boldsymbol{\Phi}_p^T[\boldsymbol{C}]\boldsymbol{\Phi}_p = 2\varsigma_p\sqrt{k_{\Phi_p} m_{\Phi_p}} \qquad \textit{(II-77)}$$

$\boldsymbol{\Phi}_p$ is the mode-shape of the undamped system with average stiffness matrix associated with mode p.
ς_p is the modal damping factor associated with mode p.
k_{Φ_p} and m_{Φ_p} are the modal stiffness and mass associated with mode p.

In the case of an identical damping factor ς for all modes, the values found in the literature typically range from 0.01 to 0.2 [130].

ζ_p can also be adjusted for each mode to try to account for the relative gear mesh contribution to the total damping via the percentage of modal strain energy stored in the gear mesh, leading to expressions of the form:

$$\zeta_p = 0.07 \times \rho_p + 0.02 \times (1 - \rho_p) \qquad \textit{(II-78)}$$

ρ_p is the percentage of modal strain energy stored in the gear mesh for mode p. 0.07 is a typical order of magnitude of mesh damping factor whereas 0.02 represents internal (structural) damping.

3 RESOLUTION

The simulation of the dynamic behaviour of a gear system can be viewed as a two-step procedure (steps a) and b) as described in **Section 5.1** of **Chapter I**). A quasi-static analysis is performed first to characterize the excitations of the system (via mesh stiffness functions and transmission errors). In a second step, these excitations are introduced as forcing terms in a dynamic model including the elements presented earlier and the dynamic response of the system is simulated by solving the equations of motion. This section presents each of these tasks successively.

3.1 Definition of the excitations (quasi-static resolution)

Depending on the modelling strategy, the inter-mesh force wrench of each gear stage of the system must be determined at each time step, prior to dynamic simulations. This wrench is characterized by the gear mesh stiffness, transmission errors and structural vector.

These time-dependent parameters are calculated using specialised software codes dedicated to the quasi-static analysis of cylindrical or spiral-bevel gears.

3.1.a) *Cylindrical gears*

Concerning spur and helical gears, the Load Distribution Program (LDP) developed at the GearLab, of the Ohio State University [131] is used. The model can calculate tooth load distribution based on gear elasticity and errors or modifications on the gear teeth. It includes the effects of bending deflections, base rotation and local contact deflections of the contacting teeth, along with the initial separations due to errors or modifications.

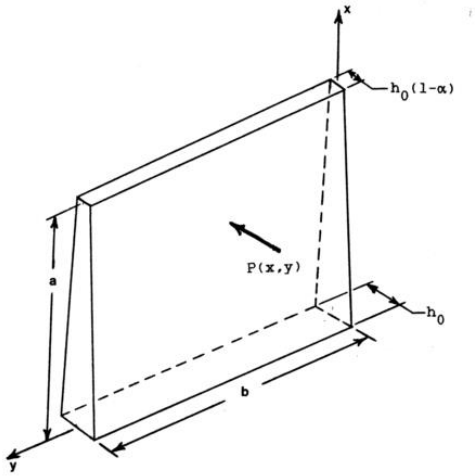

Figure II-12 : Geometry of tapered plate model, from Yakubek [14]

The bending deflections of the teeth are estimated using the model developed by Yakubek [14], which relies on a tapered plate model and a Rayleigh-Ritz method. Base rotation calculations are based on the dimensionless approximation developed by Stegemiller and Houser [16,132] deduced from finite element results and the moment image method to simulate edge effects. Finally, local contact deflections are estimated from Weber's model [133].

Involute teeth are considered so that all contact forces and deflections are in the base plane and tooth surface modification or error are modelled as initial normal separation or approach between the pinion and gear tooth flanks. Two distinct criteria are used to formulate the load distribution problem:

(a) for any potential point of contact M, the total sum of the elastic deformations and initial separations must be larger than or equal to the relative normal approach between the pinion and the gear in the base plane (condition of compatibility),
(b) the sum of all the torques acting on a gear body must be zero. In other terms, the sum of the moments generated by the contact forces about the line of action must be equal, but opposite in sign, to the applied torque.

A slack variable is introduced to rewrite the inequality equation of condition (a) as an equality and a simplex type algorithm is used to solve for the load distribution.

At each angular position of the pinion/gear pair, the contact zone is discretized into elemental cells, and for each of them, the following parameters (among others) are determined:

- position of the point of contact (centre of the elemental cell),
- radius at the point of contact from the centre of the gear body,
- load carried by each contact point,
- total tooth deflection (bending, base rotation and contact),
- total initial separation at the point of contact.

Transmission error is obtained from the sum of all of the deflections and initial separations (positive separation for material removal and negative for excess of material with respect to ideal tooth flank geometry). This value is computed for each angular position of the pinion/gear pair and at each point in the contact zone. The resulting transmission error is the minimum value obtained over all the contact points and is expressed in the direction of the line of action as:

$$TE_S = \frac{1}{\cos\beta_b} \boldsymbol{V}_G{}^T \boldsymbol{X}_S + NLTE \qquad \textit{(II-79)}$$

The elemental mesh stiffness is computed at each cell using the inverse of the precedent value and multiplying it by the normal load carried by the cell. The elemental stiffness elements are added as springs in parallel thus leading to the global mesh stiffness function.

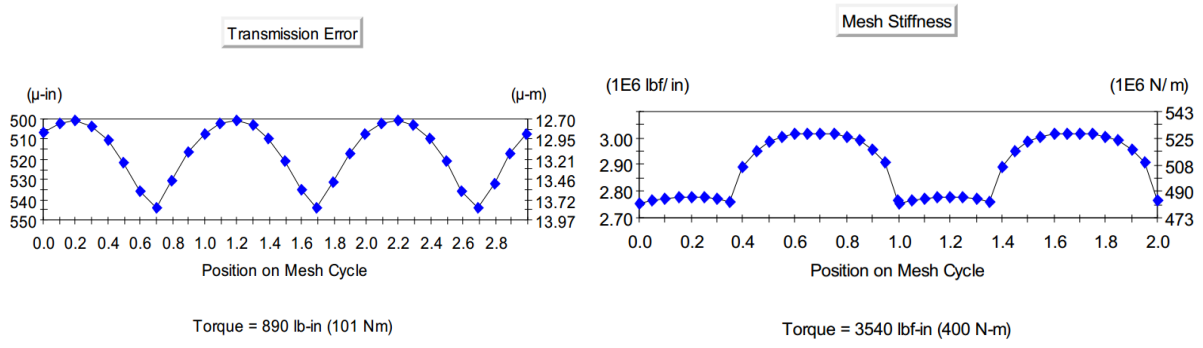

Figure II-13 : Example of LDP transmission error and mesh stiffness outputs (from [131])

In practice, two cases must be considered: one at nominal torque to determine the mesh stiffness and quasi-static transmission error TE_S functions and one at very low load to obtain the no-load transmission error $NLTE$.

For cylindrical gears, the normal to the pinion tooth flanks $\boldsymbol{n}_1$ is supposed to be constant during the meshing process and, as detailed in **Section 2.2.a)** of this chapter, its expression in frame $(\boldsymbol{X}, \boldsymbol{Y}, \boldsymbol{Z})$ is:

$$\boldsymbol{n}_1 = \begin{bmatrix} \varepsilon sin\beta_b \\ cos\beta_b sin\alpha_t \\ \zeta cos\beta_b cos\alpha_t \end{bmatrix}_{(\boldsymbol{X},\boldsymbol{Y},\boldsymbol{Z})} \quad \text{(II-8o)}$$

For most of the applications, the position of the centroid of mesh force distribution is averaged over the mesh period and G is assumed to be centered in the base plane. However, it is possible to include the time fluctuations of $\boldsymbol{O_1 G}$ using the output details obtained from LDP.

In the present configuration, the structural vector $\boldsymbol{v}_G$ for cylindrical gears is also assumed to be constant in time and mesh excitations are characterized by only three time-varying functions, i.e.:

- mesh stiffness,
- quasi-static transmission error under load TE_S,
- no-load transmission error $NLTE$.

3.1.b) *Bevel gears*

The load distribution problem for bevel gears is solved using the software ASLAN, developed at LaMCoS, INSA de Lyon by Teixeira *et al.* [101,134,135] and, here again, decomposed into three operations:

- definition of gear geometry by simulating the gear manufacturing process,
- simulation of no-load kinematics,
- load distribution calculation.

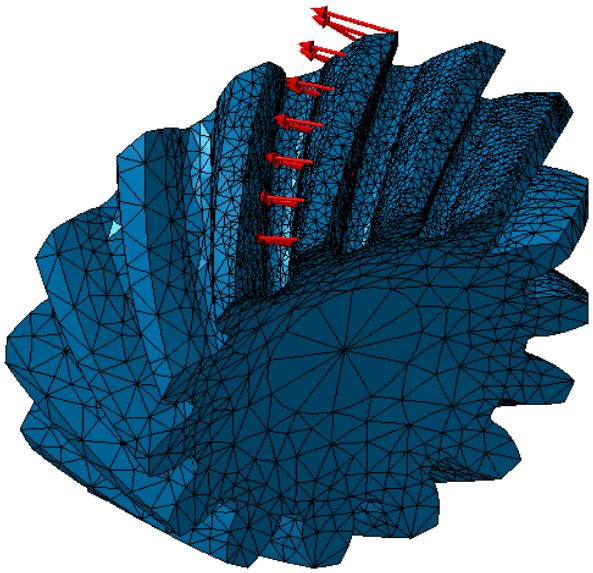

Figure II-14 : Finite element model of a spiral-bevel pinion for the calculation of the coefficients of influence

Load sharing is determined by solving the displacement compatibility conditions along with static torque equilibrium. The compatibility conditions account for bending and contact deflections, which are both characterized by coefficients of influence, and for initial separations. The structural deflections are calculated by finite elements while the local contact compliance is approximated using Boussinesq's theory for elastic half-spaces. The equations obtained from the compatibility conditions and static torque equilibrium are solved iteratively by a fixed-point method.

A number of results are provided at each angular position both for no-load and loaded conditions (transmission error, mesh stiffness, pressure distribution, etc.). The kinematic (no-load) transmission error is deduced from the geometry of the gears and the initial separations. The quasi-static transmission error under load is obtained from the relative approach between the pinion and the gear, to which the no-load transmission error is added. The global mesh stiffness is defined as the ratio between the applied normal load and the induced relative normal approach. The direction of the global mesh force and the centroid of the mesh force distribution are also calculated at each time step. Transmission error can be expressed as an angular perturbation or as a displacement. In this case, it is defined as:

$$TE_S = \boldsymbol{V}_G{}^T \boldsymbol{X}_S + NLTE \qquad \textit{(II-81)}$$

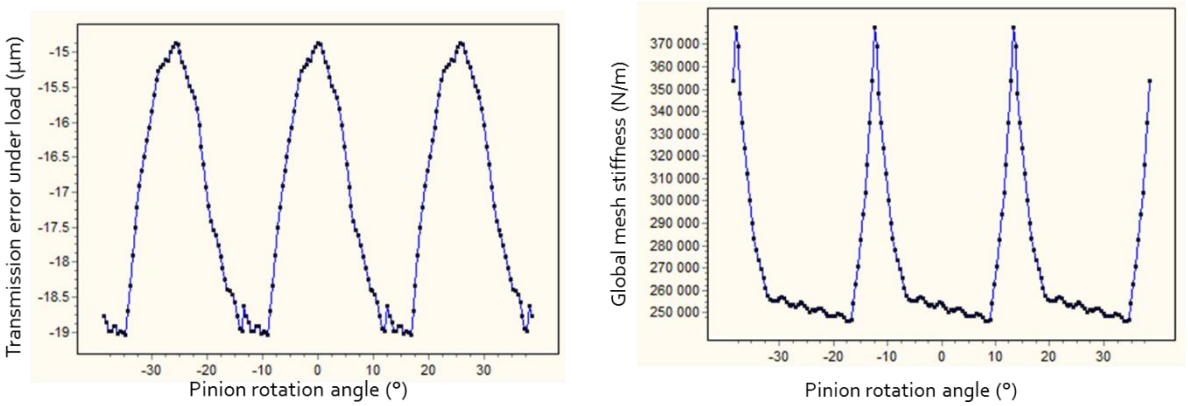

Figure II-15 : Example of ASLAN transmission error and mesh stiffness outputs

In the case of bevel gears, the time variations of the global mesh force direction cannot be neglected any longer. Therefore, the structural vector $\boldsymbol{v}_G$ has to be computed at each time step in terms of the instant normal vector $\boldsymbol{n}_1$ and the instant position G of the centroid of the mesh force distribution.

For bevel gears, mesh excitations are therefore characterized by five time-varying functions:

- mesh stiffness,
- quasi-static transmission error under load TE_S,
- no-load transmission error $NLTE$,
- position of the centroid of mesh force distribution,
- orientation of the global mesh force (normal vector).

3.2 Phase shift between successive gear stages

For gear stages separated by an intermediate shaft, the mesh period is different and the phase shift between the excitation signals depends on the mounting conditions which are often unknown.

However, if the pinions are mounted in series (one pinion meshes with at least two others), the mesh period is the same for each mesh and the phase shift between the excitation signals is imposed by geometrical considerations.

The calculation of the phase shift for a driving wheel at the extremity of the drive chain is presented on the example illustrated in Figure II-16. Stage (I), composed of the driving wheel (1) and of the first driven wheel (2) is the reference for the position of the lines of contact in the base plane. The phase shift at stage (II) (between wheels (2) and (3)) is denoted Δl. For each mesh, the contact area is limited by points T_1' and T_2'. When one line comes in contact at ${T_1'}^{(I)}$, the phase shift Δl is the distance between ${T_1'}^{(II)}$ and the closest point of contact in the base plane associated with mesh (II). It can be mathematically expressed as:

$$\Delta l = \begin{cases} S_{ba} - \varepsilon\, P_{ba} & if \quad \varepsilon\, P_{ba} \leq S_{ba} \\ S_{ba} + (1-\varepsilon)\, P_{ba} & if \quad \varepsilon\, P_{ba} > S_{ba} \end{cases} \qquad \textit{(II-82)}$$

with:

S_{ba} the apparent base tooth thickness of wheel (2)
P_{ba} the apparent base pitch
$\varepsilon = \left\| \frac{\left|{T_1'}^{(I)} {T_1'}^{(II)}\right|}{P_{ba}} \right\|$ and $\| \ \|$ is the remainder of the division.

As illustrated in Figure II-16, the distance $\left|{T_1'}^{(I)} {T_1'}^{(II)}\right|$, following the lines of action and base circles reads:

$$\left|{T_1'}^{(I)} {T_1'}^{(II)}\right| = \left|{T_1'}^{(I)} {T_2}^{(I)}\right] + \Phi R_{b2} + \left|{T_1}^{(II)} {T_1'}^{(II)}\right| \qquad \textit{(II-83)}$$

The positions of points T_1' and T_2' are imposed by the base and tip radii and, using the basic geometrical properties illustrated in Figure II-17, it comes:

$$\left|{T_1'}^{(I)} {T_2}^{(I)}\right] = \sqrt{R_{a2}^2 - R_{b2}^2} \qquad \textit{(II-84)}$$

$$\left|{T_1}^{(II)} {T_1'}^{(II)}\right| = |O_2 O_3| \sin \alpha_p^{(II)} - \sqrt{R_{a3}^2 - R_{b3}^2} \qquad \textit{(II-85)}$$

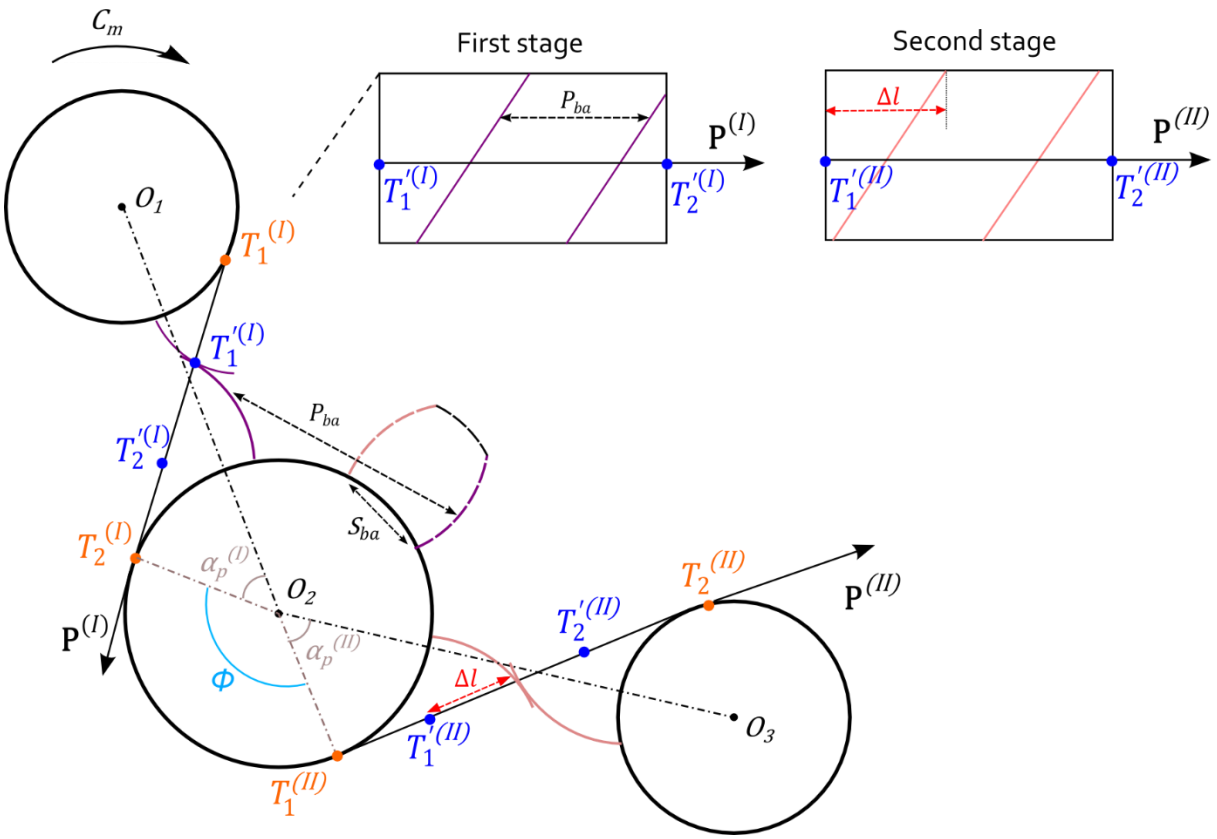

Figure II-16 : Geometrical parameters for the calculation of the phase shift between successive gear stages

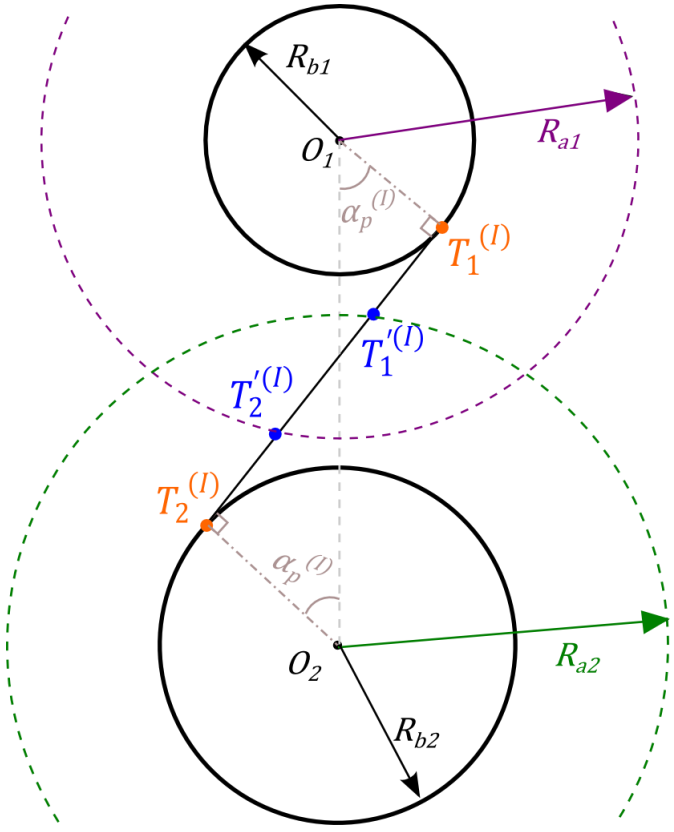

Figure II-17 : Geometrical parameters for the calculation of the contact zone boundaries

3.3 Harmonization of time discretization

Resolutions in time domain require the definition of a time step and of a total period of acquisition. For most of the cases presented in this memoir, all the teeth of a given pinion/gear pair exhibit the same profile: without any modification or with identical modifications on all teeth. In this case, the period of the excitations generated by the meshing process is equal to the mesh period of the gear pair and the quasi-static resolution can be ran over a single mesh period.

In the presence of some types of errors (e.g. pitch errors), the excitations have a period equal to the least common multiple between the rotational periods of the pinion and the gear. In such cases, the simulation time for the quasi-static problem should be long enough so as to capture all the possible combinations of contacting teeth.

Once the mesh excitations have been characterized for each gear stage, the time discretization must be re-scaled in view of the dynamic resolution. The gear stage with the smallest mesh period, and the associated time discretization used for the quasi-static analysis are taken as reference. An interpolation function is used to update the discretization of the quasi-static excitations associated with the other mesh stages of the systems, accounting for the angular velocity ratio. An illustration is given in Figure II-18.

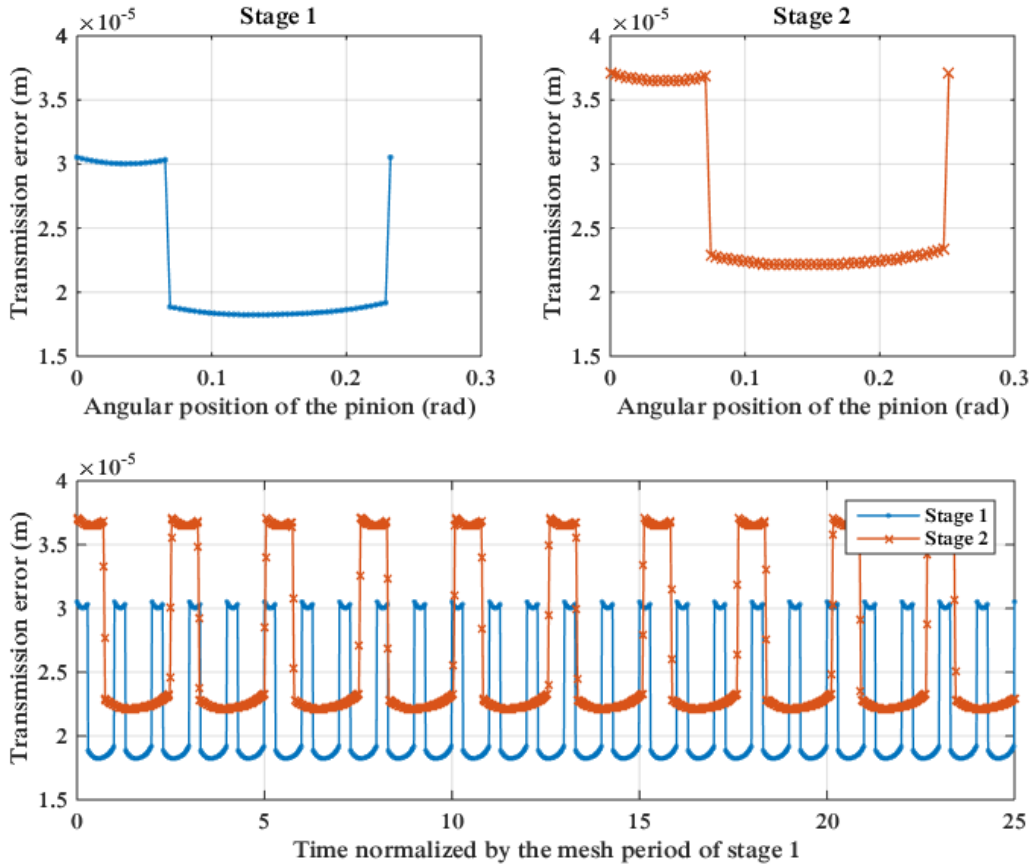

Figure II-18 : Example of the interpolation of transmission error signals

3.4 Dynamic resolution

After the preliminary quasi-static analyses, the equations of motion (II-68) are solved step-by-step in time using a Newmark integration scheme. At each time step, the stiffness matrix of the system and the forcing terms are recalculated to account for the instant mesh stiffness, transmission errors and structural vectors.

For a single-mesh system, the resolution has to be performed over several mesh periods to reach stationary regimes. For multi-stage systems, the different mesh periods have to be taken into account and the time domain of the dynamic resolution must generally by increased in order to be able to obtain stationary states. To facilitate convergence, the initial condition is set to be the static deflection, such that:

$$\begin{cases} \boldsymbol{X}(\tau = 0) = \boldsymbol{X}_S \\ \dot{\boldsymbol{X}}(\tau = 0) = \boldsymbol{0} \\ \ddot{\boldsymbol{X}}(\tau = 0) = \boldsymbol{0} \end{cases} \qquad \textit{(II-86)}$$

For speed sweep calculations, the solution in displacements, velocities and accelerations obtained at the last time increment of speed $n-1$ is used as initial condition of speed n.

3.5 Output parameters

Some key parameters have been selected as indicators of the dynamic behaviour which are defined below and will subsequently be used in the following chapters of this memoir.

3.5.a) *Critical eigenfrequencies*

The eigenfrequencies of the system are estimated using an average stiffness matrix and, for each mode p, the percentage of modal strain energy stored in mesh (L) is determined as:

$$\rho_p^{(L)} = k_m^{(L)} \frac{\boldsymbol{\Phi}_p^T \boldsymbol{V}^{(L)} \boldsymbol{V}^{(L)\,T} \boldsymbol{\Phi}_p}{\boldsymbol{\Phi}_p^T \left[\boldsymbol{K}_0 + k_m^{(L)} \boldsymbol{V}^{(L)} \boldsymbol{V}^{(L)\,T} \right] \boldsymbol{\Phi}_p} \qquad \textit{(II-87)}$$

and is considered as an indicator of the severity of one frequency with regard to pinion-gear mesh (L). Critical speeds (amplifications of tooth loads) are expected when the mesh frequency matches one of the critical eigenfrequencies of the system.

3.5.b) *Dynamic transmission error*

Following the definition of quasi-static transmission error (II-61), the local dynamic transmission error of a given mesh (L) is related to the global solution $\boldsymbol{X}$ of the equations of motion as follows:

$$TE_d^{(L)} = \boldsymbol{W}^{(L)^T} \boldsymbol{X} + NLTE^{(L)} \qquad \textit{(II-88)}$$

where the projection vector $\boldsymbol{W}^{(L)}$ is the same as that used for the definition of the no-load and loaded quasi-static transmission errors.

The time variation amplitudes of dynamic transmission errors are widely accepted as relevant indicators in gear dynamics which, here, will be quantified by their peak-to-peak amplitudes or RMS levels.

3.5.c) *Dynamic mesh force*

Dynamic mesh force at one given mesh (or stage) (L) is another characteristic parameter in gear dynamics which for both cylindrical (spur, helical) and bevel gears reads:

$$F_d^{(L)} = k^{(L)}(t) \boldsymbol{V}_G^{(L)^T} \boldsymbol{X} - F_S^{(L)} \left[\frac{k^{(L)}(t)}{k_m^{(L)}} \left(\frac{TE_S^{(L)} - NLTE^{(L)} - \boldsymbol{W}^{(L)^T} \left(\boldsymbol{X}_0 - \widehat{\boldsymbol{X}}_0^{(L)} \right)}{\boldsymbol{W}^{(L)^T} \widehat{\boldsymbol{X}}_0^{(L)}} \right) - 1 \right] \qquad \textit{(II-89)}$$

The maximum of the dynamic mesh force in steady-state conditions is representative of possible tooth overloads in dynamic conditions. This parameter is often expressed in a dimensionless form as the maximum dynamic to static mesh force ratio (known as mesh force dynamic factor):

$$DF_{mf}^{(L)} = \frac{\max\left(F_d^{(L)}\right)}{F_S^{(L)}} \qquad \textit{(II-90)}$$

4 CONCLUSION

This chapter presents the three-dimensional model developed in this work which is dedicated to the simulation of the dynamic behaviour of multi-stage gear systems. The model relies on a transmission error-based characterization of mesh excitations. The theoretical grounding is first exposed on a simple single-degree-of-freedom system to highlight how kinematic (no-load) and quasi-static loaded transmission errors control gear dynamic response.

An extension to three-dimensional systems with multiple gear stages is then presented. Mesh excitations are modelled by time-varying mesh stiffness functions and transmission errors. The formulation allows to account for mesh elasticity as well as initial separations between gear teeth (caused by tooth modifications or manufacturing and mounting errors). A specific two-node gear element is developed which can be adapted to cylindrical or bevel gears. The other components of the transmission (shafts, bearings, elastic couplings and additional inertias) can be introduced using lumped parameter elements. All the components of the system are assembled and the global equations are expressed in terms of time-varying mesh stiffness and transmission errors of each gear stage. This formulation relies on the assumption that the dynamic contact conditions are close to those in quasi-static and therefore contact losses cannot be simulated this way.

A preliminary quasi-static analysis is performed for each gear stage to characterize mesh excitations. The dynamic equations of motion are finally solved step by step in time using a Newmark integration scheme.

Chapter III
Elements of validation

This chapter presents elements of validation of the proposed transmission error-based formulation for single and double-stage systems.

The first two sections focus on single-stage systems with parallel axes.

The results from a different spur gear model are first compared with those obtained from the transmission error-based approach. Different configurations of profile modifications are studied, showing that the proposed model accurately accounts for tooth modifications.

Previous experimental evidence are presented in ***Section 2*** *and used to validate the proposed model in the case of helical gears mounted on long transmission shafts requiring three-dimensional degrees of freedom to account for bending and axial displacements.*

The third section of this chapter presents an example application to spiral-bevel gears and comparisons with results obtained by using a different modelling strategy.

Finally, the validity of the formulation is assessed on a double-stage spur gear system from the literature. The results obtained using the transmission error-based theory are compared with the simulations performed from a different modelling strategy. Different gear arrangements are investigated and the influence of profile modifications is addressed.

1 SINGLE-STAGE SPUR GEAR SYSTEM – NUMERICAL VALIDATION

This section presents the first elements of validation of the transmission error-based model. It focuses on a single-stage spur gear system, which was initially studied by Raclot [114]. The gears are first modelled without any tooth modification and two different configurations of profile relief are studied.

Raclot compared the results obtained from two different models:

- In the first one, mesh excitations are approximated by their corresponding quasi-static expressions and the equations of motion are projected in the frequency domain. The solutions are then derived by an iterative spectral method, as proposed by Perret-Liaudet [136].
- In the second model, a contact algorithm is coupled to the resolution of the dynamic equations of motion. The actual contact conditions are therefore solved at each time step and for any rotational speed, allowing to account for changes in contact pattern under dynamic conditions (and for possible contact losses).

The results obtained from this second model are used in what follows in order to evaluate the ability of the transmission error-based approach to accurately simulate mesh excitations.

1.1 Unmodified gears

The system as proposed by Raclot is depicted in Figure III-1. It is composed of a single spur gear stage and the pinion and the gear shafts are both supported by two identical bearings. Gear data are detailed in Table III-1. Table III-2 gives the shaft characteristics (using the circled element numbers of Figure III-1) and bearings. The model comprises a total of 54 degrees-of-freedom. The global damping matrix is built using the mode shapes of the system determined by considering a time-averaged stiffness matrix and a unique damping factor of 0.1 is used (cf. **Section 2.6 b)** of **Chapter II**).

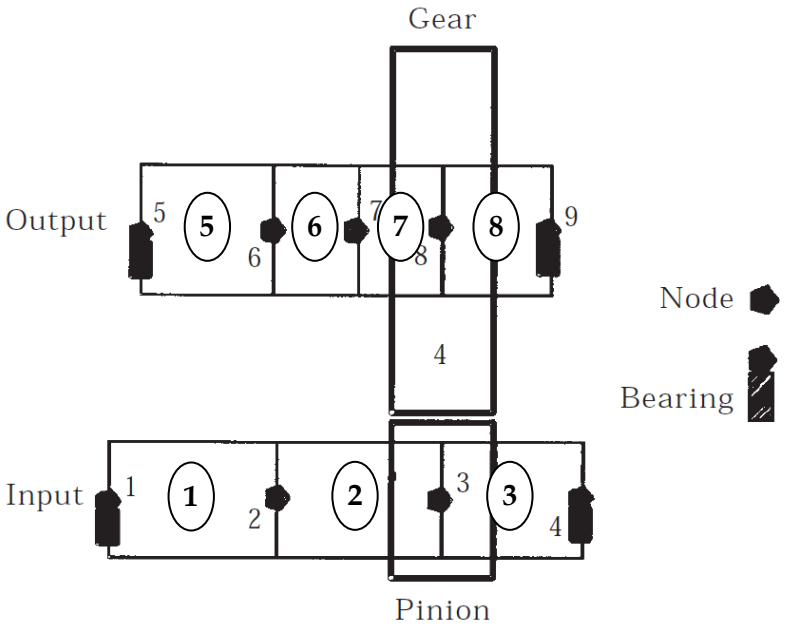

Figure III-1 : Single-stage model, from Raclot [114]

Table III-1 : Single-stage system – Gear data, from Raclot [114]

	Pinion	Gear
Number of teeth	27	63
Face width (mm)	72	
Module (mm)	4	
Pressure angle (deg)	20	
Helix angle (deg)	0	
Addendum coefficient	1.0	1.0
Dedendum coefficient	1.4	1.4
Profile shift coefficient	0	0

Table III-2 : Single-stage system – Shaft and bearing data, from Raclot [114]

Shaft	Shaft element	Length (mm)	External diameter (mm)
Input shaft	1	116.775	80
	2	116.775	80
	3	98.43	80
Ouput shaft	5	92.43	90
	6	59.69	90
	7	59.69	90
	8	76.69	90
Bearings	Radial stiffness of $4.10^8 N/m$ for all bearings		

A constant input torque of 1 500 Nm is applied at the extremity of the pinion shaft and the input speed is varied from 100 to 14 500 rpm. For each rotational speed, dynamic transmission error is computed using the definition given in **paragraph 3.5.b)** of **Chapter II**. The RMS value of the time-varying part of the dynamic transmission error signal (which Raclot refers to as transmission error shape factor) is then used for comparison purposes. Figure III-2 shows the results obtained from the transmission error-based approach presented in **Chapter II** ("TE model") compared with those from the model based on the resolution of the actual contact conditions ("local model", from Raclot [114]). Both methods provide results in very close agreement, either in the position of the predicted critical speeds or in the amplitude of the corresponding peaks.

Figure III-3 presents the same results as Figure III-2 but for a lower level of damping (unique damping factor of 0.05). One can notice that the gear dynamic behaviour is dominated by a large amplitude jump at the main critical speed, which is not reproduced by the transmission error-based model. This observation highlights the major limitation of the proposed approach: the theoretical formulation is based on the assumption that dynamic contact conditions are close to those in quasi-statics and non-linearities are not accounted for. Amplitude jumps associated with tooth separations cannot therefore be reproduced.

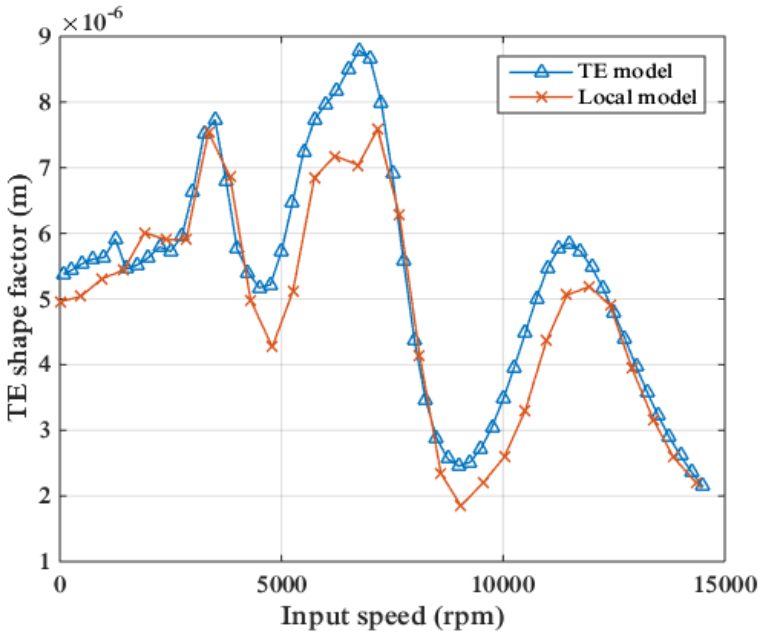

Figure III-2 : Single-stage system – Evolution of TE shape factor versus pinion speed (unmodified gears)

This limitation is considered acceptable provided that the model is dedicated to the study of heavily loaded gear systems. Moreover, the occurrence of contact losses can be anticipated from the transmission error-based approach by following the evolution of the global dynamic mesh force. When the mesh force dynamic factor exceeds 2, tooth contacts are likely to be lost. The speeds for which the dynamic factor is greater than 2 in Figure III-4 correspond to those for which the local model predicts contact losses (around 3 650 and 6500 rpm).

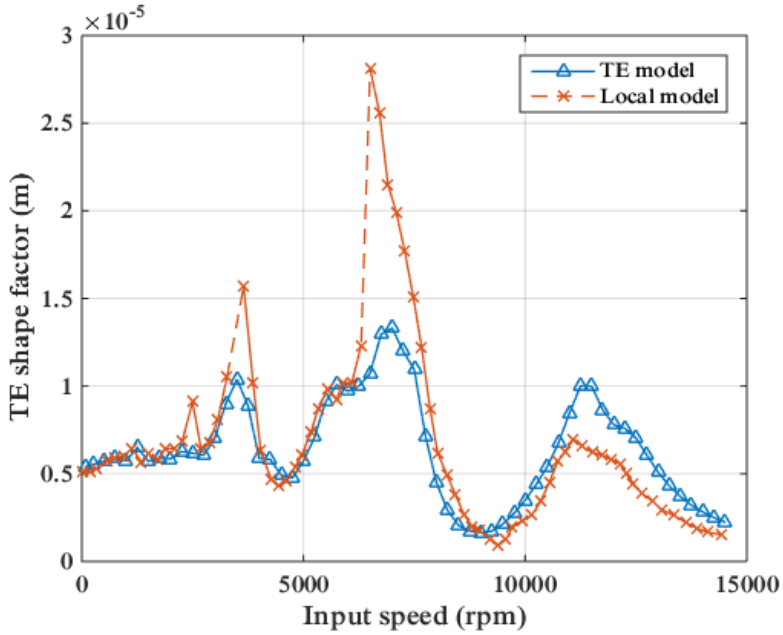

Figure III-3 : Single-stage system – Evolution of TE shape factor under reduced level of damping (5%)

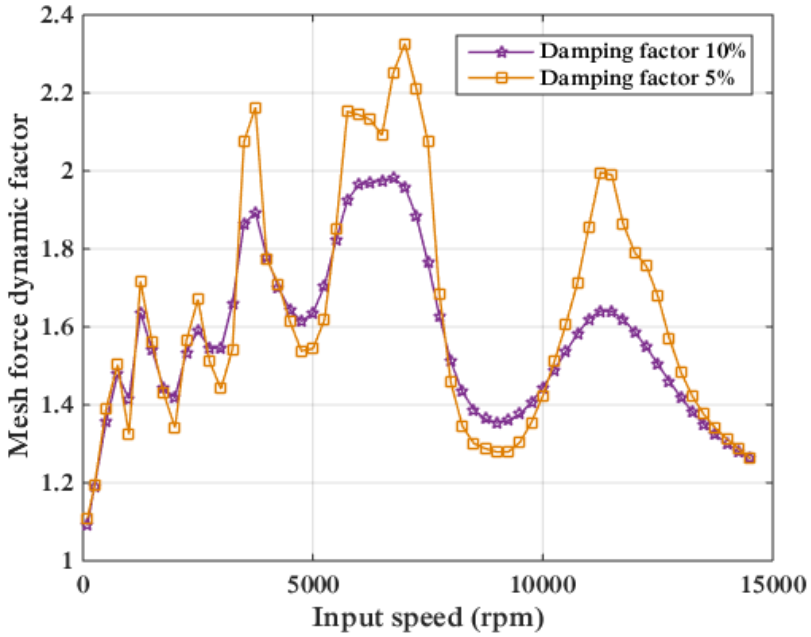

Figure III-4 : Single-stage system – Influence of damping on the evolution of the mesh force dynamic factor

These results confirm that the transmission error-based predictions are in accordance with the expected dynamic behaviour for a single gear pair with ideal errorless and unmodified teeth. The next section deals with the introduction of profile modifications and their influence on the dynamic response.

1.2 Influence of profile modifications

Following Raclot [114], two configurations of profile modifications are studied in this section and compared with the previous case with unmodified tooth profiles. The system is identical to that exposed in the previous section, with the same gear macro geometry. The profile modifications are symmetric tip reliefs with a depth of modification of 30 µm. A schematic representation of the modifications is given in Figure III-5. The three following conditions are then compared:

- unmodified profiles,
- short relief (modification applied over 20% of the active profiles),
- long relief (modification applied over 40% of the active profiles).

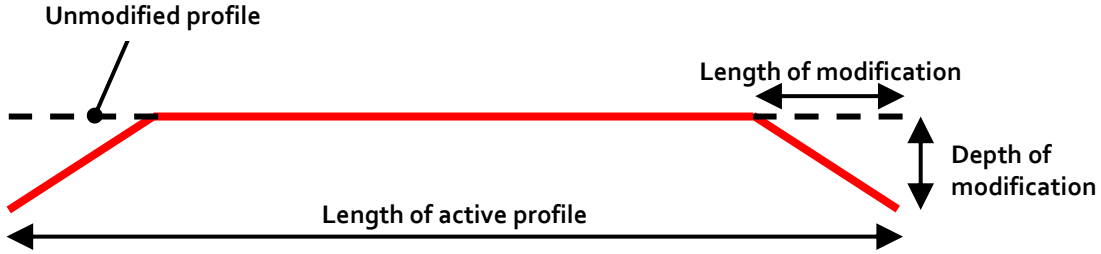

Figure III-5 : Schematic representation of linear symmetric tip relief

The results obtained with the short reliefs are shown in Figure III-6. Here too, both the local and transmission error-based models deliver very similar results. However, larger discrepancy is observed in Figure III-7 in the case of long profile modifications.

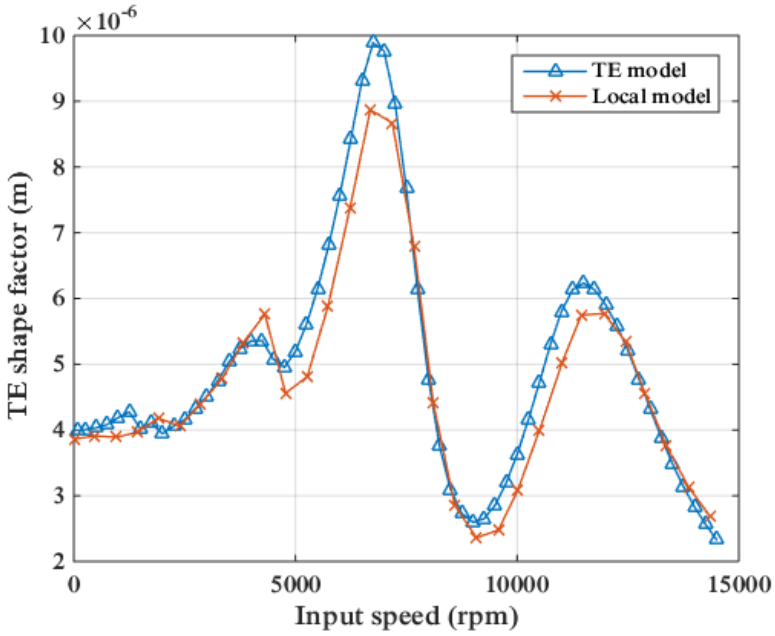

Figure III-6 : Single-stage system – Introduction of short profile modifications

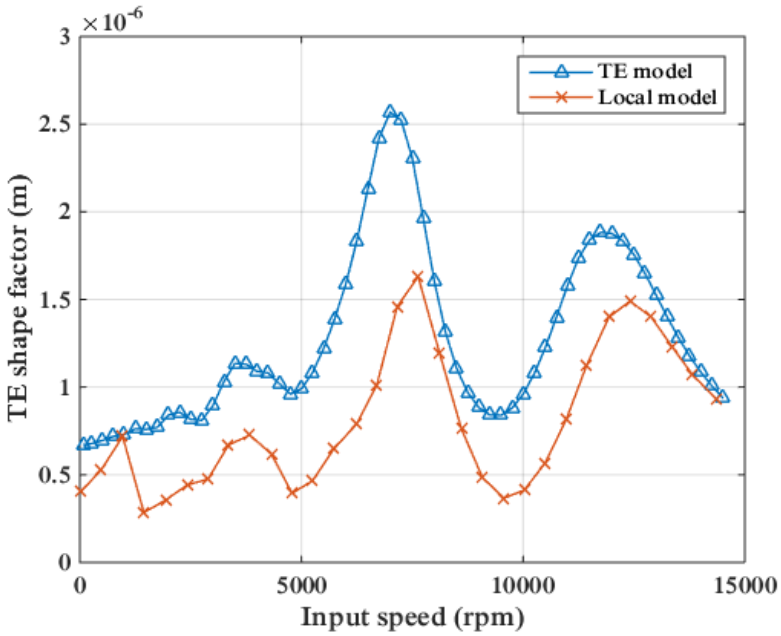

Figure III-7 : Single-stage system – Introduction of long profile modifications

The reason for the discrepancy observed over the complete range of speeds in Figure III-7 is that the long modifications were defined as optimal by Raclot, using a model based on a constant stiffness per unit of contact length [42]. The stiffness formulation used in the transmission error-based model is different and therefore, the long modifications are not as

effective in reducing the fluctuations of quasi-static transmission error and hence the dynamic amplifications near the critical speeds.

However, the comparison of the three configurations of tooth modifications shows that a significant reduction in the fluctuations of transmission errors (both quasi-static and dynamic) is obtained when long modifications are applied on tooth profiles. This trend is reproduced by both models, as illustrated in Figure III-8.

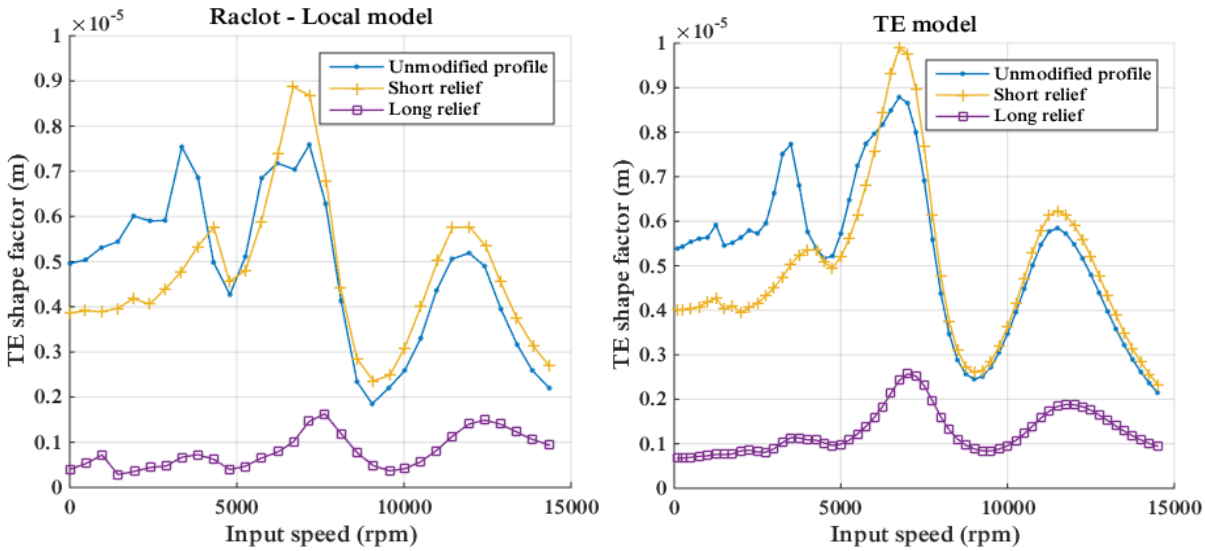

Figure III-8 : Single-stage system – Comparison of different configurations of profile modifications

The results presented in this section prove that, for systems with linear behaviour, the transmission error-based formulation is equivalent to a local model with a resolution of the contact conditions at each time step. It is also evidenced that the proposed formulation allows to account for tooth modifications. However, one of the main limitations of this approach has been pointed out by showing that contact losses cannot be reproduced.

The next section proposes to extend the validation of the transmission error-based approach by comparing experimental and numerical findings.

2 SINGLE-STAGE SPUR / HELICAL GEAR SYSTEM – EXPERIMENTAL VALIDATION

The test bench mentioned in the following section was in operation at LaMCoS – INSA Lyon in the 1990s. It was used to test high quality spur and helical gears with linear profile modifications. The experimental setup did not allow transmission error measurements but strain gauges were cemented at the fillet of some teeth making it possible to estimate root strain/stress and tooth dynamic bending moments [74].

This section presents the numerical results obtained for the spur and helical gear configurations from the transmission-error-based formulation presented in **Chapter II** and compares them to the experimental evidence.

2.1 Experimental setup

The test rig represented in Figure III-9 and Figure III-10 is an open-loop single stage spur or helical gear system. Power is supplied by a 220 kW electric motor which can operate the pinion shaft between 0 to 6000 rpm whereas the output torque (maximum 4200 Nm) is imposed by an electric generator. These elements are represented by external inertia at the extremity of the input and output shaft of 3 kg.m² for the motor and 21 kg.m² for the generator.

The shafts are supported by hydrostatic (for low speed applications) or hydrodynamic bearings which are housed in rigid casings fixed to the base of the test stand. The connections between the motor / generator and the pinion / gear shaft are ensured by elastic couplings. Axial forces are balanced by thrust bearings. The housing is made of cast iron and fixed to a concrete block resting on springs and dampers. The reduction unit is permanently jet lubricated by a lubricant (ISO VG 100) at a constant temperature of 55°C. A low pressure system provides lubrication to the gears and the hydrodynamic bearings while hydrostatic bearings are supplied in oil by a high pressure system.

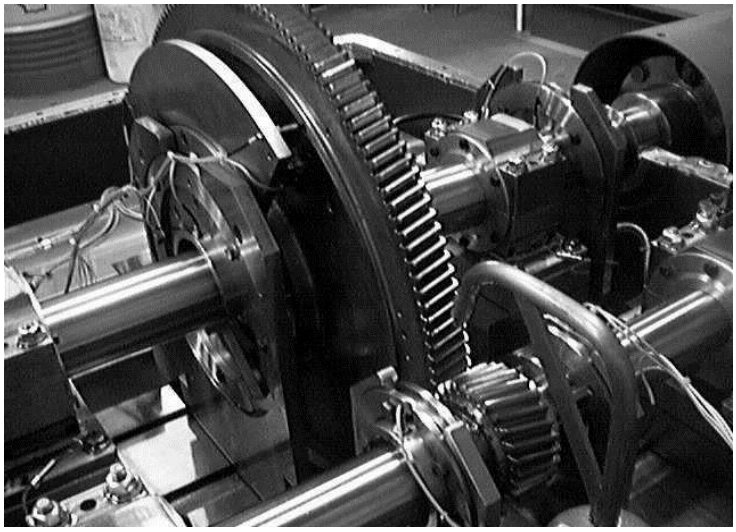

Figure III-9 : Single gear stage experimental setup, from Baud and Velex [74]

The gear characteristics are listed in Table III-3. The pinion and gear tooth profiles are modified by symmetric linear tip relief, as depicted in Figure III-5. Tooth leads are unmodified

but slight chamfers have been introduced to avoid corner contacts. Gears are made of 30CrMoV steel and ground. Profile modifications as well as pitch errors were carefully controlled and cumulative pitch errors do not exceed 20 µm on either gear (ISO quality grade 4).

The shafts (Table III-4) were manufactured to close tolerances in order not to deteriorate the accuracy of the gears. Magnetic probes positioned 90° apart are used to measure bending displacements at four different locations on each shaft. Micro uniaxial strain gauges are cemented at the root of three successive teeth on the pinion and the gear with four active gauges distributed across the face width, as shown in Figure III-11. Two slip rings mounted at the end of each shaft are used to transfer the gauge signals from the rotary to the stationary system.

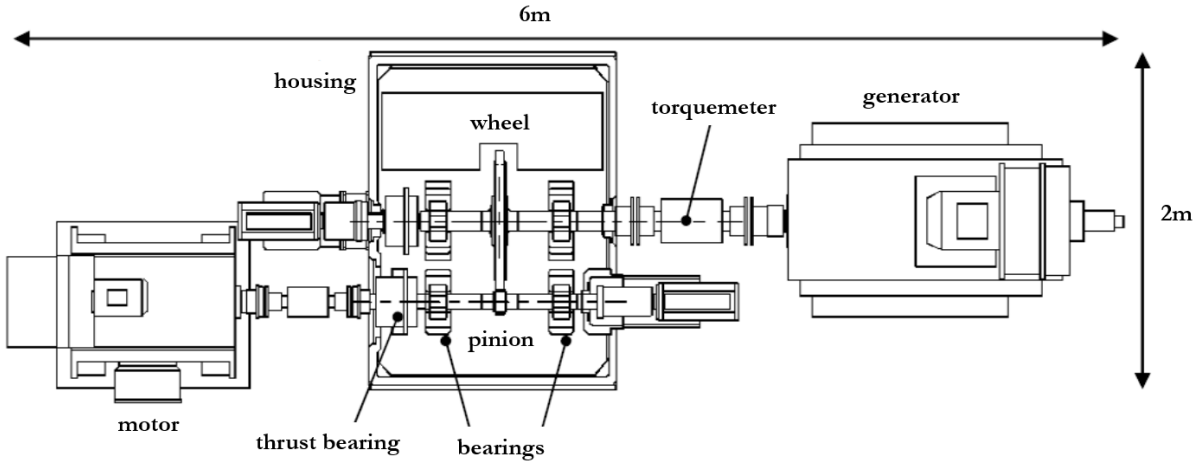

Figure III-10 : Schematic representation of the complete setup, from Baud and Velex [74]

Table III-3 : Single-stage experimental setup – Gear data

	Pinion	**Gear**
Tooth number	26	157
Module (mm)	4	
Helix angle (deg)	0 (spur) 12.5 (helical)	
Pressure angle (deg)	20	
Center distance (mm)	366 (spur) 375 (helical)	
Face width (mm)	50	40
Addendum coefficient	1	1
Dedendum coefficient	1.4	1.4
Profile shift coefficient	0.16	-0.16 (spur) -0.14 (helical)
Profile modification – Depth (µm)	20 (spur) 13 (helical)	
Profile modification – Length	20% of active profile	

Table III-4 : Single-stage experimental setup – Shaft data

	Pinion shaft	Gear shaft
Outer diameter (mm)	70	90
Inner diameter (mm)	30	30
Total length (mm)	1280	1415

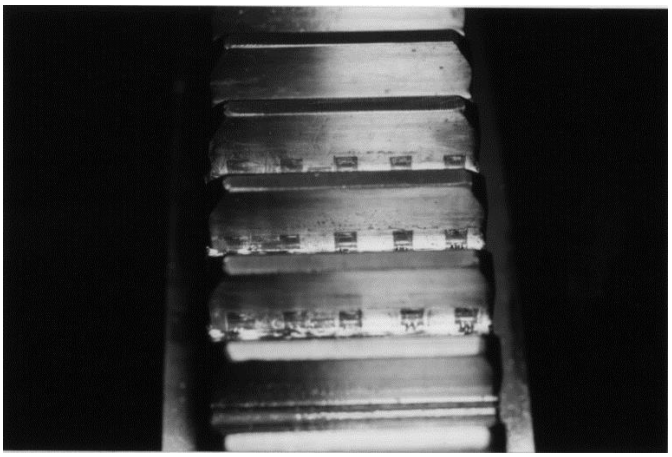

Figure III-11 : Strain gauges position, from Baud and Velex [74]

Thrust bearings are mounted on both shafts to compensate the axial forces generated by helical gears. The associated axial stiffness are given in Table III-5. The dimensions of the hydrodynamic bearings are listed in Table III-6 and the characteristics of the elastic coupling mounted on the pinion shaft can be found in Table III-7.

Table III-5 : Single-stage experimental setup – Stiffness of thrust bearings

	Pinion shaft	Gear shaft
Axial stiffness (N/m)	4.10^7	6.10^7

Table III-6 : Single-stage experimental setup – Dimensions of the hydrodynamic bearings

	Pinion shaft	Gear shaft
Diameter (mm)	70	90
Length (mm)	50	65
Radial clearance (μm)	150	110

Table III-7 : Single-stage experimental setup – Elastic coupling characteristics

Mass	9.6 kg
Polar moment of inertia	0.025 kg.m²
Torsional stiffness	$3.64\ 10^5$ N.m/rad
Bending stiffness	$1.37\ 10^4$ N.m/rad
Radial stiffness	$3.64\ 10^8$ N/m
Axial stiffness	10^8 N/m

2.2 Static behaviour

Preliminary static analyses have been performed in order to verify that the data from LDP were consistent with the strain gauge measurements at low speeds. The experimental fillet strain amplitudes have been normalized with respect to their maximum amplitudes and compared with the dimensionless tooth bending moment calculated by simulation and defined as:

$$\bar{M}_b = \frac{F_t \times L_b}{M_{bs}^{max}} \qquad (III\text{-}1)$$

where F_t is the force acting on the tooth, L_b is the tooth force lever arm taken as the difference between the base radius and the radius at the point of contact, $M_{bs}^{max}$is the maximum bending moment in quasi-static conditions.

Figure III-12 shows that the normalized bending moment $\bar{M}_b$ can be considered as representative of normalized fillet stresses. However, slight differences can be observed when the tooth is unloaded since the bending moment drops to zero whereas actual fillet stress does not because of gear blank deflections.

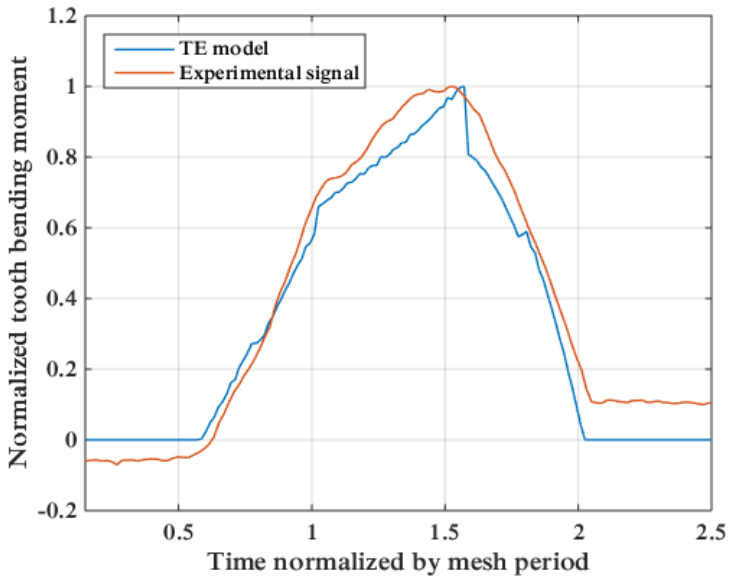

Figure III-12 : Single stage spur gear test rig – Comparison between experimental and simulated fillet stress

2.3 Dynamic behaviour – Spur gears

In what follows, the experimental measurements were obtained for the spur gear set and hydrodynamic bearings. The input speed was varied from 50 to 6 000 rpm on the pinion shaft and the torque was set to 1 540 Nm on the gear shaft. Measurements and simulations were performed for two different bearing positions: (a) a minimum bearing spacing of 320 mm and, (b) a maximum bearing spacing of 640 mm. In both cases, the pinion and the gear were centered with respect to the bearings. The stiffness and damping coefficients of the hydrodynamic bearings have been estimated using the theory of finite-length journal bearings detailed in [137] and the dimensions are given Table III-6.

The finite element model of the entire gear system (with maximum bearing spacing) is presented in Figure III-13. It should be noted that tooth modifications are accounted for in the dynamic simulations, whereas the influence of pitch errors is neglected.

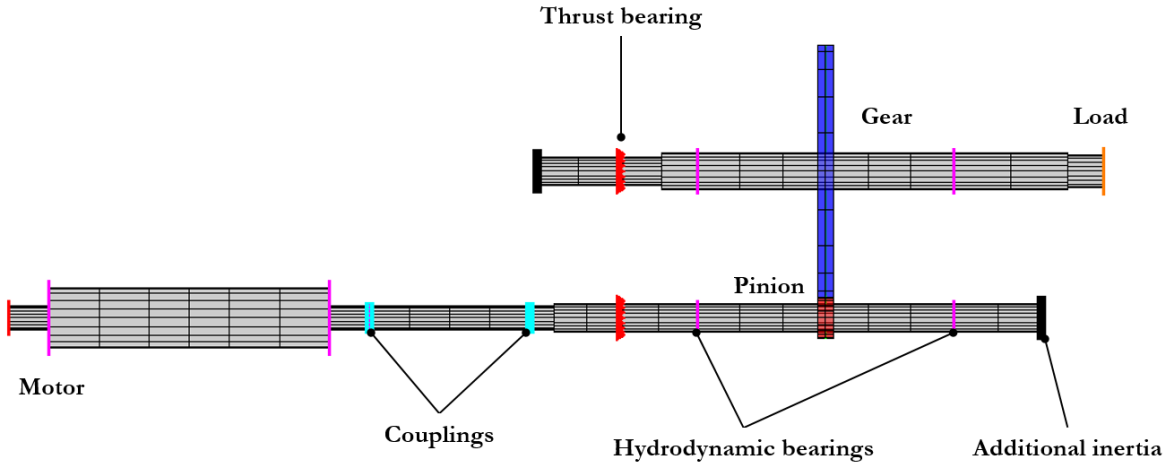

Figure III-13 : Finite element model of the single stage test rig

The damping matrix $[\boldsymbol{C}]$ is characterized using a modal approach with damping factors ς_p depending on the mesh contribution to the overall modal strain energy (cf. **Section 2.6** of **Chapter II**).

The normalized dynamic bending moment $\bar{M}_b$ (III-1) is calculated for a number of speeds and its maximum amplitude is sought over the second pinion revolution to make sure that numerical transients are all eliminated. This maximum value of the normalized bending moment is thereafter referred to as the bending moment dynamic factor. The dynamic response curves are then derived by plotting the evolutions of this maximum value versus the pinion rotational speed from which tooth critical speeds are identified as the speeds where tooth bending moments are amplified.

Figure III-14 and Figure III-15 respectively show the simulation results for (a) the minimum and (b) maximum bearing spacing together with the envelopes of experimental measurements (i.e. the maximum and minimum of the maximum normalized fillet stresses measured on several pinion revolutions). The two sets of results are in close agreement, both in terms of tooth critical speed positions and peak amplitudes. The discrepancy in terms of peak positions in Figure III-14 and Figure III-15 are caused by the softening effect induced by instant contact losses and shocks between the teeth as observed by Baud and Velex [74]. The proposed transmission error-based formulation being essentially linear, it cannot account for this particular phenomenon, as discussed in **paragraph 1.1** of this chapter. The two sets of results show the significant influence of shaft bending on the dynamic behaviour of gear transmissions and confirm that the model can accurately capture these phenomena.

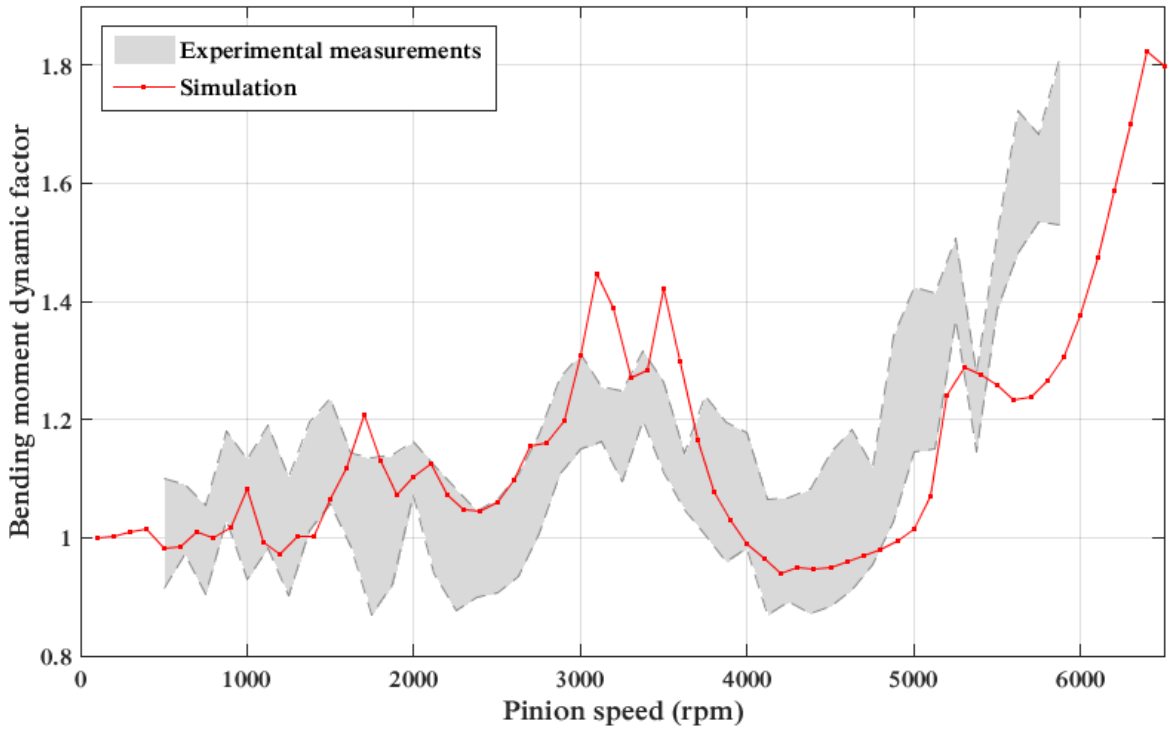

Figure III-14 : Spur gear test rig – Comparison of experimental and simulated dynamic response – Case (a)

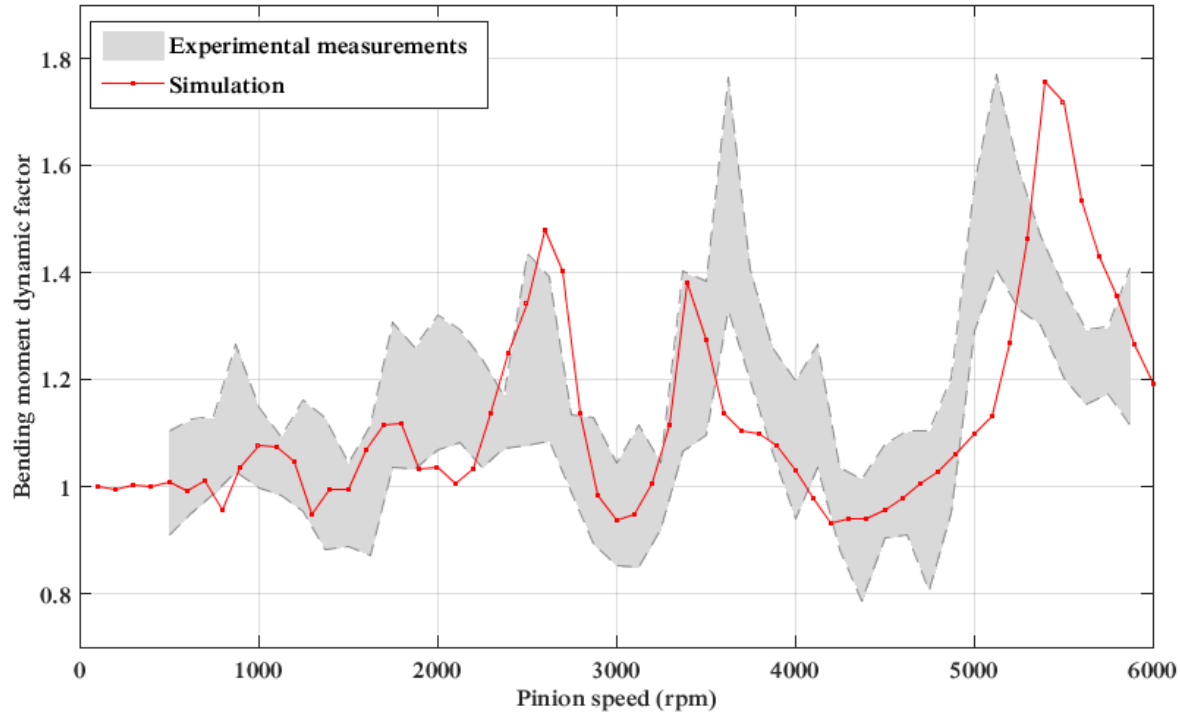

Figure III-15 : Spur gear test rig – Comparison of experimental and simulated dynamic response – Case (b)

2.4 Dynamic behaviour – Helical gears

Similar tests were conducted using the helical gear pair and the maximum bearing spacing configuration. In contrast with the spur gear results, the fillet stress distribution is not uniform across the face width and different dynamic responses are obtained for each strain gauge.

In Figure III-16, the maximum normalized bending moment is plotted against the pinion speed (red curve) and compared with the average of the four strain gauges signals for one tooth (grey envelope). Compared with spur gears, dynamic amplifications are far smaller whereas the absolute scatter over the speed range is comparable thus leading to larger relative dispersions around the average root stress amplitudes. It is believed that most of this phenomenon can be attributed to the influence of pitch errors combined with relatively light nominal loading.

However, it can be observed, here again, that the correlation between the experimental and simulated fillet stresses is satisfactory and that the positions of the tooth critical speeds are accurately predicted by the dynamic model. It can therefore be accepted that the proposed dynamic model captures most of the dynamic tooth loading characteristics for this test rig with either spur or helical gears.

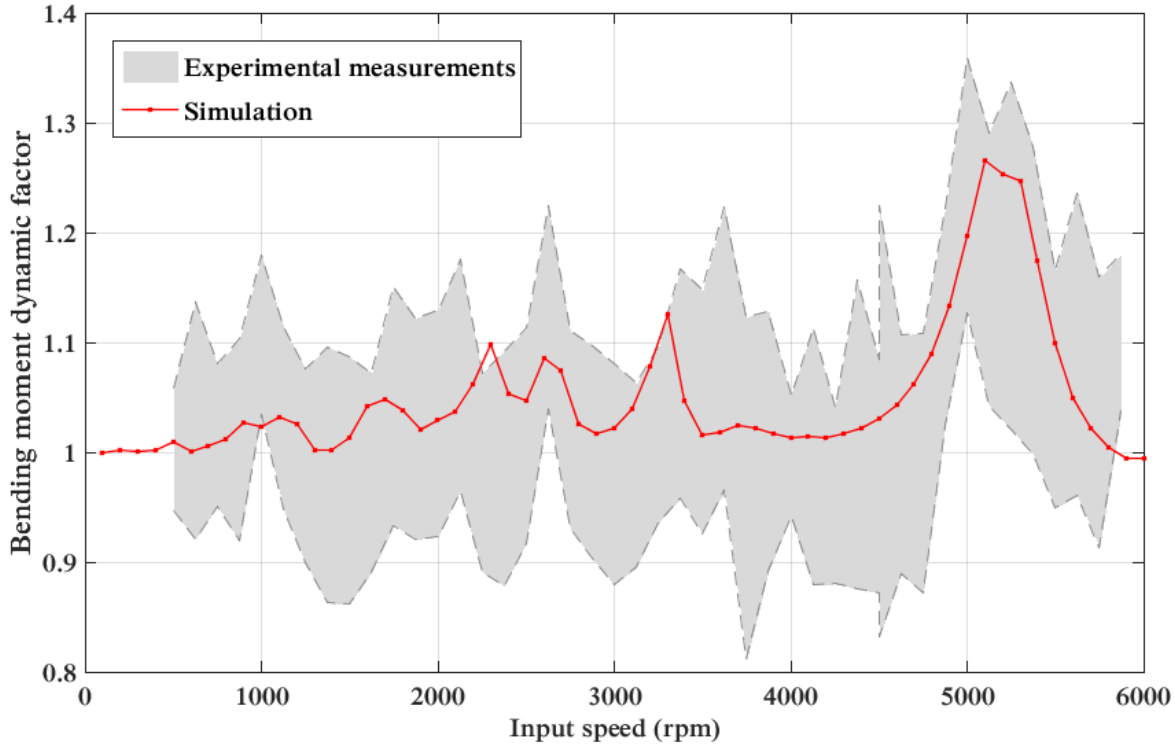

Figure III-16 : Helical gear test rig – Comparison of experimental and simulated dynamic response

3 SINGLE-STAGE SPIRAL-BEVEL GEAR SYSTEM – NUMERICAL VALIDATION

To the author's knowledge, the experimental measurements performed on bevel gears available in the literature are limited to quasi-static analyses [50,138,139] and no studies have been realised in dynamic conditions. For this reason, a numerical model developed by Wang *et al.* [101,102] is used here for validation purposes. This dynamic model is based on a local description of the instantaneous contact conditions through a discretization of the potential contact area between the pinion and the gear into elemental cells to which mesh stiffness elements (Wrinckler's elastic foundations) are attributed. This model allows the estimation of the dynamic pressure distribution between the gears in mesh and has been validated using quasi-static results from the literature.

3.1 System under study

The gears used for the validation of the dynamic model were initially studied by Simon [88,140,141]. The local dynamic model proposed by Wang managed to reproduce a similar tooth pressure distribution in quasi-static conditions [102] and was then used to study the evolution of the mesh force dynamic factor with the input speed of the system.

The main geometrical data of the spiral bevel gear pair is given in Table III-8. Further details can be found in the literature [88,140,141]. Short and stiff shaft elements are defined to eliminate the influence of shaft bending. Two identical bearings are located at the extremities of each of the pinion and gear shafts, the associated stiffness are listed in Table III-9. In accordance with Wang's model, a Rayleigh damping matrix is introduced, following the definition given in **Section 2.6** of **Chapter II**. It is proportional to the mass matrix, with a coefficient $a = 1500$.

Table III-8 : Spiral-bevel gear system – Gear data

	Pinion	**Gear**
Tooth number	13	50
Module (mm)	5	
Mean spiral angle (deg)	35	
Pressure angle (deg)	20	
Outside diameter (mm)	76.746	251.224
Face width (mm)	30	
Addendum (mm)	6.068	2.432
Dedendum (mm)	3.432	7.068
Pitch angle (deg)	14.5742	75.4258
Backlash (mm)	0.1	

Table III-9 : Spiral-bevel gear system – Bearing data

	Stiffness
Axial (N/m)	10^9
Radial (N/m)	10^9
Bending (N.m/rad)	10^4

3.2 Dynamic response

A constant input torque of 80 Nm is applied at the extremity of the pinion shaft and the rotational speed of the pinion shaft is varied between 250 and 13 250 rpm. The global mesh force is computed for each rotational speed, using the definition presented in **Section 3.5.c)** of **Chapter II**. The corresponding dynamic factor is plotted versus the input rotational speed (Figure III-17) and compared with Wang's results. A very good correlation is observed between the results from both models, in terms of critical speeds and peak amplitudes.

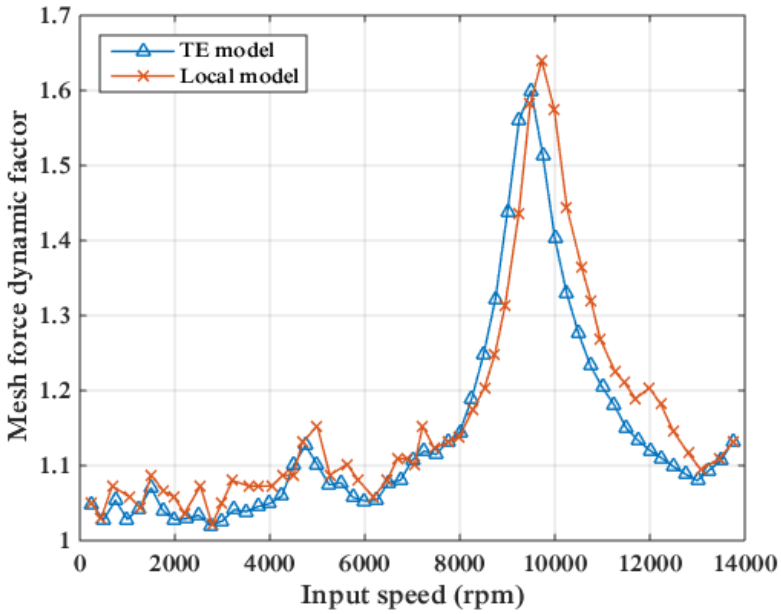

Figure III-17 : Spiral-bevel gear system – Comparison of the transmission error-based model with Wang's local model

The spectral content of the dynamic mesh force at each rotational speed is plotted in Figure III-18. The spectrum contains the fundamental and first harmonic of mesh frequency only. Besides, Figure III-18 shows that the major critical speed corresponds to a coincidence between the fundamental of the spiral-bevel gear mesh frequency and the most critical natural frequency of the system, for which 67% of the modal strain energy is stored in the mesh.

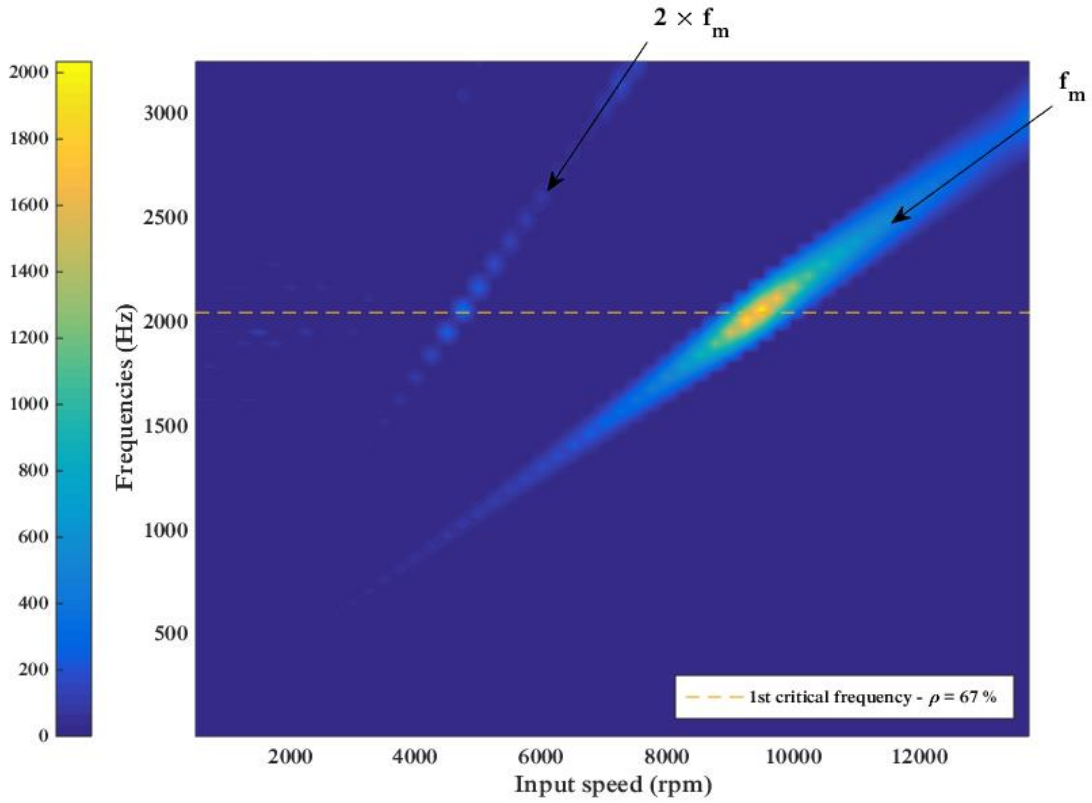

Figure III-18 : Spiral-bevel gear system – Spectral content of the global dynamic mesh force (amplitude in N) – Static mesh force 3 574 N

4 DOUBLE-STAGE SPUR GEAR SYSTEMS – NUMERICAL VALIDATION

Raclot has realised an extensive study of double-stage spur gear systems, with different gears and various profile modifications [114]. The model used is based on a simultaneous resolution of the contact conditions on the teeth and the equations of motion.

Two different gear arrangements are studied:

- a two-mesh system with four gears and an intermediate shaft between the two stages,
- a two-mesh system with three gears comprising an idler gear.

Different profile modifications are introduced and their influence on the dynamic behaviour of the system is investigated. The influence of the relative phasing between successive meshes on the dynamics of the idler gear system will be discussed in **Chapter IV**.

4.1 System with intermediate shaft

4.1.a) *Description of the system*

The first example of application is the dual-mesh spur gear system proposed by Raclot and shown in Figure III-19. The gear data are given in Table III-10. A coarse discretization of the shafts was defined by Raclot and is precisely reproduced here for the sake of comparing the two modelling approaches. The model comprises 13 nodes with 6 degrees-of-freedom per node.

The three shaft axes lie in the same plane and their dimensions are given in Table III-11 using the element labelling in Figure III-19. The material characteristics are those of steel (density 7 800 kg/m^3, Young Modulus 210 GPa). Each shaft is supported by two bearings located at its extremities. All bearings are identical (characteristics in Table III-12) and it should be noted that the gears are not centred between the bearings. The system includes no external inertia.

In this configuration, the relative phase shift between both mesh excitations is independent of the shaft position and varies with time since the mesh periods are different.

Table III-10 : Dual-mesh spur gear system with intermediate shaft – Gear data

	Pinion 1	Gear 1	Pinion 2	Gear 2
Number of teeth	27	63	25	69
Face width (mm)	72		100	
Module (mm)	4		6	
Helix angle (deg)	0			
Pressure angle (deg)	20		20	
Addendum coefficient	1.0		1.0	
Dedendum coefficient	1.4		1.4	
Shift profile coefficient	0.0		0.0	

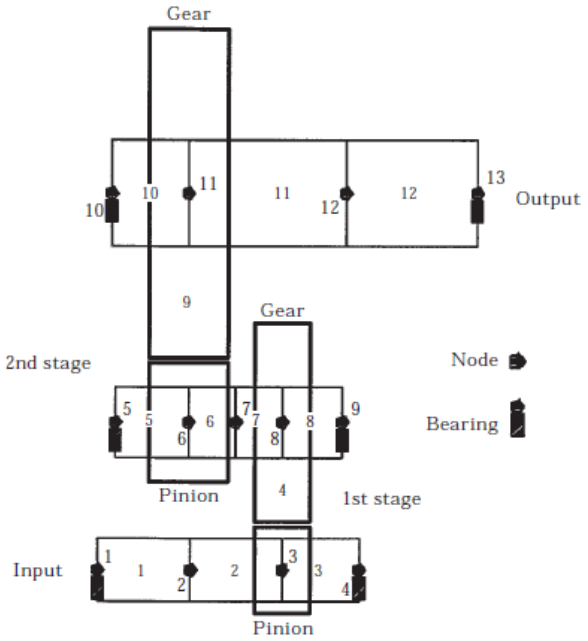

Figure III-19 : Dual-mesh spur gear system with intermediate shaft – Model of the system

Table III-11 : Dual-mesh spur gear system with intermediate shaft – Shaft data

Shaft	Shaft element	Length (mm)	External diameter (mm)
Input shaft	1	116.775	80
	2	116.775	80
	3	98.43	80
Intermediate shaft	5	92.43	90
	6	59.69	90
	7	59.69	90
	8	76.69	90
Output shaft	10	96.77	133.35
	11	183.35	133.35
	12	183.35	133.35

Table III-12 : Dual-mesh spur gear system with intermediate shaft – Bearing data

	Stiffness
Axial (N/m)	4×10^8
Radial (N/m)	4×10^8
Bending (N.m/rad)	10^{10}

4.1.b) *Dynamic analysis*

A constant 1 500 Nm input torque is applied whereas the input speed is varied between 100 and 30 000 rpm. The damping matrix is derived from the mode-shapes of the undamped system employing a unique modal damping factor of 0.1. For each rotational speed, the local dynamic transmission error associated with each mesh is calculated from the global solution vector $\boldsymbol{X}$ following definition (II-88) along with the associated shape factor (RMS of the time-varying part of the signal).

The results obtained for the unmodified gears are shown in Figure III-20 for both gear stages and it can be observed that the results of the transmission error-based formulation agree well with Raclot's findings.

Figure III-21 and Figure III-22 show that the spectral content of the dynamic transmission error at each gear stage is dominated by the associated mesh frequency (fundamental + first harmonics). Critical speeds are observed in the evolution of the transmission error shape factor when the mesh frequency (or one of its harmonics) of a gear pair matches one of the first critical frequencies (for which an important percentage of the modal strain energy is stored in the mesh).

Besides, some coupling between the two meshes can be observed in Figure III-21. The spectrum of the dynamic transmission error of stage 1 contains low amplitudes at the mesh frequency of the second gear stage. Stage 2 therefore has an influence on the dynamic behaviour of stage 1 but stage 1 does not seem to influence stage 2 (Figure III-22). The introduction of a stiffer intermediate shaft would probably amplify this coupling and generate an additional critical speed on stage 1 (around 20 000 rpm).

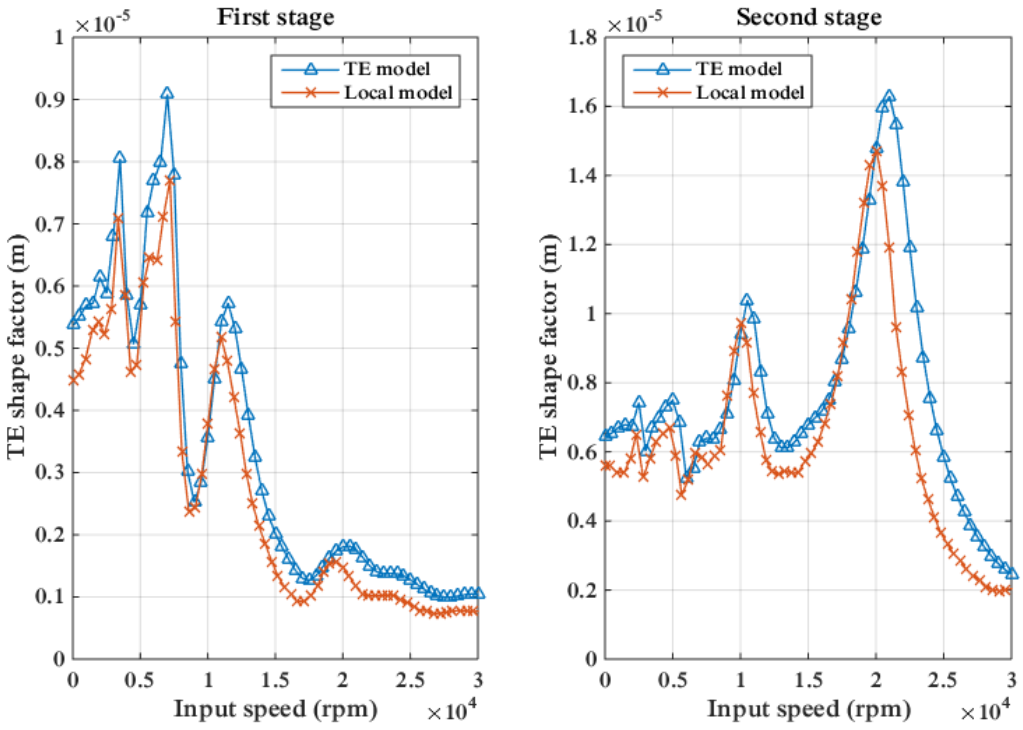

Figure III-20 : Dual-mesh spur gear system with intermediate shaft – Dynamic response of the system with unmodified gears

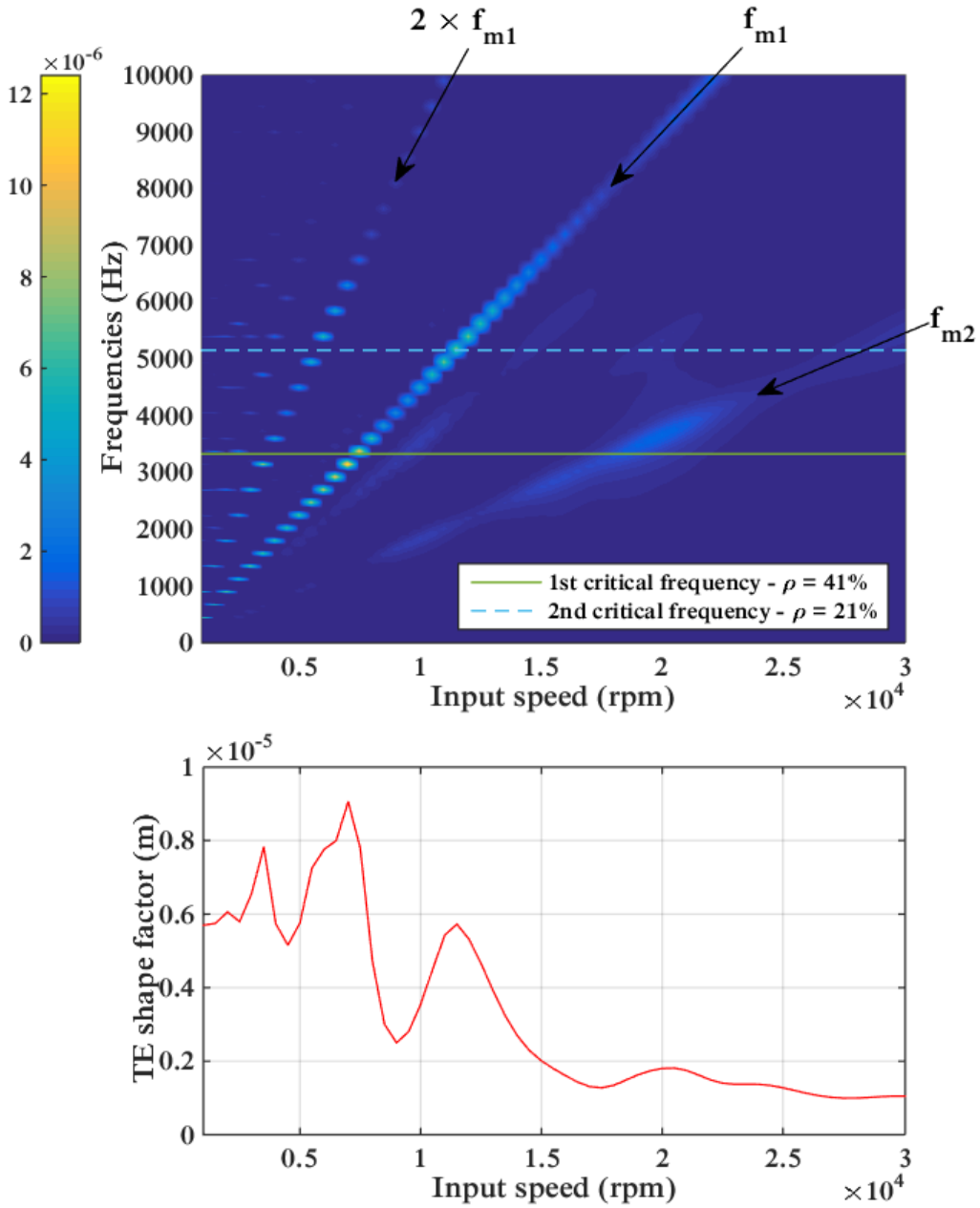

Figure III-21 : Dual-mesh spur gear system with intermediate shaft – Stage 1 –Spectral content of the dynamic transmission error (Amplitude in m)

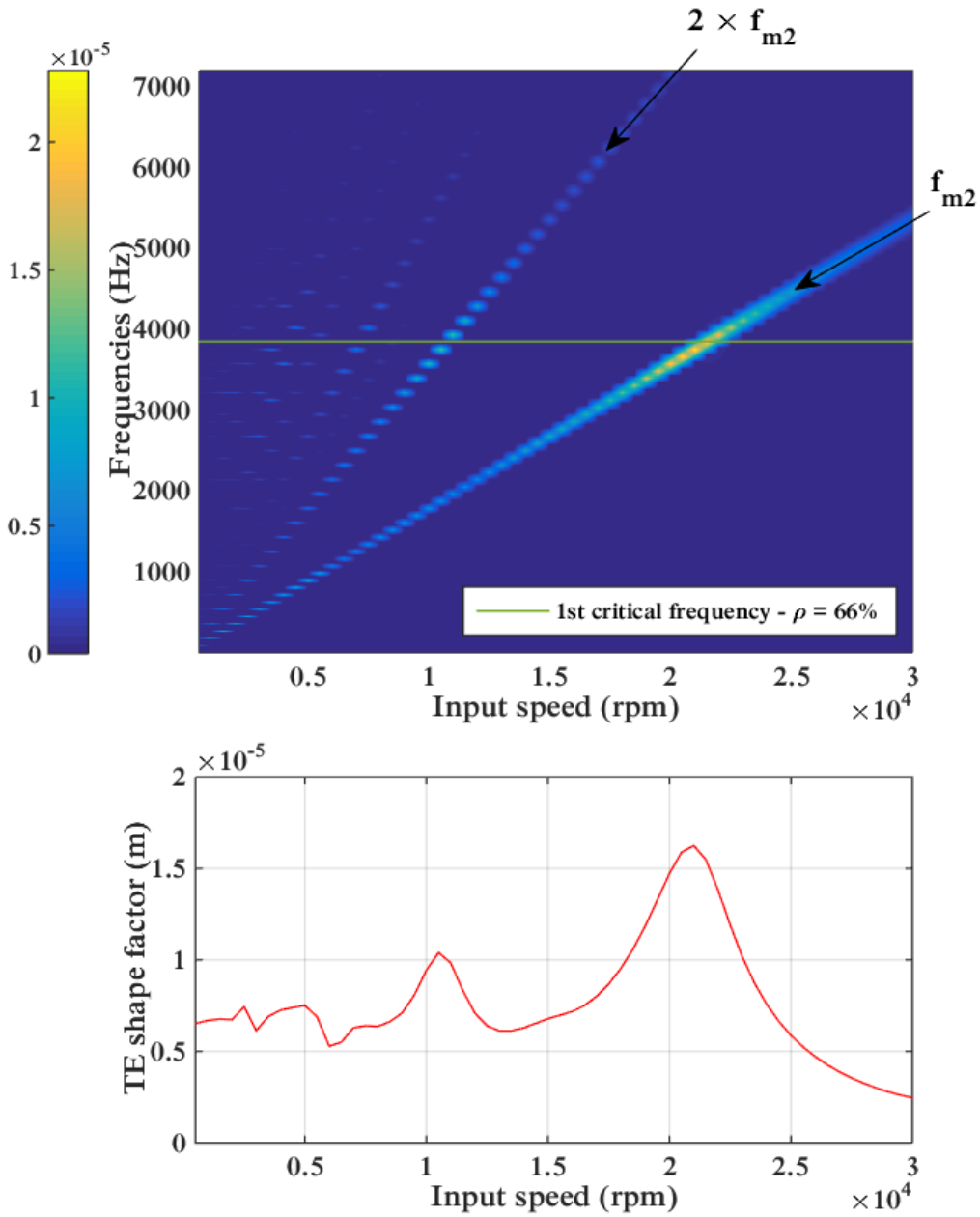

Figure III-22 : Dual-mesh spur gear system with intermediate shaft – Stage 2 – Spectral content of the dynamic transmission error (Amplitude in m)

4.1.c) *Introduction of profile modifications*

In what follows, profile modifications are introduced and the dynamic response of the system is compared with that for unmodified tooth profiles presented in the previous section. Linear symmetric tip reliefs with two different extents of modification are considered.

Table III-13 : Dual-mesh spur gear system – Definition of linear symmetric tip relief

		Stage 1	Stage 2
Short relief	**Depth of modification**	30 µm	30 µm
	Length of modification	20% of active profile	20% of active profile
Long relief	**Depth of modification**	30 µm	30 µm
	Length of modification	40% of active profile	40% of active profile

First, the gears of both stages are simultaneously modified in the same way, following the definition given in Table III-13. As visible in Figure III-23 and Figure III-24, the results obtained from the transmission error-based model are in very close agreement with Raclot's findings.

Besides, the results show that profile modifications have a significant influence on the dynamic response of the system. In particular, the long reliefs allow to reduce efficiently the dynamic amplifications over the complete speed range. These modifications were defined by Raclot as optimal as they lead to almost constant quasi-static transmission errors (using a model where the mesh stiffness per unit contact length is constant). The stiffness formulation used in the proposed model is different and therefore, the long modifications do not lead to perfectly constant quasi-static transmission errors and are therefore not as effective in reducing the dynamic amplifications close to the critical speeds.

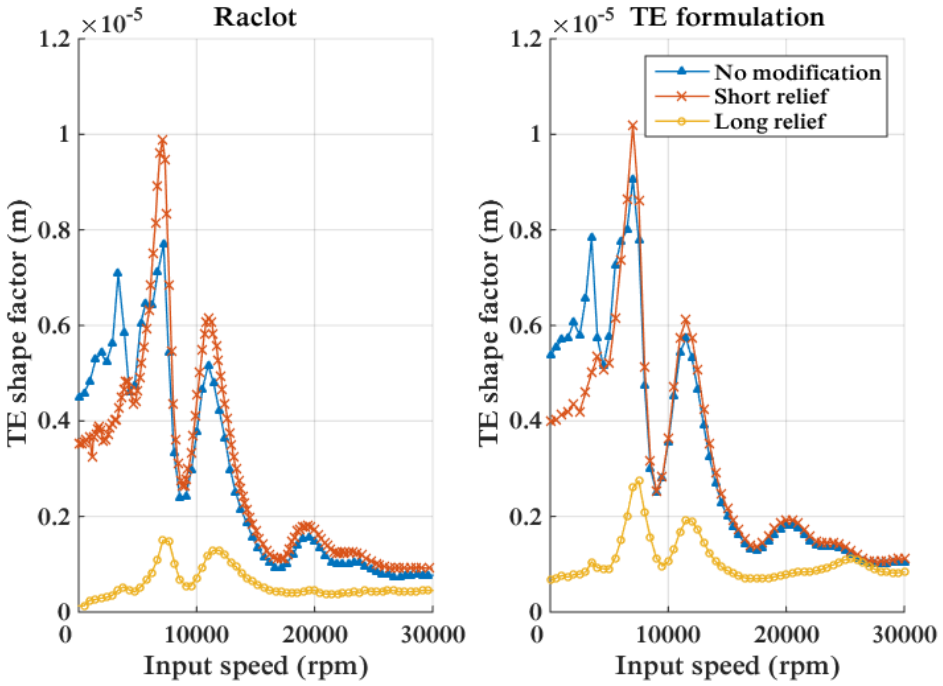

Figure III-23 : Dual-mesh spur gear system with intermediate shaft – Stage 1 – Influence of profile modifications on the dynamic response

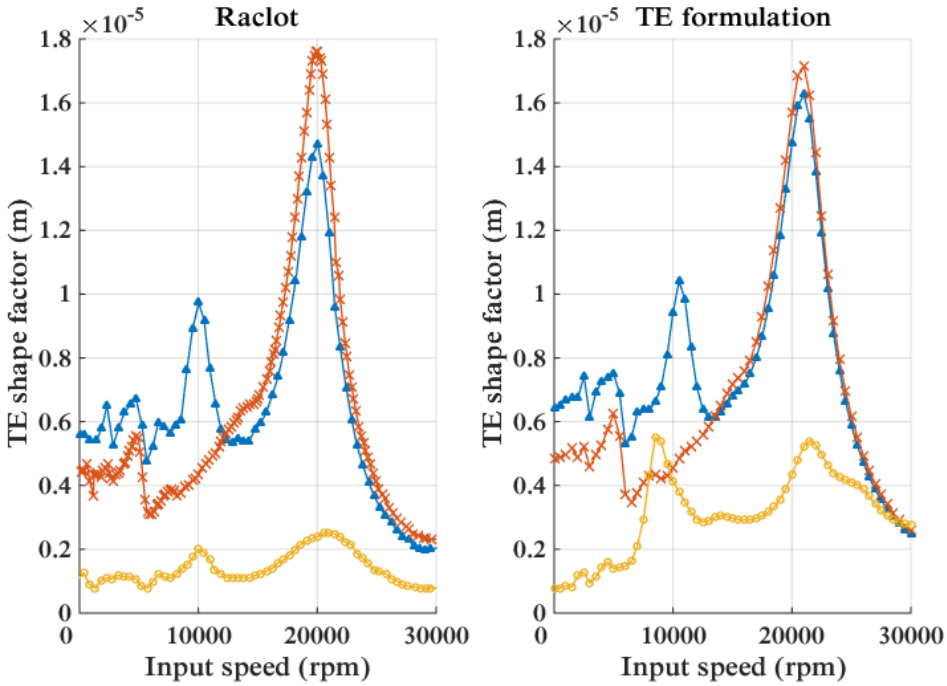

Figure III-24 : Dual-mesh spur gear system with intermediate shaft – Stage 2 – Influence of profile modifications on the dynamic response

The analysis of the spectral content of the dynamic transmission error of stage 2 in the presence of long reliefs on both gear pairs shows that the first stage influences the dynamic response of the second one (Figure III-25). The presence of long reliefs introduces non-zero no-load transmission errors functions which generate additional excitations via the rigid-body angular accelerations of the driven shafts.

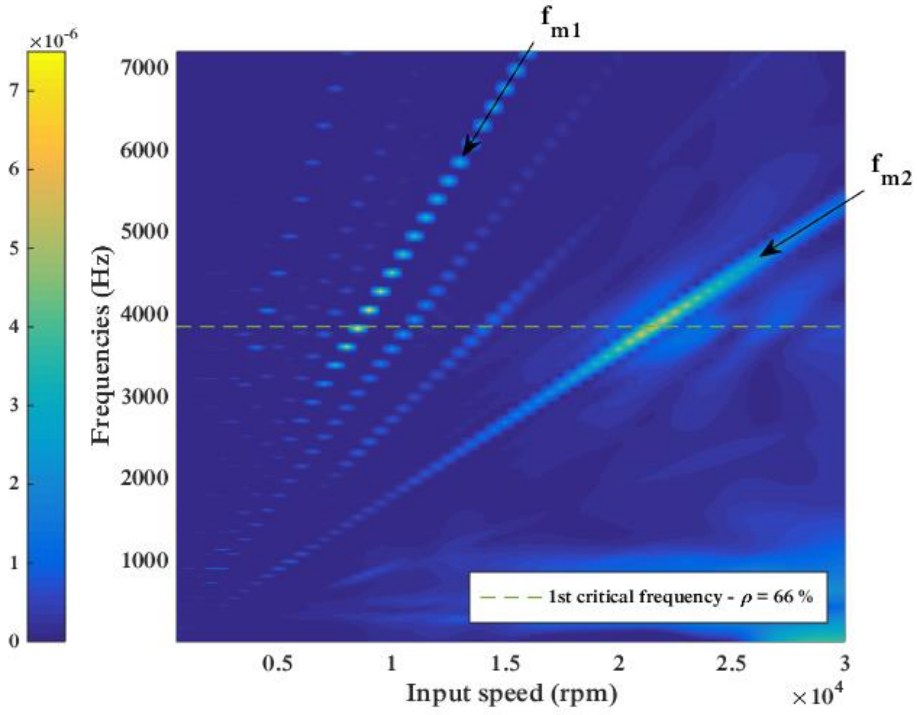

Figure III-25 : Dual-mesh spur gear system with intermediate shaft – Stage 2 – Spectral content of the dynamic transmission error in the presence of long reliefs on both gear pairs (Amplitude in m)

The interactions between the two gear stages are further investigated by introducing the long "optimal" profile modifications separately on each stage. Figure III-26 and Figure III-27 show that the dynamic response of each stage has an influence on the other one. It was observed earlier that, in the absence of tooth modifications, stage 2 has a slight influence on stage 1 (Figure III-21). Logically, the reduction of the vibration level on stage 2 is also beneficial for stage 1. The dynamic response of stage 1 is therefore lower when both stages are modified by long reliefs than when only stage 1 is modified (Figure III-26). The opposite phenomenon is observed on stage 2. Without modifications, stage 1 has no influence on stage 2 but as soon as long reliefs are introduced on stage 1, an additional excitation appears and the dynamic response of stage 2 deteriorates (Figure III-27).

These results evidence that reciprocal interactions take place between the successive gear stages of a system when both gear pairs are modified. However, in comparison with the unmodified configuration, it seems that the introduction of profile modifications on at least one of the meshes always leads to a reduction of the gear vibratory level for a system with intermediate shaft (except for some points in Figure III-27 but the difference in the vibratory level is very low). Finally, when only one gear pair is modified, the response on the other stage remains practically unchanged.

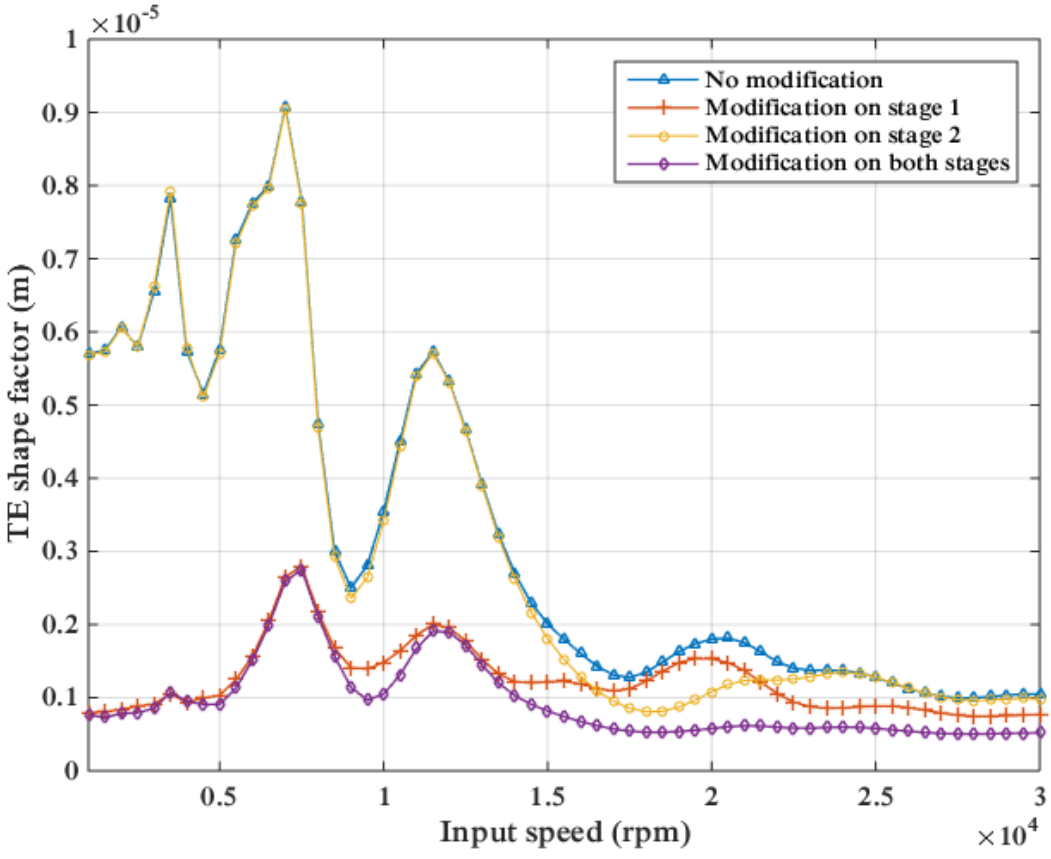

Figure III-26 : Dual-mesh spur gear system with intermediate shaft – Stage 1 – Analysis of the interactions between successive stages

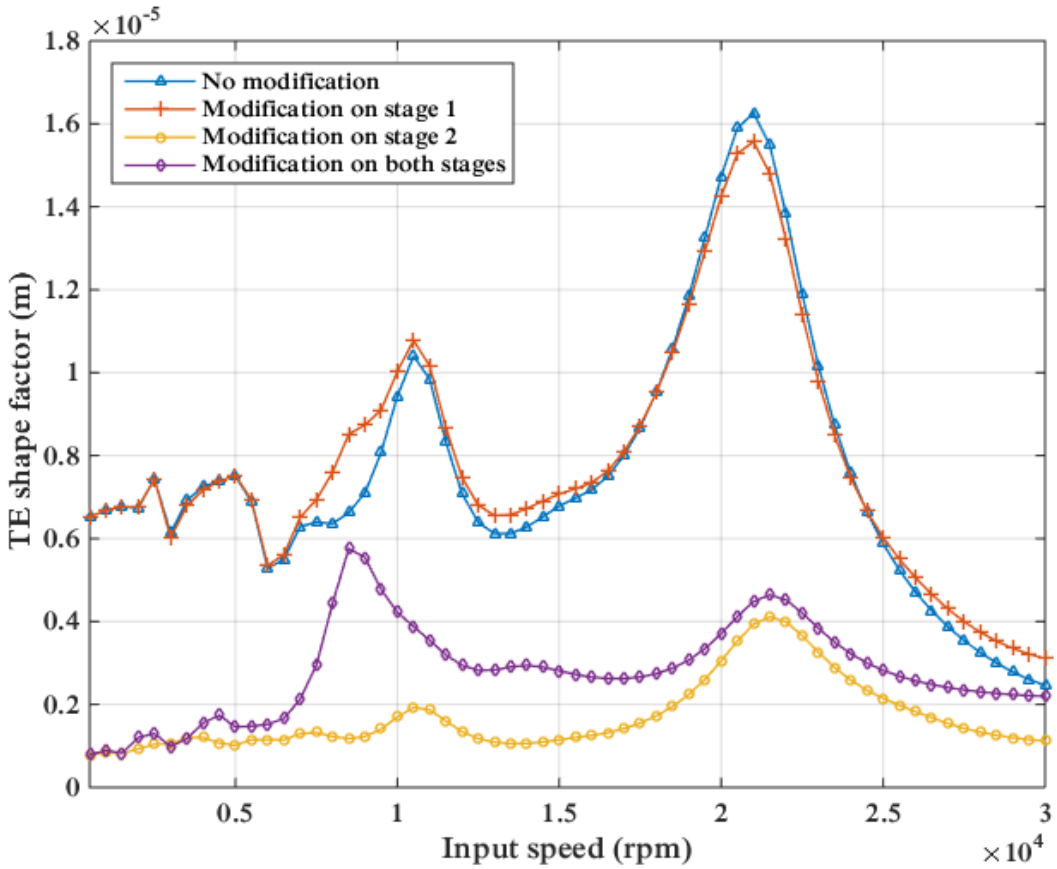

Figure III-27 : Dual-mesh spur gear system with intermediate shaft – Stage 2 – Analysis of the interactions between successive stages

4.2 System with idler gear

4.2.a) *Description of the system*

A different double-stage system is studied in this section which is composed of three pinions with an intermediate idler gear. The gear data are listed in Table III-14. The finite element model of the system is shown in Figure III-28 which comprises 9 nodes with 6 degrees-of-freedom per node for a total of 54 degrees-of-freedom.

The axes of the three shafts lie in the same plane. Each shaft is supported by two bearings located at its extremities and their dimensions are given in Table III-15 using the element labelling in Figure III-28. Shafts are made of steel (density 7 800 kg/m^3, Young Modulus 210 GPa. All bearings are identical (characteristics in Table III-16) and it should be noted that the gears are not centred between the bearings. Lumped inertia elements are added at the extremities of the input and output shaft to represent the motor and the load. For each of them, the value of the polar moment of inertia is 6 kg.m^2.

Table III-14 : Double-stage spur gear system with idler gear – Gear data

	Pinion 1	Pinion 2	Pinion 3
Number of teeth	23	39	67
Face width (mm)	60		
Module (mm)	6		
Helix angle (deg)	0		
Pressure angle (deg)	20		
Addendum coefficient	1.0		
Dedendum coefficient	1.4		
Shift profile coefficient	0.0		

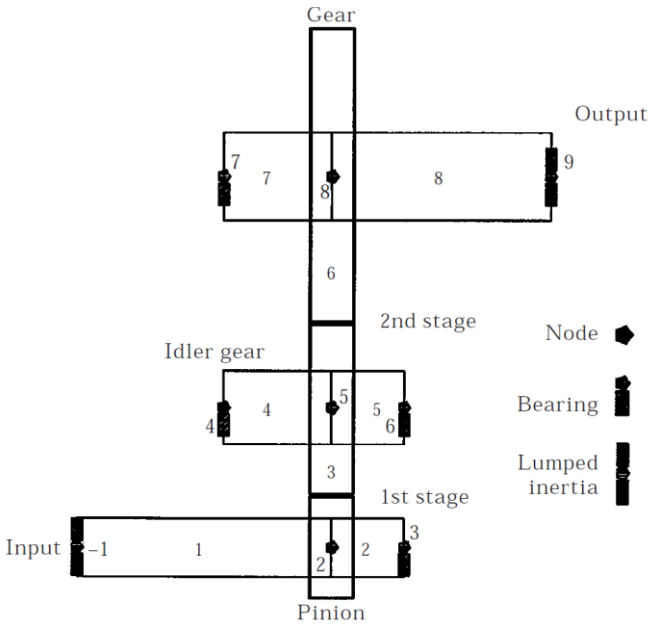

Figure III-28 : Double-stage spur gear system with idler gear – Model of the system

Table III-15 : Double-stage spur gear system with idler gear – Shaft data

Shaft	Shaft element	Length (mm)	External diameter (mm)
Input shaft	1	350	80
	2	100	80
Intermediate shaft	4	150	100
	5	100	100
Output shaft	7	150	120
	8	300	120

Table III-16 : Double-stage spur gear system with idler gear – Bearing data

	Stiffness
Axial (N/m)	4×10^8
Radial (N/m)	4×10^8
Bending (N.m/rad)	0

Prior to the global dynamic analysis, the quasi-static excitation functions are defined for each stage separately. Unlike the configuration with an intermediate shaft, the relative position of the shafts imposes the phase shift between the meshes and the mesh frequency is the same for both stages. The relative phase shift is calculated using the method detailed in **Section 3.2** of **Chapter II**. For this particular architecture (three shafts in the same plane), the phase shift happens to be almost nil. The corresponding excitation functions for the two gear meshes are shown in Figure III-29 and Figure III-30.

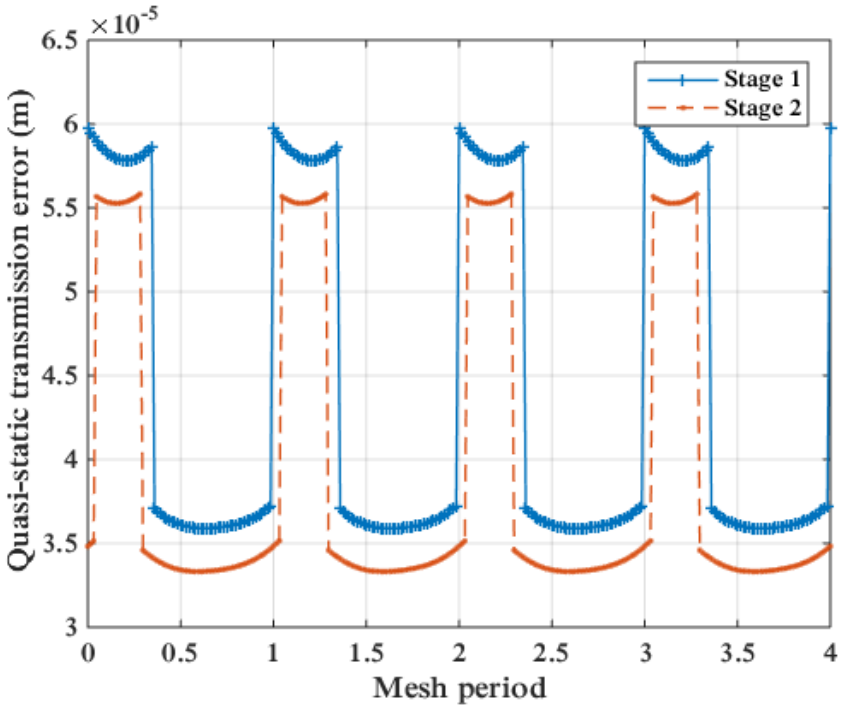

Figure III-29 : Double-stage spur gear system with idler gear – Quasi-static transmission error functions

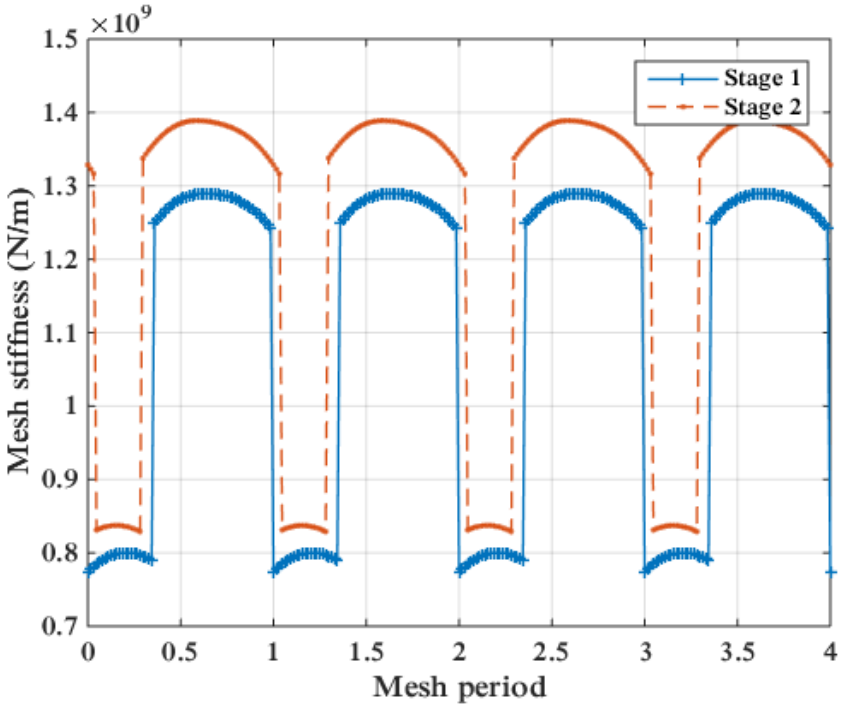

Figure III-30 : Double-stage spur gear system with idler gear – Mesh stiffness functions

4.2.b) *Dynamic analysis*

A constant input torque of 3 000 N.m is applied at the extremity of the input shaft and the input speed is varied from 100 to 14 500 rpm. The damping matrix is derived from the mode-shapes of the undamped system using a unique modal damping factor of 0.1. For each rotational speed, the local dynamic transmission error associated with each mesh is calculated from the global solution vector $\boldsymbol{X}$ following definition (II-88) along with the associated shape factor (RMS of the time-varying part of the signal).

The results obtained for the unmodified gears are shown in Figure III-31 and Figure III-32. The simulation performed from the transmission error-based formulation is in very close agreement with Raclot's findings.

Figure III-31 and Figure III-32 show that the spectral content of the dynamic transmission error at each gear stage is dominated by the mesh frequency of the system (fundamental + first harmonics). Critical speeds are observed in the transmission error shape factor curve when the mesh frequency (or one of its harmonics) of a gear pair coincides with one of the tooth critical frequencies.

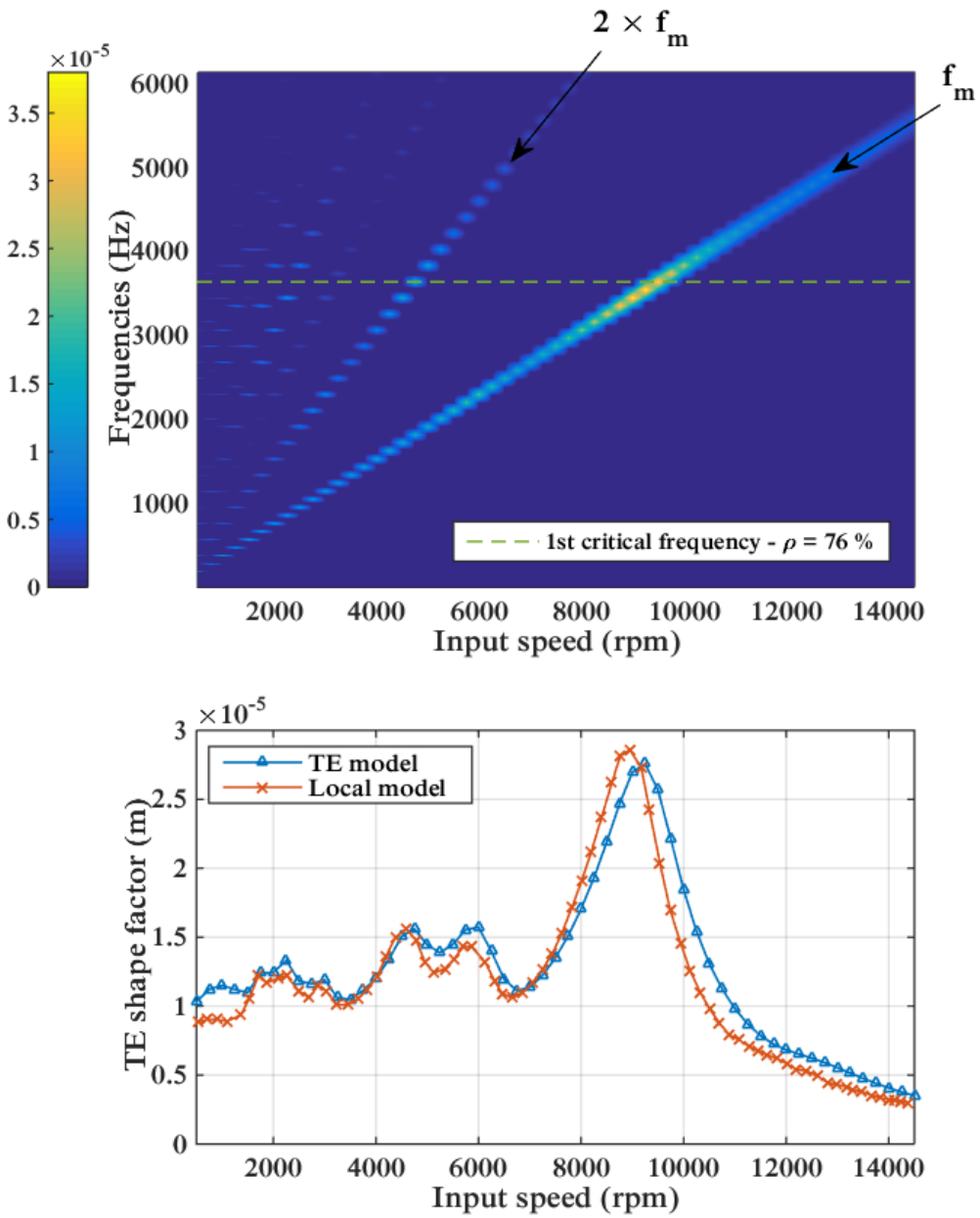

Figure III-31 : Double-stage spur gear system with idler gear – Stage 1 – Spectral content of the dynamic transmission error (Amplitude in m)

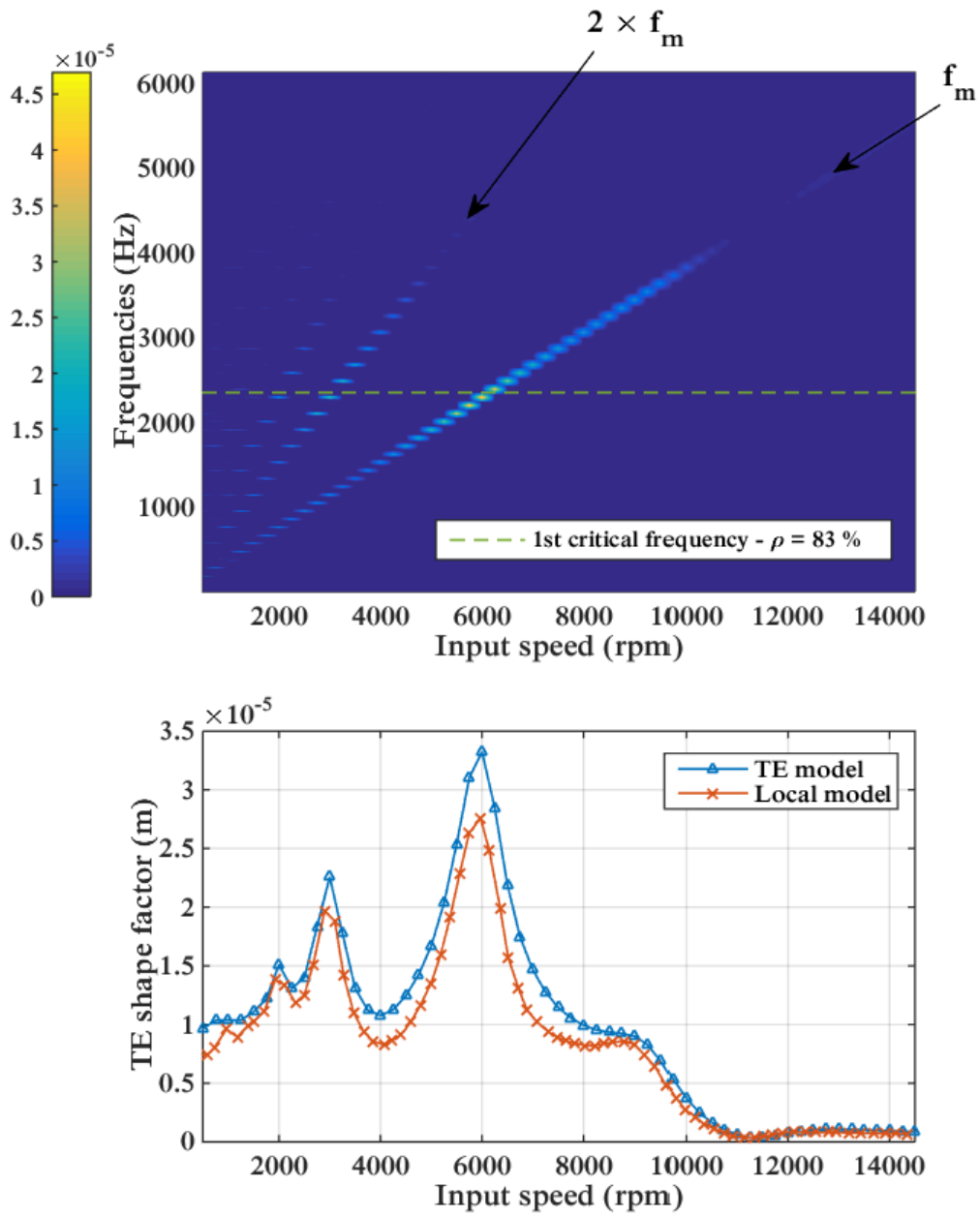

Figure III-32 : Double-stage spur gear system with idler gear – Stage 2 – Spectral content of the dynamic transmission error (Amplitude in m)

4.2.c) *Introduction of profile modifications*

In what follows, long profile modifications (amplitude 30 µm, extent 40% of the active profile) are introduced simultaneously on both gear meshes. This configuration implies that both flanks of the idler gear are modified. In a second step, the tooth profiles of each gear stage are modified alternatively. The transmission error shape factors resulting from the four configurations of profile modifications are shown in Figure III-33 and Figure III-34.

Several observations can be drawn from this analysis:

- Unlike the system with an intermediate shaft, the introduction of profile modifications on one stage is not always beneficial for the global system. It can be observed in Figure III-33 that the modification of the gear profile on stage 2 leads to an increase in the vibration level on stage 1.
- As observed on the dual-mesh system with intermediate shaft, profile modifications can be used to improve the dynamic behaviour of the system. In this case, the simultaneous introduction of profile modifications on both gear meshes causes a reduction of the vibration level for both gear stages.
- Whatever the configuration, the introduction of profile modifications does not alter the position of the major tooth critical speeds. This observation could have been anticipated since the dynamic response is mostly controlled by the mesh frequency which is unique in this system with idler gear.
- Finally, contrary to what was observed on the dual-mesh system with intermediate shaft, the introduction of profile modifications on only one of the meshes always influences the dynamic behaviour at the other gear stage, especially in the vicinity of the critical speeds.

This analysis allowed to highlight the interactions that take place between the meshes of a double-stage system with idler gear, which are more important than those observed for a dual-mesh system with intermediate shaft.

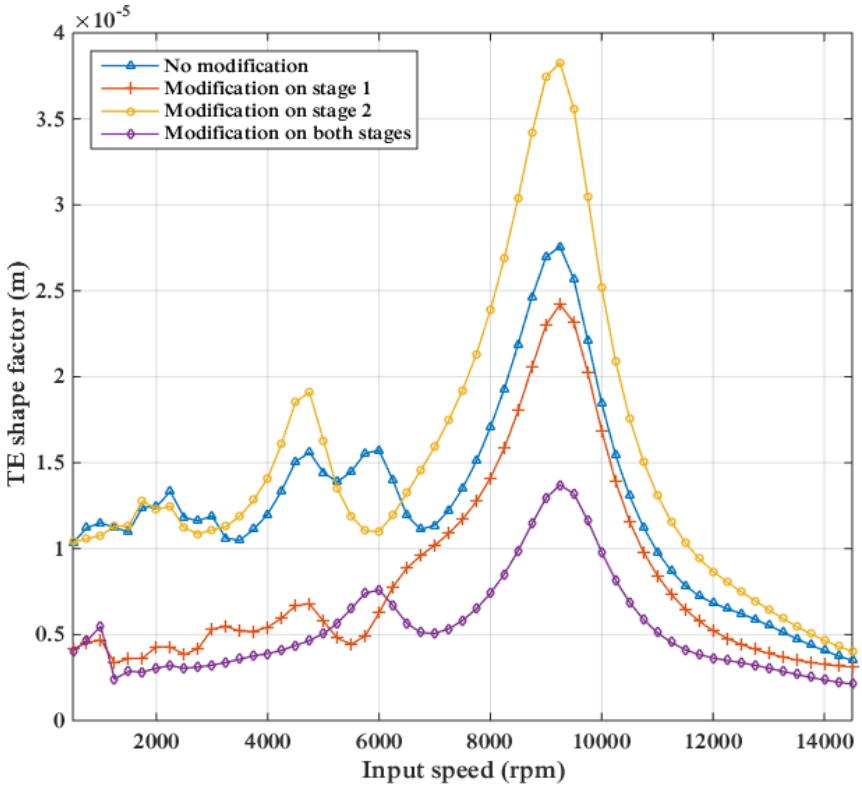

Figure III-33 : Double-stage spur gear system with idler gear – Stage 1 – Influence of profile modifications

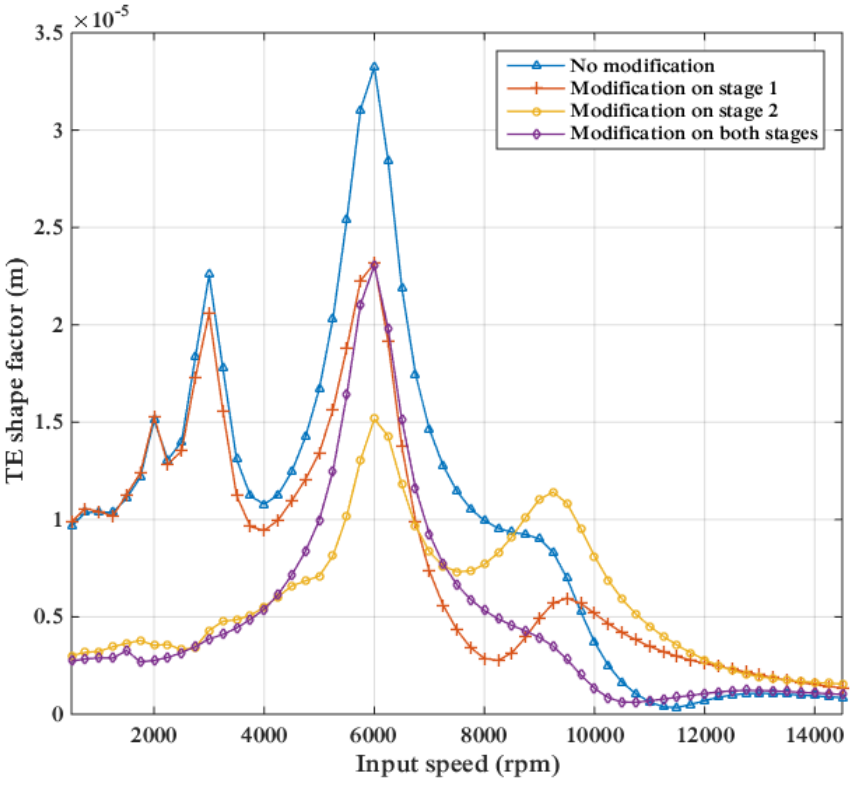

Figure III-34 : Double-stage spur gear system with idler gear – Stage 2 – Influence of profile modifications

5 Conclusion

Several numerical simulations have been performed in order to validate the results obtained on both single and multi-stage gear systems with the model presented in **Chapter II**. In this context, both parallel and intersecting shaft systems are studied and the simulation results are compared with experimental and numerical results from the literature. A good agreement is obtained for each case studied, proving that the proposed transmission error-based formulation is sound.

The first case study shows that the proposed model is well adapted to the simulation of the dynamic behaviour of single-stage spur gear systems with unmodified gears. By reducing the amount of damping, regimes with contact losses and impacts can be observed and it is confirmed that the intrinsically linear model based on transmission error cannot simulate this particular behaviour. However, it is believed that the proposed approach is adapted to heavily loaded gear systems such as helicopter transmissions.

Different configurations of profile modifications are then introduced in the model and results are correlated with the predictions derived from a more precise model accounting for the instant contact conditions on tooth flanks. It is demonstrated that the transmission error-based formulation can accurately simulate the contributions of tooth profile modifications which can be used to reduce dynamic amplifications.

Extensive comparisons with evidence from a spur and helical gear test rig are presented and it is confirmed that the model is able to simulate the dynamic behaviour of a complete reduction unit, including shaft bending and bearing effects.

The simulation of spiral-bevel gears dynamic behaviour is finally tackled. A local model from the literature is used for the validation of the transmission error-based formulation. Both models provide results in very close agreement regarding mesh force dynamic factors.

A number of dynamic analyses of a double-stage spur gear system are finally conducted and, here again, it is found that the proposed formulation is well adapted to multi-stage gears. Similar conclusions are drawn for a) a double-stage system with intermediate shaft and, b) a system with an idler gear.

Chapter IV
Application to single- and double-stage gear systems

The model presented in the previous chapters is applied to the study of the dynamic behaviour of single- and double-stage gear systems.

The first two sections are dedicated to the study of single-stage systems.

First, the pitch errors measured on the pinions and gears of the test rig presented in ***Chapter III*** *are introduced in the model. The combined influence of pitch errors and load on dynamic tooth loads is analysed.*

Two different models of this system are exploited in ***Section 2****: a) a full three-dimensional approach including the pinion, gear, shafts, bearings and couplings, and b) a simplified torsional model restricted to the pinion and gear only. The possibility to establish a linear dependency between dynamic transmission errors and dynamic tooth loads is discussed.*

The third section concerns the double-stage spur gear systems proposed by Raclot and presented in ***Chapter III****. For each gear arrangement, the dynamic response at the bearings is analysed and the influence of the relative mesh phasing on the dynamic response of the idler gear system is evaluated.*

Finally, the dynamic behaviour of multi-mesh systems comprising both cylindrical and spiral-bevel gears is tackled. The couplings between the various meshes are clearly illustrated by analysing the local dynamic transmission error spectra and, finally, the role of the shaft connecting the two meshes is highlighted.

1 SINGLE-STAGE GEAR SYSTEM – INFLUENCE OF PITCH ERRORS

Although most of the gears used for power transmission are manufactured with high precision, tooth shape errors can hardly be avoided thus altering the motion transfer between the gears. Amongst all the possible types of manufacturing errors, tooth pitch errors are very common and are known as potentially influential on mesh excitations.

Several authors studied the influence of pitch errors on tooth loads and root stresses [142] and showed that they significantly modify quasi-static transmission errors under load [143,144]. However, only a few studies directly dealt with the influence of manufacturing errors on gear dynamics [145–147]. Bihr *et al.* [146] compared nominal and topologically measured micro geometries of automotive counter gear drive train and found significant differences in noise excitations. The authors highlighted the influence of manufacturing errors on transmission error spectra and on the amplitude of dynamic tooth forces at critical speeds. Inalpolat *et al.* [147] performed dynamic simulations over a range of speeds for errorless gears and gears with deterministic or random spacing errors. The authors concluded that indexing errors lead to higher dynamic response amplitudes along with additional frequency components. They also stressed the role of the assembly configuration (such as clocking) when accounting for indexing errors.

However, the vast majority of the dynamic models do not consider pitch errors although their results compare generally well with experimental evidence. At first glance, this seems contradictory with the fact that pitch errors strongly modify transmission error signals and further studies are certainly needed in this area. Moreover, most of the results reported in the literature are limited to spur gears and extensions to helical gears are certainly useful.

The three-dimensional model of the spur / helical test rig presented in **Section 2** of **Chapter III** is used for the present study. Pitch errors were carefully measured on the tested gears [148] and the control charts are reproduced in **Appendix B**. These errors are introduced in the model of the test rig and their influence is examined on the quasi-static and dynamic behaviour of spur and helical gear systems. The combined influence of pitch errors and load is then investigated.

1.1 Quasi-static analysis

In theory, the calculation of quasi-static excitations should be performed over $Z_1 \times Z_2$ mesh periods to capture all the possible contact combinations between the pinion and gear teeth. However, the acquisition period was limited to two revolutions of the pinion to ensure a sufficient time discretization and because of computational limitations. It is believed that most of pitch error contributions to dynamic tooth loading can be captured in these conditions.

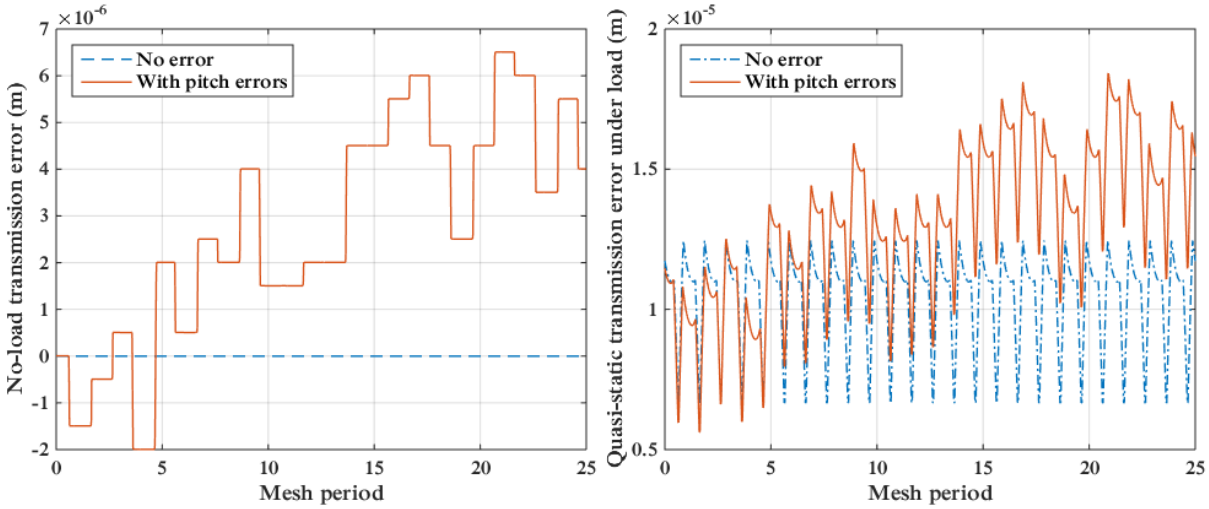

Figure IV-1 : Single-stage spur system – Time fluctuations of transmission errors with and without pitch errors

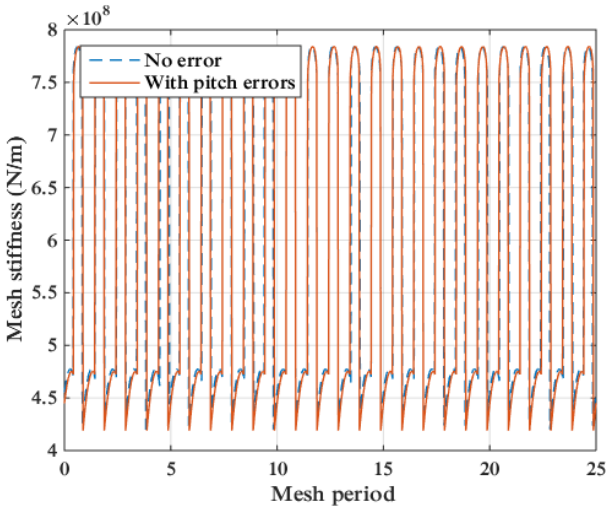

Figure IV-2 : Single-stage spur system – Time fluctuations of mesh stiffness with and without pitch errors

Figure IV-1 and Figure IV-2 show the influence of pitch errors on the time fluctuations of transmission errors and mesh stiffness. It appears clearly that the introduction of pitch errors modifies the period of the excitation signal. The spectral contents of the excitations are also altered, as shown in Figure IV-3. While the spectrum of quasi-static transmission error in the absence of tooth errors is only composed of the mesh frequency and its harmonics, additional peaks appear when pitch errors are introduced. The resulting tooth bending moments (simulated at very low speed) with and without pitch errors are shown in Figure IV-4.

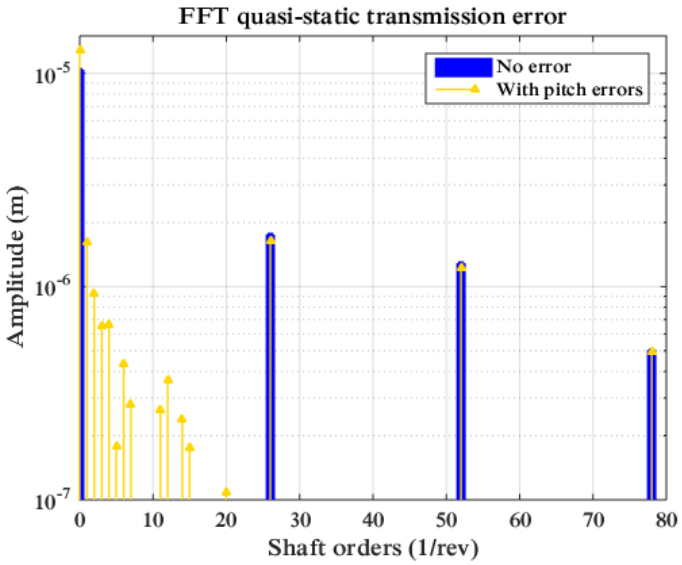

Figure IV-3 : Single-stage spur system – Influence of pitch errors on the spectral content of quasi-static transmission error

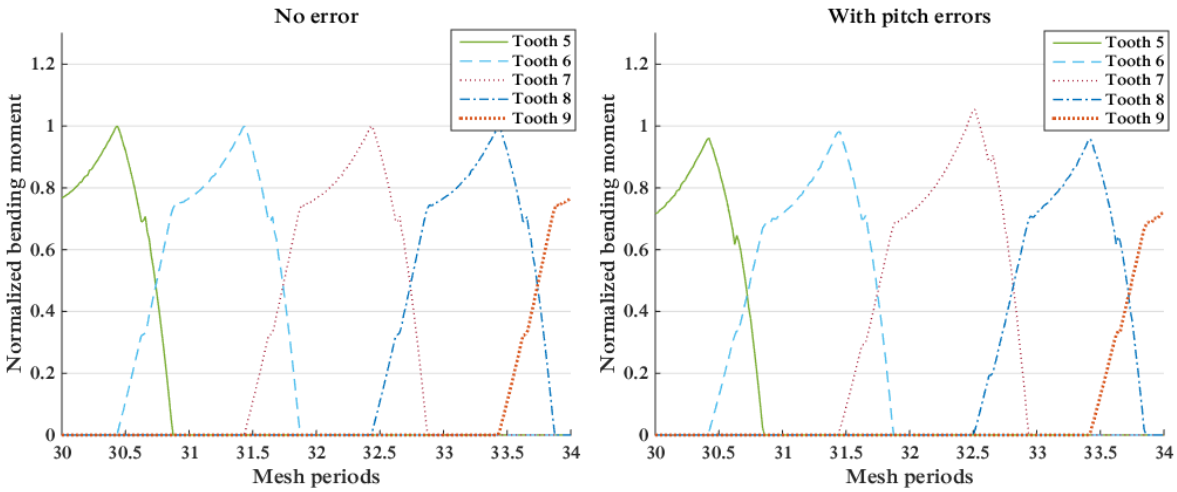

Figure IV-4 : Single-stage spur system – Influence of pitch errors on quasi-static tooth bending moment

1.2 Dynamic response

When tooth errors are considered, the dynamic factor computed at a given speed may substantially vary from one tooth pair to the next depending on the combined tooth flank deviation (cf. Figure IV-4). In order to account for this variation and in accordance with what is done for the experimental root stress signals, the maximum and minimum values are recorded at every rotational speed. It can be noticed in Figure IV-5 (spur gear case) that the band of maximum dynamic root stress amplitudes calculated from the model agrees well with the experimental envelope and the position of the tooth critical speeds is not affected by pitch errors.

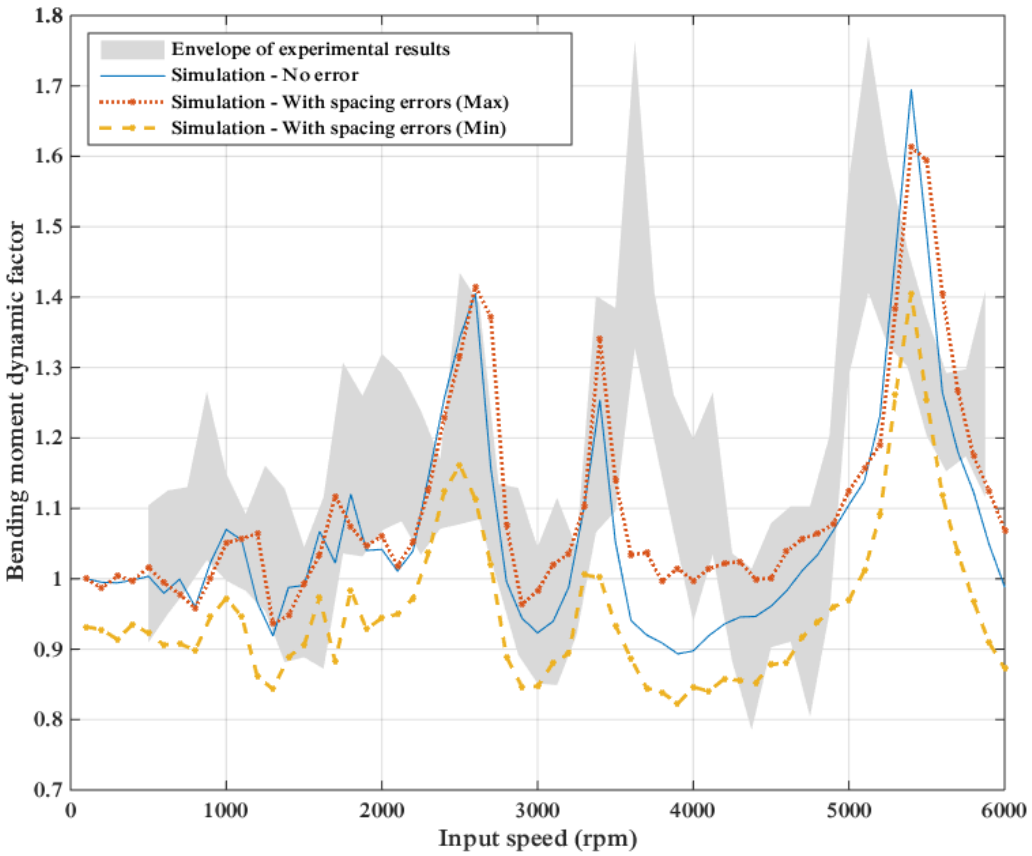

Figure IV-5 : Single-stage spur system – Dynamic response in the presence of pitch errors

The spectral content of the total mesh force is computed at different speeds and presented as a waterfall diagram in Figure IV-6 and Figure IV-7. When tooth errors are discarded, the spectrum only contains the fundamental and the harmonics of the mesh frequency, whatever the rotational speed (Figure IV-6). On the other hand, with pitch errors, additional peaks appear and the amplitudes at the mesh frequency and its harmonics tend to decrease for all speeds (Figure IV-7). These observations correlate well with the conclusions obtained by Inalpolat *et al.* on spur gears [147].

Critical eigenfrequencies are computed using the definition given in **Section 3.5.a)** of **Chapter II** and superimposed on the waterfall diagrams. The maximum amplitudes of the global mesh force are obtained when the mesh frequency or its harmonics match one of the critical eigenfrequencies. Major peaks are observed in the evolution of the maximum normalized bending moment at these rotational speeds (Figure IV-5).

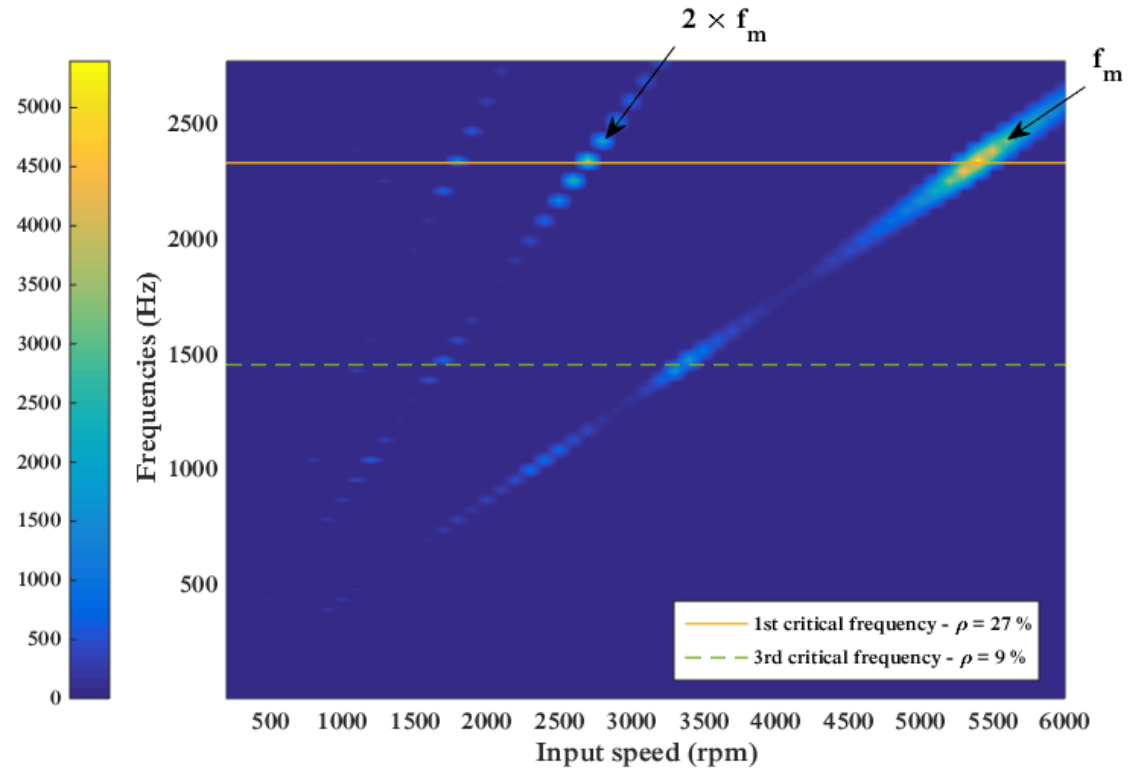

Figure IV-6 : Single-stage spur system – Spectral content of global mesh force in absence of tooth errors (amplitude in N) – Static mesh force 5 215 N

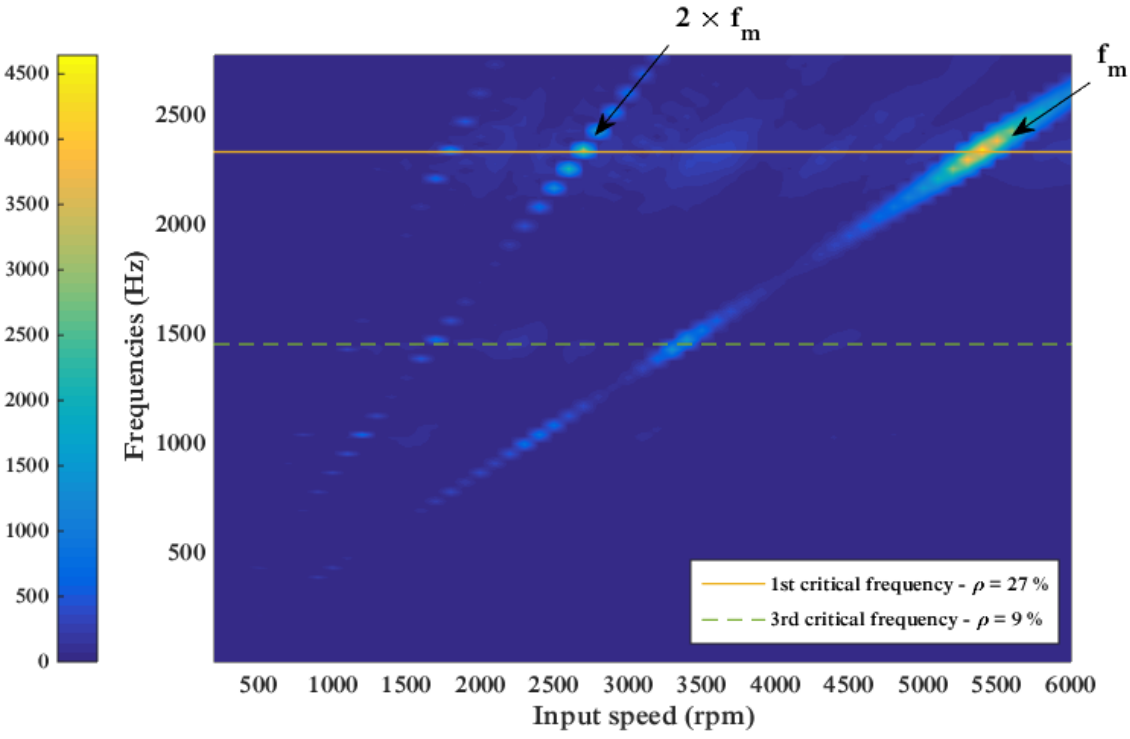

Figure IV-7 : Single-stage spur system – Spectral content of global mesh force in presence of tooth errors (amplitude in N) – Static mesh force 5 215 N

The same analysis has been conducted for helical gears. Again, the transmission error and mesh stiffness functions were simulated over two pinion revolutions. The maximum and minimum of the bending moment dynamic factor are sought on three successive teeth of the pinion, in accordance with the experimental procedure.

Results are shown in Figure IV-8. Spectral contents of the global mesh force are shown in Figure IV-9 and Figure IV-10. As for spur gears, additional peaks appear in the total mesh force spectrum when pitch errors are considered. Besides, it is also observed that the amplitudes at the mesh frequency and its harmonics significantly decrease at all speeds. The maximum amplitude at the mesh frequency is approximately 24 % of the static mesh force without pitch errors and it drops to less than 7 % in the presence of errors.

It can be concluded that the influence of pitch errors is more significant on the helical gear example than on the spur gear one and that it would have probably been necessary to perform the helical gear simulations over longer times to obtain better agreement with the measurements (Figure IV-8).

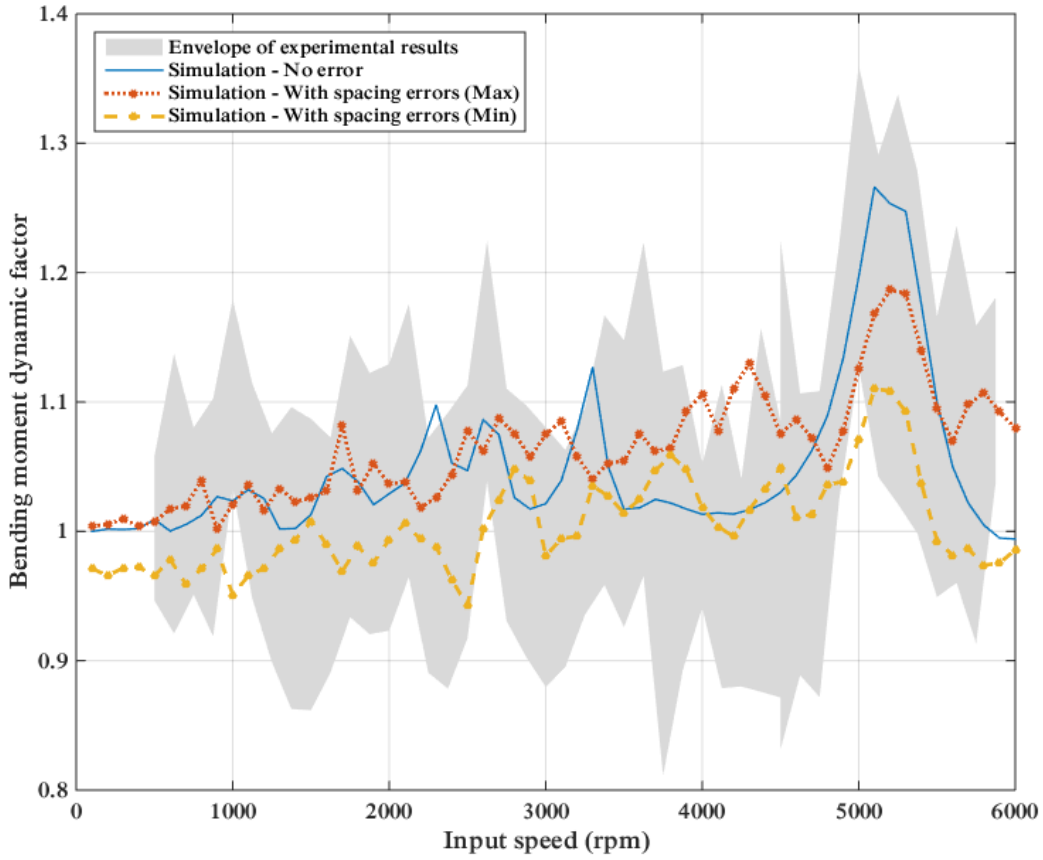

Figure IV-8 : Single-stage helical system – Dynamic response in the presence of pitch errors

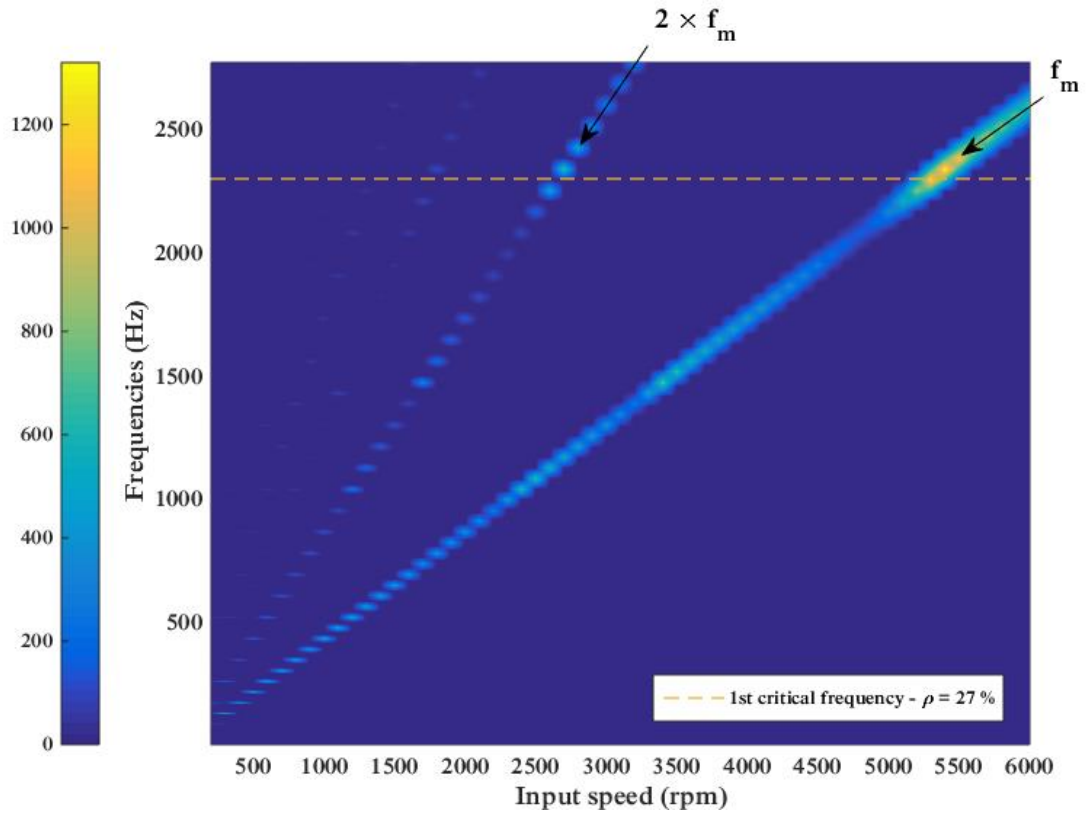

Figure IV-9 : Single-stage helical system – Spectral content of global mesh force in absence of tooth errors (amplitude in N) – Static mesh force 5 215 N

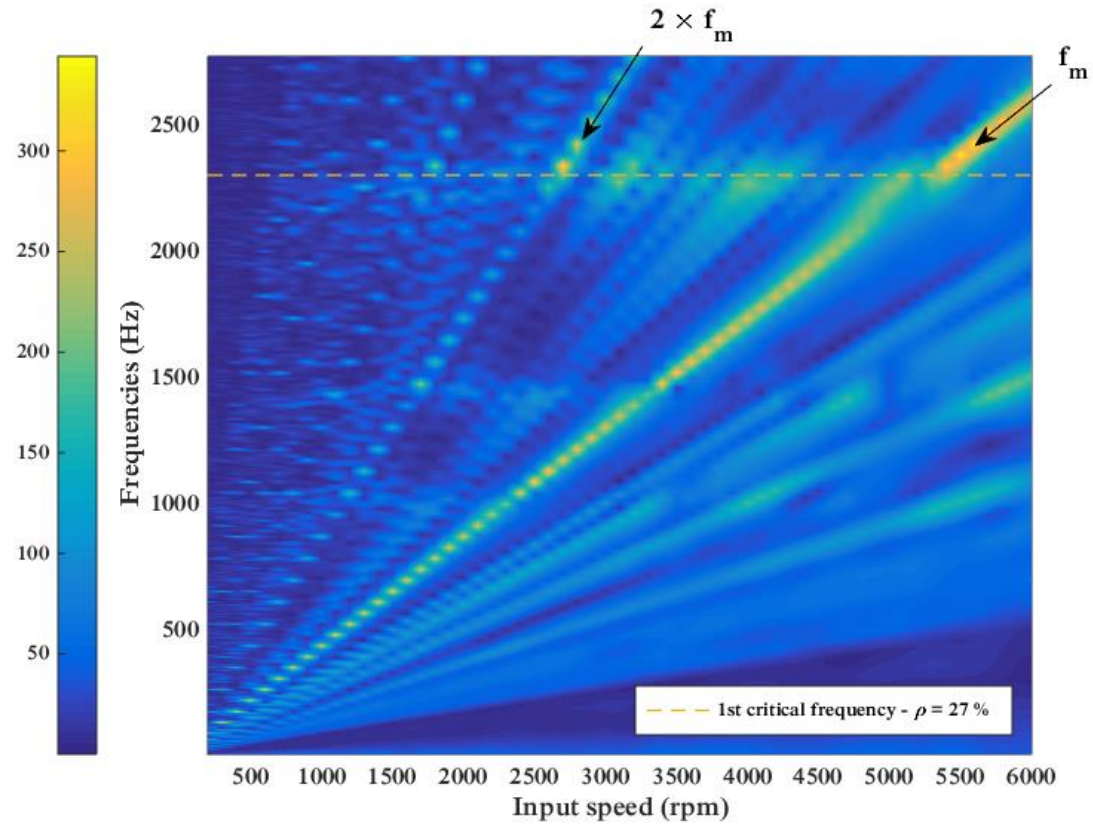

Figure IV-10 : Single-stage helical system – Spectral content of global mesh force in presence of tooth errors (amplitude in N) – Static mesh force 5 215 N

1.3 Influence of load

In this section, simulations have been performed with a higher output torque of 4270 Nm (instead of 1540 Nm in the previous sections) in order to appraise the possible combined influence of load and pitch errors on dynamic tooth loads. Results are shown in Figure IV-11 to Figure IV-13 for helical gears only, but the same conclusions were obtained for spur gears.

As previously noticed, the introduction of pitch errors does not modify the positions of tooth critical speeds. However, with a larger load, the scatter around the no-load solution decreases, as visible in Figure IV-11. In the same way, the amplitude reduction at the mesh frequency and its harmonics at critical speeds is less marked when the torque is increased, as seen in Figure IV-12 and Figure IV-13). Without pitch errors, the maximum amplitude at the mesh frequency is approximately 25 % of that of the static mesh force, and it is reduced to 18 % when pitch errors are introduced. As a reminder, a reduction of 17 % was observed after the introduction of pitch for a gear torque of 1540 Nm. It can therefore be concluded that the influence of pitch errors on the dynamic response of spur and helical gears tends to become less marked at higher loads.

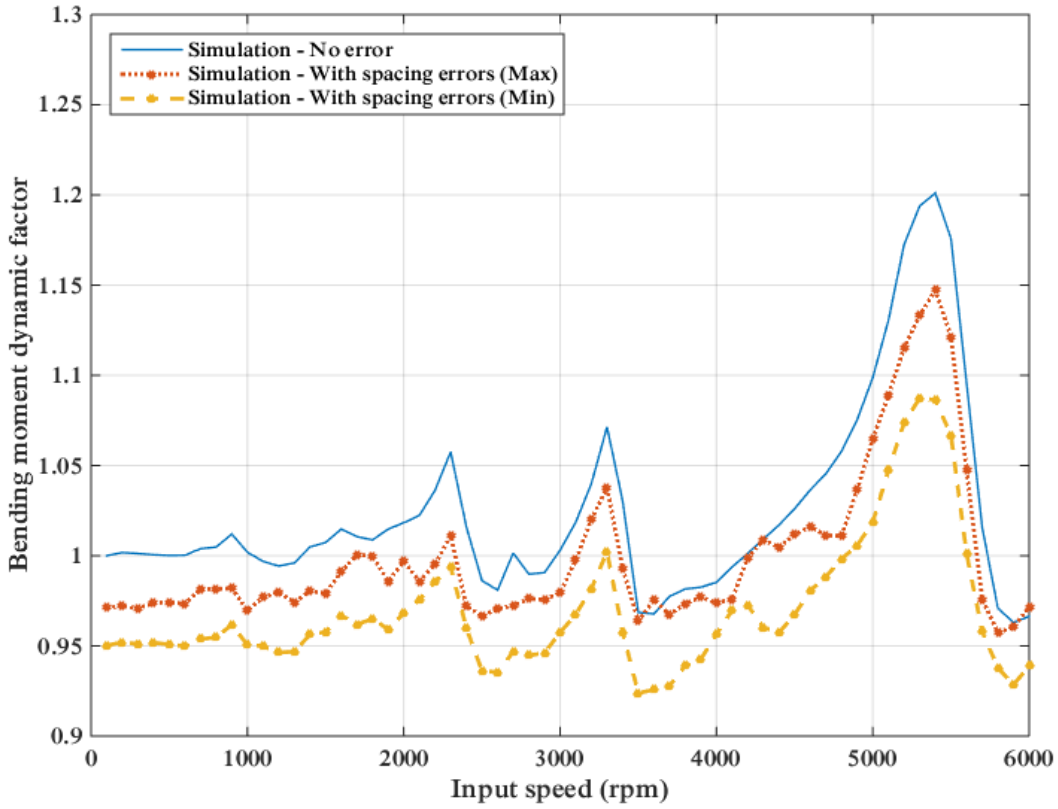

Figure IV-11 : Single-stage helical system – 4270 Nm – Dynamic response in the presence of pitch errors

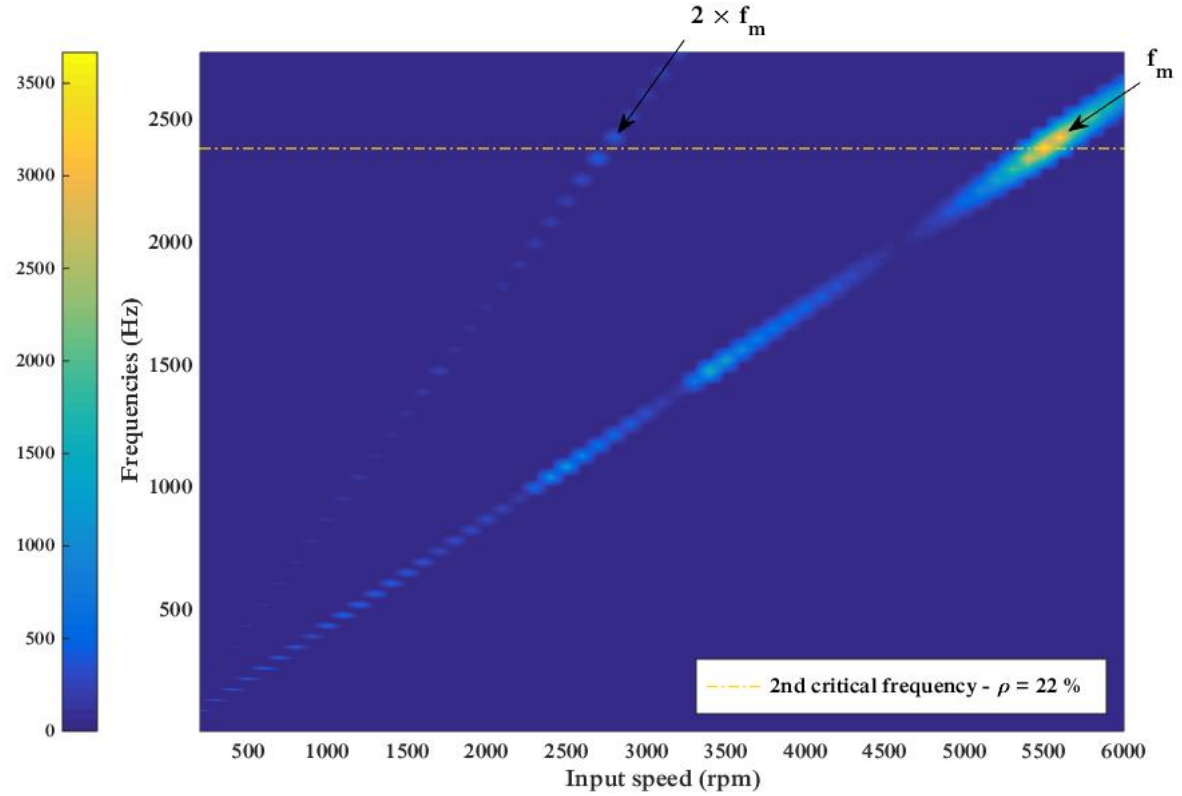

Figure IV-12 : Single-stage helical system – 4270 Nm – Spectral content of global mesh force in absence of tooth errors (amplitude in N) – Static mesh force 14 325 N

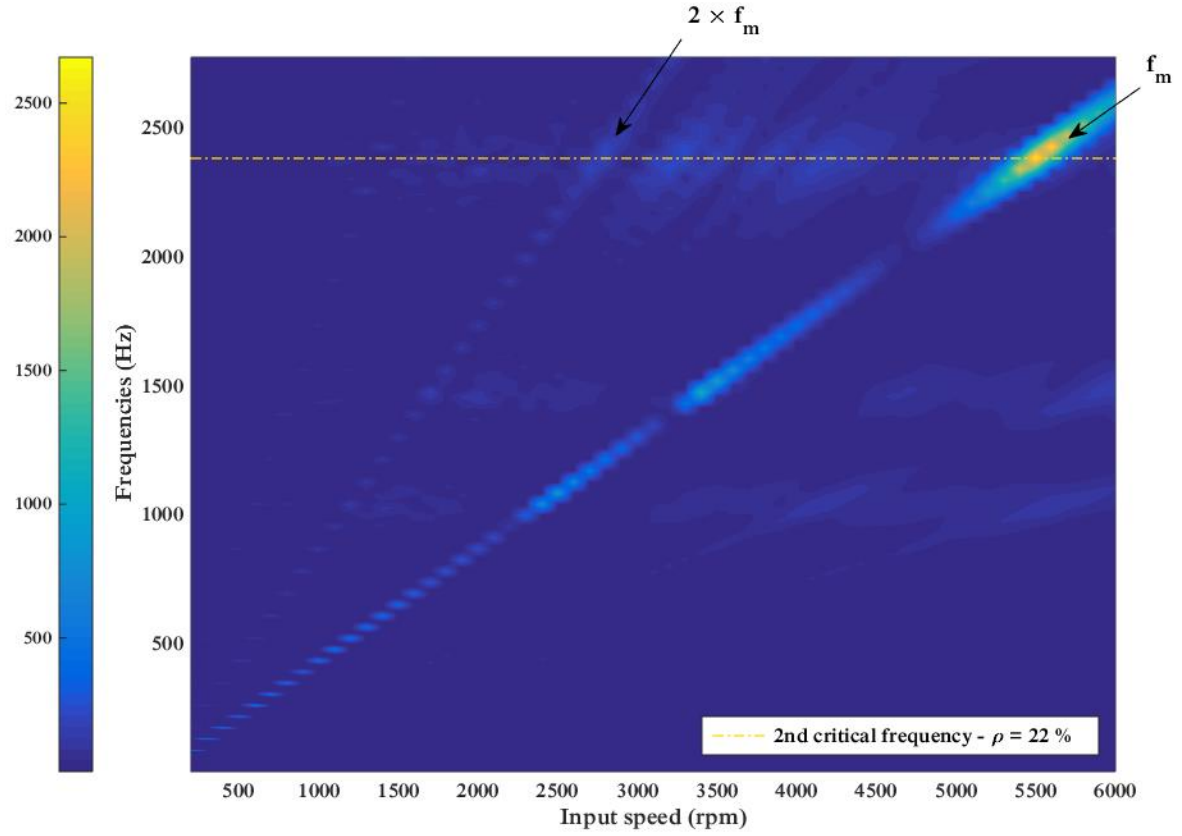

Figure IV-13 : Single-stage helical system – 4270 Nm – Spectral content of global mesh force in presence of tooth errors (amplitude in N) – Static mesh force 14 325 N

2 SINGLE-STAGE GEAR SYSTEM – CORRELATION BETWEEN THE DYNAMIC TRANSMISSION ERROR AND DYNAMIC TOOTH LOADS

Dynamic transmission error is a commonly used metric for gear vibrations although dynamic mesh forces and root stresses are more relevant criteria when considering failures and durability. In some recent studies, the possibility of a direct connection between dynamic load or stress factors and dynamic transmission errors has been investigated [51,61,62]. The evidence from the spur gear back-to-back test rig in [51,61] seems to indicate that the RMS or peak-to-peak of dynamic transmission error is proportional to tooth load / root stress. As far as the authors are aware, this linear dependency has been theoretically demonstrated for torsional models only [62], and more research is certainly required for helical gears and / or systems for which shaft bending cannot be neglected.

In this section, two different models based on the spur / helical test rig presented in **Section 2** of **Chapter III** are exploited: a) a full 3D approach which accounts for the pinion-gear pair along with the shafts, bearings, couplings and load machines, and b) a simplified torsional model restricted to the pinion and gear only. A number of results are presented to study the possibility of establishing a linear relationship between dynamic transmission error and dynamic tooth load or dynamic root stress factors.

A variety of dynamic factor definitions can be found in the literature on gear design to quantify the dynamic effects on root stresses or mesh forces. Following [51], the two following definitions are used in what follows:

$$DF_{mf} = \frac{\max(F_d)}{F_S} \qquad \textit{(IV-1)}$$

$$DF_{\sigma} = \frac{\max(\sigma_d)}{\max(\sigma_S)} \approx \frac{\max\left(\bar{M}_{b\,d}\right)}{\max(\bar{M}_{b\,S})} \qquad \textit{(IV-2)}$$

2.1 Three-dimensional models

Simulations have been performed based on the full three-dimensional test rig model with maximum bearing spacing in order to evaluate the correlation between dynamic factors and dynamic transmission errors as discussed in [51,61,62]. As opposed to the test rig used in [51,61], the test bench in Figure III-9 and Figure III-10 can hardly be assimilated to (and simulated by) a purely torsional system because of the shaft lengths along with the bearing and coupling positions. One drawback, however, is that this test rig was not instrumented for transmission error measurements and consequently only simulated transmission errors will be used in the analysis which, in view of the overall agreement with the experimental evidence, are nonetheless believed to be representative of actual signals (cf. results in **Sections 2.3** and **2.4** of **Chapter III**).

Figure IV-14 and Figure IV-15 synthetize the variations of the dynamic factors in (IV-1) and (IV-2) for both the spur and helical gears versus dynamic transmission errors. Two series of points (circles and triangles) are displayed which correspond to low-medium speed results

(circles) and higher speed results above secondary tooth critical frequencies (triangles). In Figure IV-14 (a) and Figure IV-15 (a), the abscissa is based on the theoretical findings in [62] which indicate that, for a purely torsional model, it is possible to establish the following relationship between dynamic mesh force factors DF_{mf} and the zero-to-peak amplitude of dynamic transmission errors as:

$$DF_{mf} = 1 + \frac{k_m}{F_S}(TE_d - TE_S)^{0-p} \qquad (IV\text{-}3)$$

Figure IV-14 (b) and (c) and Figure IV-15 (b) and (c) correspond to the empirical relationships proposed in [51] which relate dynamic mesh force / dynamic root stress to dynamic transmission error TE_d as:

$$\frac{F_d^{0-p}}{F_S} = \frac{TE_d^{0-p}}{\lambda} \qquad (IV\text{-}4)$$

$$DF_\sigma = \frac{\max(TE_d)}{\max(TE_S)} \qquad (IV\text{-}5)$$

with $\lambda = mean(TE_S) - mean(NLTE)$

Figure IV-14 (d) and Figure IV-15 (d) are based on the experimental findings of Hotait *et al*. [61] which confirmed, after [51] that a linear relationship could be found between DF_σ and the RMS of dynamic transmission error on their test rig. The coefficient of proportionality was found to depend on load and profile modifications and lies within the range [7.8 µm – 13.1 µm] for the examples treated.

Based on the simulation results, the following observations can be drawn:

- even if it seems that there is some degree of correlation between dynamic tooth loads or stresses and transmission errors, the linear relationships in [51,61,62] are not fully satisfactory and some significant scatter is observed which is more marked in the helical gear example,
- it also seems that depending on the speed range (below or above the secondary tooth critical speed in these examples), different behaviour is to be expected regarding the dependency between dynamic forces / stresses and dynamic transmission errors. Bifurcations can be observed with a tendency to generate two different branches in the graph which approximately correspond to the two speed regimes mentioned above.

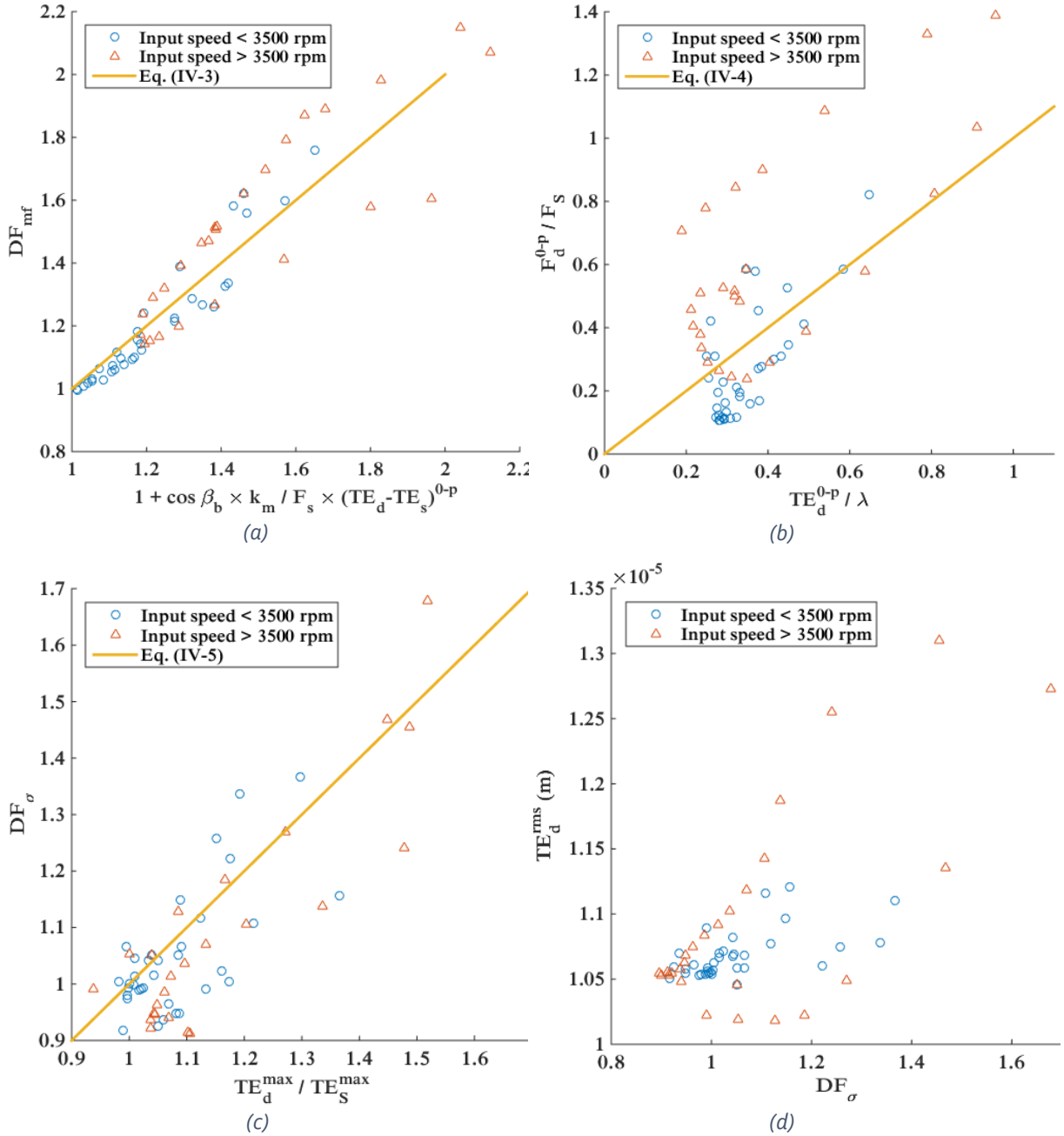

Figure IV-14 : Single-stage spur system – Correlation between dynamic factors and dynamic transmission error – Three-dimensional model

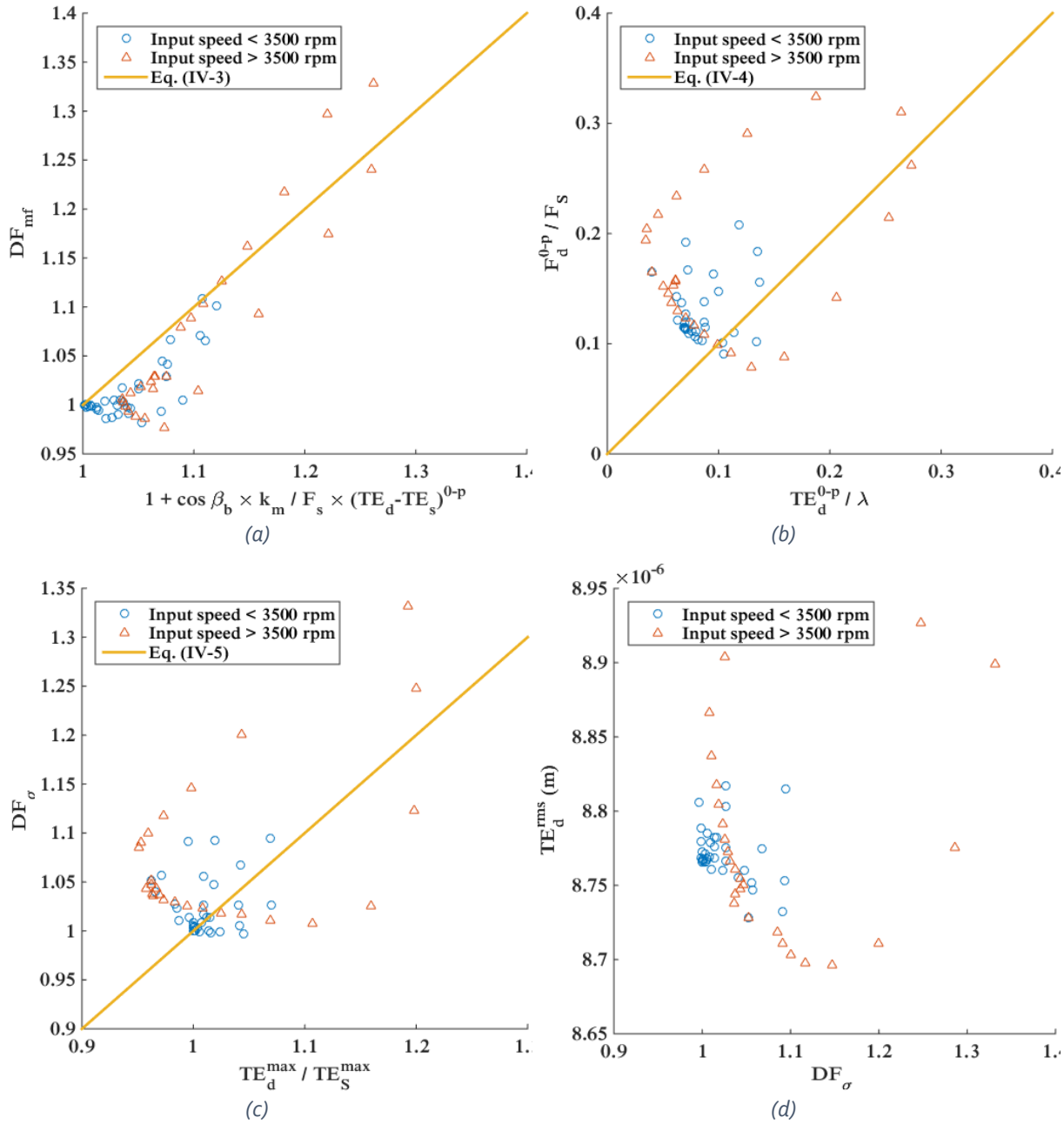

Figure IV-15 : Single-stage helical system – Correlation between dynamic factors and dynamic transmission error – Three-dimensional model

2.2 Torsional models

A reduced torsional model has been derived from the complete system described in Figure III-13. The loading conditions are the same but the pinion and gear are supposed to be mounted on very short and stiff shafts supported by rigid bearings in order to minimize the influence of shaft bending and bearing deflections. The motor shaft and the elastic couplings are not taken into account so that the driving torque is applied directly on the pinion shaft as illustrated in Figure IV-16. Gear blank deflections are taken into account in the calculation of mesh stiffness but do not interfere with the degrees of freedom attributed to the gear limited, here, to one torsional angle.

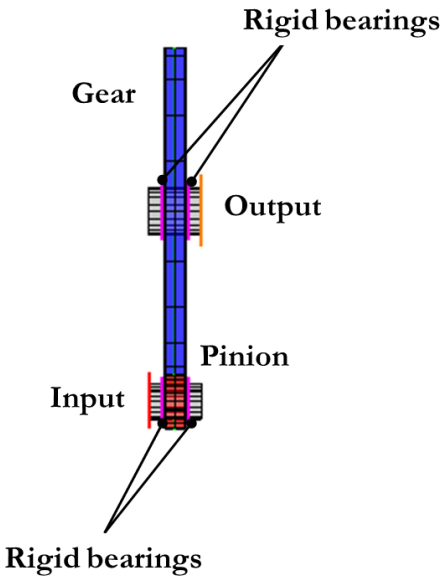

Figure IV-16 : Single-stage spur / helical system – Reduced torsional system derived from the test rig

The corresponding comparisons between dynamic transmission errors and dynamic factors are presented in Figure IV-17 and Figure IV-18 for the spur and helical gear examples. In contrast with the previous set of results obtained from the complete three-dimensional model, a linear relationship is clearly visible even if the results at higher speeds seem to deviate slightly from the linear dependency observed at lower speeds.

It is therefore postulated that dynamic tooth loading and transmission errors might be connected to some extent but in a more complex way than that suggested in [51,61]. The experimentally observed linear dependency could be a particular case related to the test rig characteristics and should be extrapolated with care. Further experimental and analytical analyses are certainly needed in this area.

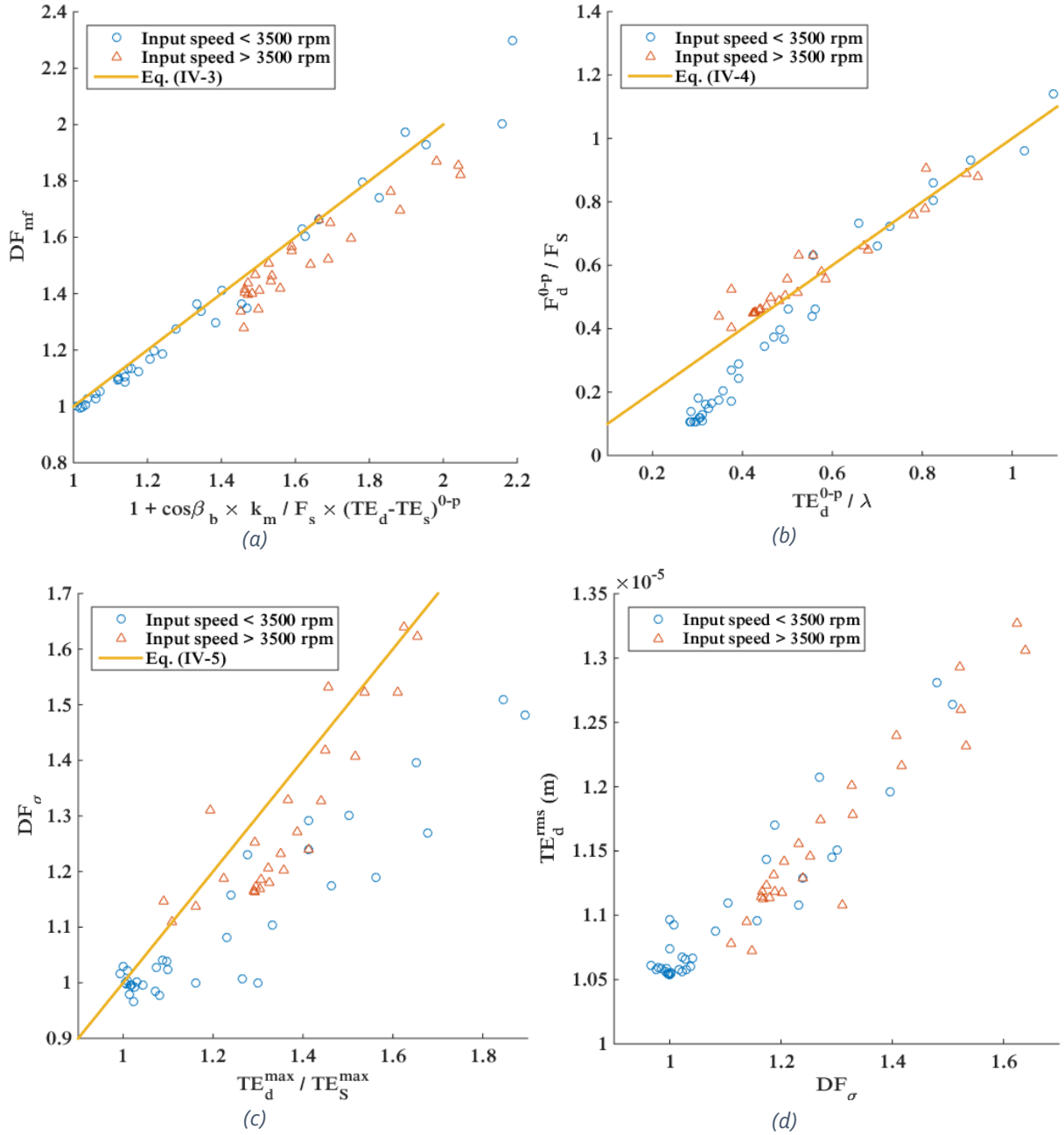

Figure IV-17 : Single-stage spur system – Correlation between dynamic factors and dynamic transmission error – Torsional model

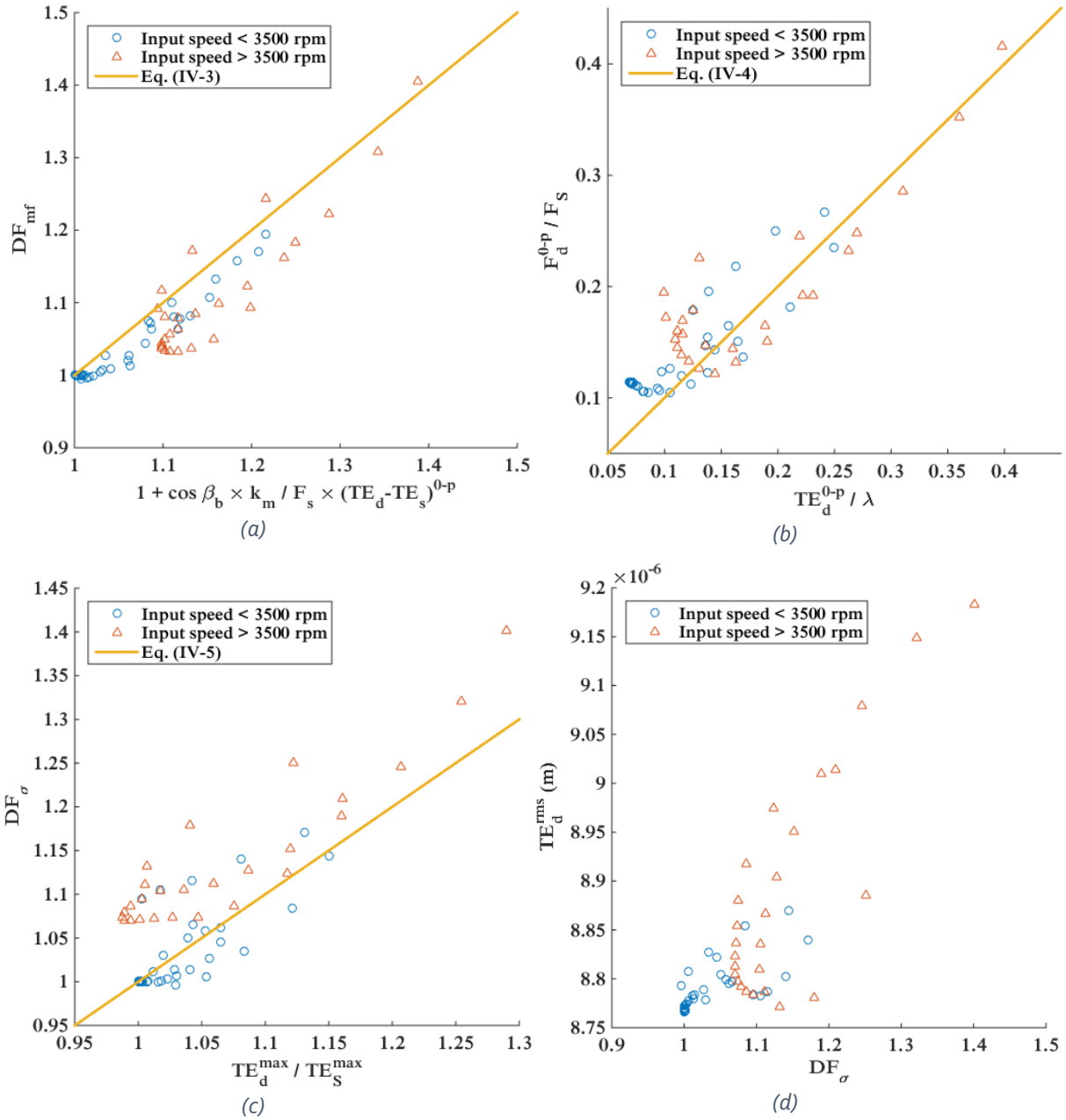

Figure IV-18 : Single-stage helical system – Correlation between dynamic factors and dynamic transmission error – Torsional model

3 DOUBLE-STAGE SPUR GEAR SYSTEMS

Following the analysis of the vibratory response at the gear meshes of double-stage spur gear systems in **Section 4** of **Chapter III**, this paragraph focuses on the analysis of the dynamic behaviour of bearings. The dynamic forces induced at the bearings by mesh excitations are the principal source of dynamic excitations on the casing and it is therefore crucial to understand how the vibrations generated at the meshes propagate to the bearings.

Besides, the influence of the relative phase shift between the successive meshes of the idler gear system is analysed.

3.1 System with intermediate shaft – Bearing response

The dynamic forces generated on the bearings by mesh excitations are computed from the solution $\boldsymbol{X}$ of the equations of motion. For each bearing, the vector of the dynamic displacement is multiplied by the associated stiffness matrix to estimate the bearing dynamic forces at each time step. The spectral content of the resulting signal is analysed for each rotational speed by using a Fast Fourier Transform and compared with the peak-to-peak dynamic force. The spectral content of the bearing dynamic force is plotted under the form of a spectrogram (frequencies versus input speeds). The mesh frequencies of the system are represented as straight lines passing through the origin of the diagram and are denoted f_{m1}, f_{m2} for the mesh frequencies of stage 1 and stage 2, respectively (and multiples for the harmonics).

In a first step, the system with unmodified gears defined in **Sections 4.1.a)** and **4.1.b)** of **Chapter III** is analysed**.** The results are shown in Figure IV-20 to Figure IV-23 for bearing 2, 3, 4 and 6 respectively (see bearing labelling in Figure IV-19). Several conclusions can be drawn:

- The spectral content of the different bearing dynamic forces is dominated by the mesh frequency (and its first harmonics) of both gear stages.
- Amplifications of the bearing dynamic forces fluctuations are observed when the mesh frequency (or its first harmonics) of one gear pair coincides with one of the major tooth critical frequencies. Similarities can therefore be noticed between the gears and bearings major critical speeds (e.g. 21 000 rpm for gear stage 2 – Figure III-22 – and bearing 3 – Figure IV-21).
- Even though bearing 4 is located closer to stage 1, its dynamic response is principally controlled by the excitations generated at stage 2 (Figure IV-22). This observation shows that strong couplings occur between the gear meshes and the surrounding elements of the system.

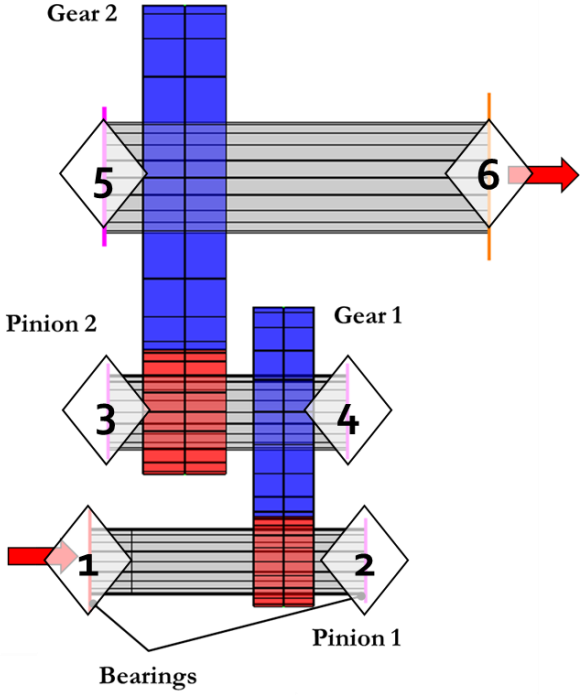

Figure IV-19 : Dual-mesh spur gear system with intermediate shaft – Bearing elements numbering

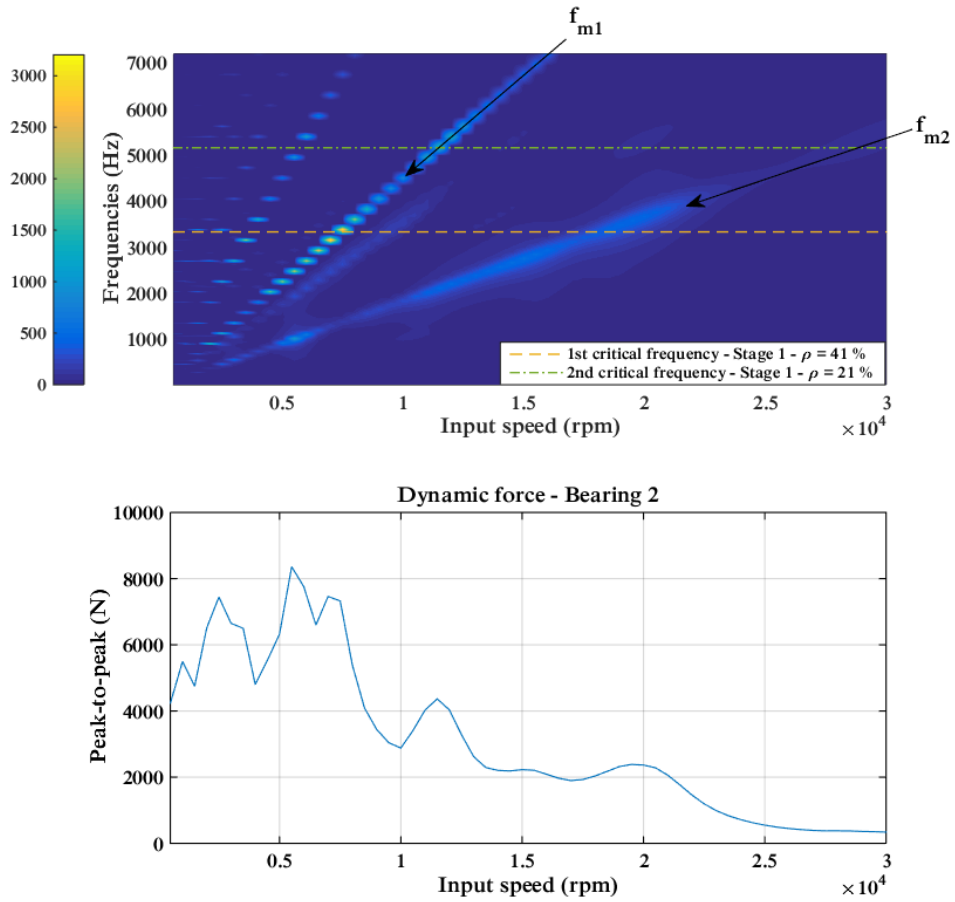

Figure IV-20 : Dual-mesh spur gear system with intermediate shaft – Bearing 2 – Spectral content of the dynamic force (Amplitude in N)

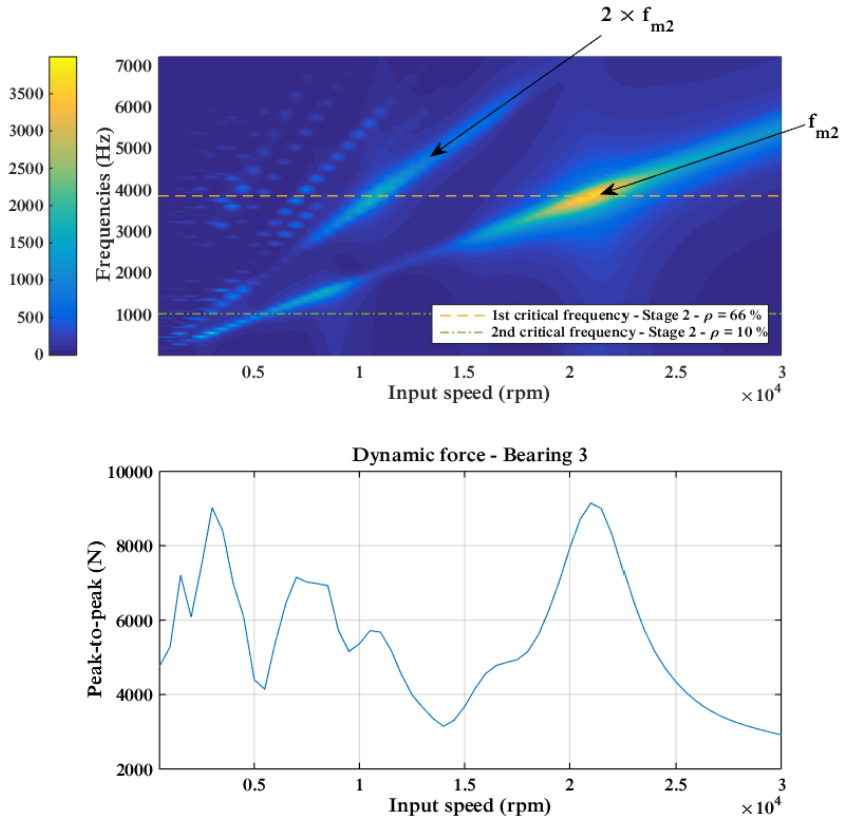

Figure IV-21 : Dual-mesh spur gear system with intermediate shaft – Bearing 3 – Spectral content of the dynamic force (Amplitude In N)

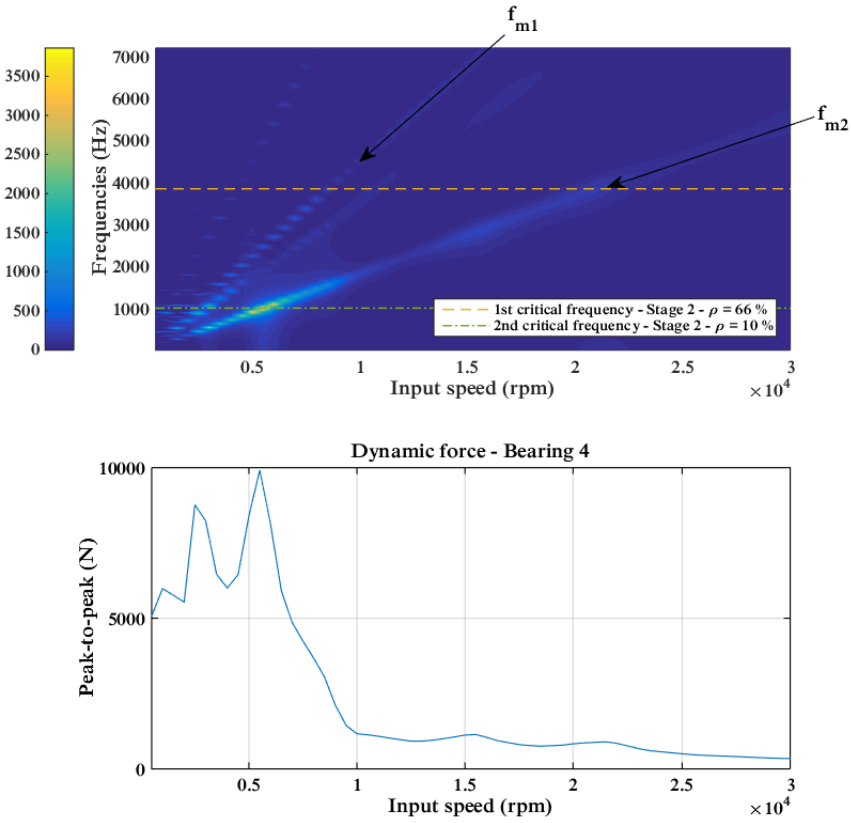

Figure IV-22 : Dual-mesh spur gear system with intermediate shaft – Bearing 4 – Spectral content of the dynamic force (Amplitude in N)

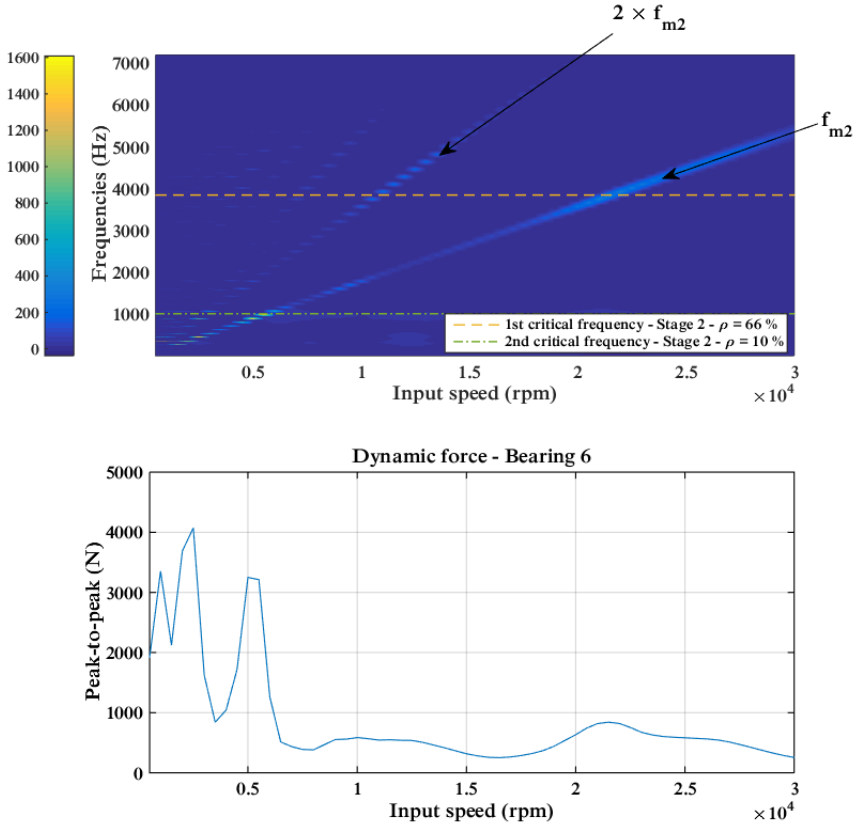

Figure IV-23 : Dual-mesh spur gear system with intermediate shaft – Bearing 6 – Spectral content of the dynamic force (Amplitude in N)

In a second phase, the same analysis is performed based on the system with modified tooth profiles, using the long profile modifications defined in **Section 4.1.c)** of **Chapter III**. It was shown that these modifications reduce significantly gear vibrations and their effect on bearing dynamic responses is investigated in what follows.

The spectral content and amplitudes of the bearing dynamic forces are shown in Figure IV-24 and Figure IV-25 for bearings 2 and 3 only but similar findings were obtained for the four other bearings of the system. It can be observed that:

- The spectral content of the bearing dynamic forces is not significantly altered by the introduction of gear profile modifications. The major components remain the mesh frequencies of both gear pairs, along with their first harmonics.
- The amplitude of the fluctuations of the bearing dynamic forces is efficiently reduced in the presence of profile modifications, over the entire range of speeds.
- This effect is not identical for all frequencies. In the spectral content of bearing 3 dynamic force (Figure IV-21 and Figure IV-25), the amplitude reduction is larger at the mesh frequency of stage 2 than at that of stage 1. As a consequence, the peak force is reduced by almost 70 % at 21 500 rpm but by only 30 % at 8 500 rpm.

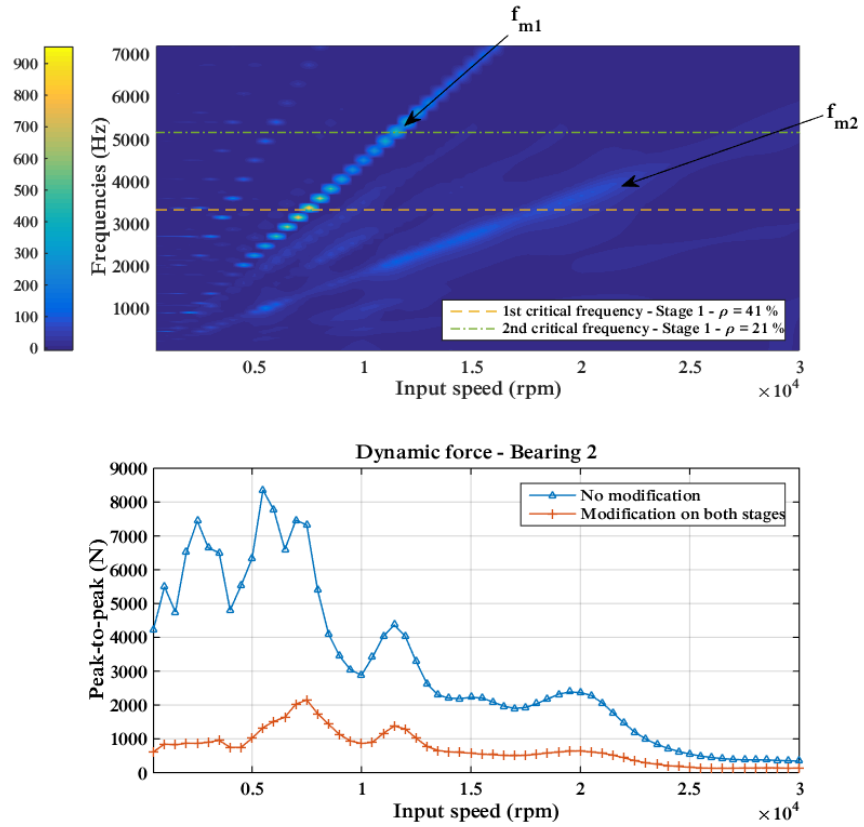

Figure IV-24 : Dual-mesh spur gear system with intermediate shaft – Bearing 2 – Influence of profile modifications on the bearing dynamic forces (Amplitude in N)

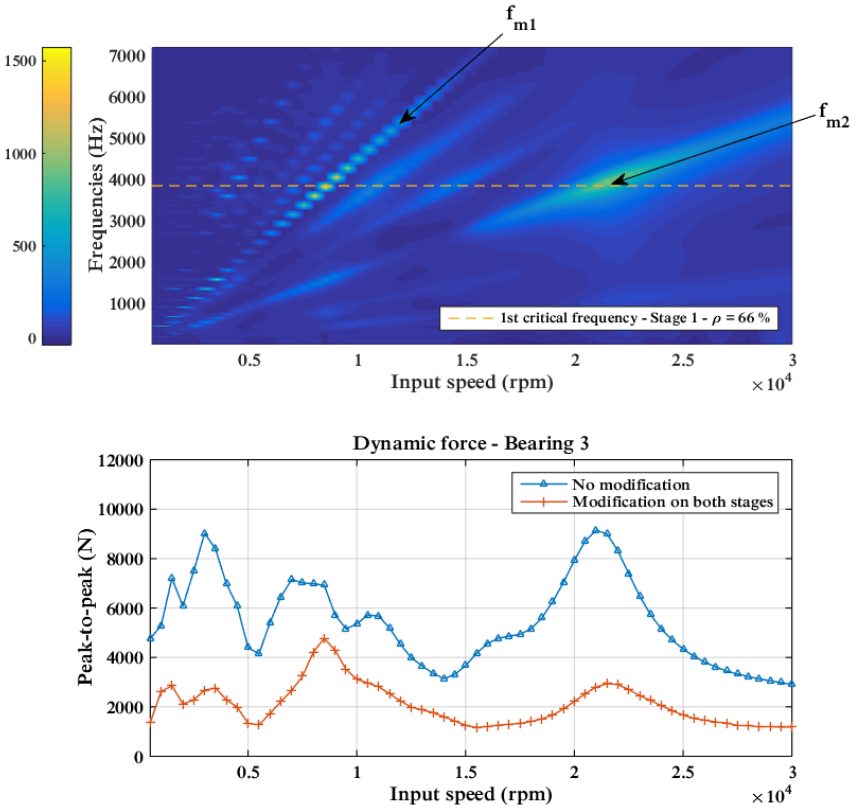

Figure IV-25 : Dual-mesh spur gear system with intermediate shaft – Bearing 3 – Influence of profile modifications on the bearing dynamic forces (Amplitude in N)

3.2 System with idler gear

3.2.a) *Influence of phase shift*

As presented in **Section 3.2** of **Chapter II**, the relative phasing between the successive meshes of a system with idler gear is imposed by the angle between the center lines. The previous results were obtained for a configuration where the shaft axes are contained in the same plane which corresponded to a phase shift close to zero (see Figure III-29 and Figure III-30). By changing the angle between the center lines by 5°, the mesh excitation functions are nearly out-of-phase (cf. Figure IV-26). Without any loss of generality, the analysis is kept limited to unmodified gears.

The results of the dynamic simulations are displayed in Figure IV-27 for stage 1 and Figure IV-28 for stage 2. The blue curves with triangular markers correspond to the results obtained for in-phase excitations, already presented in **paragraph 4.2.b)** of **Chapter III**. It can be noted that the maximum vibratory level for stage 1 is obtained when the excitations are out of phase whereas the opposite phenomenon is observed on stage 2, suggesting some form of energy transfer between the meshes.

Finally, the long reliefs defined in **Section 4.2.c)** of **Chapter III** are introduced on both gear meshes simultaneously. The corresponding results are presented in Figure IV-29 for stage 1 and in Figure IV-30 for stage 2. One can notice that, as for the configuration with nil phase shift, these profile modifications lead to a reduction in gear vibrations for both gear stages. It can reasonably be concluded that changes in phase shift between the successive meshes of an idler gear system have no impact on the effectiveness of tooth profile modifications.

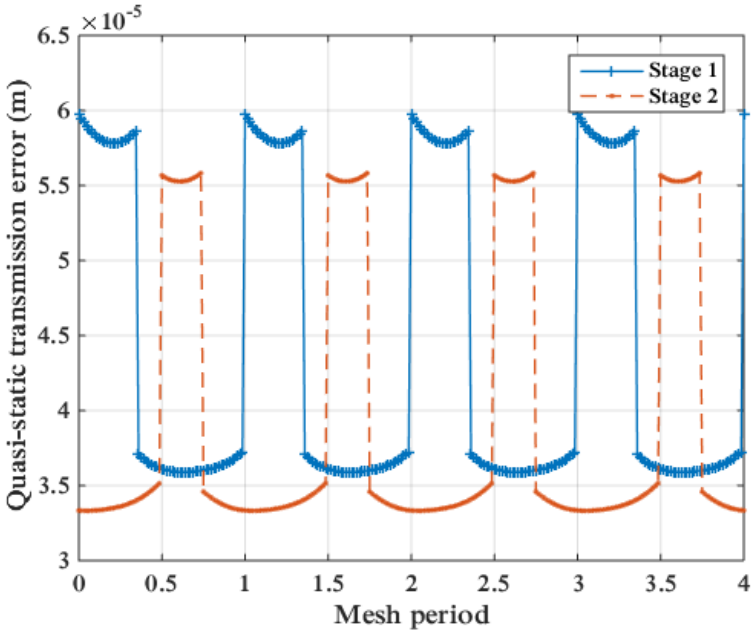

Figure IV-26 : Double-stage spur gear system with idler gear – Quasi-static transmission error functions with non-zero phase shift

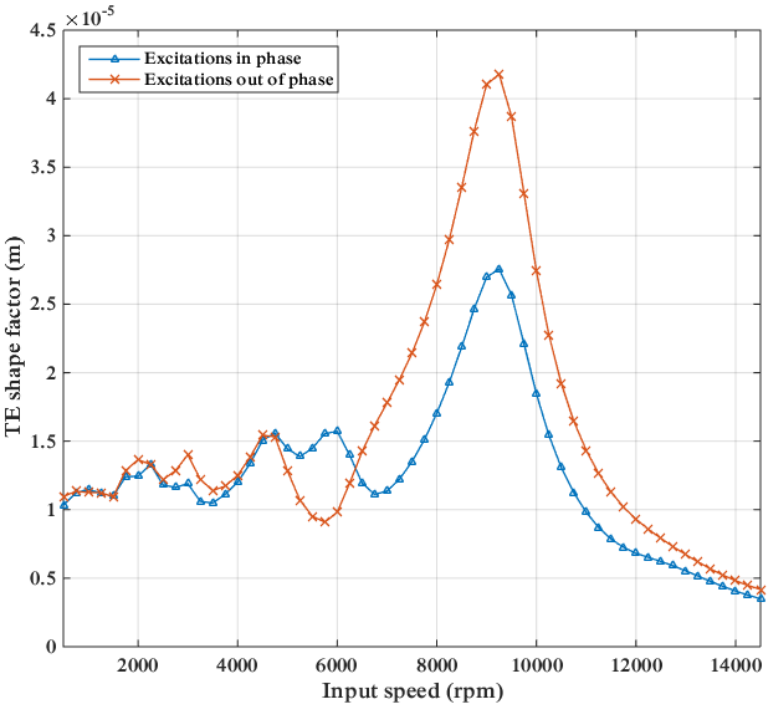

Figure IV-27 : Double-stage spur gear system with idler gear – Stage 1 – Influence of the phase shift on the gear vibratory level

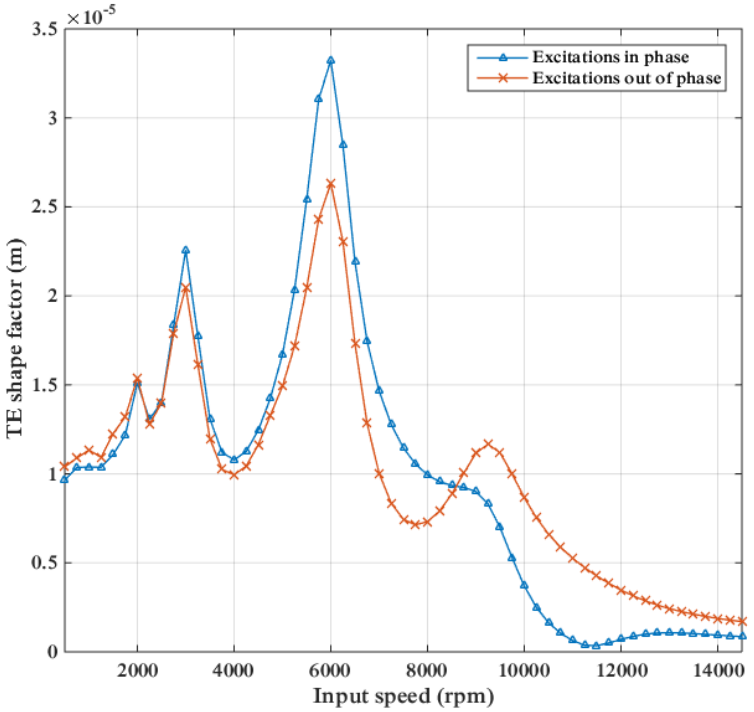

Figure IV-28 : Double-stage spur gear system with idler gear – Stage 2 – Influence of the phase shift on the gear vibratory level

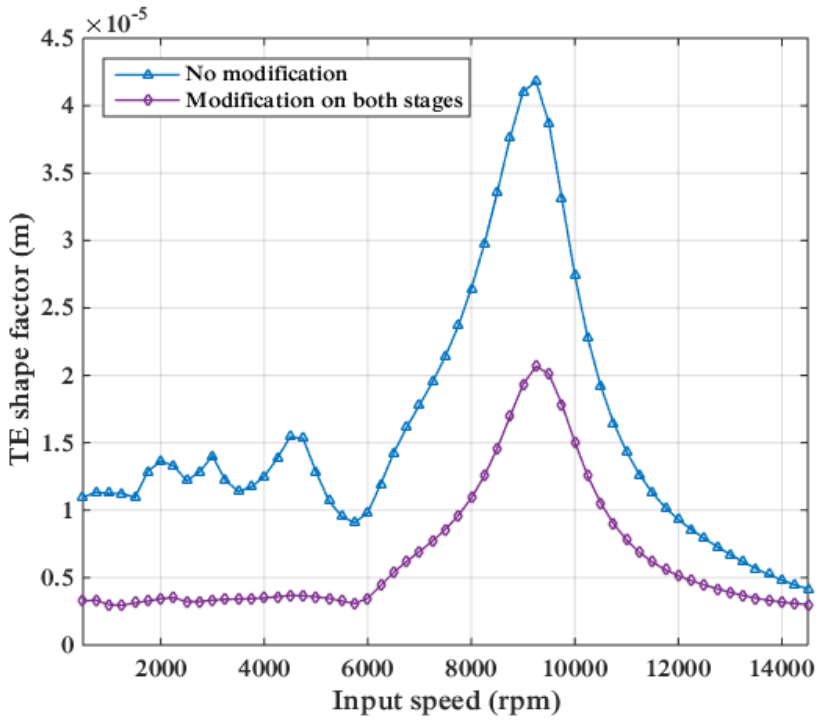

Figure IV-29 : Double-stage spur gear system with idler gear – Stage 1 – Influence of profile modifications with out-of-phase excitations

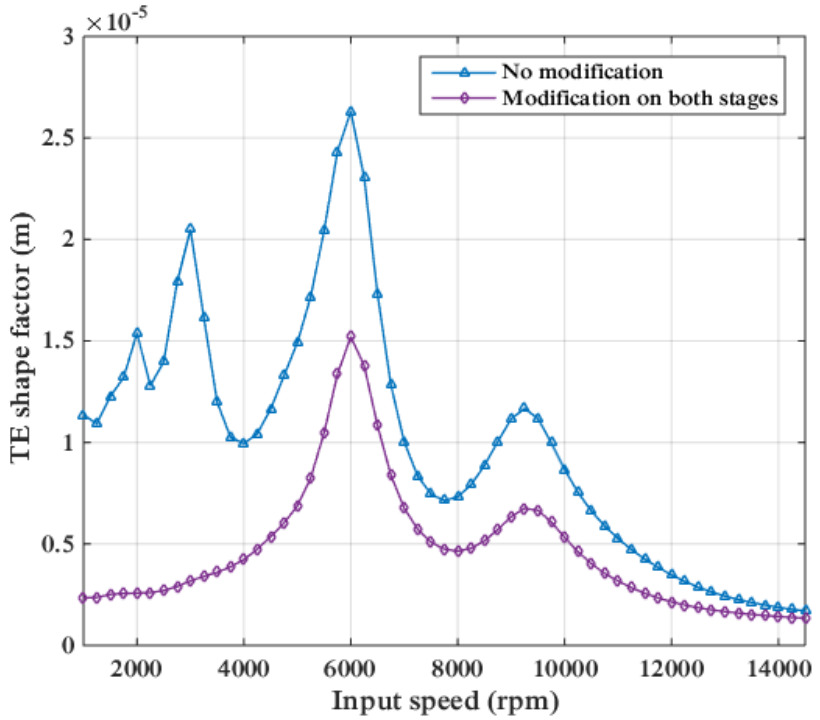

Figure IV-30 : Double-stage spur gear system with idler gear – Stage 2 – Influence of profile modifications with out-of-phase excitations

3.2.b) *Bearing response*

An analysis of the bearing dynamic response is conducted following the same method as for the system with intermediate shaft, described in **Section 3.1** of this chapter.

The analysis is first conducted on the idler gear system with unmodified gears and in-phase excitations, as presented in **Section 4.2.b)** of **Chapter III**. The results in Figure IV-32 to Figure IV-34 for bearing 2, 4 and 6 respectively (see label conventions in Figure IV-31) lead to the following conclusions (similar observations have been made on the three other bearings of the system):

- The spectral content of the dynamic forces at the bearings is limited to the mesh frequency (and first harmonics), which is the only source of excitation in this system.
- It seems that the peak-to-peak of the bearing dynamic forces is amplified when the mesh frequency matches one of the tooth critical frequencies. Thus, in these conditions, the critical speeds for bearings and gears are identical.
- A strong coupling is observed between the dynamic response of the bearing and that of the closer gear. The most critical speed in the dynamic response of bearing 2 corresponds to the major critical speed of gear stage 1 (9 250 rpm) whereas the dynamic response of bearings 4 and 6 is dominated by the critical speed of gear stage 2 (around 6 000 rpm).

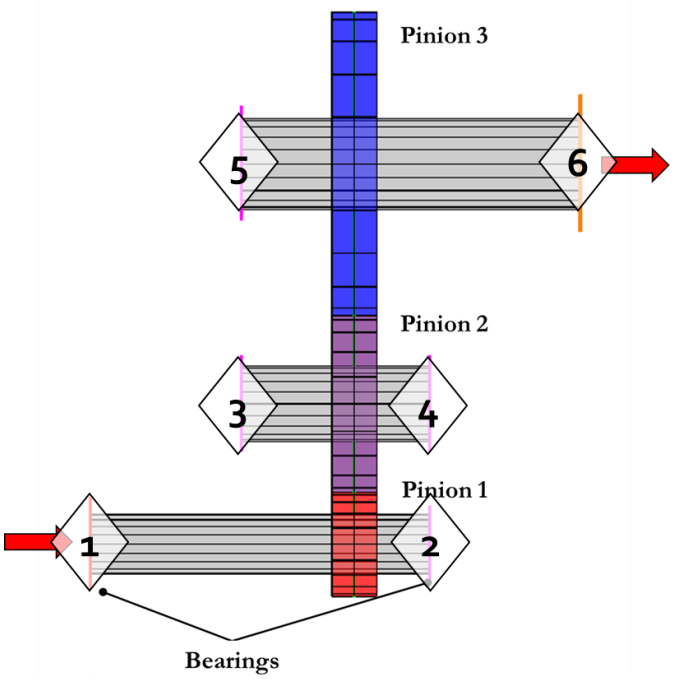

Figure IV-31 : Double-stage spur gear system with idler gear – Bearing elements numbering

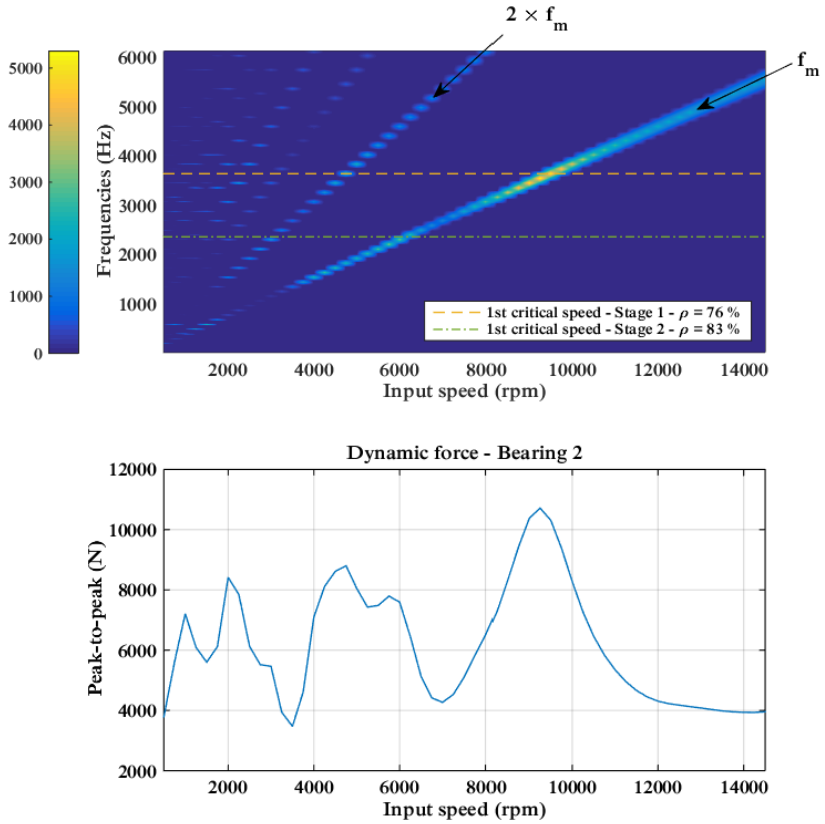

Figure IV-32 : Double-stage spur gear system with idler gear – Bearing 2 – Spectral content of the dynamic force (Amplitude in N)

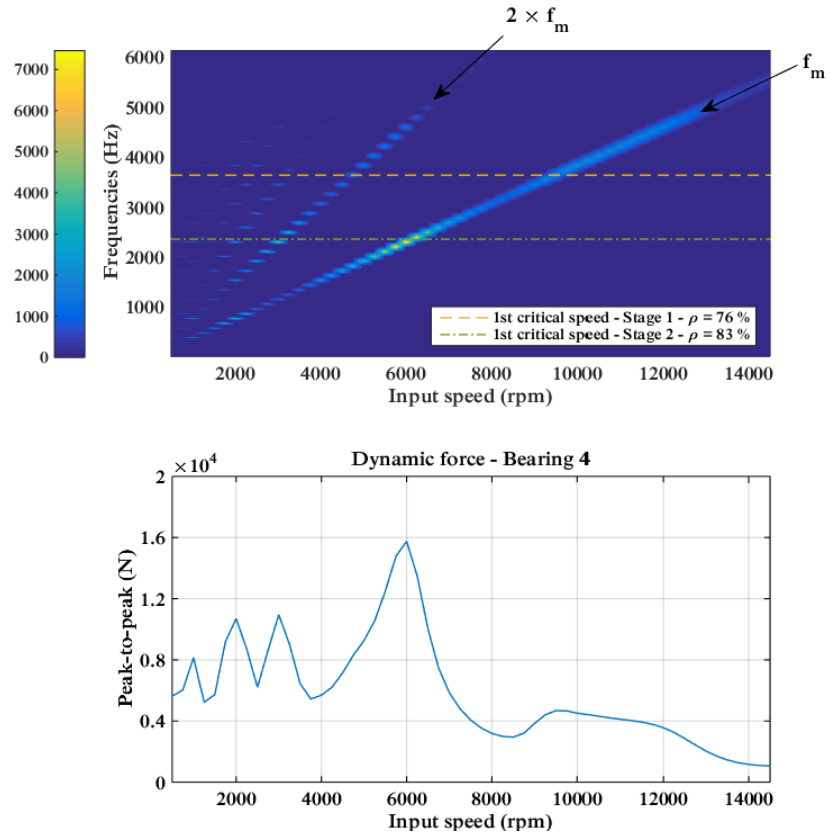

Figure IV-33 : Double-stage spur gear system with idler gear – Bearing 4 – Spectral content of the dynamic force (Amplitude in N)

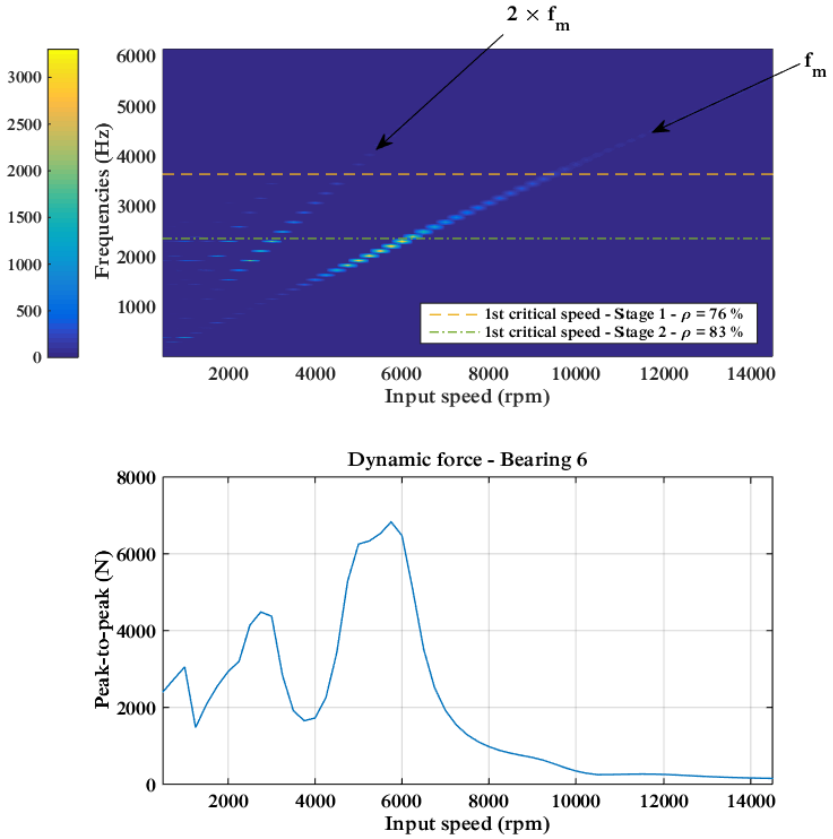

Figure IV-34 : Double-stage spur gear system with idler gear – Bearing 6 – Spectral content of the dynamic force (Amplitude in N)

Bearing dynamic responses in the presence of tooth profile modifications are now analysed (see description in **paragraph 4.2.c)** of **Chapter III**) with the objective of assessing if the profile modifications effective with regard to gear vibrations can also reduce bearing dynamic forces (and hence the dynamic excitations on the casing).

The results, presented in Figure IV-35 to Figure IV-37 indicate that the spectral content of the bearing dynamic forces is not significantly altered by the introduction of profile modifications. Whereas dynamic force amplitudes are generally lowered when the gears are modified, except for a peak at low speed (around 1 000 rpm).

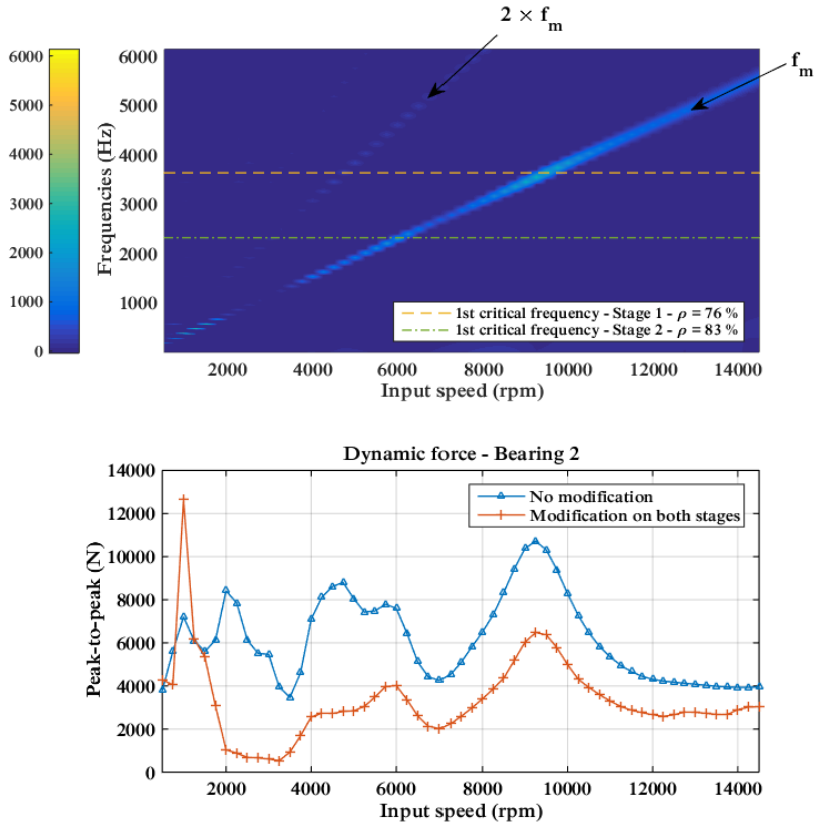

Figure IV-35 : Double-stage spur gear system with idler gear – Bearing 2 – Influence of profile modifications on the bearing dynamic forces (Amplitude in N)

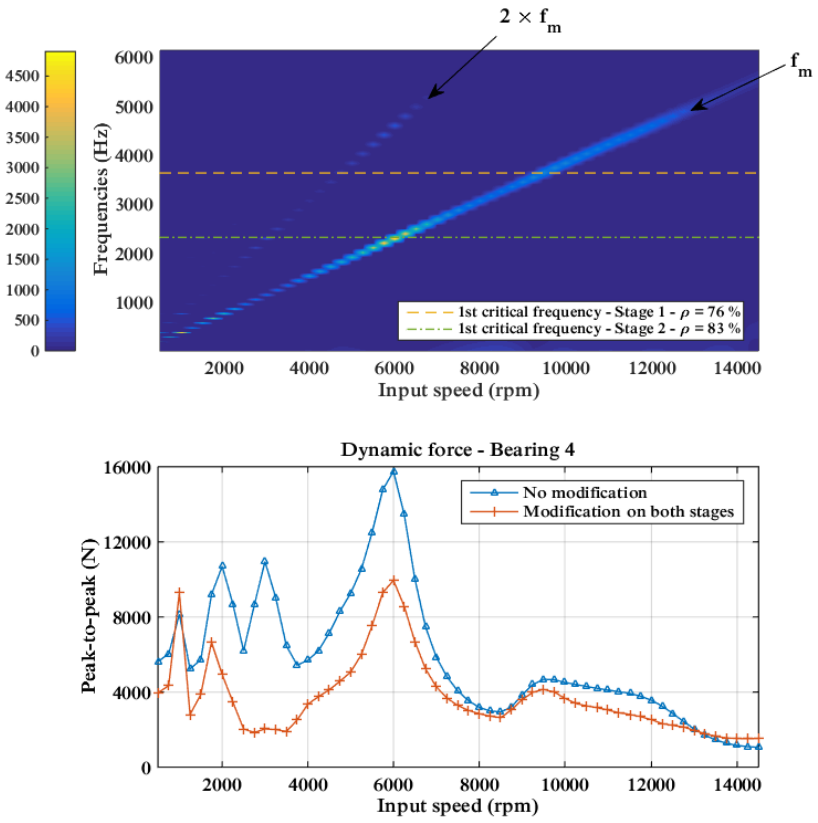

Figure IV-36 : Double-stage spur gear system with idler gear – Bearing 4 – Influence of profile modifications on the bearing dynamic forces (Amplitude in N)

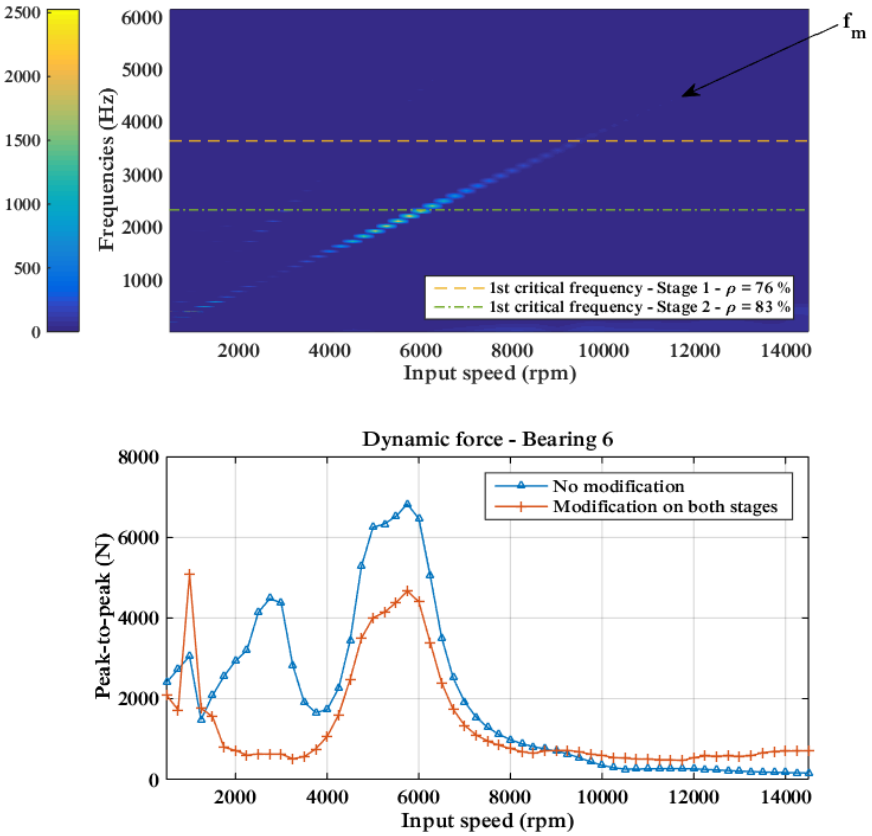

Figure IV-37 : Double-stage spur gear system with idler gear – Bearing 6 – Influence of profile modifications on the bearing dynamic forces (Amplitude in N)

4 DOUBLE-STAGE GEAR SYSTEM WITH INTERSECTING AXES

To reproduce a geometry similar to that of a helicopter gearbox, a system is now studied which combines a cylindrical and a spiral-bevel gear. The first stage is a unity-ratio cylindrical gear pair whereas the second reduction stage is made of the spiral-bevel gear studied in a single-stage system by Wang [102] and already used in a single-stage spiral-bevel system in **Section 3** of **Chapter III**.

A spur and a helical gear (with identical tooth numbers) are successively employed as stage 1. The geometry of the shaft connecting the two reduction stages is varied and the couplings between the cylindrical and spiral-bevel gears are studied for each configuration. The dynamic response at the bearings is then analysed.

4.1 Description of the system

A schematic representation of the system under consideration is shown in Figure IV-38. The cylindrical pinion / gear and the bevel pinion are centred between two bearings whereas the bevel gear is overhung. For all the applications presented in the following sections, the bearings are located at 20 mm from the centre of the nearest pinion / gear. Two additional bearings are located at the extremities of the input and output shafts. All bearings have identical characteristics, listed in Table IV-1. The shaft dimensions are also detailed in Table IV-1 (density 7 800 kg/m^3, Young Modulus 210 GPa). The length of the intermediate shaft is varied for some applications and will be subsequently specified in the following sections. The gear data are listed in Table IV-2.

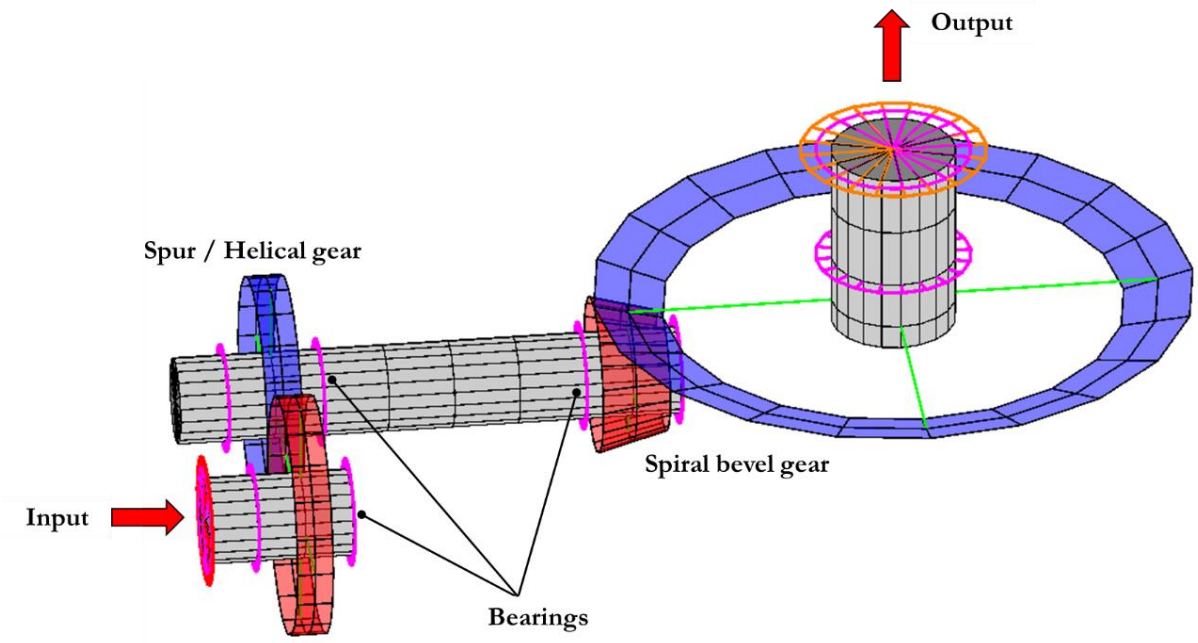

Figure IV-38 : Double-stage system with intersecting axes – System geometry

Table IV-1 : Double-stage system with intersecting axes – Shaft and bearing data

Shaft	Shaft section	Length (mm)	External diameter (mm)
Input shaft	Upstream	40	36
	Downstream	20	36
Intermediate shaft	Upstream	40	36
	Intermediate	150	36
	Downstream	20	36
Output shaft	Upstream	10	52
	Downstream	70	52
Bearing radial stiffness	10^8 N/m		
Bearing axial stiffness	10^7 N/m		

Table IV-2 : Double-stage system with intersecting axes – Gear data

	Cylindrical		Spiral-bevel	
	Pinion	**Gear**	**Pinion**	**Gear**
Tooth number	25	25	13	50
Module (mm)	4		5	
Pressure angle (deg)	20		20	
Helix angle (deg)	0 (spur) 30 (helical)		35	
Face width (mm)	15 (spur) 20 (helical)		30	
Shaft angle (deg)	0		90	
Addendum (mm)	4	4	6.068	2.432
Dedendum (mm)	5	5	3.432	7.068
Backlash (mm)	0.1		0.1	

4.2 Spur and spiral-bevel gear system

4.2.a) *Dynamic behaviour*

For this application, the first reduction stage of the system is a spur gear. A constant input torque of 400 N.m is applied on the pinion shaft and the input speed is varied from 1 to 27 000 rpm. The time-signal and spectrum of the dynamic transmission errors of both stages are computed for each rotational speed.

The critical frequencies / critical speeds correspondence is well illustrated by the Campbell diagram in Figure IV-39: at 13 000 rpm, the spur gear mesh frequency f_{m1} matches the most critical frequency associated with this mesh (5656 Hz, $\rho^{(I)} = 58\%$) which leads to a major peak in the transmission error shape factor curve. The same observation can be made for the spiral-bevel gear (Figure IV-40) whose mesh frequency f_{m2} coincides with the most

critical frequency for this stage around 18 000 rpm thus generating the largest amplitude of transmission error shape factor.

Figure IV-39 Figure IV-40 reveal that the spectral content of the local dynamic transmission error at each gear stage is dominated by its own mesh frequency. It must be noted that a very small percentage of modal strain energy ($\rho^{(II)} = 3\%$) is stored in the spiral-bevel gear mesh at 5656 Hz (major tooth critical frequency for stage 1). Conversely, at 3833 Hz (major critical frequency for stage 2), only 2% of modal strain energy is stored in the spur gear mesh. Except a slight influence of the spiral-bevel gear on stage 1 (see Figure IV-39), both meshes are almost perfectly decoupled from a dynamic viewpoint.

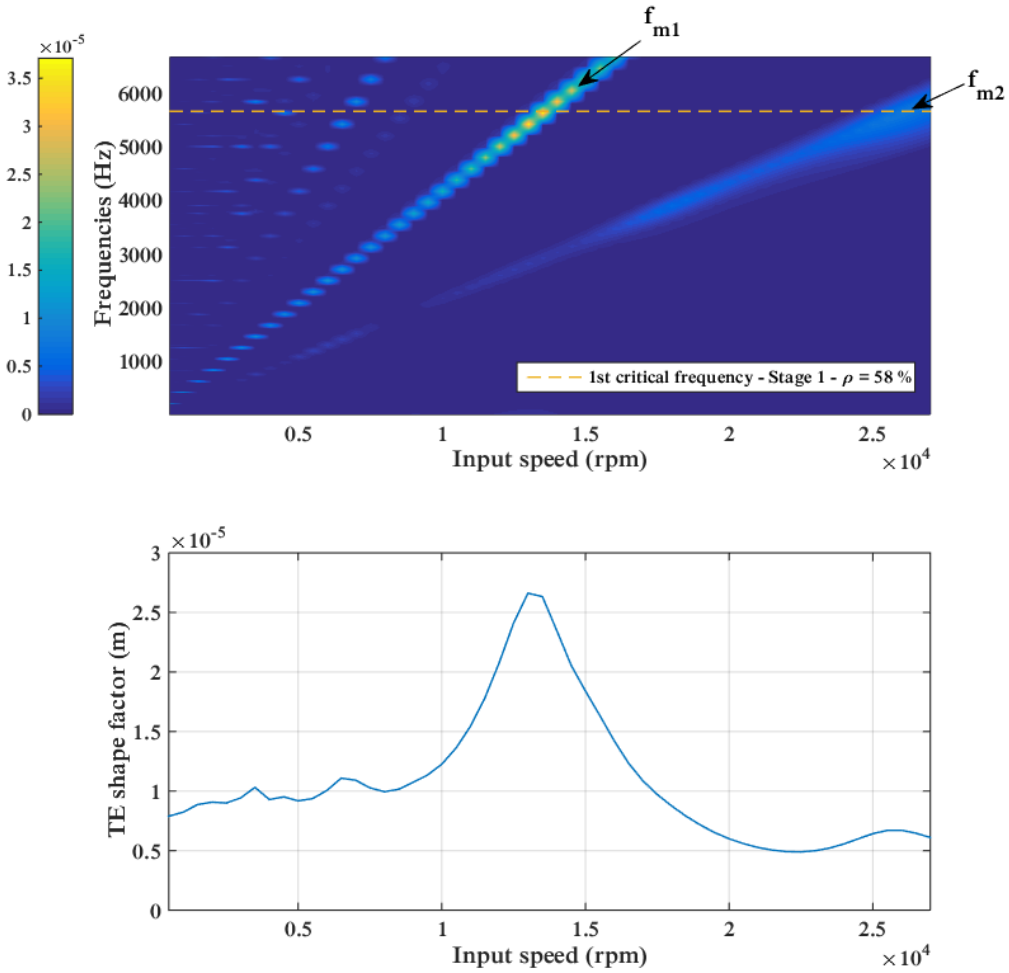

Figure IV-39 : Spur and spiral-bevel gear system – Stage 1 – Spectral content of the dynamic transmission error (Amplitude in m)

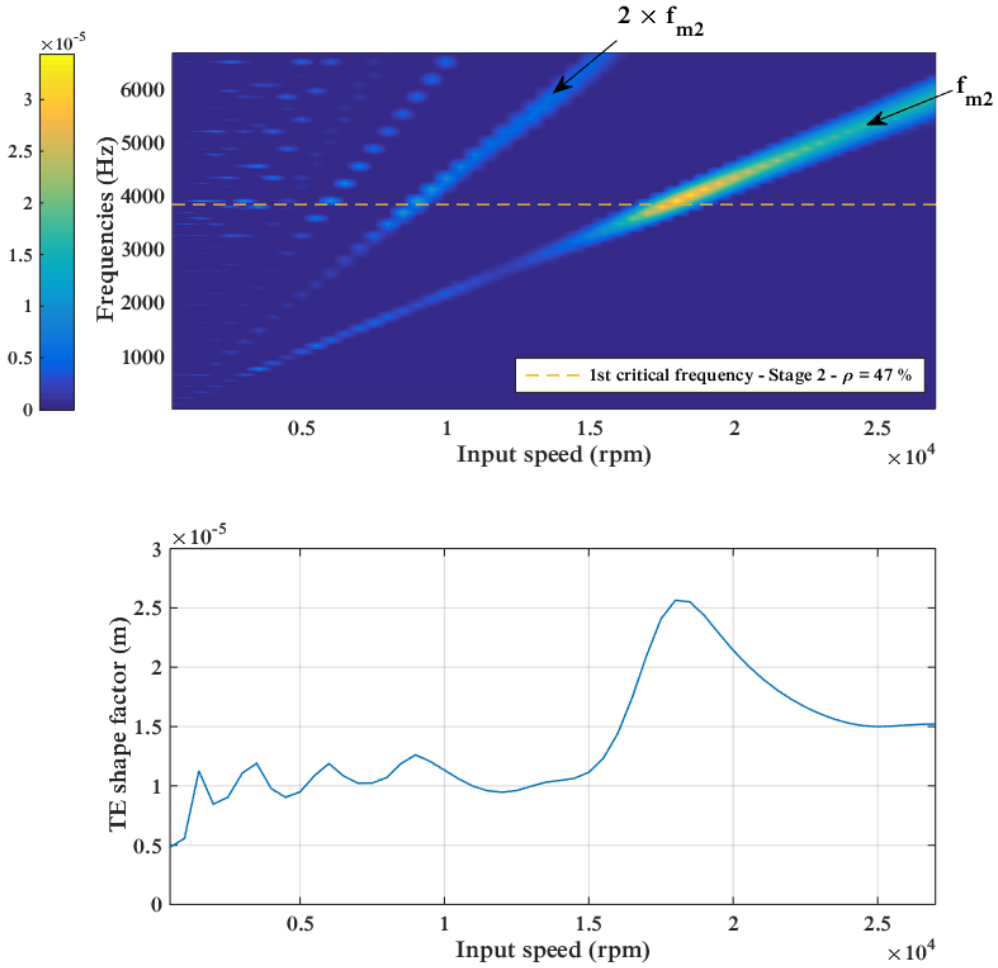

Figure IV-40 : Spur and spiral-bevel gear system – Stage 2 – Spectral content of the dynamic transmission error (Amplitude in m)

4.2.b) *Influence of the intermediate shaft on dynamic couplings*

The length of the intermediate shaft is then reduced to 50 mm in order to study the evolution of the coupling phenomena between both meshes.

In this configuration, the most critical mode for the spur gear ($\rho^{(I)} = 31\%$) also induces a significant level of modal strain energy stored in the spiral-bevel gear ($\rho^{(II)} = 19\%$). This stronger interaction is also visible in the dynamic transmission error spectrum of the spur gear (Figure IV-41) where components at the spiral-bevel gear mesh frequency emerge thus generating an additional critical speed around 22 000 rpm.

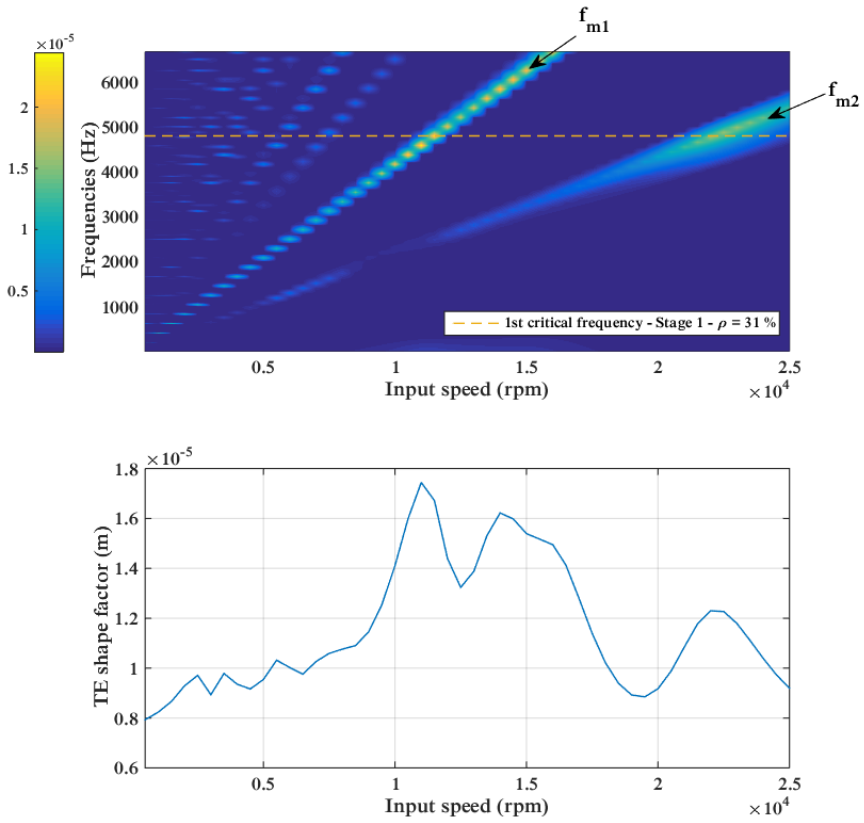

Figure IV-41 : Spur and spiral-bevel gear system – Intermediate shaft of reduced length – Stage 1 – Spectral content of the dynamic transmission error (Amplitude in m)

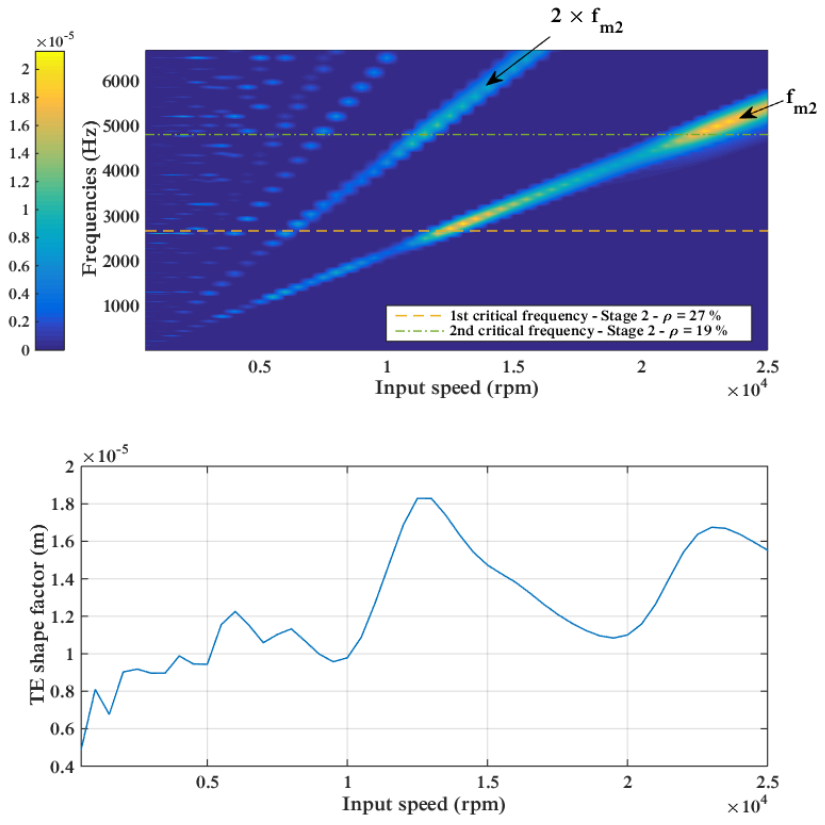

Figure IV-42 : Spur and spiral-bevel gear system – Intermediate shaft of reduced length – Stage 2 – Spectral content of the dynamic transmission error (Amplitude in m)

4.2.c) *Influence of load*

The dynamic response of the system with a 150 mm-long intermediate shaft presented in **Section 4.2.a)** of this chapter is now calculated under an input torque of 80 N.m. The evolution of the mesh force dynamic factor is compared to that obtained under an input torque of 400 N.m in order to evaluate the influence of external loading.

The results in Figure IV-43 for the cylindrical gear of stage 1 and in Figure IV-44 for the spiral-bevel gear (stage 2) show that the load has nearly no influence on the spur gear whereas significant changes are observed in the dynamic response of the spiral-bevel gear.

These observations are directly correlated to the influence of load on the quasi-static behaviour of each gear:

- The length of contact of spur gears and the associated mesh excitations are not really sensitive to load so that the fluctuations of the quasi-static transmission error at 80 and 400 N.m are similar.
- The average mesh stiffness of the spur gear is also independent of the input torque.
- Concerning the spiral-bevel gear however, the pressure distribution is significantly affected by the input load. As a consequence, the average value of the mesh stiffness decreases with decreasing load, justifying that the major critical speed is lower at 80 N.m than at 400 N.m.
- Besides, the peak-to-peak of quasi-static transmission error is higher at 400 N.m than at 80 N.m. This is why amplifications of the mesh force dynamic factor are more marked under a higher load.

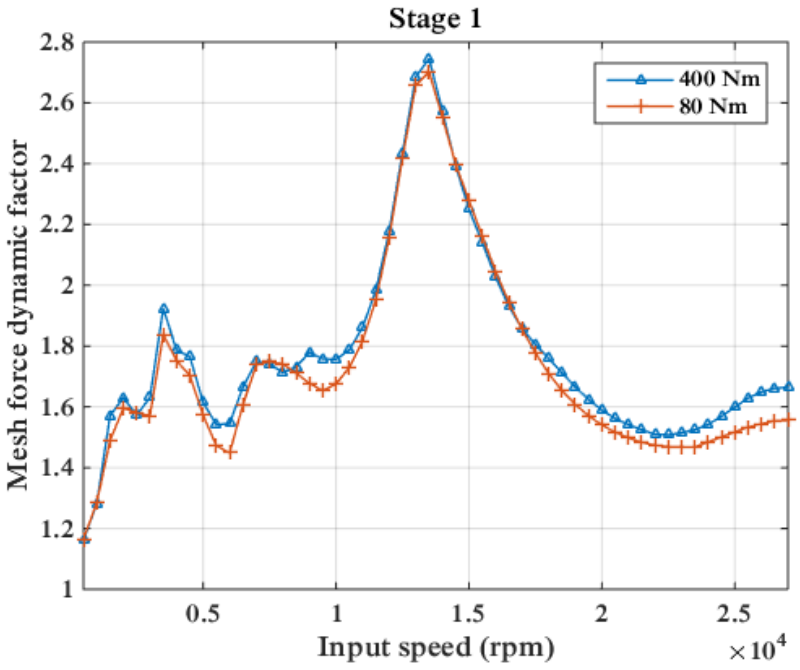

Figure IV-43 : Spur and spiral-bevel gear system – Influence of load – Stage 1

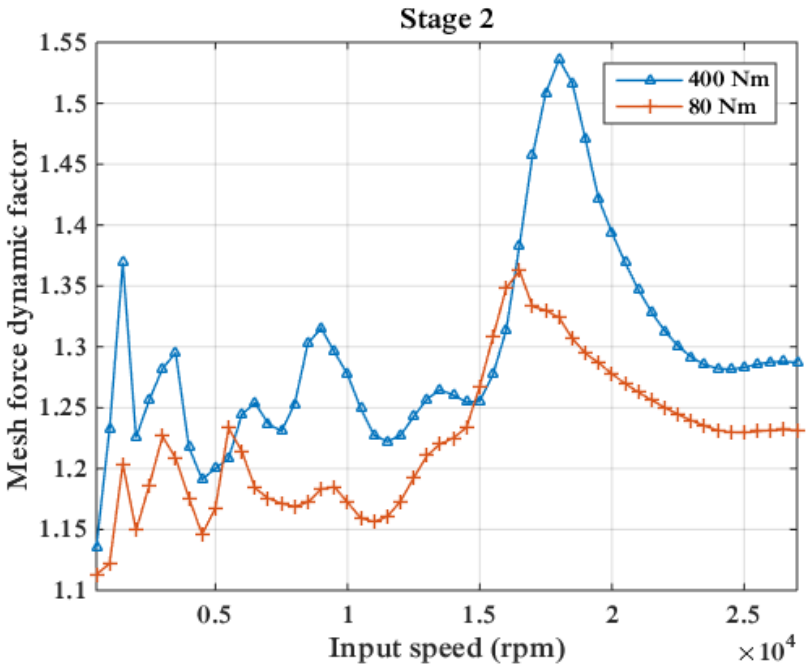

Figure IV-44 : Spur and spiral-bevel gear system – Influence of load – Stage 2

4.3 Helical and spiral-bevel gear system

The spur gear in the previous section is replaced by a helical gear whose date are listed in Table IV-2.

4.3.a) *Gear dynamic behaviour*

As for the previous application, the helical gear and the spiral-bevel pinion are connected by a 150 mm-long shaft. The pinion torque is 400 N.m and the input speed ranges from 1 to 33 000 rpm. A significant influence of the spiral-bevel gear on the helical stage can be seen in Figure IV-45. A major critical speed is observed when the mesh frequency of the spiral-bevel gear coincides with the major tooth frequency for stage 1, around 31 000 rpm. However, Figure IV-46 shows that the helical gear has no influence on the spectral content of the dynamic transmission error of stage 2.

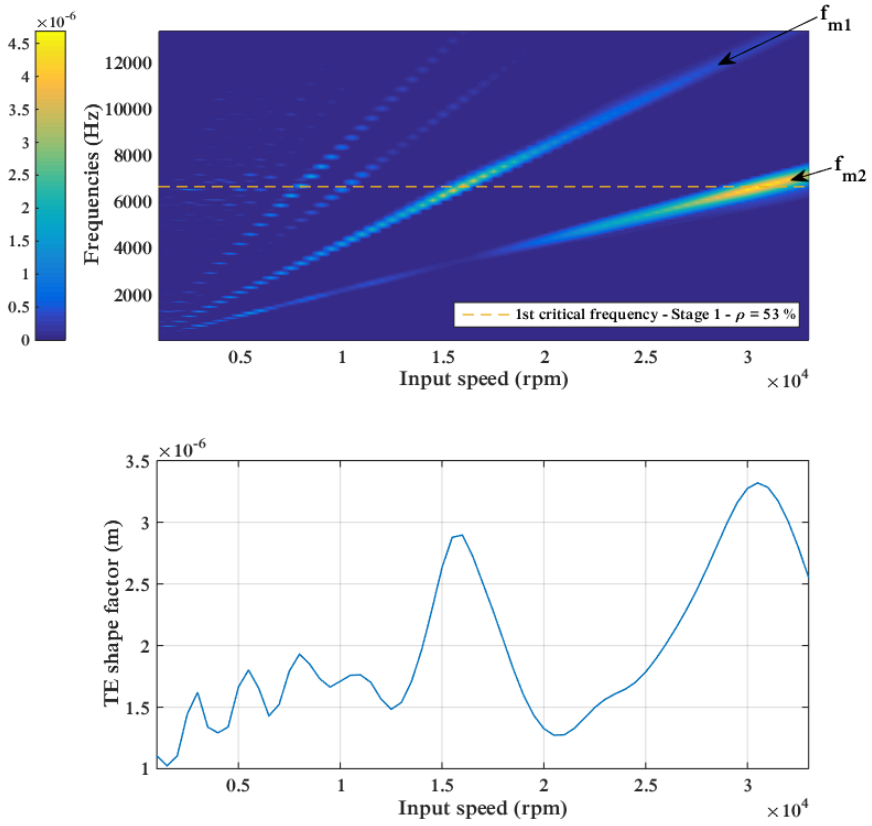

Figure IV-45 : Helical and spiral-bevel gear system – Stage 1 – Spectral content of the dynamic transmission error (Amplitude in m)

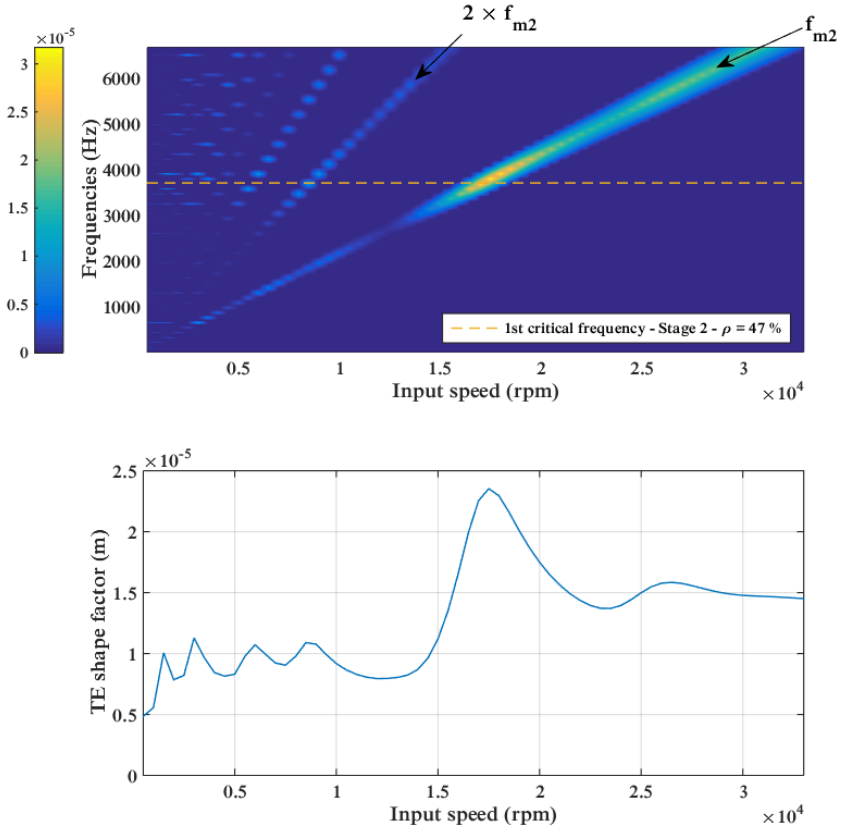

Figure IV-46 : Helical and spiral-bevel gear system – Stage 2 – Spectral content of the dynamic transmission error (Amplitude in m)

4.3.b) *Influence of the intermediate shaft*

Contrary to the spur and spiral-bevel gear system, a strong coupling therefore occurs between both meshes, even when they are located 150 mm apart, suggesting that this coupling is mainly due to axial displacements. Given that the axial stiffness of the intermediate shaft is only slightly influenced by its length, a new geometry is introduced in which the helical gear shaft and the spiral-bevel pinion shaft are connected by an elastic coupling (characteristics in Table IV-3). An illustration of this system is shown in Figure IV-47.

Table IV-3 : Helical and spiral-bevel gear system – Elastic coupling characteristics

	Stiffness
Axial (N/m)	10^6
Radial(N/m)	10^7
Torsional (N.m/rad)	10^4
Bending (N.m/rad)	10^3

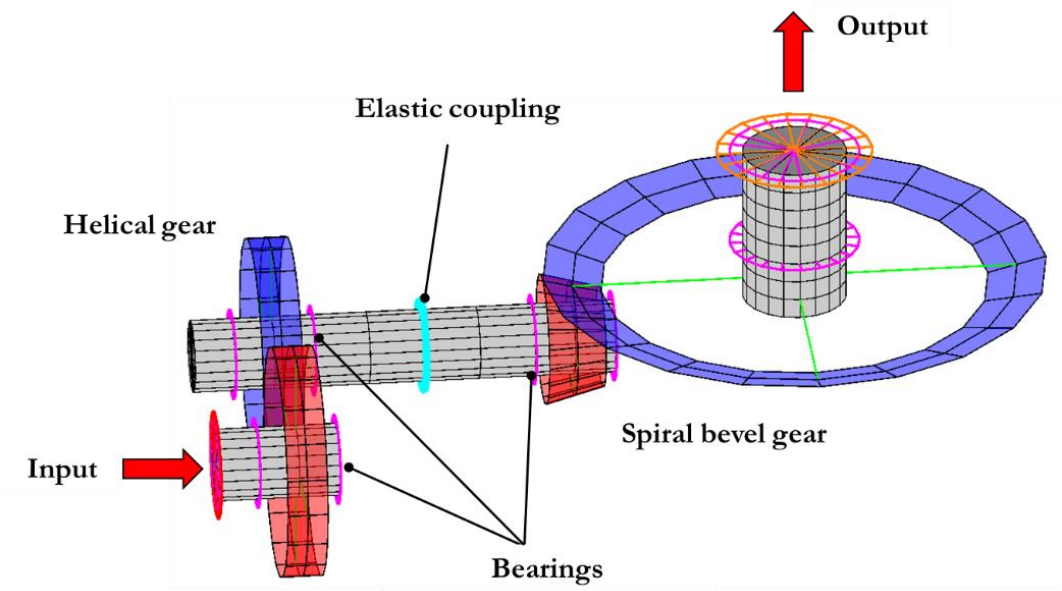

Figure IV-47 : Helical and spiral-bevel gear system – Finite element model of the system with elastic coupling

The corresponding results are shown in Figure IV-48 and Figure IV-49 for stage 1 and stage 2, respectively. Comparing Figure IV-45 and Figure IV-48, one can notice that the introduction of the elastic coupling between the helical and the spiral-bevel gears cancels the influence of the spiral-bevel gear on the helical one to a large extent. With the elastic coupling, both gears are decoupled from a dynamic point of view and the spectral content of each gear dynamic transmission error is dominated by its own mesh frequency.

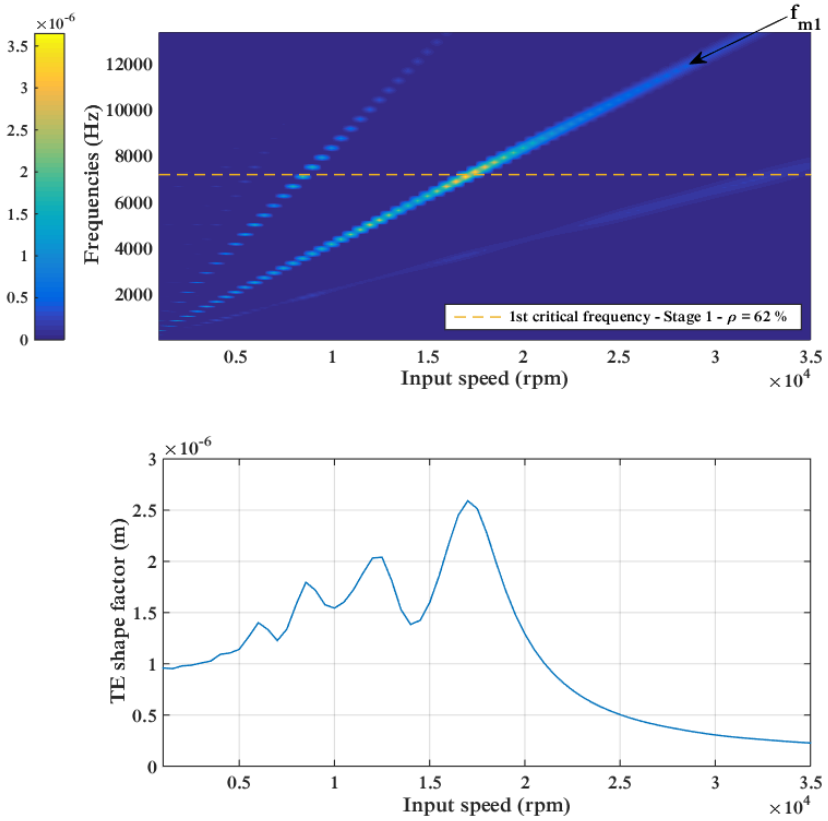

Figure IV-48 : Helical and spiral-bevel gear system with elastic coupling – Stage 1 – Spectral content of the dynamic transmission error (Amplitude in m)

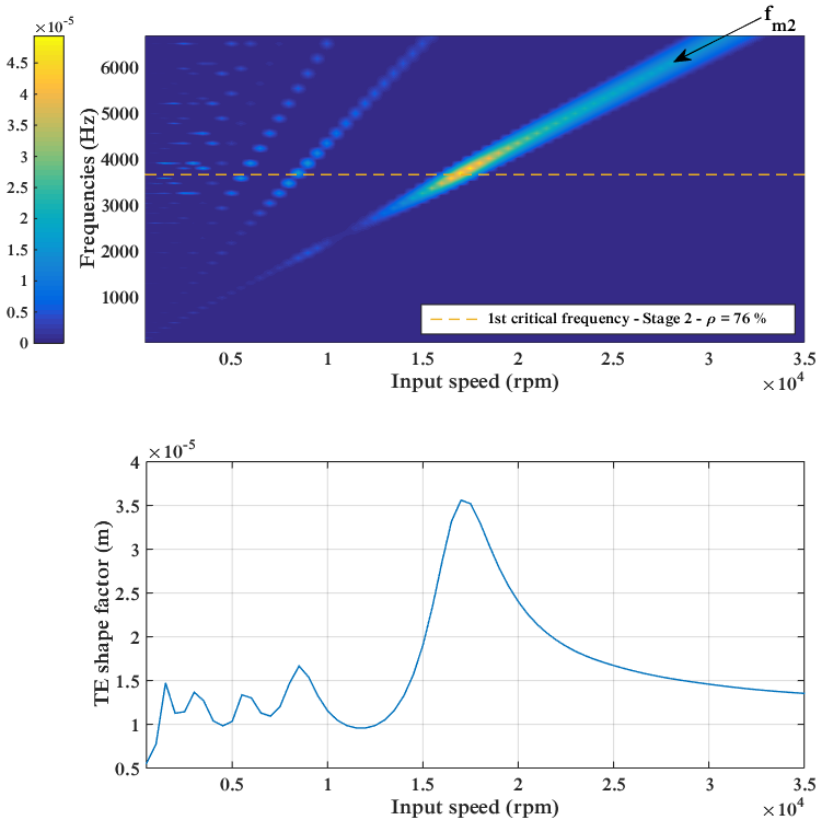

Figure IV-49 : Helical and spiral-bevel gear system with elastic coupling – Stage 2 – Spectral content of the dynamic transmission error (Amplitude in m)

4.3.c) *Bearing response*

This section is devoted to the analysis of the bearing dynamic forces in the two configurations studied previously (without and with an intermediate elastic coupling). The objective is to evaluate how couplings may affect the dynamic response at the bearings. The bearing elements labelling is shown in Figure IV-50.

Figure IV-51 to Figure IV-53 show the spectral content of the dynamic forces on bearings 2, 5 and 6 respectively. In each figure, the top image shows the results obtained for the system with continuous intermediate shaft, configuration for which a strong dynamic coupling was observed between the two gear meshes. The image at the bottom shows the spectral content obtained for the configuration with elastic coupling (Figure IV-47).

A strong influence of the spiral-bevel gear on the bearing dynamic forces can be observed in Figure IV-51 and Figure IV-52 for the case with continuous intermediate shaft. This observation shows that the excitations produced at the spiral-bevel mesh propagate through the intermediate shaft to the helical pinion shaft (bearing 2). For both bearings, this influence is significantly reduced with the introduction of an elastic coupling separating the two stages. Besides, one can notice a non-negligible reduction in dynamic force amplitudes, for all frequencies.

The dynamic forces spectrum for bearing 6 is dominated by the mesh frequency of the spiral-bevel gear and the presence of the elastic coupling brings no substantial changes although the dynamic forces are slightly attenuated (Figure IV-53).

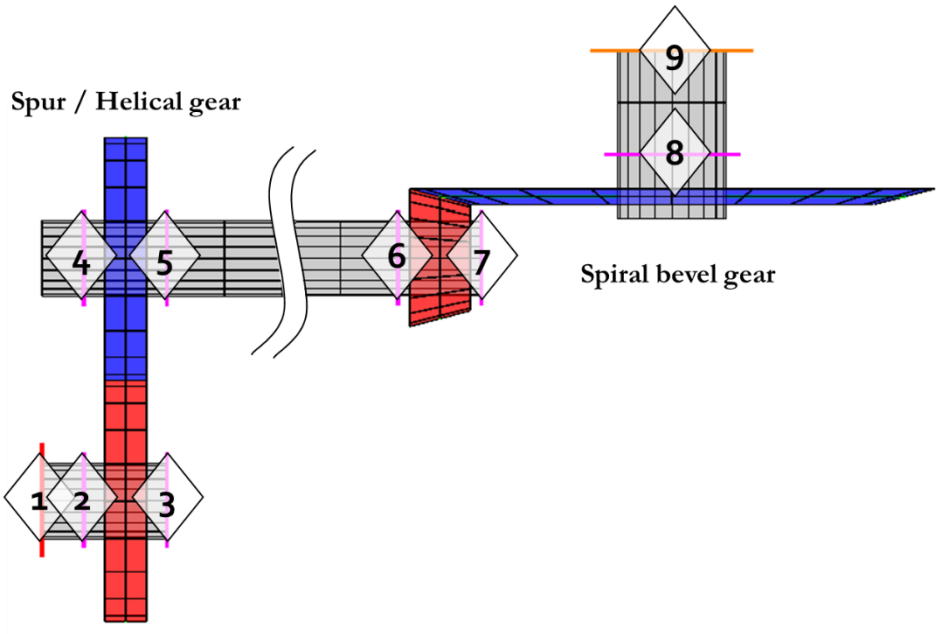

Figure IV-50 : Helical and spiral-bevel gear system – Bearing elements numbering

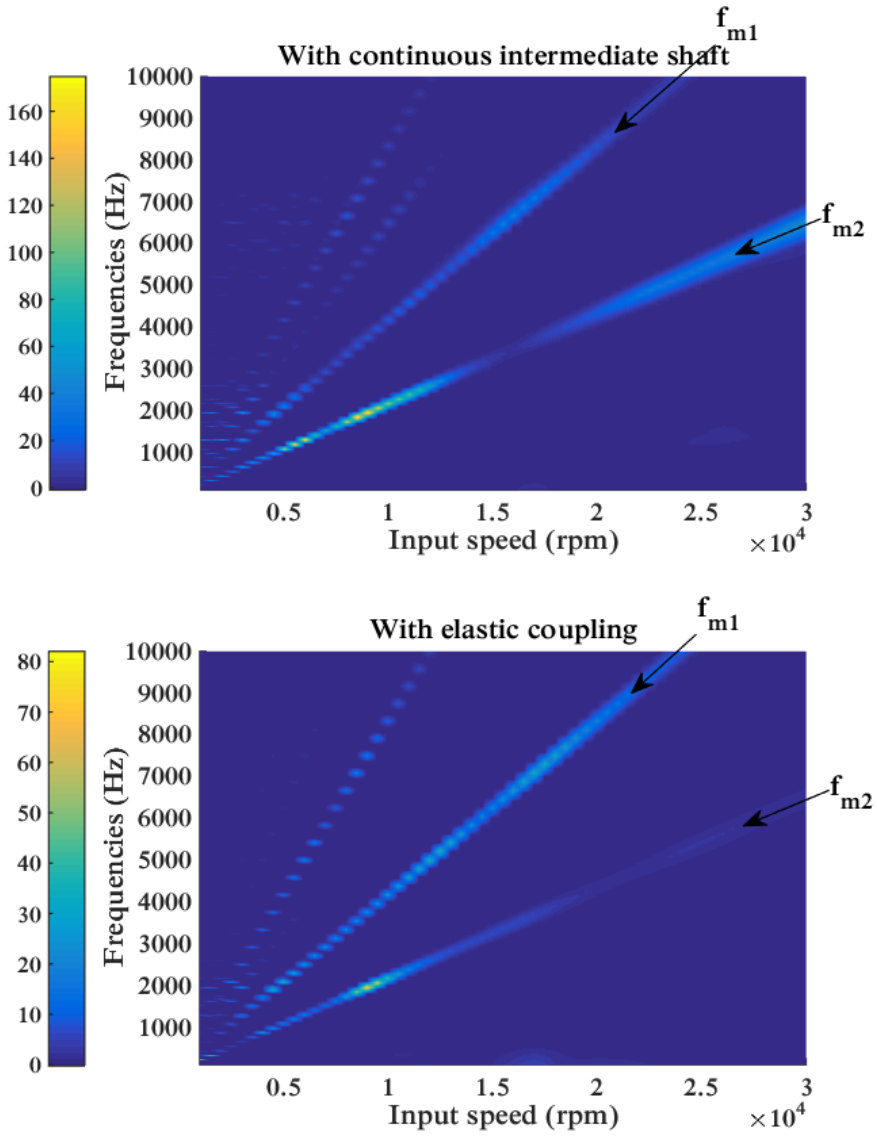

Figure IV-51 : Helical and spiral-bevel gear system – Bearing 2 – Influence of the intermediate shaft on the bearing dynamic forces (Amplitude in N)

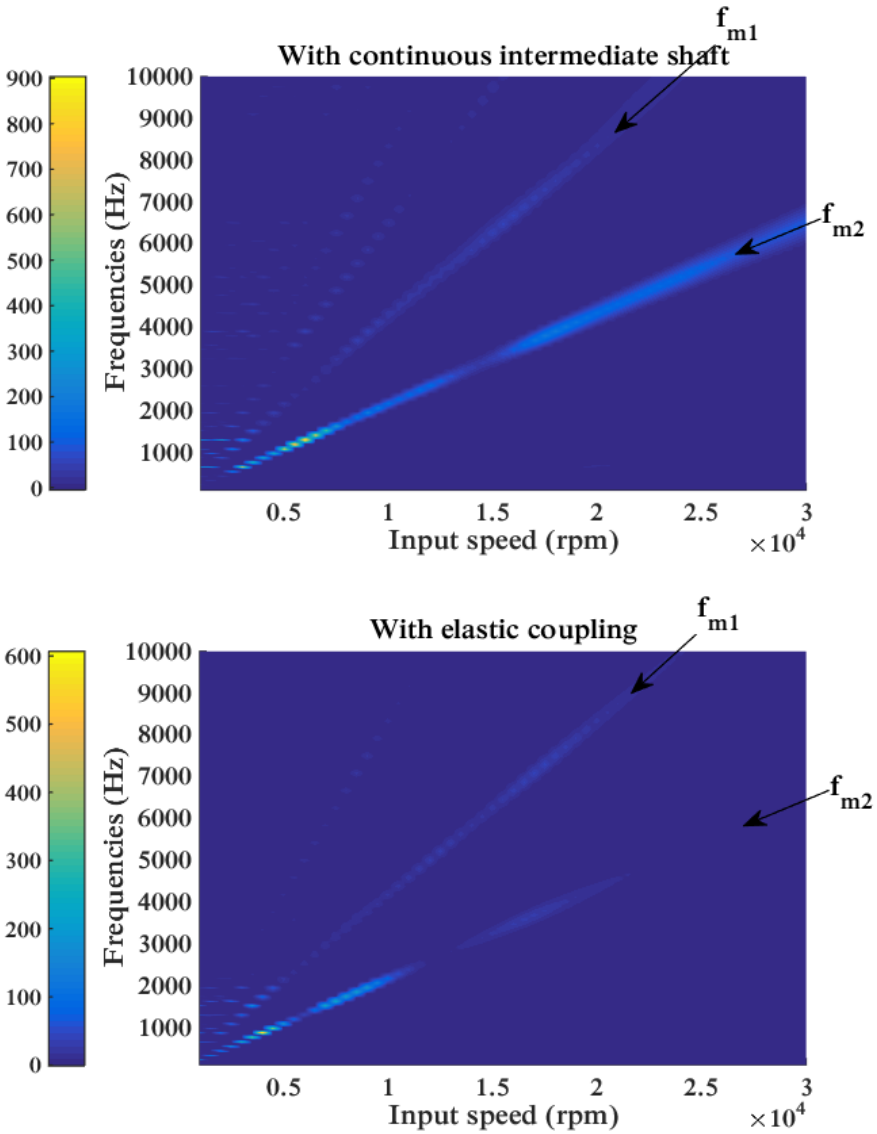

Figure IV-52 : Helical and spiral-bevel gear system – Bearing 5 – Influence of the intermediate shaft on the bearing dynamic forces (Amplitude in N)

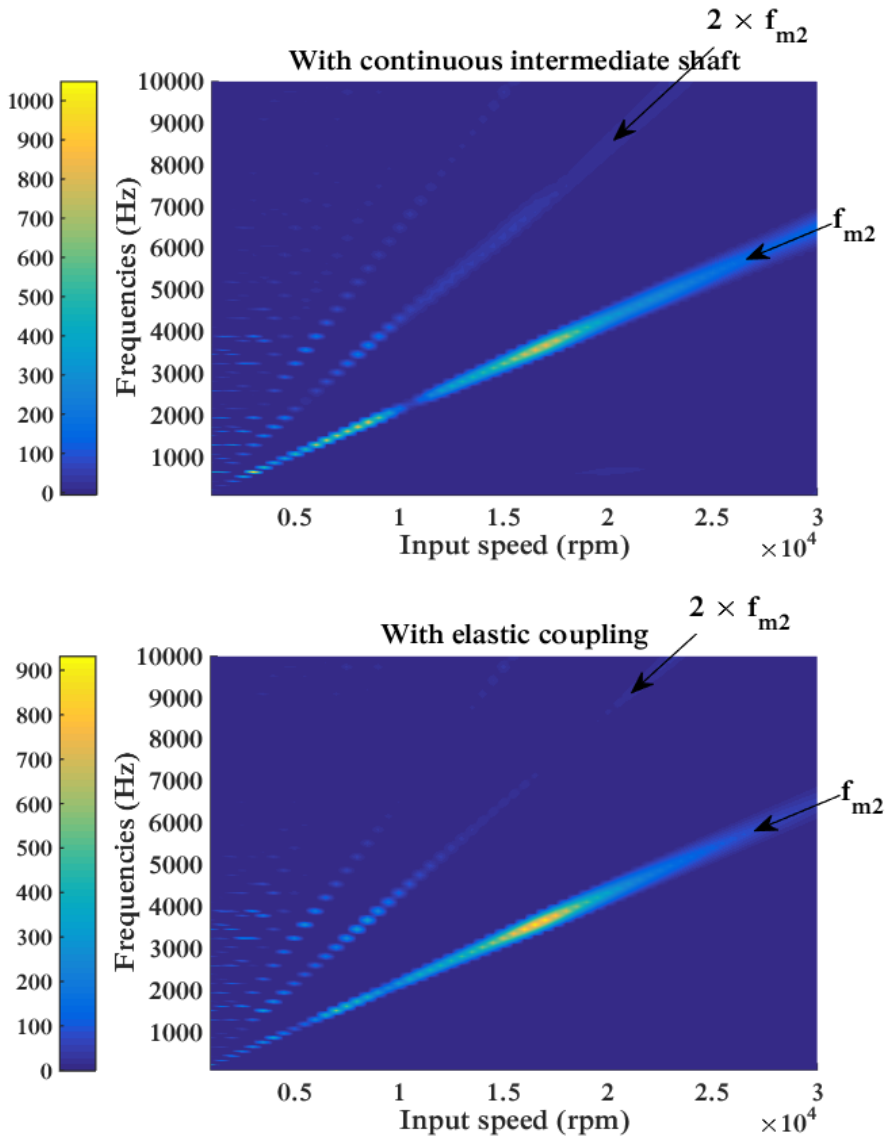

Figure IV-53 : Helical and spiral-bevel gear system – Bearing 6 – Influence of the intermediate shaft on the bearing dynamic forces (Amplitude in N)

5 CONCLUSION

This chapter has presented several applications of the transmission error-based model to the study of the dynamic behaviour of single- and double-stage gear systems with cylindrical and spiral-bevel gears.

It is observed that pitch errors can significantly modify the spectral content of the global mesh force and introduce some scatter around the no-error solution. However, they do not alter the positions of the major tooth critical speeds and their influence on the dynamic response tends to decrease with increasing loads.

Several authors have published analytical, numerical and experimental results supporting the idea that a linear relationship between dynamic transmission error and dynamic mesh force or dynamic bending stress could exist [51,61,62]. The extensive simulation results in this chapter confirm the existence of such a linear relationship but mostly for spur and helical gear systems which can effectively be described by torsional models. An influence of speed has also been reported with contrasted behaviour at medium and higher speeds which could be related to the passage of secondary tooth critical frequencies. It is therefore postulated that dynamic tooth loading and transmission errors might be connected to some extent but in a more complex way than that suggested in [51,61].

Two configurations of double-stage spur gear systems have been studied: a) a double-stage system with intermediate shaft and, b) a system with an idler gear. For each configuration, the analysis of the dynamic bearing response highlights the simultaneous influence of both gear stages and shows that profile modifications can reduce dynamic bearing force amplitudes. Two different phase shift configurations are studied on the idler gear system. It is shown that profile modifications can reduce dynamic mesh forces regardless of mesh phasing. The phase shift only influences the maximum vibration level of each gear and energy transfer between the two meshes is observed.

Finally, some original applications to cylindrical / spiral-bevel gear systems are proposed which lead to the following conclusions:

- Strong couplings occur between the cylindrical and spiral-bevel gears, modifying the spectral content of local dynamic transmission errors.
- In particular, the spiral-bevel gear influences the dynamic behaviour of the cylindrical gear stage (either spur or helical).
- Coupling intensity depends on the stiffness of the connection between the two meshes.
- For the spur / spiral-bevel gear configuration, a longer intermediate shaft may be sufficient to decouple the gear meshes.
- For the helical / spiral-bevel gear system, axial couplings seem prominent and the length of the intermediate shaft has therefore little effect. However, the introduction of an intermediate elastic coupling between the helical gear and the spiral-bevel pinion can isolate the two mesh excitations.
- The dynamic response at the bearings is also affected by the different meshes of the system. Specifically, the influence of the spiral-bevel gear is visible on the response of the bearings located on the helical pinion shaft.

- Decoupling both gear stages from a dynamic point of view allows to reduce the dynamic bearing forces fluctuations. Considering that these fluctuations are the main source of excitation of the gearbox casing, this result can be of great interest for gearbox noise reduction.

GENERAL CONCLUSION

The results presented in this memoir mainly deal with the numerical simulation of gear dynamics in the context of helicopter main gearboxes.

Gears have been long recognized as significant sources of noise and vibrations which have been widely studied particularly in the field of transport. In the vast majority of these studies, gear mesh excitations stem from a) tooth deflections under load and, b) shape deviations along with mounting errors which are often combined via the notions of mesh stiffness functions and transmission errors. Many dynamic models can be found in the literature mostly for single mesh systems which can hardly be extended to multi-stage gears with strong couplings as is the case in helicopter transmissions. Moreover, most of the research is focused on parallel axis systems and more work is certainly needed in the area of bevel gears.

In order to be able to simulate a helicopter main gearbox comprising spur, helical and spiral bevel gears, a unified theoretical framework is proposed which makes it possible to account for various gear geometries in a systematic way. The methodology relies on quasi-static results aimed at characterizing mesh excitations prior to solving the equations of motion. Gears are supposed to be rigid bodies connected by lumped stiffness elements and it is assumed that the contact conditions in dynamic and quasi-static conditions are the same. The supporting elements such as shafts and bearings are also integrated. The resulting state equations point to a linear second order differential system with time-varying stiffness matrices and forcing terms expressed in terms of transmission errors. Using a time-step integration scheme, dynamic mesh and bearing forces can be determined and used as input data for further noise analyses.

The validity of the model is assessed by comparisons with experimental evidence and benchmark numerical results from the literature. Starting with a single mesh spur gear set, a good agreement is reported except in the vicinity of tooth critical speeds with tooth contact losses and shocks, thus highlighting one of the limitations of the proposed approach which is essentially linear. However, this behaviour is rarely observed in heavily loaded helical gear sets and does not actually reduce the interest of transmission error based models in the present industrial context. A complete single mesh spur and helical gear test rig is then simulated over a broad range of speeds. For each configuration, the theoretical and experimental dimensionless root stress signals agree well proving that the theory is sound for gears with profile modifications. Considering a spiral bevel gear, the predicted transmission errors are close to what is found by combining a normal contact algorithm and the solution of the equations of motion. Comparisons are finally extended to double mesh spur gear systems with various arrangements (idler gear or two pinions on the same intermediate shaft). It can therefore be concluded that the proposed formulation can be applied to a variety of gear geometries and is adapted to the problem of helicopter main gearbox dynamic simulations.

Chapter IV is devoted to a number of applications of the modelling technique. First, the combined influence of pitch errors and load on dynamic tooth loads is analysed based on the single mesh test rig geometry previously used for validation purposes. It is observed that pitch errors strongly modify response spectra but have no influence on tooth critical speeds thus explaining why errorless models can correlate well with experimental findings as far as mesh forces are concerned. It is also shown that pitch errors contribute less at higher loads.

Using the same theoretical background, the relationship between dynamic transmission errors and dynamic tooth loads is then studied. Several authors have suggested that a linear dependency could be found between these two parameters and proposed formulae to determine tooth mesh forces from transmission error measurements and therefore avoid slip rings or telemetry to transfer signals from the rotary to the stationary systems. Massive runs have been performed which reveal that a linear relationship can exist but only when shaft bending and bearing displacements can be neglected, in line with some previous theoretical developments implying that direct transpositions from transmission error to mesh or tooth force signals need to be critically examined and cannot be generalized.

The dynamic bearing response is analysed in a double mesh system and the combined contributions of the two meshes is highlighted proving that mesh-by-mesh analyses should be employed with care. It is verified that profile modifications can reduce dynamic tooth loads and bearing forces which seems interesting in the context of structure borne noise reduction.

Finally, in order to reproduce a part of a helicopter transmission, a system comprising a spur/helical gear and a bevel gear is considered. Particular emphasis is placed on inter-mesh couplings and their consequences on bearing dynamic forces. A strong influence of the bevel gear on the rest of the system is reported and the interest of elastic couplings between the two reduction stages is discussed.

Although the proposed transmission error based model has been proved effective in simulating single and multi-mesh gears, a number of limitations have been identified which certainly require more attention and further research. First of all, the planetary systems usually used as the final reduction stage in helicopter transmissions have not been incorporated. It has been recently demonstrated that the concept of transmission error remains valid for such systems and can be used to minimize dynamic mesh forces [45,149], suggesting that dynamic models based on transmission errors can be constructed. The influence of tooth friction has been neglected but some studies show that, in some particular cases, the reversal of sliding and friction on tooth profiles can generate vibrations and noise [150]. The damping mechanism in gears are complex and certainly deserve more attention as they largely control the amplifications at critical speeds and corresponding noise levels (Ankouni *et al.* [151]). The bearing models used in this memoir are simplified and it would interesting to introduce more realistic representations including the influence of the time-varying number of loaded rolling elements which lead to parametric excitations possibly influential on casing vibrations and noise [77,78,152,153]. More effort should also be put in the simulation of thin-rimmed gears which are common in aeronautical applications and can hardly be accounted for by lumped parameter elements such as those used in this work [154,155].

REFERENCES

[1] Padmanabhan, C., Rook, T., and Singh, R., 1995, "Modeling of automotive gear rattle phenomenon: state of the art," SAE Technical Paper 951316.

[2] Lim, T. C., and Singh, R., 1989, "A Review of Gear Housing and Acoustics Literature Dynamics," The Ohio State University.

[3] Roulois, G., 2011, "Etude et simulation du bruit des transmissions principales d'hélicoptères," PhD Thesis, Université de Bourgogne.

[4] Caillet, J., and Malburet, F., 2006, "Diagnostic, analyse et modélisation du bruit et des chemins de bruit dans une cabine d'hélicoptère," Mécanique & Industries, **7**(5–6), pp. 437–444.

[5] Roulois, G., Skladanek, Y., Marrot, F., and Caillet, J., 2014, "Dynamic and acoustic simulation of helicopters drive trains," Proceedings of the International Gear Conference, Lyon, France, pp. 437–446.

[6] Coy, J., Handschuh, R., and Lewicki, D., 1987, "Identification and proposed control of helicopter transmission noise at the source," Flight Dynamics and Control and Acoustics, pp. 1045–1065.

[7] Tuplin, W. A., 1950, "Gear-tooth Stresses at High Speed," Proceedings of the Institution of Mechanical Engineers, **162**, pp. 162–167.

[8] Strauch, H., 1953, "Zahnradschwingungen," Zeitschrift des Vereins Deutscher Ingenieure, **95**, pp. 159–163.

[9] Gregory, R., Harris, S., and Munro, R., 1963, "Dynamic behaviour of spur gears," Proceedings of the Institution of Mechanical Engineers, **178**(8), pp. 207–218.

[10] Weber, C., and Banaschek, K., 1953, "Formänderung und Profilrücknahme bei gerad- und schrägverzahnten Rädern," Schriftenreihe Antriebstechnik, **11**.

[11] Attia, A. Y., 1964, "Deflection of spur gear teeth cut in thin rims," Journal of Engineering for Industry, **86**(4), pp. 333–341.

[12] Lin, H., and Liou, C., 1998, "A parametric study of spur gear dynamics," Memphis University, TN, USA.

[13] Umezawa, K., 1972, "The Meshing Test on Helical Gears under Load Transmission," Bulletin of the JSME, **15**(90), pp. 1632–1639.

[14] Yakubek, D., 1984, "Plate Bending and Finite Element Analysis of Spur and Helical Gear Tooth Deflections," MSc Thesis, The Ohio State University.

[15] Sainsot, P., Velex, P., and Duverger, O., 2004, "Contribution of Gear Body to Tooth Deflections—A New Bidimensional Analytical Formula," Journal of Mechanical Design, **126**(4), p. 748.

[16] Stegemiller, M., and Houser, D., 1993, "A three-dimensional analysis of the base flexibility of gear teeth," Journal of Mechanical Design, **115**, pp. 186–192.

[17] Lundberg, G., 1939, "Elastische Berührung zwei Halbräume," Forschung im Ingenieurwesens, **10**(5), pp. 201–211.

[18] Ajmi, M., and Velex, P., 2005, "A model for simulating the quasi-static and dynamic behaviour of solid wide-faced spur and helical gears," Mechanism and Machine Theory, **40**(2), pp. 173–190.

[19] Velex, P., 1997, Détermination de la rigidité d'engrènement - Synthèse bibliographique - Comparaisons, CETIM Technical Report.

[20] Cardou, A., and Tordion, G., 1985, "Calculation of spur gear tooth flexibility by the complex potential method," Gear Technology, (September/October), pp. 9–14.

[21] Wang, J., and Howard, I., 2004, "The torsional stiffness of involute spur gears," Journal of Mechanical Engineering Science, **218**, pp. 131–142.

[22] Vijayakar, S., 1991, "A combined surface integral and finite element solution for a three dimensional contact problem," International Journal for Numerical Methods in Engineering, **31**(1991), pp. 525–545.

[23] Vijayakar, S., and Houser, D. R., 1993, "Contact analysis of gears using a combined finite element and surface integral method," Gear Technology, pp. 26–33.

[24] Maatar, M., and Velex, P., 1996, "An Analytical Expression for the Time-Varying Contact Length in Perfect Cylindrical Gears: Some Possible Applications in Gear Dynamics," Journal of Mechanical Design, **118**(December), pp. 586–589.

[25] AFNOR, 2002, "Calculation of load capacity of spur and helical gears - Part 1: Basic principles, introduction and general influence factors," ISO6336-1 (E).

[26] Gu, X., Velex, P., Sainsot, P., and Bruyère, J., 2015, "Analytical investigations on the mesh stiffness function of solid narrow faced spur and helical gears," Proceedings of the ASME IDETC/CIE 2015, Boston, MA, USA, pp. 1–8.

[27] Stadtfeld, H., and Saewe, J., 2015, "Non-Involute Gearing, Function and Manufacturing Compared to Established Gear Designs," Gear Technology, (February), pp. 42–51.

[28] Henriot, G., 2002, "Engrenages parallèles - Étude géométrique," Techniques de l'ingénieur. Génie Mécanique.

[29] AFNOR, 2013, "Cylindrical gears - Definitions and allowable values of deviations relevant to corresponding flanks of gear teeth," ISO 1328-1.

[30] ANSI/AGMA, 2015, "Accuracy Classification System -Tangential Measurements for Cylindrical Gears," 2015-1-A01.

[31] Jelaska, D., 2012, Gears and gear drives, John Wiley & Sons Ltd.

[32] Oswald, F., and Townsend, D., 1995, "Influence of tooth profile modification on spur gear dynamic tooth strain," Proceedings of the 31st Joint Propulsion Conference and Exhibit, San Diego, CA, USA.

[33] Harris, S., 1958, "Dynamic loads on the teeth of spur gears," Proceedings of the Institution of Mechanical Engineers, **172**, pp. 87–112.

[34] Munro, R., 1989, "The DC component of gear transmission error," Proceedings of the International Power Transmission and Gearing Conference, Chicago, Illinois, pp. 467–470.

[35] Houser, D., Oswald, F., and Valco, M., 1994, "Comparison of transmission error predictions with noise measurements for several spur and helical gears," 30th AIAA/ASME/SAE/ASEE Joint Propulsion Conf., Indianapolis.

[36] Lin, H., Oswald, F., and Townsend, D., 1994, "Dynamic Loading of Spur Gears With Linear or Parabolic Tooth Profile Modifications," Mechanism and Machine Theory, **29**(8), pp. 1115–1129.

[37] Beghini, M., Presicce, F., and Santus, C., 2004, A method to define profile modification of spur gear and minimize the transmission error, AGMA Technical Report.

[38] Bonori, G., Barbieri, M., and Pellicano, F., 2008, "Optimum profile modifications of spur gears by means of genetic algorithms," Journal of Sound and Vibration, **313**(3–5), pp. 603–616.

[39] Artoni, A., Kolivand, M., and Kahraman, A., 2010, "An Ease-Off Based Optimization of the Loaded Transmission Error of Hypoid Gears," Journal of Mechanical Design, **132**(1), pp. 1–9.

[40] Mermoz, E., Astoul, J., Sartor, M., Linares, J. M., and Bernard, A., 2013, "A new methodology to optimize spiral bevel gear topography," CIRP Annals - Manufacturing Technology, **62**, pp. 119–122.

[41] Astoul, J., Mermoz, E., Sartor, M., Linares, J. M., and Bernard, A., 2014, "New methodology to reduce the transmission error of the spiral bevel gears," CIRP Annals - Manufacturing Technology, **63**, pp. 165–168.

[42] Velex, P., Bruyère, J., and Houser, D. R., 2011, "Some Analytical Results on Transmission Errors in Narrow-Faced Spur and Helical Gears: Influence of Profile Modifications," Journal of Mechanical Design, **133**(March 2011), pp. 1–11.

[43] Bruyère, J., and Velex, P., 2013, "Derivation of Optimum Profile Modifications in Narrow-Faced Spur and Helical Gears Using a Perturbation Method," Journal of Mechanical Design, **135**(7), pp. 1–8.

[44] Bruyère, J., Gu, X., and Velex, P., 2015, "On the analytical definition of profile modifications minimising transmission error variations in narrow-faced spur helical gears," Mechanism and Machine Theory, **92**, pp. 257–272.

[45] Velex, P., Chapron, M., Fakhfakh, H., Bruyère, J., and Becquerelle, S., 2016, "On transmission errors and profile modifications minimising dynamic tooth loads in multi-mesh gears," Journal of Sound and Vibration, **379**, pp. 28–52.

[46] Blankenship, G., and Kahraman, A., 1995, "Steady state forced response of a mechanical oscillator with combined parametric excitation and clearance type non-linearity," Journal of Sound and Vibration, **185**(5), pp. 743–765.

[47] Kang, M. R., and Kahraman, A., 2012, "Measurement of vibratory motions of gears supported by compliant shafts," Mechanical Systems and Signal Processing, **29**, pp. 391–403.

[48] Gregory, R. W., Harris, S. L., and Munro, R. G., 1963, "A method of measuring transmission error in spur gears of 1:1 ratio," Journal of Scientific Instruments, **40**(1), pp. 5–9.

[49] Remond, D., 1999, "Practical performances of high-speed measurement of gear transmission error or torsional vibrations with optical encoders," Measurement Science and Technology, **9**(3), pp. 347–353.

[50] Gosselin, C., Guertin, T., Remond, D., and Jeans, Y., 2000, "Simulation and experimental measurement of the transmission error of real hypoid gears under load," Journal of Mechanical Design, **122**(March 2000), pp. 109–122.

[51] Tamminana, V. K., Kahraman, A., and Vijayakar, S., 2007, "A Study of the Relationship Between the Dynamic Factors and the Dynamic Transmission Error of Spur Gear Pairs," Journal of Mechanical Design, **129**(1), pp. 75–84.

[52] Ding, H., and Kahraman, A., 2007, "Interactions between nonlinear spur gear dynamics and surface wear," Journal of Sound and Vibration, **307**(3–5), pp. 662–679.

[53] Wang, K., 1976, "Thermal elastohydrodynamic lubrication of spur gears," PhD Thesis, Northwestern University.

[54] Li, S., and Kahraman, A., 2011, "A Method to Derive Friction and Rolling Power Loss Formulae for Mixed Elastohydrodynamic Lubrication," Journal of Advanced Mechanical Design, Systems, and Manufacturing, **5**(4), pp. 252–263.

[55] Osman, T., and Velex, P., 2010, "Static and dynamic simulations of mild abrasive wear in wide-faced solid spur and helical gears," Mechanism and Machine Theory, **45**(6), pp. 911–924.

[56] Osman, T., and Velex, P., 2012, "A model for the simulation of the interactions between dynamic tooth loads and contact fatigue in spur gears," Tribology International, **46**(1), pp. 84–96.

[57] Kubo, A., Yamada, K., Aida, T., and Sato, S., 1972, "Research on ultra high speed gear devices," Bulletin of the JSME, **38**, pp. 2692–2715.

[58] Ozguven, H., and Houser, D. R., 1988, "Dynamic analysis of high speed gears by using loaded static transmission error," Journal of Sound and Vibration, **125**(1), pp. 71–83.

[59] Kahraman, A., and Singh, R., 1990, "Non-linear dynamics of a spur gear pair," Journal of Sound and Vibration, **142**(1), pp. 49–75.

[60] Velex, P., and Maatar, M., 1996, "A mathematical model for analyzing the influence of shape deviations and mounting errors on gear dynamic behaviour," Journal of Sound and Vibration, **191**(5), pp. 629–660.

[61] Hotait, M. A., and Kahraman, A., 2013, "Experiments on the relationship between the dynamic transmission error and the dynamic stress factor of spur gear pairs," Mechanism and Machine Theory, **70**, pp. 116–128.

[62] Velex, P., 2009, "On the relationship between gear dynamics and transmission errors," JSME 2009 International Motion and Power Transmission Conference, Sendaï, Japan.

[63] Dai, X., Cooley, C. G., and Parker, R. G., 2016, "Dynamic tooth root strains and experimental correlations in spur gear pairs," Mechanism and Machine Theory, **101**, pp. 60–74.

[64] Sainte-Marie, N., Velex, P., Roulois, G., and Caillet, J., 2017, "A Study on the Correlation Between Dynamic Transmission Error and Dynamic Tooth Loads in Spur and Helical Gears," Journal of Vibration and Acoustics, **139**(February), pp. 1–10.

[65] Ozguven, H., and Houser, D., 1988, "Mathematical models used in gear dynamics - A review," Journal of Sound and Vibration, **121**, pp. 383–411.

[66] Blankenship, G., and Singh, R., 1992, "A comparative study of selected gear mesh interface dynamic models," International Power Transmission and Gearing Conference, Phoenix, pp. 137–146.

[67] Johnson, D., 1958, "Excitation of resonant vibrations by gear teeth meshing effects," Proceedings of the International Conference on Gearing, Institution of Mechanical Engineers, London, UK, pp. 18–23.

[68] Kohler, H., 1959, "The mechanism and measurement of dynamic loading in spur gears," PhD Thesis, University of Sheffield.

[69] Wood, B., 1959, "Sources of vibration excitation in spur gears," PhD Thesis, University of Leeds.

[70] Parker, R. G., Vijayakar, S., and Imajo, T., 2000, "Non-linear dynamic response of a spur gear pair - Modelling and experimental comparisons," Journal of Sound and Vibration, **237**(3), pp. 435–455.

[71] Kohler, H., Pratt, A., and Thompson, A., 1970, "Dynamics and Noise of Parallel-Axis

Gearing," Proceedings of the Institution of Mechanical Engineers, **184**, pp. 111–121.

[72] Fukuma, H., Furukawa, T., and Aida, T., 1973, "Fundamental Research on Gear Noise and Vibration," Bulletin of the JSME, **16**, pp. 1094–1107.

[73] Kahraman, A., Ozguven, H. N., Houser, D. R., and Zakrajsek, J. ., 1992, "Dynamic Analysis of Geared Rotors by Finite Elements," Journal of Mechanical Design, **114**(3), pp. 507–514.

[74] Baud, S., and Velex, P., 2002, "Static and Dynamic Tooth Loading in Spur and Helical Geared Systems-Experiments and Model Validation," Journal of Mechanical Design, **124**(2), pp. 334–346.

[75] Eritenel, T., and Parker, R. G., 2012, "An investigation of tooth mesh nonlinearity and partial contact loss in gear pairs using a lumped-parameter model," Mechanism and Machine Theory, **56**, pp. 28–51.

[76] Eritenel, T., and Parker, R. G., 2012, "Three-dimensional nonlinear vibration of gear pairs," Journal of Sound and Vibration, **331**(15), pp. 3628–3648.

[77] Lim, T., and Singh, R., 1990, "Vibration transmission through rolling element bearings, part ii: system studies," Journal of sound and vibration, **139**(2), pp. 201–225.

[78] Lim, T., and Singh, R., 1991, "Vibration transmission through rolling element bearings. part iii: Geared rotor system studies," Journal of sound and vibration, **151**(1), pp. 31–54.

[79] Rigaud, E., and Sabot, J., 1996, "Effect of elasticity of shafts, bearings, casing and couplings on the critical rotational speeds of a gearbox," VDI Berichte, pp. 833–845.

[80] Rigaud, E., Sabot, J., and Perret-Liaudet, J., 1999, "Effect of Gearbox Design Parameters on the Vibratory Response of its Housing," 4th World Congress on Gearing and Power Transmission, Paris, pp. 2143–2148.

[81] Abbes, M. S., 2005, "Gearbox vibratory analysis using carrying, coupling and slave substructures," International Journal of Simulation Modelling, **4**(2), pp. 67–75.

[82] Abbes, M. S., Fakhfakh, T., Haddar, M., and Maalej, A., 2006, "Effect of transmission error on the dynamic behaviour of gearbox housing," The International Journal of Advanced Manufacturing Technology, **34**(3–4), pp. 211–218.

[83] Abbes, M., Bouaziz, S., Chaari, F., Maatar, M., and Haddar, M., 2008, "An acoustic–structural interaction modelling for the evaluation of a gearbox-radiated noise," International Journal of Mechanical Sciences, **50**, pp. 569–577.

[84] Zhou, J., Sun, W., and Tao, Q., 2014, "Gearbox Low-Noise Design Method Based on Panel Acoustic Contribution," Mathematical Problems in Engineering, **2014**, pp. 1–10.

[85] Guo, Y., Eritenel, T., Ericson, T. M., and Parker, R. G., 2014, "Vibro-acoustic propagation of gear dynamics in a gear-bearing-housing system," Journal of Sound and Vibration, **333**(22), pp. 5762–5785.

[86] Gosselin, C., Cloutier, L., and Nguyen, Q., 1995, "A general formulation for the calculation of the load sharing and transmission error under load of spiral bevel and hypoid gears," Mechanism and Machine Theory, **30**(3), pp. 433–450.

[87] Vogel, O., Griewank, A., and Bär, G., 2002, "Direct gear tooth contact analysis for hypoid bevel gears," Computer methods in applied mechanics and engineering, **191**, pp. 3965–3982.

[88] Simon, V., 2007, "Computer simulation of tooth contact analysis of mismatched spiral bevel gears," Mechanism and Machine Theory, **42**(3), pp. 365–381.

[89] Kolivand, M., and Kahraman, A., 2009, "A load distribution model for hypoid gears

using ease-off topography and shell theory," Mechanism and Machine Theory, **44**(10), pp. 1848–1865.

[90] Lim, T., and Cheng, Y., 1999, "A theoretical study of the effect of pinion offset on the dynamics of hypoid geared rotor system," Journal of Mechanical Design, **121**(December), pp. 594–601.

[91] Cheng, Y., and Lim, T. C., 2001, "Vibration Analysis of Hypoid Transmissions Applying an Exact Geometry-Based Gear Mesh Theory," Journal of Sound and Vibration, **240**(3), pp. 519–543.

[92] Cheng, Y., and Lim, T. C., 2003, "Dynamics of Hypoid Gear Transmission With Nonlinear Time-Varying Mesh Characteristics," Journal of Mechanical Design, **125**(2), p. 373.

[93] Wang, J., Lim, T. C., and Li, M., 2007, "Dynamics of a hypoid gear pair considering the effects of time-varying mesh parameters and backlash nonlinearity," Journal of Sound and Vibration, **308**, pp. 302–329.

[94] Wang, J., and Lim, T. C., 2009, "Effect of tooth mesh stiffness asymmetric nonlinearity for drive and coast sides on hypoid gear dynamics," Journal of Sound and Vibration, **319**, pp. 885–903.

[95] Li, M., Hu, H. Y., Jiang, P. L., and Yu, L., 2002, "Coupled Axial–Lateral–Torsional Dynamics of a Rotor–Bearing System Geared By Spur Bevel Gears," Journal of Sound and Vibration, **254**(3), pp. 427–446.

[96] Li, M., and Hu, H. Y., 2003, "Dynamic Analysis of a Spiral Bevel-Geared Rotor-Bearing System," Journal of Sound and Vibration, **259**(3), pp. 605–624.

[97] Gao, Q., Tanabe, M., and Nishihara, K., 2009, "Contact-impact analysis of geared rotor systems," Journal of Sound and Vibration, **319**(1–2), pp. 463–475.

[98] Peng, T., 2010, "Coupled multi-body dynamic and vibration analysis of hypoid and bevel geared rotor system," PhD Thesis, University of Cincinnati.

[99] Hua, X., 2010, "Hypoid and Spiral Bevel Gear Dynamics with Emphasis on Gear-Shaft-Bearing Structural Analysis," MSc Thesis, University of Cincinnati.

[100] Lim, T., and Singh, R., 1990, "Vibration transmission through rolling element bearings, part I: bearing stiffness formulation," Journal of sound and vibration, **139**(2), pp. 179–199.

[101] Teixeira Alves, J., Wang, J., Guingand, M., de Vaujany, J. P., and Velex, P., 2012, "Static and Dynamic Models for Spiral Bevel Gears," Mechanics & Industry, **13**(5), pp. 325–335.

[102] Wang, J., 2014, "Contribution à l'analyse du comportement dynamique d'engrenages spiro-coniques," PhD Thesis, INSA Lyon.

[103] Wang, Y., 2013, "Torque Load Effect on Multi-Point Mesh and Dynamics of Right-angle Geared Drives," MSc Thesis, University of Cincinnati.

[104] Yang, J., Wang, W., Guo, D., and Lim, T. C., 2014, "Comparative analysis of the hypoid geared rotor system dynamics applying dissimilar tooth meshing formulations," International Gear Conference, Lyon, France, pp. 763–773.

[105] Song, C., Zhu, C., Liu, H., and Ni, G., 2015, "Dynamic analysis and experimental study of a marine gearbox with crossed beveloid gears," Mechanism and Machine Theory, **92**, pp. 17–28.

[106] Wang, Y., Yang, J., Guo, D., and Lim, T. C., 2016, "Vibration and sound radiation analysis of the final drive assembly considering the gear-shaft coupling dynamics,"

Journal of Mechanical Engineering Science, **230**(7–8), pp. 1258–1275.

[107] Umezawa, K., Ajima, T., and Houjoh, H., 1986, "Vibration of three axes gear system," Bulletin of JSME, **29**(249), pp. 950–957.

[108] Iida, H., Tamura, A., and Yamamoto, H., 1986, "Dynamic characteristics of a gear train system with softly supported shafts," Bulletin of JSME, **29**(252), pp. 1811–1816.

[109] Choy, F., Tu, Y., Savage, M., and Townsend, D., 1991, "Vibration signature and modal analysis of multi-stage gear transmission," Journal of the Franklin Institute, **328**(2–3), pp. 281–298.

[110] Choy, F., and Tu, Y., 1991, "Effects of gear box vibration and mass imbalance on the dynamics of multistage gear transmission," Journal of Vibration and Acoustics, **113**(3), pp. 333–344.

[111] Kahraman, A., 1994, "Dynamic analysis of a multi-mesh helical gear train," Journal of Mechanical Design, **116**(3), pp. 706–712.

[112] Vinayak, H., Singh, R., and Padmanabhan, C., 1995, "Linear dynamic analysis of multi-mesh transmissions containing external, rigid gears," Journal of Sound and Vibration, **185**(1), pp. 1–32.

[113] Vinayak, H., and Singh, R., 1998, "Multi-body dynamics and modal analysis of compliant gear bodies," Journal of Sound and Vibration, **210**(2), pp. 171–214.

[114] Raclot, J., and Velex, P., 1999, "Simulation of the dynamic behaviour of single and multi-stage geared systems with shape deviations and mounting errors by using a spectral method," Journal of sound and vibration, **220**, pp. 861–903.

[115] Kubur, M., Kahraman, A., Zini, D. M., and Kienzle, K., 2004, "Dynamic Analysis of a Multi-Shaft Helical Gear Transmission by Finite Elements: Model and Experiment," Journal of Vibration and Acoustics, **126**(3), pp. 398–406.

[116] Al-shyyab, A., and Kahraman, A., 2005, "Non-linear dynamic analysis of a multi-mesh gear train using multi-term harmonic balance method: period-one motions," Journal of Sound and Vibration, **284**(1–2), pp. 151–172.

[117] Al-shyyab, A., and Kahraman, A., 2005, "Non-linear dynamic analysis of a multi-mesh gear train using multi-term harmonic balance method: sub-harmonic motions," Journal of Sound and Vibration, **279**(1–2), pp. 417–451.

[118] Liu, G., and Parker, R. G., 2007, "Nonlinear dynamics of idler gear systems," Nonlinear Dynamics, **53**(4), pp. 345–367.

[119] Liu, G., and Parker, R. G., 2008, "Dynamic Modeling and Analysis of Tooth Profile Modification for Multimesh Gear Vibration," Journal of Mechanical Design, **130**(12), p. 121402.

[120] Liu, G., and Parker, R. G., 2012, "Nonlinear, parametrically excited dynamics of two-stage spur gear trains with mesh stiffness fluctuation," Journal of Mechanical Engineering Science, **226**(8), pp. 1939–1957.

[121] Walha, L., Fakhfakh, T., and Haddar, M., 2009, "Nonlinear dynamics of a two-stage gear system with mesh stiffness fluctuation, bearing flexibility and backlash," Mechanism and Machine Theory, **44**(5), pp. 1058–1069.

[122] Fakhfakh, H., Bruyère, J., Velex, P., and Becquerelle, S., 2014, "Simulation of the Dynamic Behavior of a Multi-stage Geared Systems with Tooth Shape Deviations and External Excitations," Proceedings of the Multiphysics Modelling and Simulation for Systems Design Conference, Sousse, Tunisia, pp. 369–378.

[123] Fakhfakh, H., Bruyère, J., Velex, P., and Becquerelle, S., 2014, "A torsional dynamic model of multi-stage geared systems submitted to internal and external excitations," International Gear Conference, Lyon, France, pp. 576–585.

[124] Terauchi, Y., Nadano, H., and Nohara, M., 1982, "On the effect of the tooth profile modification on the dynamic load and the sound level of the spur gear," Bulletin of JSME, **25**(207), pp. 1474–1481.

[125] Perret-liaudet, J., Carbonelli, A., Rigaud, E., Nelain, B., Bouvet, P., and Vialonga, C. J., 2014, "Modeling of Gearbox Whining Noise," SAE Technical Paper 2014-01-2090.

[126] Remond, D., Velex, P., and Sabot, J., 1993, Comportement dynamique et acoustique des transmissions par engrenages, Publication du CETIM.

[127] Greenhill, L., Bickford, W., and Nelson, H., 1985, "A conical beam finite element for rotor dynamics analysis," Journal of Vibration, Acoustics, Stress, and Reliability in Design, **107**, pp. 421–430.

[128] Cowper, G., 1966, "The shear coefficient in Timoshenko's beam theory," Journal of applied mechanics, **6**(4), pp. 335–340.

[129] Velex, P., and Ajmi, M., 2006, "On the modelling of excitations in geared systems by transmission errors," Journal of Sound and Vibration, **290**, pp. 882–909.

[130] Velex, P., 2001, "Some problems in the modelling of gear dynamic behaviour," The JSME International Conference on Motion and Power Transmissions, Fukuoka, Japan, pp. 45–50.

[131] GearLab, 2002, "User's manual for Load Distribution Program."

[132] Stegemiller, M., 1986, "The effects of base flexibility on thick beams and plates used in gear tooth deflection models," MSc Thesis, The Ohio State University.

[133] Weber, C., 1949, The deformation of loaded gears and the effect on their load-carrying capacity.

[134] de Vaujany, J.-P., Guingand, M., Remond, D., and Icard, Y., 2007, "Numerical and Experimental Study of the Loaded Transmission Error of a Spiral Bevel Gear," Journal of Mechanical Design, **129**(2), p. 195.

[135] Teixeira Alves, J., Guingand, M., and de Vaujany, J.-P., 2010, "Set of functions for the calculation of bending displacements for spiral bevel gear teeth," Mechanism and Machine Theory, **45**(2), pp. 349–363.

[136] Perret-Liaudet, J., 1996, "An original method for computing the response of a parametrically excited forced system," Journal of Sound and Vibration, **196**, pp. 165–177.

[137] Frêne, J., 2004, "Butées et paliers hydrodynamiques," Techniques de l'ingénieur, article B5320, pp. 1–38.

[138] Handschuh, R. F., and Bibel, G. D., 1999, "Experimental and Analytical Study of Aeroespace Spiral Bevel Gear Tooth Fillet Stresses," Journal of Mechanical Design, Transactions of the ASME, **121**(4), pp. 565–572.

[139] Hotait, M. A., Kahraman, A., and Nishino, T., 2011, "An Investigation of Root Stresses of Hypoid Gears with Misalignments," Journal of Mechanical Design, **133**(7), pp. 1–9.

[140] Simon, V., 2007, "Load Distribution in Spiral Bevel Gears," Journal of Mechanical Design, **129**(2), pp. 201–209.

[141] Simon, V., 2008, "Influence of tooth errors and misalignments on tooth contact in spiral bevel gears," Mechanism and Machine Theory, **43**(10), pp. 1253–1267.

[142] Handschuh, M. J., Kahraman, A., and Milliren, M. R., 2014, "Impact of Tooth Spacing Errors on the Root Stresses of Spur Gear Pairs," Journal of Mechanical Design, **136**(June), pp. 1–10.

[143] Milliren, M. R., 2011, "An experimental investigation into the influence of various errors on the transmission error and root stresses of spur gears," MSc Thesis, The Ohio State University.

[144] Handschuh, M. J., 2013, "An investigation into the impact of random spacing errors on static transmission error and root stresses of spur gear pairs," MSc Thesis, The Ohio State University.

[145] Bonori, G., and Pellicano, F., 2007, "Non-smooth dynamics of spur gears with manufacturing errors," Journal of Sound and Vibration, **306**(1–2), pp. 271–283.

[146] Bihr, J., Heider, M., Otto, M., Stahl, K., Kume, T., Kato, M., Stahl, P. K., Kume, T., and Kato, M., 2014, "Gear noise prediction in automotive transmissions," International Gear Conference 2014, Lyon, France, pp. 457–465.

[147] Inalpolat, M., Handschuh, M., and Kahraman, A., 2015, "Influence of indexing errors on dynamic response of spur gear pairs," Mechanical Systems and Signal Processing, **60–61**, pp. 391–405.

[148] Baud, S., 1998, "Développement et validation sur banc d'essais de modèles du comportement dynamique de réducteurs à engrenages à axes parallèles," PhD Thesis, INSA de Lyon.

[149] Chapron, M., Velex, P., Bruye, J., and Becquerelle, S., 2016, "Optimization of Profile Modifications With Regard to Dynamic Tooth Loads in Single and Double-Helical Planetary Gears With Flexible Ring-Gears," Journal of Mechanical Design, **138**(February), p. 23301.

[150] Velex, P., and Cahouet, V., 2000, "Experimental and numerical investigations on the influence of tooth friction in spur and helical gear dynamics," Journal of Mechanical Design, **122**(December 2000), pp. 515–522.

[151] Ankouni, M., Lubrecht, A. A., and Velex, P., 2016, "Modelling of damping in lubricated line contacts – Applications to spur gear dynamic simulations," Proceedings of the Institution of Mechanical Engineers, Part C: Journal of Mechanical Engineering Science, **230**(7–8), pp. 1222–1232.

[152] Abbes, M. S., Hentati, T., Maatar, M., Fakhfakh, T., and Haddar, M., 2011, "Dynamic analysis of helical gears supported by rolling element bearings," Journal of Theoretical and Applied Mechanics, **41**(1), pp. 33–50.

[153] Fargere, R., and Velex, P., 2013, "Influence of Clearances and Thermal Effects on the Dynamic Behavior of Gear-Hydrodynamic Journal Bearing Systems," Journal of Vibration and Acoustics, **135**(December), pp. 1–16.

[154] Bettaïeb, M. N., Velex, P., and Ajmi, M., 2007, "A Static and Dynamic Model of Geared Transmissions by Combining Substructures and Elastic Foundations—Applications to Thin-Rimmed Gears," Journal of Mechanical Design, **129**(2), pp. 184–194.

[155] Guilbert, B., Velex, P., Dureisseix, D., and Cutuli, P., 2016, "A Mortar-Based Mesh Interface for Hybrid Finite-Element / Lumped-Parameter Gear Dynamic Models — Applications to Thin-Rimmed Geared Systems," Journal of Mechanical Design, **138**(December), pp. 1–11.

ANNEXES

A. SHAFT ELEMENT

The shaft elements rely on Timoshenko's beam theory. Each element comprises two nodes with six degrees-of-freedom per node (three translations and three rotations) and is attributed 12x12 mass, stiffness and damping matrices. This type of element allows to account for traction/compression (u_1, u_2), bending $(v_1, v_2, w_1, w_2, \varphi_1, \varphi_2, \psi_1, \psi_2)$ and torsion (θ_1, θ_2).

In order to reproduce complex geometries of gearbox shafts by a minimum number of degrees-of-freedom, a conical beam finite element has been implemented [127]. Following the works of Cowper [128], shear effects are accounted for by using a shear coefficient K which, for a hollow circular cross-section, reads:

$$K = \frac{6(1+\nu)(1+m^2)^2}{(7+6\nu)(1+m^2)^2 + (20+12\nu)m^2}$$

where ν is Poisson's ratio of the shaft material and m is the ratio of inner to outer radius.

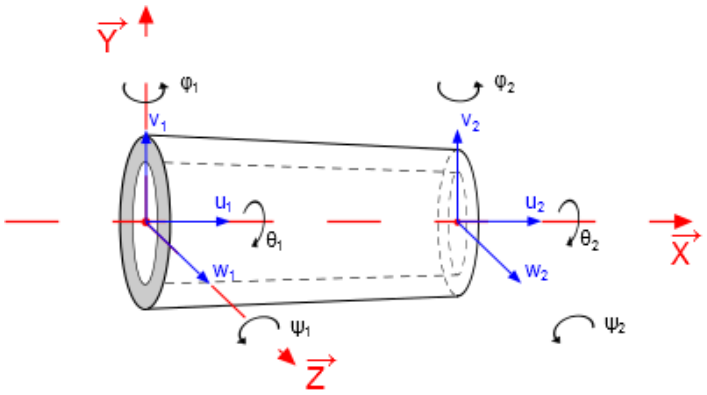

Figure A-1: Conical shaft element – Degrees of freedom and local frame

Average and ratio of the radii:

$$r = \frac{r_1 + r_2}{2} \quad ; \quad R = \frac{R_1 + R_2}{2}$$

$$\gamma = \frac{r_2}{r_1} \quad ; \quad \sigma = \frac{R_2}{R_1}$$

Cross-section areas :

$$A_{i1} = \pi(R_1^2 - r_1^2) \quad ; \quad A_{i2} = \pi(R_2^2 - r_2^2)$$

$$S = \frac{A_{i1} + A_{i2}}{2} \quad ; \quad S_r = K \times S$$

$$\alpha_1 = 2\frac{R_1^2(\sigma-1) - r_1^2(\gamma-1)}{R_1^2 - r_1^2} \quad ; \quad \alpha_2 = \frac{R_1^2(\sigma-1)^2 - r_1^2(\gamma-1)^2}{R_1^2 - r_1^2}$$

Cross-section inertias:

$$I_1 = \pi \frac{R_1^4 - r_1^4}{4} \quad ; \quad I_2 = \pi \frac{R_2^4 - r_2^4}{4}$$
$$J_1 = \pi \frac{R_1^4 - r_1^4}{2} \quad ; \quad J_2 = \pi \frac{R_2^4 - r_2^4}{2}$$

$$\delta_1 = 4\frac{R_1^4(\sigma-1) - r_1^4(\gamma-1)}{R_1^4 - r_1^4} \quad ; \quad \delta_2 = 6\frac{R_1^4(\sigma-1)^2 - r_1^4(\gamma-1)^2}{R_1^4 - r_1^4}$$
$$\delta_3 = 4\frac{R_1^4(\sigma-1)^3 - r_1^4(\gamma-1)^3}{R_1^4 - r_1^4} \quad ; \quad \delta_4 = \frac{R_1^4(\sigma-1)^4 - r_1^4(\gamma-1)^4}{R_1^4 - r_1^4}$$

Shear modulus:

$$G = \frac{E}{2+2v}$$

Shear factor:

$$a = \frac{12E}{G\,Sr\,L^2}\frac{I_1 + I_2}{2}$$

The shaft element includes the effect of shear on flexure stiffness (Timoshenko beam element). The global mass and stiffness matrices can be expressed as:

$$\boldsymbol{K} = \boldsymbol{K}_{ax} + \boldsymbol{K}_{tor} + \boldsymbol{K}_b \quad ; \quad \boldsymbol{M} = \boldsymbol{M}_{ax} + \boldsymbol{M}_{tor} + \boldsymbol{M}_b$$

with:

a) Traction / compression :

$$\boldsymbol{K}_{ax} = \begin{bmatrix} A & -A \\ -A & A \end{bmatrix} \rightarrow \begin{pmatrix} u_1 \\ u_2 \end{pmatrix} \quad ; \quad \boldsymbol{M}_{ax} = \begin{bmatrix} L_1 & L_2 \\ L_2 & L_3 \end{bmatrix} \rightarrow \begin{pmatrix} u_1 \\ u_2 \end{pmatrix}$$

with:

$$A = \frac{EA_{i1}}{6L}(6 + 3\alpha_1 + 2\alpha_2)$$

$$L_1 = \frac{A_{i1}\rho L}{60}(20 + 5\alpha_1 + 2\alpha_2) \; ; \; L_2 = \frac{A_{i1}\rho L}{60}(10 + 5\alpha_1 + 3\alpha_2) \; ; \; L_3 = \frac{A_{i1}\rho L}{60}(20 + 15\alpha_1 + 12\alpha_2)$$

b) Torsion

$$\boldsymbol{K}_{tor} = \begin{bmatrix} B & -B \\ -B & B \end{bmatrix} \rightarrow \begin{pmatrix} \theta_1 \\ \theta_2 \end{pmatrix} \quad ; \quad \boldsymbol{M}_{tor} = \begin{bmatrix} T_1 & T_2 \\ T_2 & T_3 \end{bmatrix} \rightarrow \begin{pmatrix} \theta_1 \\ \theta_2 \end{pmatrix}$$

with:

$$B = \frac{GJ_1}{60L}(60 + 30\delta_1 + 20\delta_2 + 15\delta_3 + 12\delta_4)$$

$$T_1 = \frac{J_1 \rho L}{420}(140 + 35\delta_1 + 14\delta_2 + 7\delta_3 + 4\delta_4) \quad ; \quad T_2 = \frac{J_1 \rho L}{420}(70 + 35\delta_1 + 21\delta_2 + 14\delta_3 + 10\delta_4)$$

$$T_3 = \frac{J_1 \rho L}{420}(140 + 105\delta_1 + 21\delta_2 + 70\delta_3 + 60\delta_4)$$

c) Flexure

$$\boldsymbol{K}_b = \begin{bmatrix} C & 0 & 0 & D & -C & 0 & 0 & -G \\ 0 & C & -D & 0 & 0 & -C & G & 0 \\ 0 & -D & E & 0 & 0 & D & H & 0 \\ D & 0 & 0 & E & -D & 0 & 0 & H \\ -C & 0 & 0 & -D & C & 0 & 0 & G \\ 0 & -C & D & 0 & 0 & C & -G & 0 \\ 0 & G & H & 0 & 0 & -G & F & 0 \\ -G & 0 & 0 & H & G & 0 & 0 & F \end{bmatrix} \rightarrow \begin{pmatrix} v_1 \\ w_1 \\ \varphi_1 \\ \psi_1 \\ v_2 \\ w_2 \\ \varphi_2 \\ \psi_2 \end{pmatrix}$$

$$\boldsymbol{M}_b = \begin{bmatrix} A_1 & 0 & 0 & B_1 & D_1 & 0 & 0 & -E_1 \\ 0 & A_1 & -B_1 & 0 & 0 & D_1 & E_1 & 0 \\ 0 & -B_1 & C_1 & 0 & 0 & -E_2 & F_1 & 0 \\ B_1 & 0 & 0 & C_1 & E_2 & 0 & 0 & F_1 \\ D_1 & 0 & 0 & E_2 & A_2 & 0 & 0 & -B_2 \\ 0 & D_1 & -E_2 & 0 & 0 & A_2 & B_2 & 0 \\ 0 & E_1 & F_1 & 0 & 0 & B_2 & C_2 & 0 \\ -E_1 & 0 & 0 & F_1 & -B_2 & 0 & 0 & C_2 \end{bmatrix} \rightarrow \begin{pmatrix} v_1 \\ w_1 \\ \varphi_1 \\ \psi_1 \\ v_2 \\ w_2 \\ \varphi_2 \\ \psi_2 \end{pmatrix}$$

with:

$$C = \frac{EI_1}{35L^3(1+a)^2}(420 + 420a + 210\delta_1 + 210a\delta_1 + 168\delta_2 + 140a\delta_2 + 147\delta_3 + 105a\delta_3 + 132\delta_4 + 84a\delta_4)$$

$$D = \frac{EI_1}{35L^2(1+a)^2}(210 + 210a + 70\delta_1 + 70a\delta_1 + 49\delta_2 + 35a\delta_2 + 42\delta_3 + 21a\delta_3 + 38\delta_4 + 14a\delta_4)$$

$$E = \frac{EI_1}{420L(1+a)^2}(1680 + 2100a + 420a^2 + 420\delta_1 + 630a\delta_1 + 210a^2\delta_1 + 224\delta_2 + 280a\delta_2 + 140a^2\delta_2 + 168\delta_3 + 147a\delta_3 + 105a^2\delta_3 + 144\delta_4 + 84a\delta_4 + 84a^2\delta_4)$$

$$F = \frac{EI_1}{420L(1+a)^2}(1680 + 2100a + 420a^2 + 1260\delta_1 + 1470a\delta_1 + 210a^2\delta_1 + 1064\delta_2 + 1120a\delta_2 + 140a^2\delta_2 + 924\delta_3 + 903a\delta_3 + 105a^2\delta_3 + 816\delta_4 + 756a\delta_4 + 84a^2\delta_4)$$

$$G = \frac{-EI_1}{35L^2(1+a)^2}(210 + 210a + 140\delta_1 + 140a\delta_1 + 119\delta_2 + 105a\delta_2 + 105\delta_3 + 84a\delta_3 + 94\delta_4 + 70a\delta_4)$$

$$H = \frac{-EI_1}{420L(1+a)^2}(-840 - 420a + 420a^2 - 420\delta_1 - 210a\delta_1 + 210a^2\delta_1 - 364\delta_2 - 140a\delta_2 + 140a^2\delta_2 - 336\delta_3 - 105a\delta_3 + 105a^2\delta_3 - 312\delta_4 - 84a\delta_4 + 84a^2\delta_4)$$

$$A_1 = \frac{A_{i1}\rho L}{1260(1+a)^2}\left(468 + 108\alpha_1 + 38\alpha_2 + 21a^2(20 + 5\alpha_1 + 2\alpha_2) + 6a(147 + 35\alpha_1 + 13\alpha_2)\right)$$

$$B_1 = \frac{A_{i1}\rho L^2}{2520(1+a)^2}\left(132 + 42\alpha_1 + 17\alpha_2 + 21a^2(5 + 2\alpha_1 + \alpha_2) + 3a(77 + 27\alpha_1 + 12\alpha_2)\right)$$

$$C_1 = \frac{A_{i1}\rho L^3}{5040(1+a)^2}\left(48 + 18\alpha_1 + 8\alpha_2 + 3a^2(14 + 7\alpha_1 + 4\alpha_2) + 3a(28 + 12\alpha_1 + 6\alpha_2)\right)$$

$$D_1 = \frac{A_{i1}\rho L}{1260(1+a)^2}\left(162 + 81\alpha_1 + 46\alpha_2 + 21a^2(10 + 5\alpha_1 + 3\alpha_2) + 3a(126 + 63\alpha_1 + 37\alpha_2)\right)$$

$$E_1 = \frac{A_{i1}\rho L^2}{2520(1+a)^2}\left(78 + 36\alpha_1 + 19\alpha_2 + 21a^2(5 + 2\alpha_1 + \alpha_2) + 3a(63 + 27\alpha_1 + 14\alpha_2)\right)$$

$$F_1 = \frac{-A_{i1}\rho L^3}{5040(1+a)^2}\left(24 + 12\alpha_1 + 10\alpha_2 + 3a^2(14 + 7\alpha_1 + 4\alpha_2) + 6a(14 + 7\alpha_1 + 4\alpha_2)\right)$$

$$A_2 = \frac{A_{i1}\rho L}{1260(1+a)^2}\left(468 + 360\alpha_1 + 290\alpha_2 + 21a^2(20 + 15\alpha_1 + 12\alpha_2) + 6a(147 + 112\alpha_1 + 90\alpha_2)\right)$$

$$B_2 = \frac{A_{i1}\rho L^2}{2520(1+a)^2}\left(132 + 90\alpha_1 + 65\alpha_2 + 21a^2(5 + 3\alpha_1 + 2\alpha_2) + 3a(77 + 50\alpha_1 + 35\alpha_2)\right)$$

$$C_2 = \frac{A_{i1}\rho L^3}{5040(1+a)^2}\left(48 + 30\alpha_1 + 20\alpha_2 + 3a^2(14 + 7\alpha_1 + 4\alpha_2) + 6a(14 + 8\alpha_1 + 5\alpha_2)\right)$$

$$E_2 = \frac{A_{i1}\rho L^2}{2520(1+a)^2}\left(78 + 42\alpha_1 + 25\alpha_2 + 21a^2(5 + 3\alpha_1 + 2\alpha_2) + 3a(63 + 36\alpha_1 + 23\alpha_2)\right)$$

B. GEAR CONTROL CHARTS

1 Pitch errors on spur gears

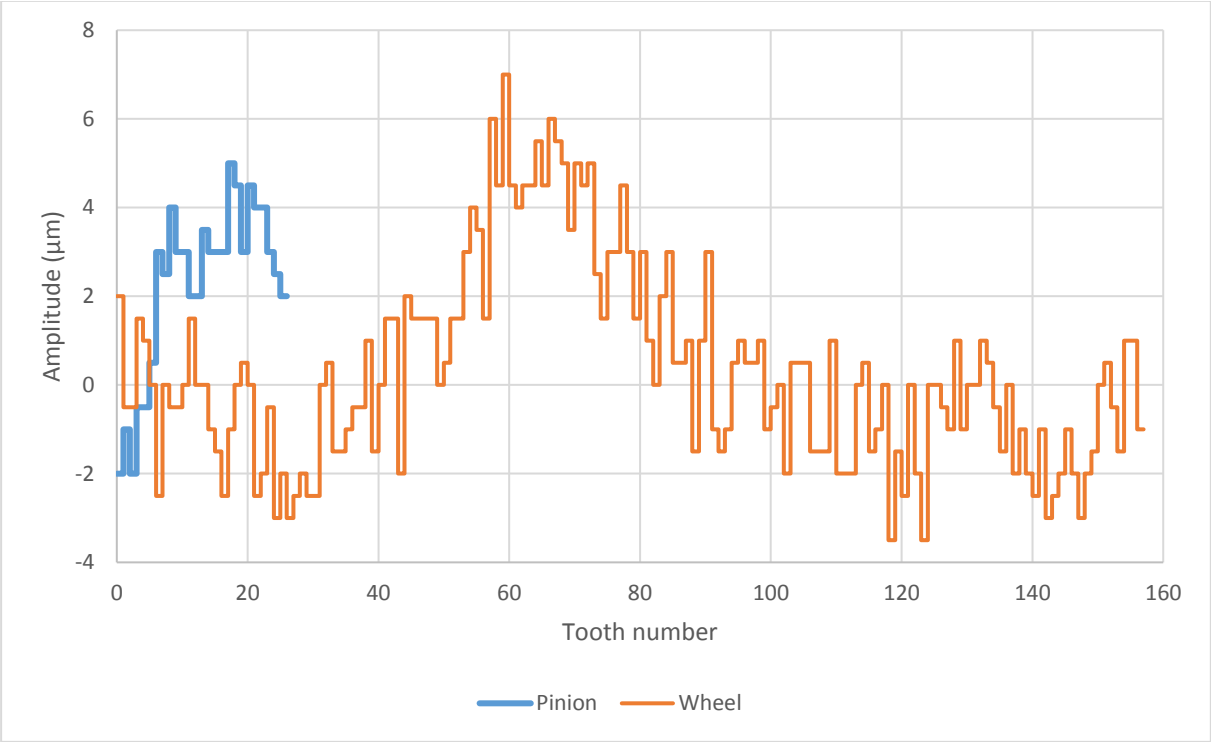

2 Pitch errors on helical gears

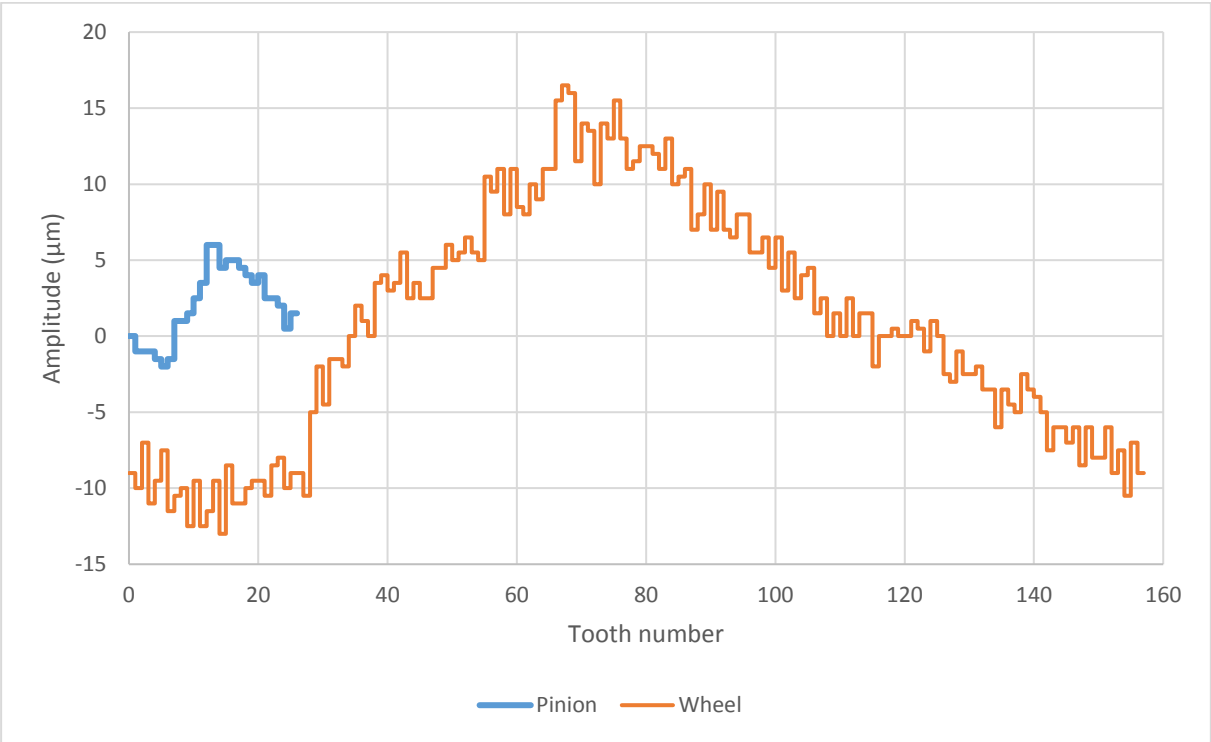

RESUME ETENDU EN FRANÇAIS

Ce manuscrit de thèse ayant été rédigé en anglais, un résumé étendu des travaux et des principaux résultats est proposé en français dans cette annexe. Les références bibliographiques correspondent à celles du manuscrit.

1 INTRODUCTION

Des mesures de bruits réalisées par le service Acoustique Interne et Externe d'Airbus Helicopters ont montré que la boîte de transmission principale des hélicoptères contribue fortement au bruit perçu par les passagers en cabine. Elle génère en effet plusieurs raies émergeant fortement du bruit large bande et dont les fréquences se situent dans la plage de sensibilité maximale de l'oreille humaine (entre 1 000 et 5 000 Hz). Les engrenages composant la boîte de transmission, soumis à de fortes vitesses de rotation, génèrent des vibrations qui se propagent à travers les arbres jusqu'aux roulements. Les efforts dynamiques induits aux roulements sont une source d'excitation pour le carter, lequel devient à son tour une source de bruit rayonné.

Dans un contexte d'amélioration permanente du confort acoustique des usagers et pour répondre aux nouvelles directives environnementales qui régissent l'exposition au bruit, il est nécessaire d'optimiser le comportement vibro-acoustique de ces boîtes. Les travaux de recherche présentés dans ce manuscrit se concentrent donc sur le développement d'un modèle numérique permettant de prédire le comportement dynamique de transmissions composées de plusieurs étages d'engrenages de différents types (cylindriques et spiro-coniques).

2 ETAT DE L'ART

2.1 Sources d'excitations et erreurs de transmission

Différentes stratégies de modélisation ont été développées pour prédire le comportement dynamique de transmissions par engrenages. En revanche, l'ensemble des auteurs semble s'accorder sur les sources d'excitations à l'origine des vibrations des engrenages. Ces sources peuvent être classées en deux catégories distinctes.

En premier lieu, on considère les déformations élastiques qui surviennent dès lors que les dentures en prise transmettent de la charge. Ces déformations sont caractérisées par le concept de raideur d'engrènement, qui représente la rigidité de la liaison entre un pignon et une roue en prise. Cette raideur varie naturellement au cours de l'engrènement car le nombre de dents en contact n'est pas constant au cours d'un cycle. Les fluctuations de la raideur d'engrènement sont donc considérées comme source d'excitation dans la grande majorité des modèles existants. Sa définition et sa quantification restent toutefois sujets à débat et ont été traitées par de nombreux auteurs. De nombreux modèles distinguent les différentes déformations qui contribuent à la raideur d'engrènement globale (flexion de la dent, déformation du contact, rotation de la base…) et se basent sur des méthodes analytiques pour caractériser chacune

d'elles. D'autres approches permettent de déterminer directement la raideur globale, par utilisation des éléments finis par exemple.

La seconde source d'excitation provient des écarts de forme. La plupart des engrenages présentent des profils en développante de cercle qui ont l'avantage d'être conjugués et de permettre un transfert uniforme des vitesses. Toute déviation par rapport à ces profils parfaits conjugués entraîne une perturbation des conditions de contact et devient une source d'excitation. Ces déviations sont parfois involontaires (erreurs liées au procédé de fabrication ou au montage) mais peuvent aussi avoir été introduites de manière intentionnelle (corrections de profil ou bombé par exemple).

Cette seconde source d'excitation est très communément caractérisée par le concept d'erreur de transmission. Cette notion a initialement été introduite par Harris en 1958 [33] et est définie comme "pour toute position angulaire instantanée d'une roue menante, la déviation angulaire de la roue menée par rapport à la position qu'elle aurait occupée si les dentures étaient rigides et non corrigées" [9] (Illustration 1).

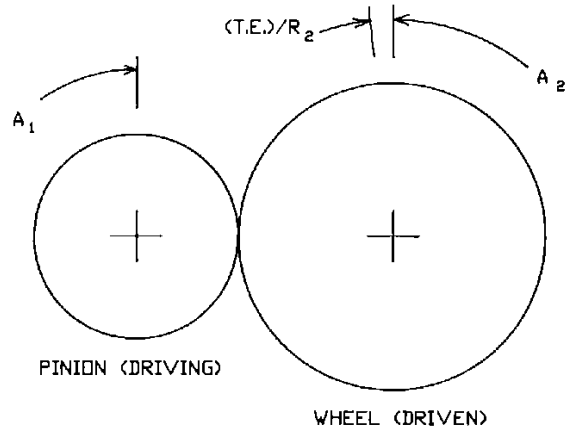

	PINION	WHEEL
NUMBER OF TEETH	Z_1	Z_2
BASE RADIUS	R_1	R_2
THEORETICAL ANGULAR POSITION	A_1	$A_2 = A_1 . Z_1 / Z_2$
ACTUAL ANGULAR POSITION	A_1	$A_2 + (T.E.)/R_2$
ACTUAL POSITION IN LINEAR TERMS	$A_1 R_1$	$A_2 R_2 + (T.E.)$ $= A_1 R_1 + (T.E.)$

Illustration 1 : Définition de l'erreur de transmission, d'après Munro [34]

L'erreur de transmission se définit dans trois conditions de fonctionnement différentes :

- L'erreur de transmission cinématique se mesure lorsque les engrenages en prise ne transmettent pas de charge et à faible vitesse de rotation. On l'appelle aussi erreur de transmission à vide. Elle correspond à l'écart maximal aux flancs de dents parfaits lorsque l'on considère tous les points de contact du plan d'action à un instant donné. Elle traduit donc les erreurs d'assemblage, erreurs de pas et certains types de corrections et est ainsi nulle pour des engrenages parfaits non corrigés.

- L'erreur de transmission quasi-statique est obtenue sous charge et à faible vitesse de rotation. Elle tient donc compte des déflections que les dentures subissent sous l'effet de la charge. Elle varie en fonction du nombre de dents en prise, ou longueur de contact et de manière opposée par rapport à la raideur d'engrènement. Une corrélation a été expérimentalement démontrée entre les variations temporelles de l'erreur de transmission quasi-statique et la réponse dynamique des engrenages (bruit et vibrations). L'erreur de transmission est donc reconnue comme représentative des excitations liées à l'engrènement et est utilisée dans de nombreuses études dynamiques, soit comme critère d'optimisation soit directement comme terme d'excitation.
- L'erreur de transmission dynamique est souvent utilisée comme indicateur de la réponse dynamique des engrenages. Elle est l'équivalent de l'erreur de transmission quasi-statique mais tient compte des effets dynamiques lorsque ceux-ci ne peuvent être ignorés (vitesses de rotation importantes).

2.2 Modèles dynamiques

La littérature compte un grand nombre de modèles dédiés à la prédiction du comportement dynamique de systèmes simple-étage à axes parallèles (dentures droites ou hélicoïdales). Les premiers modèles mathématiques datent des années 1950 et sont pour la plupart réduits à un ou deux degrés de liberté. Ces modèles intègrent uniquement la souplesse de la denture et sont largement inspirés des modèles de type masse-ressort.

Dès la fin des années 1960, ces modèles ont été étendus pour prendre en compte les couplages qui s'opèrent entre les engrenages et leurs éléments de support (arbres et roulements). Dans un certain nombre de ces modèles, l'engrènement est représenté par des fonctions périodiques d'excitations définies en amont de l'analyse dynamique (généralement l'erreur de transmission et la raideur d'engrènement) [71,73]. Une autre catégorie de modèles repose sur la résolution simultanée des équations du mouvement et des conditions de contact et s'affranchit ainsi de la caractérisation préliminaire des fonctions d'excitation [18,60,76].

Plus récemment encore, certains modèles ont été proposés qui intègrent les contributions du carter en plus de celles des arbres et des roulements [80,83–85]. Ces développements s'appuient sur la méthode des éléments finis qui permet une représentation précise de la géométrie du carter. Dans la grande majorité de ces modèles, l'ensemble engrenages-arbres-roulements est modélisé par une des approches citées au paragraphe précédent.

Outre les engrenages à axes parallèles, les engrenages coniques sont aussi largement utilisés dans les transmissions mécaniques pour leur fonction de renvoi d'angle. Pourtant, les modèles dédiés à l'analyse de leur comportement dynamique semblent remonter seulement à la fin des années 1990. La plupart de ces modèles reposent sur une définition préliminaire des conditions de contact, via une analyse quasi-statique qui permet de définir les fonctions d'excitations liées à l'engrènement [92,94,98,105]. Teixeira, Wang *et al.* [101,102] ont comparé une approche de ce type avec un modèle dans lequel les conditions de contact et les équations du mouvement sont résolues simultanément. Les auteurs ont montré que les deux techniques de modélisation conduisent à des résultats concordants.

Finalement, après que des résultats expérimentaux aient montré des couplages entre les différents engrenages d'une transmission [105], des modèles ont été spécialement développés pour la prédiction du comportement dynamique des systèmes multi-engrènements. Les modèles les plus simples sont limités à deux degrés de liberté pour deux étages de réduction [107] et les plus complexes permettent d'inclure un nombre multiple d'engrènements [122] et reposent sur une résolution simultanée des conditions de contact et des équations du mouvement [114]. Différentes architectures ont été étudiées, avec des engrènements décalés [115,120] ou en cascade [111,118,119] mais il semble qu'aucun n'ait encore permis d'intégrer des assemblages d'engrenages de différents types (cylindriques et coniques).

3 MODELISATION DU COMPORTEMENT DYNAMIQUE DE SYSTEMES A ENGRENAGES PAR L'ERREUR DE TRANSMISSION

La revue de littérature a mis en évidence une méthodologie en trois étapes, communément utilisée pour la simulation du comportement vibro-acoustique de transmissions par engrenages [85,125], et adoptée dans le cadre de ces travaux :

a) Caractérisation des sources d'excitations principales (reposant principalement sur la raideur d'engrènement et l'erreur de transmission),
b) Calcul de la réponse dynamique du système soumis aux excitations causées par l'engrènement et détermination des efforts dynamiques résultants aux roulements,
c) Simulation du rayonnement acoustique du carter soumis aux efforts dynamiques aux roulements.

L'étape a) consiste en une analyse cinématique et quasi-statique de chaque engrènement qui permet de définir les conditions de contact et de déterminer les variations temporelles des fonctions d'excitation. L'étape b) repose sur la résolution dynamique des équations du mouvement pour le système engrenages-arbres-roulements et l'étape c) consiste à simuler le comportement vibro-acoustique de la boîte de transmission, carter inclus.

L'avantage principal de cette approche est de permettre des études paramétriques et phases d'optimisation à chacune des étapes. Elle permet aussi de réduire les temps de calcul par rapport à une résolution simultanée en dynamique des équations du mouvement et des conditions de contact. Enfin, il est attendu que cette approche permette de modéliser simultanément et de manière identique des engrenages à axes parallèles et des engrenages coniques.

3.1 Equations du mouvement

En considérant les corps des engrenages comme rigides, une approche de type mécanique des solides indéformables est adoptée pour écrire le torseur des efforts d'engrènement. Le frottement entre les dentures est négligé et la normale est supposée identique en tous points de contact, ce qui permet d'écrire après développement le torseur sous une forme compacte :

$$\boldsymbol{F}_{mesh} = -F_m \boldsymbol{v}_G \qquad (1)$$

F_m est l'effort normal d'engrènement et $\boldsymbol{v}_G$ est dénommé le vecteur structure de l'engrenage. Il dépend de la géométrie des dentures.

Six degrés de liberté sont attribués au pignon et à la roue afin de tenir compte des déformées de traction/compression, flexion et torsion. Ils représentent des déplacements infinitésimaux qui se superposent aux rotations de corps rigides de chacun des membres. Ils sont écrits sous la forme du vecteur $\boldsymbol{q}$ de dimension 12. Le torseur des efforts d'engrènement peut être réécrit à partir de ces degrés de liberté comme :

$$\boldsymbol{F}_{mesh} = -k(t,\boldsymbol{q})[\boldsymbol{v}_G\boldsymbol{v}_G^T]\boldsymbol{q} + f\big(t,\delta e(M)\big)\boldsymbol{v}_G \tag{2}$$

$k(t,\boldsymbol{q})$ est la raideur d'engrènement, dépendante du temps et possiblement non-linéaire. $f\big(t,\delta e(M)\big)$ est une fonction scalaire, variable au cours du temps et dépendante des écarts initiaux aux points de contact potentiels M.

Le concept d'erreur de transmission est introduit à ce stade. Projetée dans le plan de base, l'erreur de transmission quasi-statique est définie comme suit :

$$TE_S = \boldsymbol{W}^T\boldsymbol{X}_S + NLTE \tag{3}$$

$\boldsymbol{W}$ est un vecteur de projection, non spécifié à ce stade et $NLTE$ désigne l'erreur de transmission à vide, définie à partir du même vecteur de projection $\boldsymbol{W}$ et des rotations de corps-rigides des engrenages $\boldsymbol{X}_R$ en présence des éventuelles erreurs et corrections :

$$NLTE = \boldsymbol{W}^T\boldsymbol{X}_R \tag{4}$$

En utilisant ces deux définitions, le terme d'excitations lié aux écarts initiaux peut être exprimé en fonction de l'erreur de transmission quasi-statique TE_S et de l'erreur de transmission à vide $NLTE$. On peut alors réécrire le torseur des efforts d'engrènement lié à chaque étage d'engrenages en fonction :

- de la raideur d'engrènement,
- de l'erreur de transmission quasi-statique,
- de l'erreur de transmission à vide,
- du vecteur structure.

En supposant que les conditions de contact sont identiques en dynamique et en conditions quasi-statiques, les équations du mouvement pour un système à N engrènements s'écrivent :

$$\begin{aligned}\frac{1}{T_m^2}\boldsymbol{M}\boldsymbol{X}'' + \frac{1}{T_m}\boldsymbol{C}\boldsymbol{X}' + \left(\boldsymbol{K}_{sys} + \sum_{L=1}^{N}\boldsymbol{K}_G^{(L)}(\tau)\right)\boldsymbol{X} \\ = \boldsymbol{F}_0 + \sum_{L=1}^{N} F_S^{(L)}\left[\left(1+\frac{\Delta k^{(L)}(\tau)}{k_m^{(L)}}\right)\left(\frac{TE_S^{(L)} - NLTE^{(L)} - \boldsymbol{W}^{(L)^T}\left(\boldsymbol{X}_0 - \widehat{\boldsymbol{X}}_0^{(L)}\right)}{\boldsymbol{W}^{(L)^T}\widehat{\boldsymbol{X}}_0^{(L)}}\right) - 1\right]\boldsymbol{V}_G^{(L)} \\ + \boldsymbol{F}_{\dot{\Omega}}(\tau)\end{aligned} \tag{5}$$

$\boldsymbol{F}_{\dot{\Omega}}(\tau)$ est un terme d'excitations lié aux possibles fluctuations des vitesses de corps rigides (causées par des erreurs ou des corrections).

Ces équations intègrent les contributions des éléments de support (arbres, accouplements élastiques et roulements). Des éléments à paramètres concentrés sont utilisés pour représenter

les accouplements et les roulements tandis que les éléments d'arbre se basent sur la théorie des poutres de Timoshenko.

3.2 Analyse quasi-statique

Comme présenté plus haut, la première étape de la méthode mise en application est la résolution des conditions de contact en quasi-statique, qui permet de déterminer les fonctions d'excitations liées au phénomène d'engrènement. Des logiciels dédiés sont utilisés pour l'étude des engrenages cylindriques d'une part, et des engrenages spiro-coniques d'autre part.

Pour les engrenages cylindriques, l'étude est réalisée à partir du logiciel Load Distribution Program (LDP) développé par le GearLab à l'Université de l'Ohio [131]. Le modèle prend en compte l'élasticité des dentures, ainsi que les potentielles erreurs ou corrections. Dans le cas des dentures droites et hélicoïdales, la normale au contact est considérée constante au cours du temps et déterminée à partir des paramètres géométriques de l'engrenage. L'effort d'engrènement est appliqué au centre de la fenêtre d'engrènement et cette position est elle aussi constante au cours du temps. Les excitations générées par un engrenage cylindrique sont donc caractérisées par trois fonctions du temps :

- la raideur d'engrènement,
- l'erreur de transmission quasi-statique TE_S,
- l'erreur de transmission à vide $NLTE$.

Dans le cas des engrenages spiro-coniques, le logiciel ASLAN est utilisé pour résoudre les conditions de contact. Ce logiciel est développé au sein du LaMCoS, INSA de Lyon par Teixeira *et al.* [101,134,135]. Il repose sur une modélisation par éléments finis du pignon et de la roue et utilise la méthode des coefficients d'influence pour le calcul de la répartition de charge. Contrairement aux engrenages cylindriques, la direction et le point d'application de l'effort normal sont recalculés à chaque pas de temps. Les excitations générées par un engrenage spiro-conique sont donc représentées par cinq fonctions du temps :

- la raideur d'engrènement,
- l'erreur de transmission quasi-statique TE_S,
- l'erreur de transmission à vide $NLTE$,
- la position du barycentre de la distribution des efforts,
- l'orientation de l'effort d'engrènement.

3.3 Analyse dynamique

Après l'analyse quasi-statique, les équations du mouvement (5) sont résolues pas-à-pas dans le temps à partir de l'algorithme de Newmark. La matrice de raideur globale et les termes au second membre sont recalculés à chaque pas de temps pour tenir compte des valeurs instantanées de la raideur d'engrènement, des erreurs de transmission et des vecteurs structure. Afin d'accélérer la convergence de la solution, la déformée statique du système est utilisée comme condition initiale du problème.

L'erreur de transmission dynamique est calculée sur le même modèle que l'erreur de transmission quasi-statique à partir de la solution globale aux équations du mouvement $\boldsymbol{X}$. Pour chaque étage d'engrènement (L), on a :

$$TE_d^{(L)} = \boldsymbol{W}^{(L)^T}\boldsymbol{X} + NLTE^{(L)} \qquad (6)$$

$\boldsymbol{W}$ est le même vecteur de projection que celui utilisé pour la définition des erreurs de transmission quasi-statique et à vide.

Les variations temporelles de l'erreur de transmission dynamique sont reconnues comme un indicateur pertinent du comportement dynamique des engrenages. On fera donc par la suite référence au crête-à-crête ou au RMS de l'erreur de transmission dynamique.

L'effort d'engrènement dynamique F_d est un autre paramètre caractéristique de la dynamique des engrenages. Pour chaque étage d'engrenage (L) (cylindrique comme spiro-coniques), il s'écrit :

$$F_d^{(L)} = k^{(L)}(t)\boldsymbol{V}_G^{(L)^T}\boldsymbol{X} - F_S^{(L)}\left[\frac{k^{(L)}(t)}{k_m^{(L)}}\left(\frac{TE_S^{(L)} - NLTE^{(L)} - \boldsymbol{W}^{(L)^T}\left(\boldsymbol{X}_0 - \widehat{\boldsymbol{X}}_0^{(L)}\right)}{\boldsymbol{W}^{(L)^T}\widehat{\boldsymbol{X}}_0^{(L)}}\right) - 1\right] \quad (7)$$

Le maximum de l'effort dynamique en régime stationnaire est représentatif des surcharges dynamiques à la denture. Ce paramètre est communément représenté sont une forme adimensionnée comme le rapport maximum effort dynamique / effort statique (coefficient dynamique) :

$$DF_{mf}^{(L)} = \frac{\max\left(F_d^{(L)}\right)}{F_S^{(L)}} \quad (8)$$

4 ELEMENTS DE VALIDATION

Afin de confirmer la pertinence du modèle proposé, divers résultats numériques et expérimentaux de la littérature sont utilisés. Les différents cas de comparaison portent sur des systèmes simple étage à axes parallèles ou concourants ainsi que sur des systèmes à deux étages d'engrenages droits.

4.1 Système simple-étage à axes parallèles

Pour ce premier cas de validation, les résultats expérimentaux obtenus par Baud et Velex [74] sont utilisés. Le banc d'essai (Illustration 2) est un système en boucle ouverte comprenant un étage d'engrenages à denture droite ou hélicoïdale. Des jauges uni-axiales sont disposées en pieds de dent sur trois dents successives du pignon et de la roue.

La vitesse de rotation du pignon est successivement incrémentée de 100 à 6000 tr/min et à chaque vitesse, le moment de flexion dynamique en pied de dent est calculé. Sa valeur maximale est adimensionnée par le moment maximal en conditions statiques et ce résultat est comparé aux relevés de jauges. Une bonne corrélation est obtenue dans le cas d'un engrenage à dentures droites (Illustration 3), tant en termes de positions des vitesses critiques qu'en termes d'amplitude des pics. Des comparaisons similaires ont été réalisées en faisant varier la distance entre les paliers supportant les arbres du pignon et de la roue, ainsi que pour une denture hélicoïdale. Dans chacun des cas étudiés, les résultats numériques sont en bon accord avec les relevés expérimentaux.

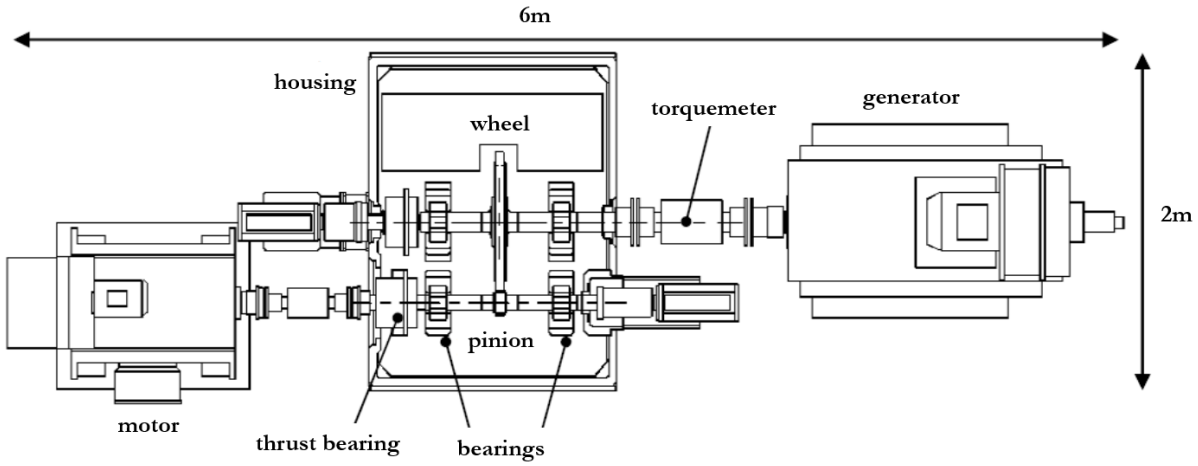

Illustration 2 : Schéma du banc d'essai, d'après Baud et Velex [74]

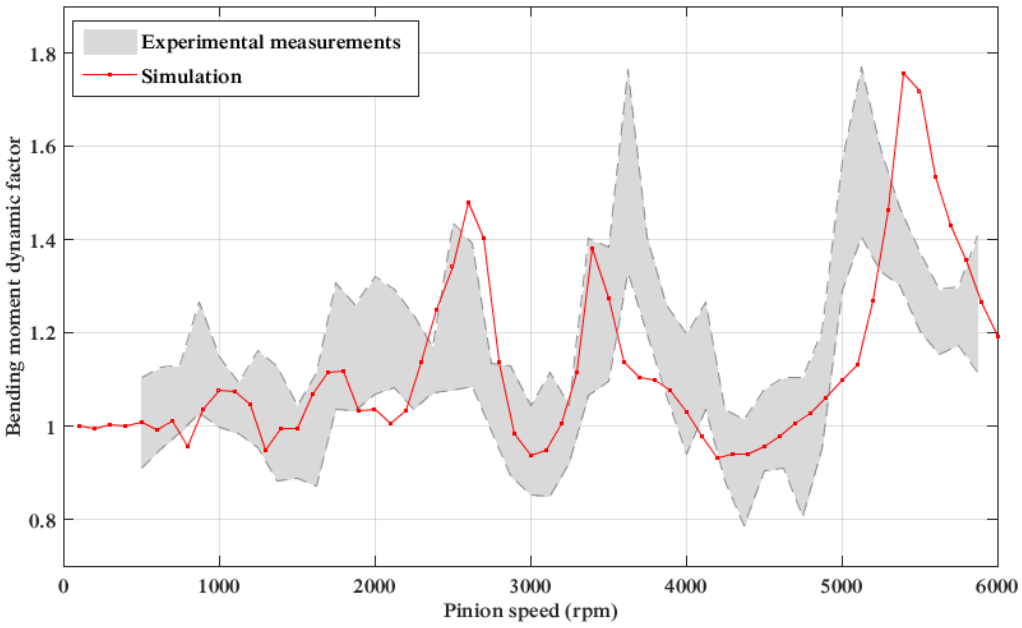

Illustration 3 : Système à axes parallèles – Comparaison du moment de flexion simulé avec les relevés de jauge de Baud et Velex [74]

4.2 Système simple-étage à axes concourants

Pour cette étude, des résultats obtenus à partir d'un modèle dynamique local développé par Wang *et al.* [102] sont utilisés. Le coefficient dynamique est calculé pour plusieurs vitesses de rotation et les résultats obtenus à partir des deux modèles sont comparés. Une très bonne corrélation est observée, validant la pertinence du modèle basé sur l'erreur de transmission pour la simulation du comportement dynamique d'engrenages spiro-coniques.

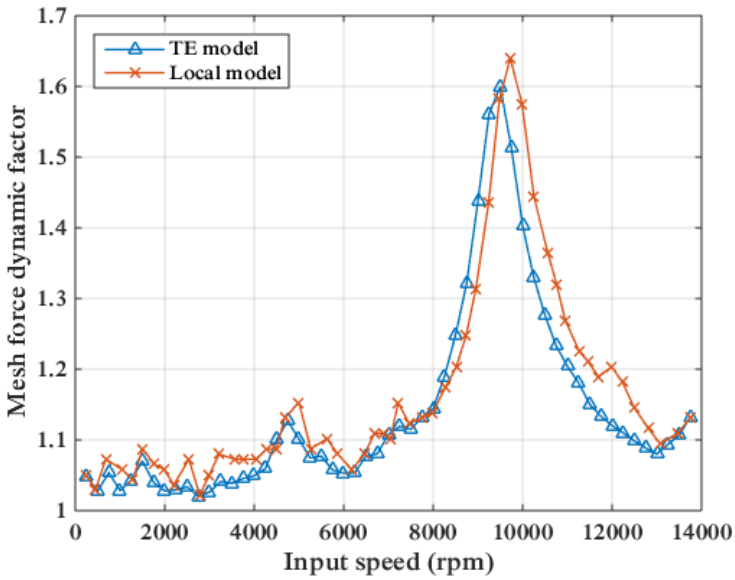

Illustration 4 : Système à axes concourants – Comparaison du modèle basé sur l'erreur de transmission avec le modèle local de Wang [102]

4.3 Système double-étage à axes parallèles

Le système reproduit ici a initialement été étudié par Raclot [114]. Il se compose de deux étages d'engrenages à dentures droites séparés par un arbre intermédiaire (Illustration 5). Les axes des trois arbres sont contenus dans un même plan. Un couple constant de 1 500 N.m est appliqué sur le pignon et un balayage en vitesses est réalisé entre 100 et 30 000 tr/min. A chaque vitesse de rotation, l'erreur de transmission dynamique locale associée à chaque engrènement est calculée à partir du vecteur solution $\boldsymbol{X}$ ainsi que le facteur de forme associé (RMS des fluctuations temporelles).

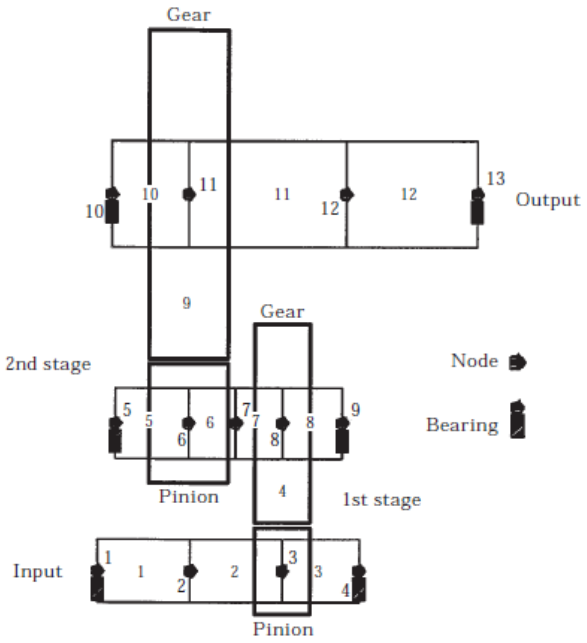

Illustration 5 : Système double étage à axes parallèles – Modèle éléments finis du système d'après Raclot [114]

Les résultats obtenus sont présentés en Illustration 6 (étage 1) et Illustration 7 (étage 2) pour trois configurations : (a) dentures non corrigées, (b) corrections de profil courtes, et (c) corrections de profil longues. Les résultats du modèle basé sur l'erreur de transmission sont en bon accord avec le modèle local de Raclot. Des observations similaires ont été obtenues à l'issue de l'étude d'un système composé de trois pignons en cascade. On peut donc conclure que la formulation proposée est adaptée aux systèmes double-étage et qu'elle permet de tenir compte des corrections de profil.

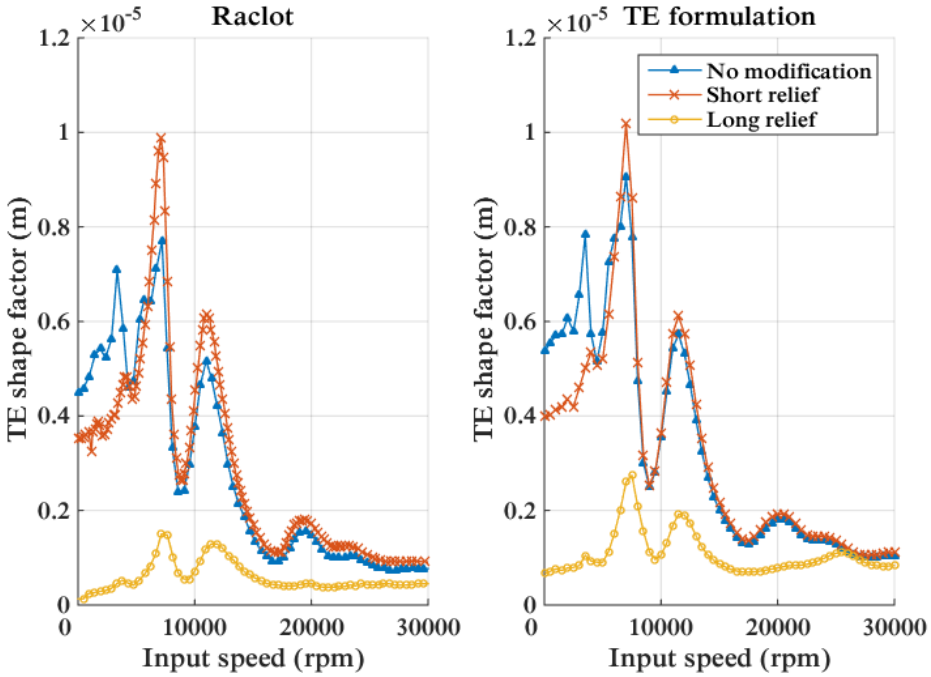

Illustration 6 : Système double étage à axes parallèles – Comparaison du modèle local et du modèle basé sur l'erreur de transmission (Etage 1)

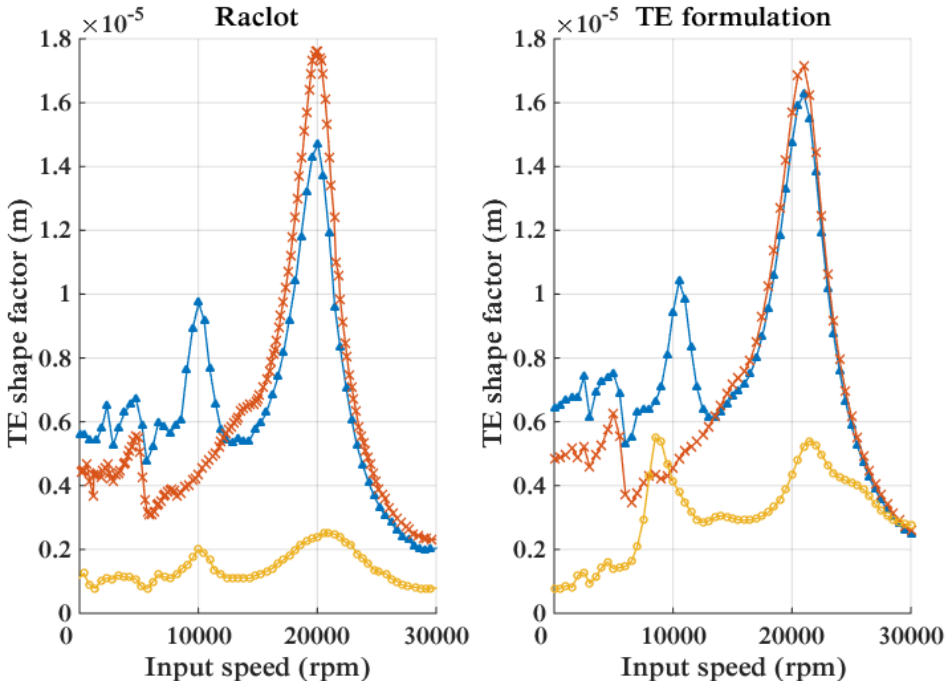

Illustration 7 : Système double étage à axes parallèles – Comparaison du modèle local et du modèle basé sur l'erreur de transmission (Etage 2)

5 ETUDE DYNAMIQUE DE SYSTEMES SIMPLE ET DOUBLE-ETAGE

5.1 Influence des erreurs de pas

L'influence des erreurs de pas sur le comportement dynamique des transmissions par engrenages est étudiée à partir du modèle du banc d'essai exploité par Baud [74]. Les erreurs relevées sur les engrenages testés ont été introduites dans le modèle. Elles entraînent des variations du facteur dynamique d'une paire de dents à la suivante, en fonction des erreurs combinées. Pour chaque vitesse de rotation, on calcule donc le maximum et le minimum du facteur dynamique. On observe sur l'Illustration 8 que les erreurs de pas ne modifient pas la position des vitesses critiques mais font apparaître une dispersion autour de la solution sans erreur. On note que la largeur de la plage simulée est proche de celle de l'enveloppe expérimentale (surface grisée), confirmant la capacité du modèle à prendre en compte ce type d'erreurs.

Cette étude a par ailleurs permis de montrer que l'influence des erreurs de pas est plus importante pour une denture hélicoïdale que pour une denture droite, et finalement que cette influence tend à diminuer lorsque la charge augmente.

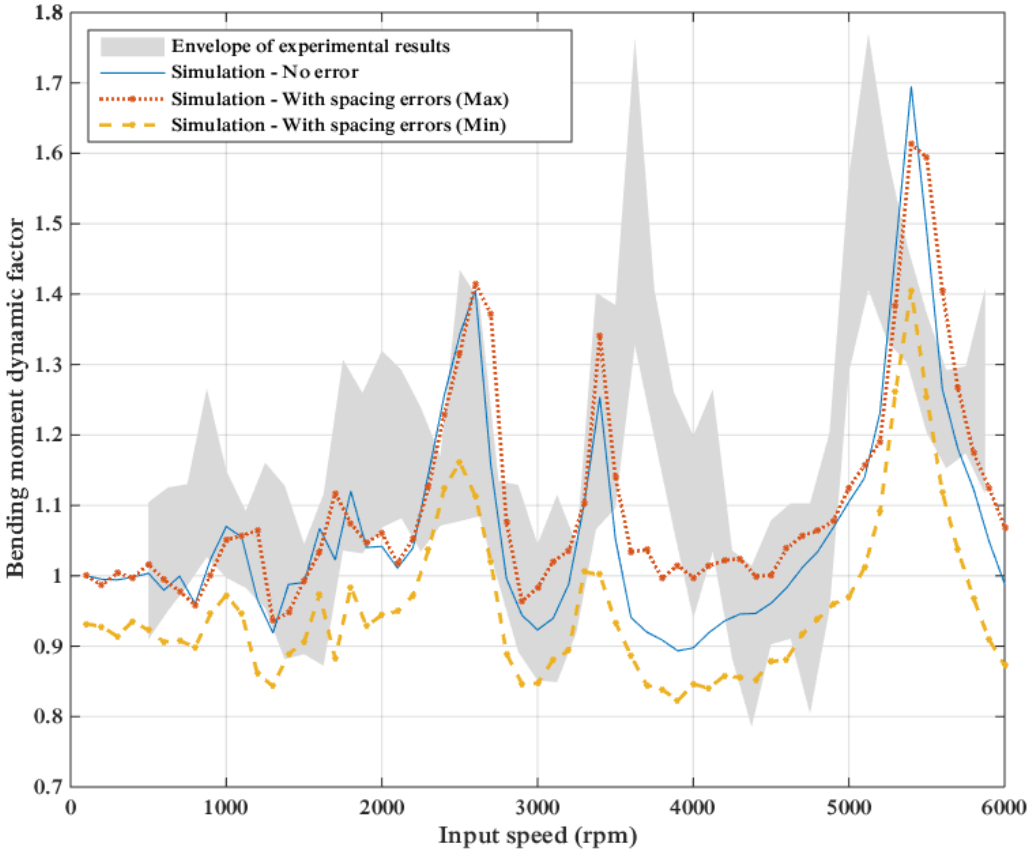

Illustration 8 : Système simple-étage à axes parallèles – Influence des erreurs de pas

5.2 Corrélation entre l'erreur de transmission dynamique et les charges dynamiques à la denture

L'erreur de transmission dynamique est couramment utilisée pour caractériser le comportement vibratoire des engrenages tandis que les efforts dynamiques à la denture sont un critère plus pertinent dans le cadre des études de résistance. Plusieurs études ont donc été conduites afin de déterminer dans quelle mesure ces deux paramètres peuvent être reliés. Certaines observations expérimentales semblent indiquer une relation de proportionnalité entre le RMS ou crête-à-crête de l'erreur de transmission dynamique et les efforts à la denture, ou contraintes en pied de dent [51,61]. Cependant, la seule démonstration théorique d'une relation linéaire entre ces deux critères reste limitée aux seuls modèles torsionnels [62].

Cette étude se propose d'étendre ces investigations à des systèmes pour lesquels les effets de flexion d'arbre ne peuvent être négligés, ainsi qu'à des engrenages à denture hélicoïdale. Pour cela, deux modèles du banc d'essai présenté dans la **Section 4.1** sont exploités : a) un modèle tridimensionnel tenant compte de la paire d'engrenages ainsi que des arbres, roulements et accouplements et b) un modèle réduit torsionnel incluant uniquement le pignon et la roue. Dans ce qui suit, le coefficient d'effort dynamique est défini tel que :

$$DF_{mf} = \frac{\max(F_d)}{F_S} \tag{9}$$

Les Illustrations 9 et 10 présentent les variations de l'effort à la denture (coefficient dynamique défini en (9) ou crête-à-crête) en fonction de l'erreur de transmission dynamique. Deux séries de points sont utilisées afin de distinguer les vitesses faibles (cercles) des vitesses supérieures à la seconde vitesse critique principale (triangles).

L'Illustration 9 montre les résultats obtenus dans le cadre d'une denture droite et l'Illustration 10 correspond à une denture hélicoïdale. Dans chaque illustration, les figures (a) et (b) ont été obtenues à partir du modèle tridimensionnel complet, tandis que les figures (c) et (d) sont issues du modèle réduit torsionnel.

L'abscisse des figures (a) et (c) est basée sur les développements théoriques proposés en [62] qui indiquent que, dans le cas d'un modèle purement torsionnel, une relation linéaire peut être établie entre l'effort dynamique à la denture et l'amplitude zéro-à-crête de l'erreur de transmission dynamique, sous la forme :

$$DF_{mf} = 1 + \frac{k_m}{F_S}(TE_d - TE_S)^{0-p} \tag{10}$$

Les figures (b) et (d) correspondent à la relation proposée dans [51] sur la base de résultats expérimentaux qui relie l'effort dynamique à la denture à l'erreur de transmission dynamique par :

$$\frac{F_d^{0-p}}{F_S} = \frac{TE_d^{0-p}}{\lambda} \tag{11}$$

où $\lambda = mean(TE_S) - mean(NLTE)$

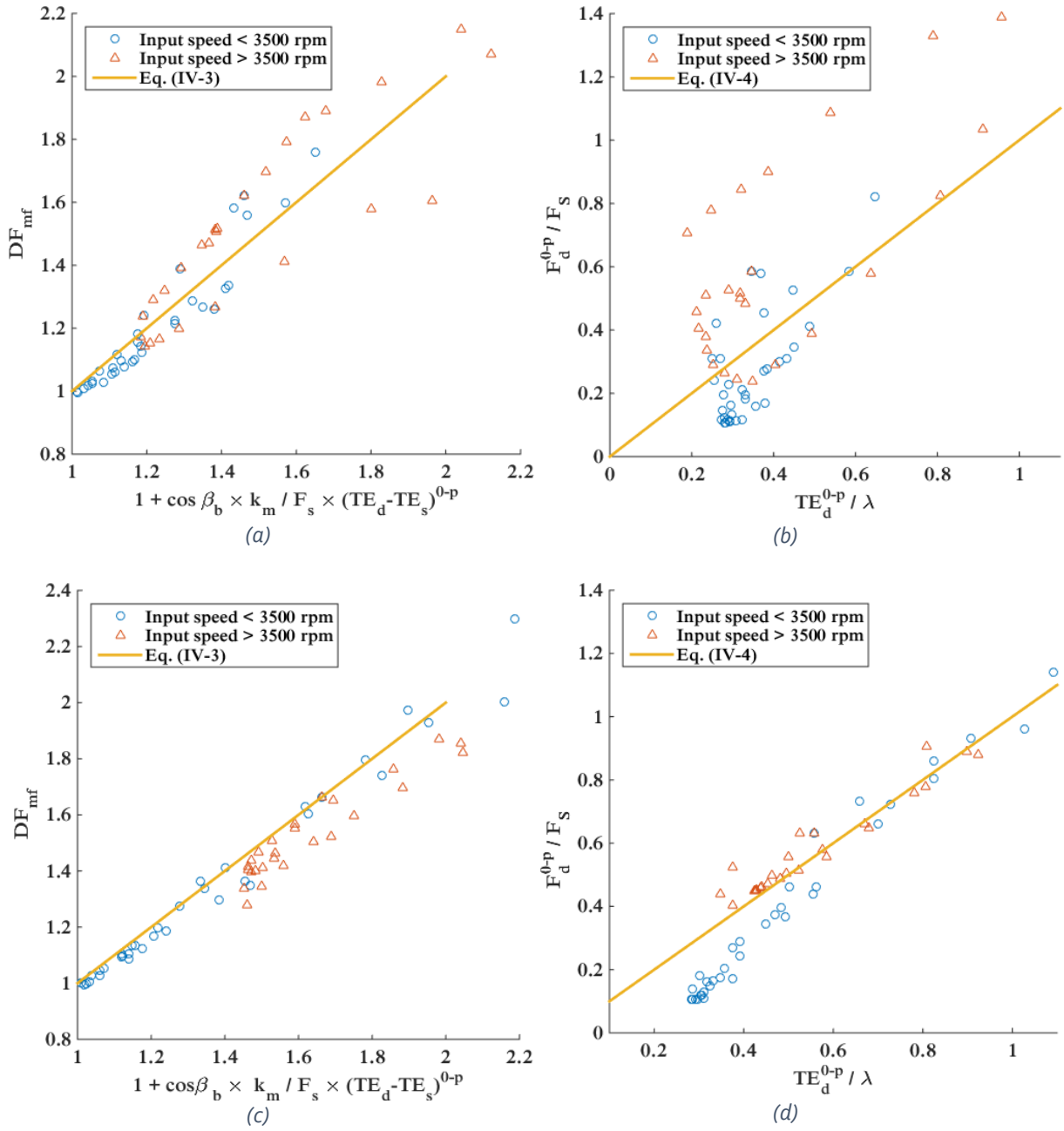

Illustration 9 : Engrenages à denture droite – (a) et (b) : modèle tridimensionnel complet, (c) et (d) : modèle réduit torsionnel

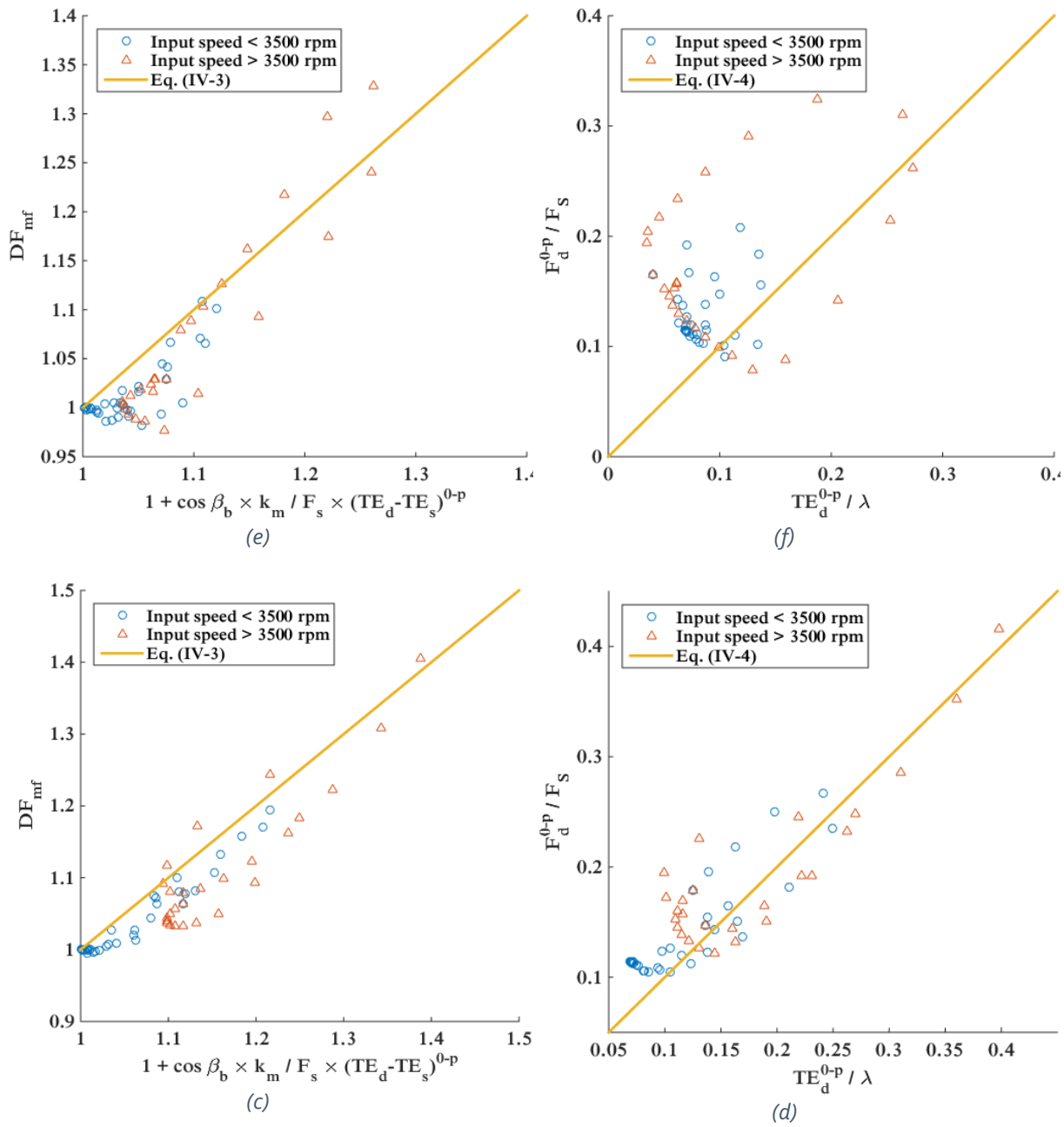

Illustration 10 : Engrenages à denture hélicoïdale – (a) et (b) : modèle tridimensionnel complet, (c) et (d) : modèle réduit torsionnel

Les conclusions suivantes sont tirées des résultats des différentes simulations :

- les relations linéaires proposées dans les références [51,61,62] ne sont pas complétement satisfaisantes dans le cas d'un système tridimensionnel (figures (a) et (b)) et une importante dispersion est observée, qui semble plus marquée dans le cas des dentures hélicoïdales (Illustration 10),
- une relation linéaire est en revanche clairement identifiable sur les résultats obtenus à partir des modèles torsionnels (figures (c) et (d)),
- la vitesse semble jouer un rôle important et une bifurcation est observée à partir d'un certain régime de vitesses (tendance mentionnée par Dai *et al.* [63]).

5.3 Système double-étage à axes concourants

Dans le but de reproduire une architecture similaire à celle d'une boîte de transmission d'hélicoptère, un nouveau système est étudié qui se compose d'un engrenage cylindrique (denture droite ou hélicoïdale) et d'un engrenage spiro-conique (Illustration 11).

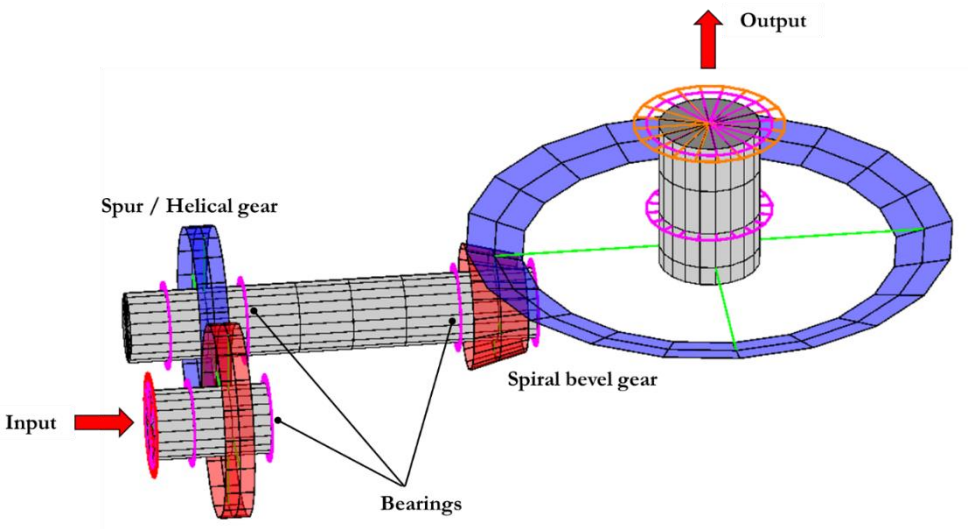

Illustration 11 : Modèle du système double-étage à axes concourants

Les Illustrations 12 et 13 montrent les erreurs de transmission dynamiques locales calculées dans le cas où le premier étage de réduction est un engrenage à denture hélicoïdale. Un balayage est réalisé sur la vitesse de rotation du pignon d'entrée et la FFT des signaux d'erreurs de transmission dynamiques est calculée à chaque vitesse de rotation. Le résultat est présenté sous forme de spectrogramme sur lequel on peut identifier les différentes fréquences caractéristiques du système. f_{m_1} désigne la fréquence d'engrènement de l'engrenage cylindrique et f_{m_2} celle de l'engrenage spiro-conique. L'Illustration 12 montre que l'engrenage spiro-conique a une forte influence sur la réponse dynamique de l'engrenage cylindrique, entrainant une amplification de la réponse dynamique (vitesse critique), autour de 31 000 tr/min.

L'étude de la réponse aux niveaux des différents roulements du système a aussi permis de mettre en avant une forte influence de l'engrenage spiro-conique sur l'ensemble du système, témoignant d'importants phénomènes entre les deux engrenages. Ces phénomènes peuvent être atténués en réduisant la raideur de connexion entre les deux étages de réduction, soit par une augmentation de la longueur de l'arbre intermédiaire dans le cas d'une denture droite, soit par l'introduction d'un accouplement élastique dans le cas d'une denture hélicoïdale.

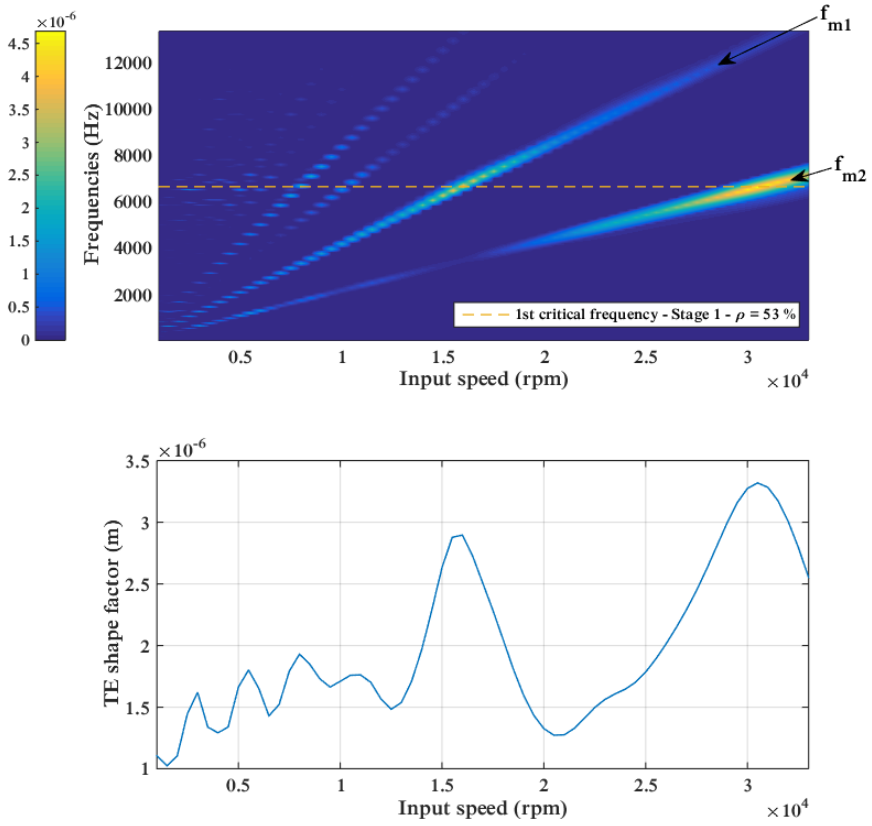

Illustration 12 : Système double-étage à axes concourants – Contenu spectral de l'erreur de transmission dynamique (engrenage cylindrique)

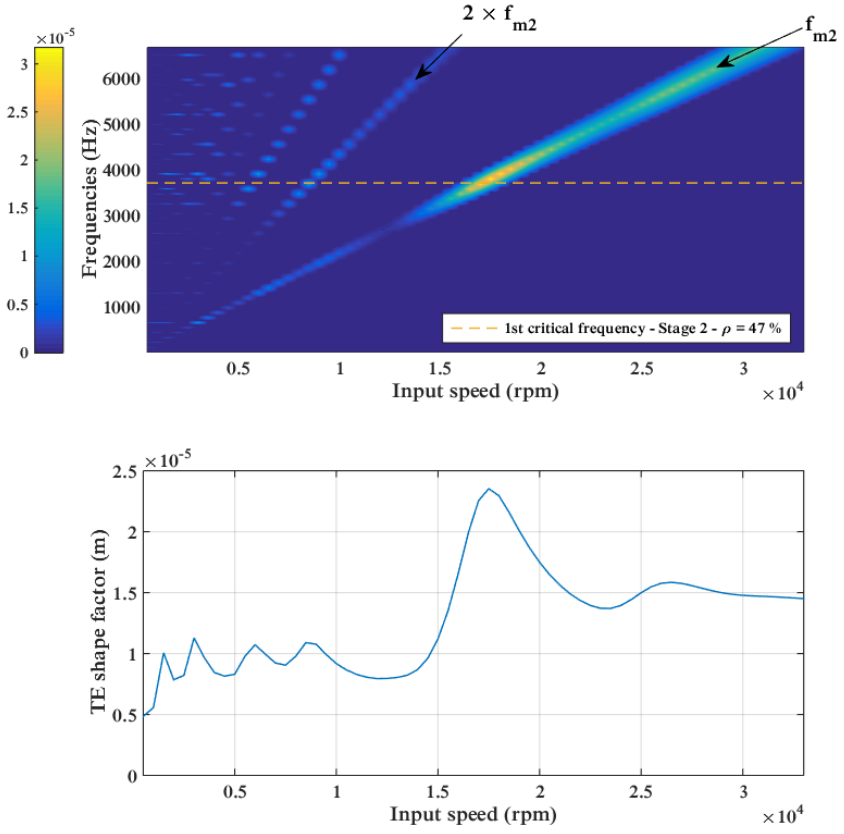

Illustration 13 : Système double-étage à axes concourants – Contenu spectral de l'erreur de transmission dynamique (engrenage spiro-conique)

6 CONCLUSION

Les transmissions par engrenages sont sources de vibrations et de bruit. De nombreux modèles sont proposés dans la littérature pour prédire le comportement dynamique de ces systèmes, mais la plupart concernent des transmissions à un seul étage de réduction (avec axes parallèles ou concourants), qui ne sont plus applicables dès lors que de forts couplages interviennent entre les engrenages successifs d'une boîte (comme c'est le cas dans les BTP). Par ailleurs, les modèles développés pour des systèmes à plusieurs étages semblent exclusivement dédiés aux systèmes à axes parallèles et ne permettent donc pas d'intégrer de renvoi d'angle.

Les travaux présentés dans ce manuscrit portent donc sur le développement d'un modèle numérique dédié à la simulation du comportement dynamique des boîtes de transmission principales (BTP) d'hélicoptères. Ce modèle permet de représenter des systèmes comportant plusieurs étages d'engrenages de différents types (cylindriques et spiro-coniques) par une approche similaire. Il repose sur une caractérisation des excitations liées à l'engrènement par des fonctions périodiques, principalement : (a) la raideur d'engrènement, et (b) les erreurs de transmission. Le modèle inclut la contribution des éléments de supports (arbres, roulements, accouplements élastiques) et permet donc de déterminer la réponse dynamique au niveau des roulements. Une analyse vibro-acoustique du carter peut être réalisée ultérieurement en utilisant les efforts dynamiques aux roulements issus de l'analyse dynamique du système engrenages-arbres-roulements.

La validité du modèle est vérifiée en reproduisant des études numériques et expérimentales de la littérature. Les différentes comparaisons réalisées permettent de démontrer la pertinence de la formulation proposée pour des engrenages cylindriques et spiro-coniques, avec ou sans corrections et erreurs, ainsi que pour des systèmes à deux étages de réduction.

Le modèle est appliqué pour plusieurs études portant sur des systèmes simple- et double-étage. Celles-ci traitent : (i) de l'influence des erreurs de pas sur la dynamique des engrenages, (ii) de la relation entre l'erreur de transmission dynamique et les efforts dynamiques à la denture, et (iii) des phénomènes de couplage intervenant dans des systèmes à plusieurs étages de réduction. La dernière application porte sur une architecture plus proche d'une boîte de transmission d'hélicoptère, combinant un engrenage cylindrique et un engrenage spiro-conique. Les résultats numériques témoignent des effets de couplage qui interviennent entre les deux étages de réduction, et de la forte influence des excitations générées par l'engrenage spiro-conique sur le reste du système.

Plusieurs perspectives de développement peuvent être identifiées à l'issue de ces travaux. La première concerne l'introduction des trains épicycloïdaux, qui constituent le dernier étage de réduction de la BTP dans la plupart des hélicoptères lourds. Plus d'attention pourrait aussi être accordée à la modélisation des éléments de roulements, ainsi qu'à la représentation de l'amortissement. Un autre axe de recherche concerne l'influence de la prise en compte du frottement à la denture sur la réponse dynamique du système, notamment au niveau des roulements. Enfin, l'introduction de géométries de type voile mince, couramment utilisées en aéronautique mérite certainement d'être étudiée.

SCIENTIFIC CONTRIBUTIONS

The work presented in this manuscript has led so far to several international journal papers and has been presented in different international conferences listed below:

Journal publications

Sainte-Marie, N., Velex, P. Roulois, G., Caillet, J., 2017, "A study on the correlation between dynamic transmission error and dynamic tooth loads in spur and helical gears", *Journal of Vibration and Acoustics*, **139** (February)

Conference publications and oral presentations

Sainte-Marie, N., Velex, P. Roulois, G., Caillet, J., 2016, "Multi-mesh dynamic models based on transmission errors", *International Conference on Power Transmissions*, Chongqing, China

Sainte-Marie, N., Velex, P. Roulois, G., Marrot, F., 2015, "Transmission error based simulations of the dynamic response of geared systems – On the influence of spacing errors on spur and helical gear dynamics", *VDI International Conference on Gears*, Munich, Germany

Sainte-Marie, N., Velex, P. Roulois, G., Marrot, F., 2015, "On the correlation between dynamic transmission error and dynamic tooth loads in three-dimensional gear systems", *ASME Power Transmission and Gearing conference*, Boston, Massachusetts, USA

FOLIO ADMINISTRATIF

THESE DE L'UNIVERSITE DE LYON OPEREE AU SEIN DE L'INSA LYON

NOM : SAINTE-MARIE DATE de SOUTENANCE : 09/12/2016

Prénoms : Nina

TITRE :
A transmission-error-based gear dynamic model – Applications to single- and multi-mesh transmissions

NATURE : Doctorat Numéro d'ordre : 2016LYSEI133

Ecole doctorale : MEGA

Spécialité : Génie Mécanique

RESUME :
Les spectres de bruit mesurés en cabine d'hélicoptère montrent que la boîte de transmission principale (BTP) est un des principaux contributeurs au bruit perçu par les usagers. Elle génère en effet plusieurs raies émergeant fortement du bruit large bande et dont les fréquences se situent dans la plage de sensibilité maximale de l'oreille humaine.

Dans un contexte d'amélioration permanente du confort acoustique des usagers, un modèle numérique est développé pour prédire le comportement dynamique des BTP. Les équations du mouvement sont écrites sur la base de fonctions du temps représentatives des excitations générées par l'engrènement (raideur d'engrènement et erreurs de transmission).

Plusieurs éléments de validation sont présentés pour confirmer la pertinence de la formulation proposée. Différents résultats numériques et expérimentaux de la littérature sont utilisés à des fins de comparaison, montrant que le modèle s'applique aux systèmes à simple étage de réduction, par engrenage cylindrique ou spiro-conique. La validation est ensuite étendue aux systèmes à deux étages de réduction et les résultats confirment que la formulation basée sur les erreurs de transmission permet de tenir compte des corrections de profil.

Finalement, le modèle est utilisé pour diverses applications. Premièrement, l'influence des erreurs de pas sur le comportement dynamique de transmissions par engrenages est discutée, ainsi que l'influence combinée du niveau de chargement appliqué. Dans un second temps, la relation entre l'erreur de transmission dynamique et différents coefficients dynamiques est étudiée. Le contenu spectral de la réponse au niveau des roulements est ensuite analysé pour des systèmes à deux engrènements cylindriques et l'influence de différents paramètres est discutée. Enfin, une application est réalisée sur un système comprenant un engrenage cylindrique et un engrenage spiro-conique. Les phénomènes de couplage entre les étages successifs sont mis en évidence ainsi que la contribution des deux engrènements au contenu spectral de la réponse aux roulements.

MOTS-CLÉS :
Multi-stage gear transmissions, Three-dimensional model, Transmission errors, Dynamics, Vibration

Transmissions par engrenages multi-étages, Modèle tridimensionnel, Erreurs de transmission, Dynamique, Vibration

Laboratoire de recherche :
Laboratoire de Mécanique des Contact et des Structures (LaMCoS)

Directeur de thèse:
Professeur Philippe VELEX

Président de jury :
Professeur Jean-Luc DION

Composition du jury :
Nevzat ÖZGÜVEN, Peter TENBERGE, Michèle GUINGAND,
Jean-Luc DION, Fabrice VILLE, Philippe VELEX, Guillaume ROULOIS